ISSN 2500-316X (Online)

RUSSIAN TECHNOLOGICAL JOURNAL

РОССИЙСКИЙ ТЕХНОЛОГИЧЕСКИЙ ЖУРНАЛ

Information systems.
Computer sciences.
Issues of information security

Multiple robots (robotic centers) and systems.
Remote sensing and non-destructive testing

Modern radio engineering and telecommunication systems

Micro- and nanoelectronics.
Condensed matter physics

Analytical instrument engineering and technology

Mathematical modeling

Economics of knowledge-intensive and high-tech enterprises and industries.
Management in organizational systems

Product quality management. Standardization

Philosophical foundations of technology and society

12+
www.rtj-mirea.ru

12(4) 2024

ISSN 2500-316X (Online)

RUSSIAN TECHNOLOGICAL JOURNAL

РОССИЙСКИЙ ТЕХНОЛОГИЧЕСКИЙ ЖУРНАЛ

- Information systems. Computer sciences. Issues of information security
- Multiple robots (robotic centers) and systems. Remote sensing and non-destructive testing
- Modern radio engineering and telecommunication systems
- Micro- and nanoelectronics. Condensed matter physics
- Analytical instrument engineering and technology
- Mathematical modeling
- Economics of knowledge-intensive and high-tech enterprises and industries. Management in organizational systems
- Product quality management. Standardization
- Philosophical foundations of technology and society

- Информационные системы. Информатика. Проблемы информационной безопасности
- Роботизированные комплексы и системы. Технологии дистанционного зондирования и неразрушающего контроля
- Современные радиотехнические и телекоммуникационные системы
- Микро- и наноэлектроника. Физика конденсированного состояния
- Аналитическое приборостроение и технологии
- Математическое моделирование
- Экономика наукоемких и высокотехнологичных предприятий и производств. Управление в организационных системах
- Управление качеством продукции. Стандартизация
- Мировоззренческие основы технологии и общества

Russian Technological Journal
2024, Vol. 12, No. 4

Russian Technological Journal
2024, том 12, № 4

https://www.rtj-mirea.ru

https://doi.org/10.32362/2500-316X

ISSN 2500-316X (Online)

Russian Technological Journal
2024, Vol. 12, No. 4

Publication date July 30, 2024.

The peer-reviewed scientific and technical journal highlights the issues of complex development of radio engineering, telecommunication and information systems, electronics and informatics, as well as the results of fundamental and applied interdisciplinary researches, technological and economical developments aimed at the development and improvement of the modern technological base.

Periodicity: bimonthly.
The journal was founded in December 2013. The titles were «Herald of MSTU MIREA» until 2016 (ISSN 2313-5026) and «Rossiiskii tekhnologicheskii zhurnal» from January 2016 until July 2021 (ISSN 2500-316X).

Founder and Publisher:
Federal State Budget
Educational Institution of Higher Education
«MIREA – Russian Technological University»
78, Vernadskogo pr., Moscow, 119454 Russia.

The journal is included into the List of peer-reviewed science press of the State Commission for Academic Degrees and Titles of Russian Federation. The Journal is included in Russian State Library (RSL), Russian Science Citation Index, eLibrary, Socionet, Directory of Open Access Journals (DOAJ), Directory of Open Access Scholarly Resources (ROAD), Google Scholar, Ulrich's International Periodicals Directory.

The registration number ПИ № ФС 77 - 81733 was issued in August 19, 2021 by the Federal Service for Supervision of Communications, Information Technology, and Mass Media of Russia.

The subscription index of *Pressa Rossii*: **79641**.

Russian Technological Journal
2024, том 12, № 4

Дата опубликования 30 июля 2024 г.

Научно-технический рецензируемый журнал освещает вопросы комплексного развития радиотехнических, телекоммуникационных и информационных систем, электроники и информатики, а также результаты фундаментальных и прикладных междисциплинарных исследований, технологических и организационно-экономических разработок, направленных на развитие и совершенствование современной технологической базы.

Периодичность: один раз в два месяца.
Журнал основан в декабре 2013 года. До 2016 г. издавался под названием «Вестник МГТУ МИРЭА» (ISSN 2313-5026), а с января 2016 г. по июль 2021 г. под названием «Российский технологический журнал» (ISSN 2500-316X).

Учредитель и издатель:
федеральное государственное бюджетное образовательное учреждение высшего образования
«МИРЭА – Российский технологический университет»
119454, РФ, г. Москва, пр-т Вернадского, д. 78.

Журнал входит в Перечень ведущих рецензируемых научных журналов ВАК РФ, в которых должны быть опубликованы основные научные результаты диссертаций на соискание ученой степени кандидата наук и доктора наук, индексируется в РГБ, РИНЦ, eLibrary, Соционет, Directory of Open Access Journals (DOAJ), Directory of Open Access Scholarly Resources (ROAD), Google Scholar, Ulrich's International Periodicals Directory.

Регистрационный номер и дата принятия решения о регистрации СМИ ПИ № ФС 77 - 81733 от 19.08.2021 г. СМИ зарегистрировано Федеральной службой по надзору в сфере связи, информационных технологий и массовых коммуникаций (Роскомнадзор).

Индекс по объединенному каталогу «Пресса России» **79641**.

https://www.rtj-mirea.ru

Editorial Board

Редакционная коллегия

Contents

Information systems. Computer sciences. Issues of information security

7 *Andrey S. Zuev, Dmitrii A. Leonov*
About managing the number of simultaneously functioning software robots of different types

23 *Evgeniy F. Pevtsov, Tatyana A. Demenkova, Alexander O. Indrishenok, Vladimir V. Filimonov*
Identification of digital device hardware vulnerabilities based on scanning systems and semi-natural modeling

Multiple robots (robotic centers) and systems. Remote sensing and non-destructive testing

40 *Igor I. Dawlyud*
Calculation of the main operational characteristics of a tethered high-altitude ship-based system

51 *Alexey A. Manushkin, Nikolay N. Potrachov, Alexander V. Stepanov, Evgeny Yu. Usachev*
Tomographic task solution using a dichotomous discretization scheme in polar coordinates and partial system matrices invariant to rotations

Modern radio engineering and telecommunication systems

59 *Mihail S. Kostin, Konstantin A. Boikov*
Digital technologies for signal radio vision and radio monitoring

70 *Alexander V. Ksendzuk, Vyacheslav F. Fateev*
Principles of construction of nanosatellite radar systems based on global navigation satellite system reflectometry

84 *Van D. Nguyen*
Studying the influence of correction codes on coherent reception of M-PSK signals in the presence of noise and harmonic interference

Micro- and nanoelectronics. Condensed matter physics

96 *Andrey A. Guskov, Nikita V. Bezvikonnyi, Sergey D. Lavrov*
Kretschmann configuration as a method to enhance optical absorption in two-dimensional graphene-like semiconductors

Mathematical modeling

106 *Bakhtierzhon Pashshoev, Denis A. Petrusevich*
Neural network analysis in time series forecasting

Содержание

Информационные системы. Информатика. Проблемы информационной безопасности

7 *А.С. Зуев, Д.А. Леонов*
Об управлении численностью одновременно функционирующих программных роботов различных видов

23 *Е.Ф. Певцов, Т.А. Деменкова, А.О. Индришенок, В.В. Филимонов*
Выявление аппаратных уязвимостей цифровых устройств на основе систем сканирования и полунатурного моделирования

Роботизированные комплексы и системы. Технологии дистанционного зондирования неразрушающего контроля

40 *И.И. Давлюд*
Расчет основных эксплуатационных характеристик привязной высотной системы корабельного базирования

51 *А.А. Манушкин, Н.Н. Потрахов, А.В. Степанов, Е.Ю. Усачев*
Решение томографической задачи с использованием дихотомической схемы дискретизации в полярных координатах и парциальных системных матриц, инвариантных к вращениям

Современные радиотехнические и телекоммуникационные системы

59 *М.С. Костин, К.А. Бойков*
Цифровые технологии сигнального радиовидения и радиомониторинга

70 *А.В. Ксендзук, В.Ф. Фатеев*
Принципы построения бортовых радиолокационных систем наноспутников, основанных на приеме отраженных сигналов спутниковых навигационных систем

84 *В.З. Нгуен*
Исследование влияния корректирующих кодов на когерентный прием сигналов с многопозиционной фазовой манипуляцией при наличии шумовой и гармонической помех

Микро- и наноэлектроника. Физика конденсированного состояния

96 *А.А. Гуськов, Н.В. Безвиконный, С.Д. Лавров*
Конфигурация Кречмана как метод увеличения оптического поглощения в двумерных графеноподобных полупроводниках

Математическое моделирование

106 *Б. Пашшоев, Д.А. Петрусевич*
Анализ нейросетевых моделей для прогнозирования временных рядов

Information systems. Computer sciences. Issues of information security

Информационные системы. Информатика. Проблемы информационной безопасности

UDC 007.52, 519.673, 519.687.1, 519.687.2, 519.852
https://doi.org/10.32362/2500-316X-2024-12-4-7-22
EDN BUECFJ

RESEARCH ARTICLE

About managing the number of simultaneously functioning software robots of different types

Andrey S. Zuev [@], **Dmitrii A. Leonov**

MIREA – Russian Technological University, Moscow, 119454 Russia
[@] *Corresponding author, e-mail: zuev_a@mirea.ru*

Abstract

Objectives. The study sets out to justify the relevance and investigate approaches for solving the problem of managing the number of simultaneously functioning software robots of various types under conditions of limited computational resources and changes in sets of executable tasks.

Methods. A proposed solution is based on models and methods of scenario management, linear programming, inventory management, queuing theory, and machine learning. The described methods are valid for different compositions and preconditions for generating initial data, as well as ensuring the relevance horizons of the obtained solutions.

Results. The initial data is obtained via the presented approach for determining the computational resource parameters for operating a single software robot. The resources are determined by analyzing the composition of the software and information services used by an actual software robot. Problem statements and mathematical models are developed for cases involving scenario management and linear programming methods. Methods for real-time management of the number of software robots and their sequential local optimization are proposed based on the abovementioned solution sequences. The developed method for generating statistical data based the results of applying the sequential local optimization method is used to identify deficient and non-deficient computational resources. Some results of working in the multi-functional center of RTU MIREA software robots developed on the Atom.RITA platform are outlined.

Conclusions. The emerging problem of managing the number of simultaneously operating software robots of various types for cases involving scenario control methods and linear programming is formalized. This problem is relevant in the field of automation of business processes of organizations. The use of mathematical methods for solving this problem opens up opportunities for expanding the functional capabilities of robotic process automation platforms, as well as increasing their economic efficiency to create competitive advantages by optimizing the use of IT infrastructure components.

Keywords: software robot, digital employee, robotic process automation, business process automation, software robotization

• **Submitted:** 23.04.2024 • **Revised:** 27.05.2024 • **Accepted:** 29.05.2024

For citation: Zuev A.S., Leonov D.A. About managing the number of simultaneously functioning software robots of different types. *Russ. Technol. J.* 2024;12(4):7–22. https://doi.org/10.32362/2500-316X-2024-12-4-7-22

Financial disclosure: The authors have no a financial or property interest in any material or method mentioned.

The authors declare no conflicts of interest.

НАУЧНАЯ СТАТЬЯ

Об управлении численностью одновременно функционирующих программных роботов различных видов

А.С. Зуев [@], **Д.А. Леонов**

МИРЭА – Российский технологический университет, Москва, 119454 Россия
[@] *Автор для переписки, e-mail: zuev_a@mirea.ru*

Резюме

Цели. Изложение постановки, обоснование актуальности и предложение методов решения задачи управления численностью одновременно функционирующих программных роботов различных видов в условиях ограниченности вычислительных ресурсов и изменений состава совокупностей задач, поступающих на выполнение.

Методы. Задачу предложено решать, применяя модели и методы сценарного управления, линейного программирования, управления запасами, массового обслуживания и машинного обучения, соответствующие различным составам и предпосылкам формирования исходных данных, а также обеспечивающие различные горизонты актуальности получаемых решений.

Результаты. В целях формирования исходных данных задачи авторами предложен подход к определению состава и параметров вычислительных ресурсов, требующихся для функционирования одного программного робота, основанный на анализе состава используемого им программного обеспечения и информационных сервисов. Для случаев применения методов сценарного управления и линейного программирования составлены постановки и математические модели соответствующих задач, а на основе последовательностей их решения предложены метод оперативного управления численностью программных роботов и метод последовательной локальной оптимизации их численности. Предложен основанный на обработке результатов применения метода последовательной локальной оптимизации способ формирования статистических данных, позволяющих идентифицировать дефицитные и недефицитные вычислительные ресурсы. Изложены некоторые результаты применения программных роботов, разрабатываемых на платформе «Атом.РИТА», в интересах многофункционального центра РТУ МИРЭА.

Выводы. Сформулирована и формализована для случаев применения методов сценарного управления и математического аппарата линейного программирования новая и актуальная в сфере автоматизации бизнес-процессов организаций задача управления численностью одновременно функционирующих программных роботов различных видов. Решение данной задачи с применением различных математических методов открывает перспективы расширения функциональных возможностей платформ программной роботизации, а также повышения экономической эффективности их применения и формирования дополнительных конкурентных преимуществ посредством оптимизации использования компонентов ИТ-инфраструктуры.

Ключевые слова: программный робот, цифровой сотрудник, robotic process automation, автоматизация бизнес-процессов, программная роботизация

• **Поступила:** 23.04.2024 • **Доработана:** 27.05.2024 • **Принята к опубликованию:** 29.05.2024

Для цитирования: Зуев А.С., Леонов Д.А. Об управлении численностью одновременно функционирующих программных роботов различных видов. *Russ. Technol. J.* 2024;12(4):7–22. https://doi.org/10.32362/2500-316X-2024-12-4-7-22

Прозрачность финансовой деятельности: Авторы не имеют финансовой заинтересованности в представленных материалах или методах.

Авторы заявляют об отсутствии конфликта интересов.

INTRODUCTION

Over the last 10 years, one of the main sources of the improved efficiency of legal entities, government and commercial structures, etc., (hereinafter—organizations) consists in the automation of business processes to delegate repetitive, routine and non-analytical tasks and actions from employees to specialized services [1–3]. Various subject-oriented information systems [4, 5], such as electronic document management, personnel management, warehouse logistics, accounting, interaction with target audience and clients, project management, analytical and intelligent systems, etc., can serve as tools for automating business processes. At the same time, the use of application software in the business processes of organizations implies the presence of appropriate personnel, who use this software to perform business tasks included in the business functions assigned to them in accordance with their allocated roles [6].[1] In the present work, a business task is understood as a typical sequence of actions of an employee using a set of software tools to achieve a given result taking into account the changing composition of input data.

A logical and innovative direction having occurred during the development of business process automation consists in software robotization systems known as robotic process automation (RPA) [7, 8]. RPA software, which implements technologies for the development and application of software robots (SR), comprises special applications whose operational scenarios reproduce typical sequences of actions carried out by employees using combinations of software tools.[2] Since December 4, 2023, RPAs are legally defined by the Ministry for Digital Technology, Communication and Mass Media of the Russian Federation.[3]

An important feature of an RPA is the possibility for an SR to work with the totality of information systems and services that are not provided with a means of integration and interoperability in accordance with embedded functional scenarios or algorithms [9]. There are currently several RPA-platforms on the international[4] and Russian[5] software markets that provide tools for development and management of SR functionality.

Software robots partially or fully replace employees of an organization in its business processes in terms of performing typical business tasks, i.e., they either act as “digital employees” functioning in accordance with a specific business role, which is traditionally provided for in the staff schedule [10], or they function as “digital assistants” of real employees [11]. The advantages of a digital employee for an organization are obvious [12, 13]: a 24/7/365 work schedule, no working conditions or salary requirements, elimination of recruiting procedures, training, work control, personnel “turnover”, etc.

Business tasks subject to software robotization will be referred to as robotic automation tasks (RAT). We will assume that there is a mutually unambiguous correspondence between RATs and the SRs that perform them, each SR corresponding to a separate RAT. Based on the results of executing the scenario of a particular business task, each of its instances is either considered as successfully completed (which should correspond to the vast majority of cases), or is added to the list of incidents that require additional consideration by an employee, including in cases of unsatisfactory completion of the SR functioning scenario. One of the advantages of using SRs is the ease of scaling their application when changing the intensity of business tasks, which will be further understood as the number of their repetitions or instances requiring execution for some given period of time. Necessary indicators of business processes fulfillment efficiency can be provided as a result of increasing or decreasing the number of simultaneously functioning SR corresponding to these business processes. Under conditions of limited computational resources allocated for their application in compliance with the required performance indicators of the corresponding business processes, the simultaneous application of a set of SR types, each having the possibility of replication in different quantities, the management of the number of simultaneously functioning SRs of different types becomes a relevant problem.

[1] On Amending the Classifier of Programs for Electronic Computing Machines and Databases Approved by Order of the Ministry of Digital Development, Communications and Mass Media of the Russian Federation No. 486 of September 22, 2020. Order of the Ministry of Digital Development, Communications and Mass Media of the Russian Federation No. 974 dated December 22, 2022. http://publication.pravo.gov.ru/Document/View/0001202304200009 (in Russ.). Accessed March 22, 2024.

[2] On Approval of the Classifier of Programs for Electronic Computing Machines and Databases. Order of the Ministry of Digital Development, Communications and Mass Media of the Russian Federation No. 486 dated September 22, 2020. https://digital.gov.ru/ru/documents/7362/ (in Russ.). Accessed March 26, 2024.

[3] On Amending the Classifier of Programs for Electronic Computing Machines and Databases Approved by Order of the Ministry of Digital Development, Communications and Mass Media of the Russian Federation No. 486 dated September 22, 2020. Order of the Ministry of Digital Development, Communications and Mass Media of the Russian Federation No. 1041 dated December 04, 2023. http://publication.pravo.gov.ru/document/0001202403110026 (in Russ.). Accessed March 26, 2024.

[4] Top-31 best robotic process automation software on the market. https://www.zaptest.com/rpa-tools-top-31-best-robotic-process-automation-software-on-the-market. Accessed March 22, 2024.

[5] Russian market of RPA-systems. Tadviser November 8, 2022. https://www.tadviser.ru/index.php/Статья:Российский_рынок_RPA-систем (in Russ.). Accessed March 22, 2024.

1. DESCRIPTION OF SR NUMBER MANAGEMENT TASK

As application software and executed as processes in the operating system, SRs consume computational resources, which should be considered as not only finite, but also subject to optimization. Problems that arise in this connection are relevant both for individual organizations using SRs in terms of minimizing the costs of their operation, as well as for the providers of cloud "factories" of SRs [14, 15] in the context of optimizing the costs of maintaining the corresponding IT infrastructure.

In the IT infrastructure of organizations that use SRs and/or supply services to ensure their operation, the solution of the abovementioned problems requires the development, justification and implementation of both architectural and infrastructural solutions. Architectural solutions can be considered, for example, in the context of ensuring information security, including the operation of SR on physical and virtual machines in open and protected circuits [16, 17]. Infrastructure solutions imply the allocation of physical and/or virtual machines with certain parameters and characteristics that provide computational resources sufficient for the functioning of a certain set of SR of several types in compliance with the required performance indicators of the corresponding business processes of the organization. Computational resources can be understood as:

- number of threads of the central processing unit (CPU);
- amount of random-access memory (RAM);
- amount of the internal data storage device (hard disk drive, HDD and/or solid-state drive, SSD);
- amount of video memory and the number of graphics processing unit (GPU) cores;
- number of simultaneous terminal sessions;
- bandwidth of a wired or wireless transmission network channel, etc.

The information and technological infrastructure of SR functionality is one of the key parameters predetermining the effectiveness of their application. Therefore, its formation should take into account, among other things, the following aspects:

- composition of software and information services with which the SR interacts is determined by the content of the corresponding business task and predetermines the requirements to the operating environment of its functioning to the required computational resources;
- while several SRs from some set of their types can operate simultaneously, the permissible combinations of their numbers are limited by the allocated computational resources;
- in case of a large variety of types of SR, as well as under conditions of their "factory" implementation, the set of applied SR can be decomposed into subsets corresponding to separate business processes and/or structural subdivisions of the organization with allocation of separate (independent) volumes of computational resources;
- due to changes in the intensities of business tasks performed by SRs (the number of their repetitions, instances requiring execution for a given period of time), it becomes rational to vary the number of SRs of corresponding types while limiting the computational resources allocated for the realization of their entire set (the set of types and instances of each type);
- changes in parameter and business processes requirements, including those business tasks solved by SR, may affect the number of SRs and intensity of corresponding tasks.

Considering the abovementioned aspects of the implementation of SR aggregates, the task of managing the number of simultaneously functioning SRs of various types under conditions of limited computational resources, changing intensities of RPAs, as well as varying requirements to the parameters of the corresponding business processes, becomes of practical importance. Such an optimization approach, which involves different statements corresponding to the particular prerequisites for the formalization of the initial data, can be solved using a range of formulations and mathematical instruments [18].

Various RPA-platforms include a component of managing the operation of SRs ("master" or "orchestrator"), which performs the functions of starting and stopping them (including in accordance with the specified schedule), managing licenses, integration, versioning, logs, analytics, accesses, etc. Taking into account a certain composition of formalized constraints and requirements, the dynamic optimization of the number of simultaneously functioning SRs of different types can be considered as an additional functionality of this control component, providing the expansion of competitive advantages of the RPA-platform by optimizing the use of IT-infrastructure components to ensure the functioning of SRs.

Some of the different approaches and methods for solving the formulated problem are compared in Table 1:

- scenario management—available variants of the number of SRs of different types are considered as a set of management scenarios from which the most rational is selected according to the current intensity of forming the business tasks;
- mathematical tool of linear programming—optimal numbers of SRs of various types are determined on

Table 1. Comparison of some methods of solving the task under consideration

Applied mathematical tool	Features of the mathematical tool used	Relevance period of the decision	Application result
Scenario approach to management (described in this article)	Situational response to changing intensities of business tasks is performed	Operational (immediate)	Rationalization in accordance with changes in input data
Machine learning models	Iterative pre-training of the neural network is assumed	Operational (immediate)	
Linear programming (described in this article)	In separate periods of time the previously accumulated business tasks are performed and a new set of business tasks is formed for performance	Short-term	Optimization according to the result of processing of accumulated input data
Inventory management models	Patterns of generation of business tasks with the passage of time are assumed to be known	Medium-term	
queuing theory		Long-term	

the basis of aggregates of corresponding business tasks to be performed over a certain period of time;

- inventory management models—based on formalization of the dynamics of business tasks receipt for processing and their execution by the SRs;
- queuing theory—regularities of change of business task intensities over time are assumed to be known (specified or formalized as a result of a preliminary analysis);
- since SR instances of corresponding types are considered as channels of a queuing theory, their number can be varied to control the characteristics of the considered system;
- machine learning models—the construction and/or training of neural networks is assumed for automating decision-making regarding the number of simultaneously functioning SRs of various types in accordance with the dynamics and/or forecasts of changes in the values of some set of formalized constraints and requirements.

As well as assuming the presence of assumptions corresponding to them concerning the available structure and the results of preliminary formalization of its initial data, the different methods of solving the problem under consideration allow us to provide different horizon of autonomy for the implementation of the obtained solution without requiring further correction.

In the following section, different formulations of the problem under consideration are described for the cases of scenario management and a mathematical linear programming apparatus. A detailed description of its formulations and formalizations using other mathematical apparatuses, including those not listed in Table 1, will be the subject of a future work.

2. APPROACH FOR DETERMINING THE COMPOSITION AND PARAMETERS OF COMPUTATIONAL RESOURCES REQUIRED FOR THE SR

The first stage of forming the initial data of the task under consideration consists in determining the composition and amount of computational resources required for the functioning of one SR of each type. For this purpose, a table similar to Table 2 can be used to form the required data as a result of systematization of software and information services involved in the performance of relevant business tasks. Such computational hardware resources as the number of CPU threads, amount of RAM, number of GPU cores, amount of internal data storage, maximum available number of terminal sessions, bandwidth of the communication channel, etc., can be considered as limited within the organization's IT infrastructure allocated for the purposes of software robotization and additive across the entire set of simultaneously functioning SRs.

3. TASK STATEMENT FOR THE CASE OF SCENARIO MANAGEMENT APPLICATION

In cases of operative (instantaneous) variation of numbers of simultaneously functioning SRs of different types, the application of scenario management becomes expedient. In accordance with a one-step (current) change in the intensity of business tasks (the number of their instances received for processing at a moment in time), it may be necessary to make an instantaneous decision on the transition to a scenario corresponding to the given conditions that involves a combination of the

Table 2. Determination of the computational resources required by the SRs based on the composition of used software

Computational resource	Software used	Resource required by the software	Number of copies of the software required by the SR			
			Robot No. 1	Robot No. 2	…	Robot No. *n*
RAM capacity, MB (resource No. 1)	Software No. 1 (browser)	O_{11}	3	0	…	1
	Software No. 2 (word processor)	O_{12}	1	2	…	0
	…	…	…	…	…	…
	Software No. *k* (mail)	O_{1k}	1	1	…	1
SR needs for resource No. 1		Value	$3O_{11} + O_{12} + \ldots + O_{1k}$	$2O_{12} + \ldots + O_{1k}$	…	$O_{11} + \ldots + O_{1k}$
		Designation	a_{11}	a_{12}	…	a_{1n}
Number of CPU threads (resource No. 2)	Software No. 1 (browser)	P_{21}	3	0	…	1
	Software No. 2 (word processor)	P_{22}	1	2	…	0
	…	…	…	…	…	…
	Software No. *k* (mail)	P_{2k}	1	1	…	1
SR needs for resource No. 2		Value	$3P_{21} + P_{22} + \ldots + P_{2k}$	$2P_{22} + \ldots + P_{2k}$	…	$P_{21} + \ldots + P_{2k}$
		Designation	a_{21}	a_{22}	…	a_{2n}
…	…	…	…	…	…	…
Data storage capacity, MB (resource No. *m*)	Software No. 1 (browser)	H_{m1}	3	0	…	1
	Software No. 2 (word processor)	H_{m2}	1	2	…	0
	…	…	…	…	…	…
	Software No. *k* (mail)	H_{mk}	1	1	…	1
SR needs for resource No. *m*		Value	$3H_{m1} + H_{m2} + \ldots + H_{mk}$	$2H_{m2} + \ldots + H_{mk}$	…	$H_{m1} + \ldots + H_{mk}$
		Designation	a_{m1}	a_{m2}	…	a_{mn}

number of simultaneously functioning SRs of different types. Different approaches to the realization of scenario control of the numbers of simultaneously functioning SRs obtained from some set of their species are possible. Two approaches proposed by the authors are outlined below.

Assuming that one SR of type j consumes a_{ij} computational resources of type i when performing its corresponding business task of the same type j, we introduce the following designations:

- b_i are the available (limited) volumes of computational resources of the types $i = \overline{1,m}$, where m is their number;
- x_j are the numbers of simultaneously functioning SR of the types $j = \overline{1,n}$, where n is their number;
- c_j is the performance of one SR of type j, equal to the number of instances of a business task of this type j performed by it during a unit time period;
- $e_j \geq 1$ are the coefficients of relative priority of business tasks of respective types $j = \overline{1,n}$.

We will call scenarios $P_k = (x_{k1}, x_{k2}, ..., x_{kn})$, where $k = \overline{1,p}$, the options of simultaneous use of specific quantities x_{kj}, $j = \overline{1,n}$ SR of each of the types. Here, we consider only the scenarios admissible for realization on the basis of the total amounts of required computational resources.

In order to determine the composition of admissible scenarios, each associated with the maximum use of one or more allocated computational resources, we can use an auxiliary table similar to Table 3 to structure the search of combinations of the number of simultaneously functioning robots of each type. When moving to each subsequent row of the table, the computational resources are redistributed in favor of the SR with a higher order number.

Preliminary formation of the composition of acceptable scenarios allows us not to perform their formation at each solution of the task under consideration, but to determine the rational (not excessive) composition of functioning SRs by selecting a scenario from those contained in scenario tables such as Table 3.

There are 2 possible approaches to the development of scenario tables:

1. Formation of a complete scenario composition including scenarios with incomplete utilization of computational resources. This leads to the inclusion in the scenario table of the results of a complete search of possible combinations of SRs. While increasing computational resources, it reduces the logical complexity of analyzing the scenario table content. For example, formulas (4) and (7) proposed by the authors below can be applied without checking additional relevant conditions (5) and (8). This approach is more appropriate for small amounts of allocated computational resources and/or a small number of SR types.

Table 3. Determination of the composition of scenarios of simultaneous operation of the SR with maximum utilization of one or several allocated computational resources

Scenarios	Number of functioning robots of types j							
	1	2	3	4	5	...	$n-1$	n
P_1	Q	0	0	0	0	...	0	0
P_2	$Q-1$	1	0	0	0	...	0	0
P_3	$Q-1$	0	2	0	0	...	0	0
P_4	$Q-1$	0	1	2	0	...	0	0
P_5	$Q-1$	0	1	1	1	...	0	0
P_6	$Q-1$	0	0	3	1	...	0	0
...	...	...	...	...	...	...	...	...
P_k	$Q-1$	0	0	0	0	...	0	r
P_{k+1}	$Q-2$	2	0	0	0	...	0	0
...	...	...	...	...	...	...	...	...
P_{p-1}	0	0	0	0	0	...	1	$R-1$
P_p	0	0	0	0	0	...	0	R

2. Formation of scenario composition with maximum use of one or several allocated computational resources. While leading to a significant reduction in the number of records in the scenario table, it necessitates checking the possibility of reducing the number of simultaneously functioning SRs. In this regard, the formulas (4) and (7) proposed by the authors below will require verification of additional corresponding conditions (5) and (8). This approach is more appropriate for large amounts of allocated computational resources and/or a large number of types of SRs.

The efficiency of the above-described approaches should be studied for each specific task of managing the number of simultaneously functioning SRs. While the approach that provides the most expected speed of solving the corresponding task will naturally be preferred, each of the approaches forms the initial data for determining the corresponding realizable scenario.

The implemented scenario predetermines the number of business tasks of each type performed by the corresponding set of SRs for a single period of time. A change in the realized scenario leads to a change in the composition of simultaneously functioning SRs. These changes can be determined once with the help of

a transition table similar to Table 4 for all possible pairs of considered acceptable scenarios from Table 3 and further used for automatic selection of the most rational scenario, to which it is expedient to switch from the currently used one under the conditions of the observed change in the intensity of receiving the business tasks.

Let us designate the change in the number of simultaneously functioning SRs of species j as a result of the change from scenario x to scenario y through z_j^{xy}. Then T^{xy} (1) is the vector of changes in the numbers of simultaneously functioning SRs during the transition from scenario x to scenario y:

$$T^{xy} = (z_1^{xy}, z_2^{xy}, ..., z_n^{xy}). \quad (1)$$

The vector of corresponding changes in productivity of business tasks of types j can be calculated by the formula:

$$U^{xy} = (c_1 z_1^{xy}, c_2 z_2^{xy}, ..., c_n z_n^{xy}). \quad (2)$$

The first proposed approach to scenario-based management of SR functioning consists in matching scenarios and task sets at a given unit of time to the tasks coming in for implementation.

Let us assume that for a single period of time a pending set of business tasks of types j (taking into account their quantities not executed at previous stages), described by a vector of non-negative integer components F, has been formed:

$$F = (f_1, f_2, ..., f_n), \quad (3)$$

then scenario G, which can be considered as the most rational for realization in the next period of time, can be determined on the basis of Table 3 by the formula:

$$G = \min_{k=\overline{1,p}} G_k, \text{ where } G_k = \sqrt{\sum_{j=1}^{n} e_j (f_j - c_j x_{kj})^2}$$

$$\text{or } G_k = \sum_{j=1}^{n} e_j \left| f_j - c_j x_{kj} \right|, \ k = \overline{1,p}, \quad (4)$$

at that, if $f_j - c_j x_{kj} \le 0$, then the corresponding summand j is considered to be equal to zero, and the number of robots x_{kj}^* of type j, which does not need to be launched, can be determined by the formula:

Table 4. Example of a transitional table—changes in the numbers of functioning SRs under changing scenarios

Change of scenarios		Change in the number of functioning robots of the types j							
Initial scenario	New scenario	1	2	3	4	5	…	$n-1$	n
P_1	P_1	0	0	0	0	0	…	0	0
P_1	P_2	−1	+1	0	0	0	…	0	0
P_1	P_3	−1	0	+2	0	0	…	0	0
P_1	P_4	−1	0	+1	+2	0	…	0	0
P_1	P_5	−1	0	+1	+1	+1	…	0	0
P_1	P_6	−1	0	0	+3	+1	…	0	0
…	…	…	…	…	…	…	…	…	…
P_1	P_k	−1	0	0	0	0	…	0	$+r$
P_1	P_{k+1}	−2	+2	0	0	0	…	0	0
…	…	…	…	…	…	…	…	…	…
P_1	P_p	$-Q$	0	0	0	0	…	0	$+R$
P_2	P_1	+1	−1	0	0	0	…	0	0
…	…	…	…	…	…	…	…	…	…
P_{p-1}	P_1	$+Q$	0	0	0	0	…	−1	$-R+1$
P_p	P_1	$+Q$	0	0	0	0	…	0	$-R$

Table 5. Input data for Fig. 1 ($e_j = 1, j = \overline{1,n}$)

Time period	Set of tasks to perform				Set of tasks completed by the SR				Value according to formula (4)
	f_1	f_2	f_3	Point	c_1x_{k1}	c_2x_{k2}	c_3x_{k3}	Point	
1	2	2	3	B(2; 2; 3)	2	1	2	D(2; 1; 2)	$\sqrt{2}$ or 2
2	3	2 + 1	1 + 1	C(5; 4; 4)	2	2	0	G(4; 3; 2)	$2\sqrt{2}$ or 4
3	1 + 1	3 + 1	2 + 2	A(6; 7; 6)	2	4	2	Z(6; 7; 4)	2 or 2

$$x_{kj}^{*} = \left\lfloor c_j x_{kj} - f_j \right\rfloor. \quad (5)$$

The second proposed approach to scenario-based management of SR functioning consist in comparing the results of scenario changes and changes in the composition of the sets of tasks to be performed in a given unit of time.

Let us assume that for a unit period of time of realization of some scenario t, changes in the numbers of business tasks of types j to be performed (taking into account their numbers not performed at previous stages) are described by a vector of non-negative integer components F^*:

$$F^* = (f_1, f_2, ..., f_n), \quad (6)$$

then the scenario G, which can be considered as most rational for transition to implementation, can be determined on the basis of Table 4 by the formula:

$$G = \min_{k=\overline{1,p}} G_k, \text{ where } G_k = \sqrt{\sum_{j=1}^{n} e_j (f_j - c_j z_j^{tk})^2}$$

$$\text{or } G_k = \sum_{j=1}^{n} e_j \left| f_j - c_j z_j^{tk} \right|, \ k = \overline{1,p}, \quad (7)$$

at that, if $f_j - c_j z_j^{tk} \le 0$, then the corresponding summand j is considered to be equal to zero, and the number of robots x_{kj}^{**} of type j, which does not need to be launched, can be determined by the formula:

$$x_{kj}^{**} = \left\lfloor c_j z_j^{tk} - f_j \right\rfloor. \quad (8)$$

Generalization of proposed approaches. Formulas (4) and (7) in the part of calculation of G_k values are made for Euclidean and Minkowski metrics and allow us to choose the vector G of the smallest length among all vectors, which are the result of subtraction of the vector of productivity or change of productivity of performance of business tasks of types j from the vector of pending business tasks or the vector of changes in the number of pending business tasks.

Vector G enables to determine the scenario k, which is the most rational for application, or to which it is most rational to switch from scenario t in accordance with the current intensity of business tasks at the moment of time. That is, the management of the number of simultaneously functioning SR types j is reduced to the maximum possible repetition of the dynamics of intensity or dynamics of change in the intensity of business tasks with a delay of one-unit time interval. The conditional illustration is presented in Fig. 1. The axes f_1, f_2, and f_3 correspond to three types of business tasks and corresponding SRs; the initial data are given in Table 5.

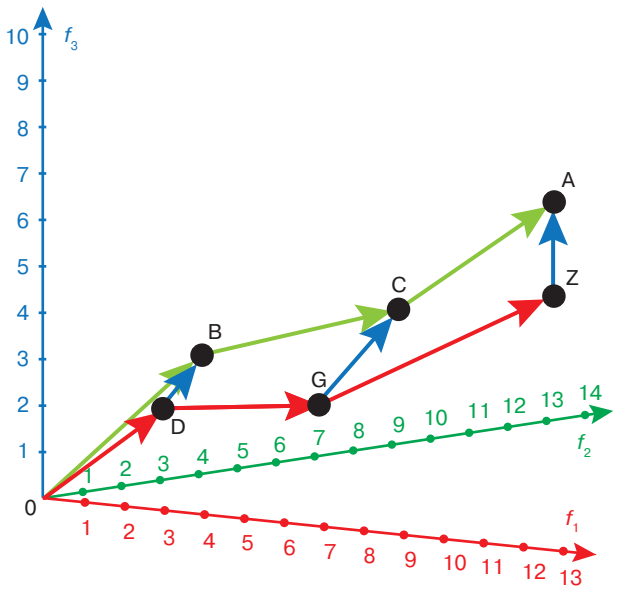

Fig. 1. Examples of vectors illustrating the application of formulas (4) and (7)

Thus, the proposed method of operative management of the number of functioning SRs from some set of their types under the conditions of limited computational resources and dynamic changes in the composition of the business tasks for execution does not require the solution of optimization tasks.

4. TASK STATEMENT FOR THE CASE OF THE LINEAR PROGRAMMING APPLICATION

The application of the mathematical apparatus of integer linear programming becomes expedient in those cases when the content of business processes enables the fulfillment of previously accumulated business tasks to be performed in short-term (single) periods of time and parallel formation of sets of business tasks that should be performed. Thus, not only is a set of business tasks to be performed formed at each small-time interval, which requires optimization of the number of SRs of corresponding types for the next time interval, but also a set of SRs optimized in accordance with the set of tasks formed in the previous time interval functions.

Initial data:

- n is the number of SR types and the corresponding number of types of business tasks to be performed;
- m is the number of types of limited computational resources;
- P_j are the designations (names) of the SR types, $j=\overline{1,n}$;
- Z_j are the designations (names) of the business task types, $j=\overline{1,n}$;
- c_j is the performance of one SR of P_j type, equal to the number of instances of a business task of the corresponding Z_j type performed by them during a unit time period;
- d_j is the number of instances of a business task of the corresponding type Z_j to be performed at the moment of solving the optimization task;
- e_j are the fixed coefficients of relative priority of business tasks of the corresponding Z_j types;
- f_j are the variable coefficients of relative priority of business tasks of the corresponding Z_j types, determined before solving the optimization task on the basis of d_j values by different methods, for example, by the formula:

$$f_j=\frac{d_j}{\sum_{j=1}^{n} d_j},\ j=\overline{1,n}, \tag{9}$$

- x_j is the number of simultaneously functioning robots of the type P_j;
- S_i are the names of types of limited computational resources, $i=\overline{1,m}$;
- b_i is the available (limited) amount of computational resource of S_i type;
- a_{ij} is the consumption of computational resource of S_i type during the operation of one SR of P_j type, where $i=\overline{1,m}$ and $j=\overline{1,n}$.

Task statement: Such a combination of values x_j, $j=\overline{1,n}$ (the plan of functioning of SR of P_j type) should be determined at which the number of executed instances of corresponding business tasks Z_j will be maximum taking into account their priority coefficients e_j and f_j; the consumed volumes of computational resources of each of S_i types, $i=\overline{1,m}$ will not exceed the corresponding constraints b_i; the number of executed instances of business tasks of all P_j types will not exceed their number d_j to be executed at the moment of solving the optimization task.

Note: in accordance with different conditions of the task statement and prerequisites for solving this task, any variants of combining the presence of coefficients e_j and f_j, $j=\overline{1,n}$ (10) may be taken into account in the composition of the target function.

The mathematical model of the task comprises:

- a target function maximizing the total number of executed instances of business tasks Z_j, $j=\overline{1,n}$, taking into account their priority coefficients e_j and f_j, as well as the performance of SR of P_j types;
- a system of constraints that takes into account: the limited b_i computational resources of S_i types, $i=\overline{1,m}$; the set d_j of business tasks to be performed by Z_j types, $j=\overline{1,n}$, formed at the moment of solving the optimization task; the requirements of non-negativity and integer values of variables x_j, which are a consequence of the fact that they correspond to the number of simultaneously functioning SRs of P_j types;

$$\begin{cases} \sum_{j=1}^{n} a_{ij}x_j \le b_i, i=\overline{1,m}, \\ c_j x_j \le d_j, j=\overline{1,n}, \\ x_j \ge 0, j=\overline{1,n}, \\ x_j - \text{int.}, j=\overline{1,n}, \end{cases} \tag{10}$$

$$F=\sum_{j=1}^{n} c_j e_j f_j x_j \to \max.$$

The system of constraints of the task under consideration may also include additional conditions describing, for example, a restriction on the total number of simultaneously functioning SRs (simultaneous number of terminal sessions):

$$\sum_{j=1}^{n} x_j \le X.$$

Within the framework of the above task statement (10), the period of operation of a set of SRs is divided into single time segments, within each of which a set of business tasks to be performed is accumulated. After obtaining a solution to the optimization problem

for implementation during the next time segment, the optimization problem solution obtained during the previous time segment is directly implemented. The number of business tasks not accepted for execution by the SR based on the results of the optimization task solution can be determined by the following formula:

$$g_j = d_j - c_j x_j,\ j = \overline{1,n}. \quad (11)$$

The values $g_j, j = \overline{1,n}$, are added to the set of business tasks to be performed in the next single time period; the increase of their values during the consecutive solution of the optimization task under consideration signals the insufficiency of computational resources allocated for the operation of the SR. The duration T of the single time period under consideration can be determined dynamically, e.g., as a result of controlling the maximum allowable accumulated number W_j of the business-task instances $P_j, j = \overline{1,n}$. In this case, it is reasonable to adjust the values of c_j, for example, according to the following formula, taking into account the constants t_j—durations of execution by SR P_j of one task of the type Z_j :

$$c_j = \left\lfloor \frac{T}{t_j} \right\rfloor, j = \overline{1,n}. \quad (12)$$

The initial data for the analysis of the use of the allocated computational resources is formed on the basis of the results of multiple solutions of the considered optimization task. Let the set of tasks $V, |V| = k$ be solved and ordered chronologically for optimum solutions $\mathbf{x}(x_1^p, x_2^p, \ldots, x_n^p), p = \overline{1,k}$, which time series of values of incomplete utilization of computational resources of S_i types can be formed by the following formula:

$$S_i^p = b_i - \sum_{j=1}^{n} a_{ij} x_j^p, i = \overline{1,m}, p = \overline{1,k}. \quad (13)$$

Each set of values $S_i^p, p = \overline{1,k}$ can be studied using methods of time series analysis and random variables characteristics in order to identify computational resources that are scarce or require increase, as well as non-deficient resources that can be reduced. Future research will be devoted to clarifying this direction.

Thus, the authors propose a method of sequential local optimization based on solving the tasks of integer linear programming for the number of simultaneously functioning SRs from a set of their types under the conditions of limited allocated computational resources and the formation of sets of incoming business tasks. A method for the formation of statistical data based on processing the results of application of the method of sequential local optimization is also proposed to identify deficit and non-deficit computational resources by means of application of known methods of analysis of time series and characteristics of random variables.

5. EXPERIENCE WITH THE USE OF SR IN RTU MIREA

The Institute of Information Technologies (IIT) of MIREA – Russian Technological University (RTU MIREA) uses the software robotization platforms Atom.RITA[6] (Grinatom[7], Russia) and ROBIN (Robin[8], Russia) in the educational process in accordance with the relevant cooperation agreements and license contracts. Within the framework of development of cooperation with Rosatom State Corporation[9] and the Digital University project[10] IIT RTU MIREA has started to implement the project "Roboticization of the multifunctional center" since November 2023 to apply the RPA-platform Atom.RITA for development, implementation and administration of SR in business processes of the multifunctional center of the University:

- the object of the study is a multifunctional center comprising a structural subdivision within the Department of Educational and Social Work, which provides services to students on scholarships, dormitory accommodation, obtaining certificates, and other issues;
- the object of the study is business processes performed by the multifunctional center to enable the possibility of software robotization of their implementation;
- the subject of the study is represented by the project team of the multifunctional center and IIT employees;
- the objective of the study is to reduce the labor intensity of business processes of a multifunctional center by means of singling out business tasks that enable the performance via SR in their composition.

The composition of the studied business processes and corresponding business tasks is presented in Table 6.

Table 7 presents scenarios for some of the SRs listed in Table 6.

Table 8 shows the calculation of computational resources required by the considered SRs to perform

[6] https://greenatom.ru/atom-rita/ (in Russ.). Accessed June 17, 2024.

[7] https://greenatom.ru/ (in Russ.). Accessed June 17, 2024.

[8] https://rpa-robin.ru/ (in Russ.). Accessed June 17, 2024.

[9] https://www.rosatom.ru/index.html (in Russ.). Accessed June 17, 2024.

[10] https://minobrnauki.gov.ru/upload/iblock/e16/dv6edzmr0og5dm57dtm0wyllr6uwtujw.pdf (in Russ.). Accessed June 17, 2024.

their respective business tasks using software and information services:

- robot 1—implementation of requests for certificate of the place of study;
- robot 2—implementation of applications for issuance of income certificates;
- robot 3—ending out alerts to students regarding expired passports.

Table 6. Business processes and business tasks under study

Business process	Business tasks (SR)
Processing of applications received from students	1. Implementation of requests for vacations after the state final attestation. 2. Implementation of applications for the issuance of a certificate of income. 3. Implementation of requests for the confirmation of study letter. 4. Implementation of requests for issuance of a certificate of residence in the dormitory. 5. Transfer of applications to the archive and deletion of certificates with the term of more than 1 month.
Transfer of data on students to the State Unitary Enterprise "Moscow Social Register"	1. Collection of consents for data transfer to the State Unitary Enterprise "Moscow Social Register". 2. Data transfer to the State Unitary Enterprise "Moscow Social Register". 3. Acceptance and processing of the application for the production of a scholarship card.
Informing the students	1. Sending out signed certificates from the educational institution. 2. Sending alerts to students regarding expired passports.

Table 7. General operational scenarios for some of the SRs under consideration

SRs	Operating scenario
Implementation of applications for issuance of a certificate of income	1. Login to the personal account of the employee of RTU MIREA. 2. Going to the Applications section, selecting the appropriate type of application. 3. Processing of data from the application. 4. Classification of applications into processed and rejected. 5. Downloading applications as Excel files. 6. Change of status for each uploaded request in its Excel file. 7. Distribution of Excel files to accounting departments.
Implementation of requests for the issuance of a confirmation of study letter	1. Login to the personal account of the employee of RTU MIREA. 2. Going to the Applications section, selecting the appropriate application type. 3. Processing of data from the application. 4. Logging in to the Tandem.University information system. 5. Classification of applications into processed and rejected. 6. Downloading a Word file with issuance. 7. Logging into the cloud of RTU MIREA. 8. Downloading the help file to the cloud of RTU MIREA.
Sending signed issuances from the place of study	1. Login to the personal account of the staff member of RTU MIREA. 2. Going to the Applications section, selecting the appropriate type of application. 3. Logging in to the RTU MIREA cloud. 4. Forming a link to a file with a signed certificate. 5. Attaching the link to the file to the corresponding application and closing it.
Sending alerts to students regarding expired passports	1. Logging in to Tandem.University. 2. Filling in the report form in Tandem.University. 3. Downloading and processing an Excel file with data on students. 4. Logging in to the personal account of an employee of RTU MIREA. 5. Go to the Announcements Control Panel section. 6. Formation of publication with notification about expired passports with sending by list from the Excel file formed earlier. 7. Mailing to addressees from the publication with notification.

Table 8. Calculation of computational power required by some SRs used in the multifunctional center of RTU MIREA

Computational resource	Software used	Resource required by the software	Resource requirements of the SR			Total demand
			Robot No. 1	Robot No. 2	Robot No. 3	
RAM capacity, MB (resource No. 1)	Browser	$O_{11} = 120$	120 + 60 + 60	120 + 60 + 60	120 + 60 + 60	720
	Word processor	$O_{12} = 85$	0	85 + 60	85 + 60	290
	Tabular processor	$O_{13} = 65$	0	65 + 65	65 + 65	260
	Mail	$O_{14} = 65$	0	65 + 65	65 + 65	260
SR need for resource No. 1			240	645	645	1530
Number of CPU threads (Resource No. 2)	Browser	$P_{21} = 1$	1	1	1	3
	Word processor	$P_{22} = 1$	0	1	1	2
	Tabular processor	$P_{23} = 1$	0	1	1	2
	Mail	$P_{24} = 1$	0	1	1	2
SR need for resource No. 2			1	4	4	9
Data storage capacity, MB (Resource No. 3)	Browser	$H_{31} = 2048$	2048	2048	2048	6144
	Word processor	$H_{32} = 1024$	0	1024	1024	2048
	Tabular processor	$H_{33} = 1024$	0	1024	1024	2048
	Mail	$H_{34} = 512$	0	512	0	512
	File storage	not required	2048	100	100	2248
SR need for resource No. 3			4096	4708	4196	13000

The differences in the formation of Table 8 content from Table 2 confirm that the amount of computational resource (for example, RAM) consumed by a SR can be determined not only by the fact of parallel use of a certain number of versions of some software product or information service, but also by the amount of information being processed in them—open files, tabs, etc.

Since January 10, 2024, the multifunctional center of RTU MIREA has been operating a robot that produces certificates of study in an educational organization (certificates from the place of study) based on electronic applications in the student's personal cabinet. As at July 07, 2024, this robot has successfully processed more than 46800 applications and issued more than 45700 certificates. The time of execution of one application by an employee of the multifunctional center is 155 s. The time of execution of one application by the SR is 100 s, indicating that in this case two thirds of the employee's time is spent waiting for the results of the software and information services used. During 183 days of the SR operation, the saving of the working time fund of the multifunctional center employees exceeded 2015 man-hours or more than 251 man-days.

Figure 2 shows the dynamics of day-by-day receipt of requests for issuance by the SR of the certificate from the place of study specified in Table 7.

Based on the data presented in Fig. 2, we conclude that the task of managing the number of simultaneously functioning SRs of some set of their types considered in this paper under the conditions of limited allocated computational resources and changes in the number of tasks of the corresponding types is relevant both within the framework of the above-described project "Robotization of the multifunctional center" (taking

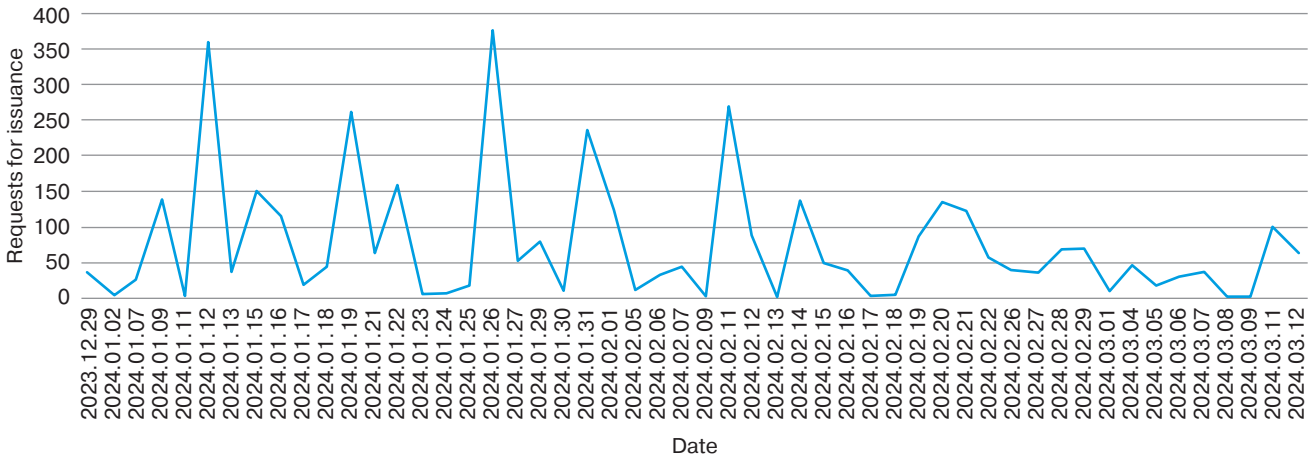

Fig. 2. Dynamics of requests for the issuance of certificates from the place of study

into account the commissioning of SRs from Table 7 in 2024 and 2025), as well as falling within the remit of further software robotization of business processes.

CONCLUSIONS

The automatic optimization of the composition of simultaneously functioning SRs in accordance with the number of incoming business tasks and amount of computational resources allocated for their operation is one of the directions of development of functional capabilities of RPA-platforms, providing their additional competitiveness by minimizing the cost of maintenance (rent) of the required IT infrastructure components.

The material presented in this paper establishes a basis and opens prospects for a new direction of research. This direction is not only universal within the field of software robotization technology, but also in demand both in the context of ensuring import substitution of foreign RPA-platforms and the need to improve the efficiency of organizations (business entities) functioning in the national economy of the Russian Federation.

Authors' contributions. The authors' contributions to this article are consistent with the principles of supervisor–postgraduate student interaction.

A.S. Zuev—task statement, advice on conducting, summarizing and evaluating the results of all stages of the study.

D.A. Leonov—formulation and formalization of the considered tasks, development of the outlined approaches and methods.

REFERENCES

1. Eliferov V.G., Repin V.V. *Biznes-protsessy. reglamentatsiya i upravlenie* (*Business Processes. Regulation and Management*). Moscow: INFRA-M; 2024. 319 p. (in Russ.).
2. Dolganova O.I. *Biznes-protsessy: analiz, modelirovanie, tekhnologii sovershenstvovaniya* (*Business Processes: Analysis, Modeling, Improvement Technologies*). Moscow: KnoRus; 2022. 324 p. (in Russ.).
3. Denisenko V.Yu. Automation of Manufacturing Business Processes in the Context of Industry 4.0 in Industrial Enterprises. *Voprosy Innovatsionnoi Ekonomiki*. 2020;10(2):1007–1014 (in Russ.). https://doi.org/10.18334/vinec.10.2.100878
4. Kolbanev M.O., Korshunov I.L. (Eds.). *Metodologicheskie osnovaniya tekhnologicheskikh innovatsii tsifrovoi ekonomiki* (*Methodological Foundations of Technological Innovations of the Digital Economy*). St. Petersburg: Saint Petersburg State University of Economics; 2023. 203 p. (in Russ.).
5. Eremina I.I., Frolova O.N., Nimazova L.N. *Platforma 1S: Predpriyatie kak instrument sovershenstvovaniya tekhniko-ekonomicheskogo planirovaniya predpriyatiya* (*1C Platform: Enterprise as a Tool for Improving Technical and Economic Planning of an Enterprise*). Kazan: Center for Support of Development Programs of Kazan Federal University; 2023. 112 p. (in Russ.).
6. Seryshev R.V. *Instrumenty upravleniya biznes-protsessami organizatsii* (*Tools for Managing Business Processes of an Organization*). Moscow: Rusains; 2023. 276 p. (in Russ.).
7. Ribeiro J., Lima R., Eckhardt T., Paiva S. Robotic Process Automation and Artificial Intelligence in Industry 4.0 – A Literature review. *Procedia Computer Science*. 2021;181(1):51–58. https://doi.org/10.1016/j.procs.2021.01.104

8. Frantsuzov I.V. The Strategic Role of Applying RPA Technologies and the Emergence of a new Technological Mode. *Izvestiya Yugo-Zapadnogo gosudarstvennogo universiteta. Seriya: Ekonomika. Sotsiologiya. Menedzhment = Proceedings of the Southwest State University. Series: Economy. Sociology. Management*. 2020;10(6):258–269 (in Russ.).
9. Bashlykova A.A. *Interoperabel'nost' i bezopasnost' funktsionirovaniya vychislitel'nykh i intellektual'nykh system* (*Interoperability and Security of Computing and Intelligent Systems Operation*). Moscow: MIREA; 2022. 137 p. (in Russ.). ISBN 978-5-7339-1645-3
10. Ermolaeva A.S., Selivanova M.A., Nemtsev V.N., Solomatin P.S. The Analysis of Implementation of Robotic Process Automation RPA: The Experience of Russian and Foreign Companies. In: Popkova E.G., Sergi B.S. (Eds.). *Modern Global Economic System: Evolutional Development vs. Revolutionary Leap. Lecture Notes in Networks and Systems.* 2021. V. 198. P. 1483–1492. https://doi.org/10.1007/978-3-030-69415-9_164
11. Séguin S., Benkalaï I. Robotic Process Automation (RPA) Using an Integer Linear Programming Formulation. *Cybernetics and Systems*. 2020;51(4):357–369. https://doi.org/10.1080/01969722.2020.1770503
12. Sosnilo A.I., Solovev R.S. Assessing the Impact of RPA on the Modern Economic System. *Upravlencheskoe konsul'tirovanie = Administrative Consulting*. 2022;2(158):63–69 (in Russ.). https://doi.org/10.22394/1726-1139-2022-2-63-69
13. Kutukov N.Y., Vazhdaev A.N. Application of Robotic Process Automation Technology in Education. *Doklady Tomskogo gosudarstvennogo universiteta sistem upravleniya i radioelektroniki* (*Doklady TUSUR*) *= Proceedings of TUSUR University*. 2023;26(2):88–92 (in Russ.). https://doi.org/10.21293/1818-0442-2023-26-2-88-92
14. Degtyareva V.V., Panchenko K.P. Evaluation of the Effectiveness of the Technology to Justifying its Implementation in the Transport and Logistics Industry. *Pervyi ekonomicheskii zhurnal = First Economic Journal*. 2023;1(331):50–57 (in Russ.). https://doi.org/10.58551/20728115_2023_1_50
15. Nikishchenkov S.A., Garanin A.V. Using Software Robots to Automate Business Processes on the Railroad. *Transportnoe delo Rossii = Transport Business in Russia*. 2023;4:163–165 (in Russ.).
16. Badmaeva A.D., Pererva O.L. Risks of Implementing RPA Technology at a Knowledge-based Enterprise. *Nauchnyi rezul'tat. Ekonomicheskie issledovaniya = Research Result. Economic Research*. 2020;6(3):46–52 (in Russ.). https://doi.org/10.18413/2409-1634-2020-6-3-0-6
17. Zarooni L., El Khatib M. Robotics process automation (RPA) and project risk management. *International Journal of Business Analytics and Security* (*IJBAS*). 2023;3(1):74–90. https://doi.org/10.54489/ijbas.v3i1.198
18. Shiboldenkov V.A., Khan D.M. Implementation of Robotic Process Automation Based on a Multi-Criterial Mathematical Model. *Razvitie i bezopasnost' = Development and Security*. 2023;4(20):62–73. Available from URL: https://ds.nntu.ru/frontend/web/ngtu/files/nomera/2023/04/062.pdf

СПИСОК ЛИТЕРАТУРЫ

1. Елиферов В.Г., Репин В.В. *Бизнес-процессы. Регламентация и управление*. М.: ИНФРА-М; 2024. 319 с.
2. Долганова О.И. *Бизнес-процессы: анализ, моделирование, технологии совершенствования*. М.: КноРус; 2022. 324 с.
3. Денисенко В.Ю. Автоматизация производственных бизнес-процессов в условиях Индустрии 4.0 на промышленных предприятиях. *Вопросы инновационной экономики.* 2020;10(2):1007–1014. https://doi.org/10.18334/vinec.10.2.100878
4. *Методологические основания технологических инноваций цифровой экономики*; под ред. М.О. Колбанева, И.Л. Коршунова. СПб.: Изд-во Санкт-Петербургского гос. экономического ун-та; 2023. 203 с.
5. Еремина И.И., Фролова О.Н., Нимазова Л.Н. *Платформа 1С: Предприятие как инструмент совершенствования технико-экономического планирования предприятия*. Казань: Центр поддержки программ развития Казанского федерального университета; 2023. 112 с.
6. Серышев Р.В. *Инструменты управления бизнес-процессами организации*. М.: Русайнс; 2023. 276 с.
7. Ribeiro J., Lima R., Eckhardt T., Paiva S. Robotic Process Automation and Artificial Intelligence in Industry 4.0 – A Literature review. *Procedia Computer Science*. 2021;181(1):51–58. https://doi.org/10.1016/j.procs.2021.01.104
8. Французов И.В. Стратегическая роль применения RPA-технологий в условиях современного технологического уклада. *Известия Юго-Западного государственного университета. Серия: Экономика. Социология. Менеджмент*. 2020;10(6):258–269.
9. Башлыкова А.А. *Интероперабельность и безопасность функционирования вычислительных и интеллектуальных систем*. М.: РТУ МИРЭА; 2022. 137 с. ISBN 978-5-7339-1645-3
10. Ermolaeva A.S., Selivanova M.A., Nemtsev V.N., Solomatin P.S. The Analysis of Implementation of Robotic Process Automation RPA: The Experience of Russian and Foreign Companies. In: Popkova E.G., Sergi B.S. (Eds.). *Modern Global Economic System: Evolutional Development vs. Revolutionary Leap. Lecture Notes in Networks and Systems.* 2021. V. 198. P. 1483–1492. https://doi.org/10.1007/978-3-030-69415-9_164
11. Séguin S., Benkalaï I. Robotic Process Automation (RPA) Using an Integer Linear Programming Formulation. *Cybernetics and Systems*. 2020;51(4):357–369. https://doi.org/10.1080/01969722.2020.1770503
12. Соснило А.И., Соловьев Р.С. Оценка влияния технологии роботизации бизнес-процессов на современную экономическую систему. *Управленческое консультирование*. 2022;2(158):63–69. https://doi.org/10.22394/1726-1139-2022-2-63-69

13. Кутуков Н.Ю., Важдаев А.Н. Применение в образовании технологии автоматизации Robotic Process Automation. *Доклады Томского государственного университета систем управления и радиоэлектроники* (*Доклады ТУСУР*). 2023;26(2):88–92. https://doi.org/10.21293/1818-0442-2023-26-2-88-92
14. Дегтярева В.В., Панченко К.П. Оценка эффективности RPA-технологий для обоснования их внедрения в транспортно-логистическую отрасль. *Первый экономический журнал*. 2023;1(331):50–57. https://doi.org/10.58551/20728115_2023_1_50
15. Никищенков С.А., Гаранин А.В. Использование программных роботов для автоматизации бизнес-процессов на железной дороге. *Транспортное дело России*. 2023;4:163–165.
16. Бадмаева А.Д., Перерва О.Л. Риски внедрения технологии RPA на наукоемкое предприятие. *Научный результат. Экономические исследования*. 2020;6(3):46–52. https://doi.org/10.18413/2409-1634-2020-6-3-0-6
17. Zarooni L., El Khatib M. Robotics process automation (RPA) and project risk management. *International Journal of Business Analytics and Security* (*IJBAS*). 2023;3(1):74–90. https://doi.org/10.54489/ijbas.v3i1.198
18. Шиболденков В.А., Кхан Д.М. Внедрение роботизированной автоматизации процессов на основе многокритериальной математической модели. *Развитие и безопасность*. 2023;4(20):62–73. URL: https://ds.nntu.ru/frontend/web/ngtu/files/nomera/2023/04/062.pdf

About the authors

Andrey S. Zuev, Cand. Sci. (Eng.), Associate Professor, Director of the Institute of Information Technologies, MIREA – Russian Technological University (78, Vernadskogo pr., Moscow, 119454 Russia). E-mail: zuev_a@mirea.ru. RSCI SPIN-code 6737-5778, https://orcid.org/0000-0002-1797-7585

Dmitrii A. Leonov, Postgraduate Student, Senior Lecturer, Department of Practical and Applied Informatics, Institute of Information Technologies, MIREA – Russian Technological University (78, Vernadskogo pr., Moscow, 119454 Russia). E-mail: leonov@mirea.ru. RSCI SPIN-code 1381-7071, https://orcid.org/0009-0004-9775-6820

Об авторах

Зуев Андрей Сергеевич, к.т.н., доцент, директор Института информационных технологий, ФГБОУ ВО «МИРЭА – Российский технологический университет» (119454, Россия, Москва, пр-т Вернадского, д. 78). E-mail: zuev_a@mirea.ru. SPIN-код РИНЦ 6737-5778, https://orcid.org/0000-0002-1797-7585

Леонов Дмитрий Алексеевич, аспирант, старший преподаватель, кафедра практической и прикладной информатики, Институт информационных технологий, ФГБОУ ВО «МИРЭА – Российский технологический университет» (119454, Россия, Москва, пр-т Вернадского, д. 78). E-mail: leonov@mirea.ru. SPIN-код РИНЦ 1381-7071, https://orcid.org/0009-0004-9775-6820

Translated from Russian into English by Lyudmila O. Bychkova
Edited for English language and spelling by Thomas A. Beavitt

Information systems. Computer sciences. Issues of information security
Информационные системы. Информатика. Проблемы информационной безопасности

UDC 004.31
https://doi.org/10.32362/2500-316X-2024-12-4-23-39
EDN DRCIUV

RESEARCH ARTICLE

Identification of digital device hardware vulnerabilities based on scanning systems and semi-natural modeling

Evgeniy F. Pevtsov,
Tatyana A. Demenkova [@],
Alexander O. Indrishenok,
Vladimir V. Filimonov

MIREA – Russian Technological University, Moscow, 119454 Russia
[@] Corresponding author, e-mail: demenkova@mirea.ru

Abstract

Objectives. The development of computer technology and information systems requires the consideration of issues of their security, various methods for detecting hardware vulnerabilities of digital device components, as well as protection against unauthorized access. An important aspect of this problem is to study existing methods for the possibility and ability to identify hardware errors or search for errors on the corresponding models. The aim of this work is to develop approaches, tools and technology for detecting vulnerabilities in hardware at an early design stage, and to create a methodology for their detection and risk assessment, leading to recommendations for ensuring security at all stages of the computer systems development process.

Methods. Methods of semi-natural modeling, comparison and identification of hardware vulnerabilities, and stress testing to identify vulnerabilities were used.

Results. Methods are proposed for detecting and protecting against hardware vulnerabilities: a critical aspect in ensuring the security of computer systems. In order to detect vulnerabilities in hardware, methods of port scanning, analysis of communication protocols and device diagnostics are used. The possible locations of hardware vulnerabilities and their variations are identified. The attributes of hardware vulnerabilities and risks are also described. In order to detect vulnerabilities in hardware at an early design stage, a special semi-natural simulation stand was developed. A scanning algorithm using the Remote Bitbang protocol is proposed to enable data to be transferred between *OpenOCD* and a device connected to the debug port. Based on scanning control, a verification method was developed to compare a behavioral model with a standard. Recommendations for ensuring security at all stages of the computer systems development process are provided.

Conclusions. This paper proposes new technical solutions for detecting vulnerabilities in hardware, based on methods such as FPGA system scanning, semi-natural modeling, virtual model verification, communication protocol analysis and device diagnostics. The use of the algorithms and methods thus developed will allow developers to take the necessary measures to eliminate hardware vulnerabilities and prevent possible harmful effects at all stages of the design process of computer devices and information systems.

Keywords: hardware vulnerability, digital components, half-life modeling, diagnostics, scanning, verification

• **Submitted:** 30.08.2023 • **Revised:** 13.01.2024 • **Accepted:** 03.06.2024

For citation: Pevtsov E.F., Demenkova T.A., Indrishenok A.O., Filimonov V.V. Identification of digital device hardware vulnerabilities based on scanning systems and semi-natural modeling. *Russ. Technol. J*. 2024;12(4):23–39. https://doi.org/10.32362/2500-316X-2024-12-4-23-39

Financial disclosure: The authors have no a financial or property interest in any material or method mentioned.

The authors declare no conflicts of interest.

НАУЧНАЯ СТАТЬЯ

Выявление аппаратных уязвимостей цифровых устройств на основе систем сканирования и полунатурного моделирования

Е.Ф. Певцов,
Т.А. Деменкова [@],
А.О. Индришенок,
В.В. Филимонов

МИРЭА – Российский технологический университет, Москва, 119454 Россия
[@] *Автор для переписки, e-mail: demenkova@mirea.ru*

Резюме

Цели. Развитие вычислительной техники и информационных систем требует рассмотрения вопросов их безопасности, различных методов обнаружения аппаратных уязвимостей цифровых компонентов устройств и защиты от несанкционированного доступа. Важным аспектом данных проблем является исследование существующих методов на возможность и способность выявить аппаратные ошибки или произвести поиск ошибок на соответствующих моделях. Цель работы – разработка подходов, инструментов и технологии для обнаружения уязвимостей в аппаратном обеспечении на ранней стадии проектирования, создание методики их обнаружения и оценки риска, рекомендаций по обеспечению безопасности на всех этапах процесса разработки вычислительных систем.

Методы. Использованы методы полунатурного моделирования, сравнения и выявления аппаратных уязвимостей, стресс-тестирования для выявления уязвимостей.

Результаты. Предложены методы обнаружения и защиты от аппаратных уязвимостей, являющихся критически важным аспектом в обеспечении безопасности вычислительных систем. Для обнаружения уязвимостей в аппаратном обеспечении использованы методы сканирования портов, анализа протоколов связи и диагностики устройств. Определены возможные места нахождения аппаратных уязвимостей, их вариации, описаны атрибуты аппаратных уязвимостей и риски. Для обнаружения уязвимостей в аппаратном обеспечении на ранней стадии проектирования разработан специальный стенд полунатурного моделирования. Предложен алгоритм сканирования с использованием протокола Remote Bitbang, который позволяет передавать данные между *OpenOCD* и подключенным к отладочному порту устройством. На основе управления сканированием

разработан метод верификации, реализующий сравнение поведенческой модели с эталоном. Приведены рекомендации по обеспечению безопасности на всех этапах процесса разработки вычислительных систем.
Выводы. В данной работе предложены новые технические решения для обнаружения уязвимостей в аппаратном обеспечении, основанные на таких методах, как сканирование системы на программируемой логической интегральной схеме, полунатурное моделирование, верификация по виртуальной модели, анализ протоколов связи и диагностика устройств. Применение разработанных алгоритмов и способов позволит разработчикам предпринять необходимые меры по устранению аппаратных уязвимостей и предотвращению возможных вредоносных воздействий на всех этапах процесса проектирования устройств вычислительной техники и информационных систем.

Ключевые слова: аппаратная уязвимость, цифровые компоненты, полунатурное моделирование, диагностика, сканирование, верификация

• **Поступила:** 30.08.2023 • **Доработана:** 13.01.2024 • **Принята к опубликованию:** 03.06.2024

Для цитирования: Певцов Е.Ф., Деменкова Т.А., Индришенок А.О., Филимонов В.В. Выявление аппаратных уязвимостей цифровых устройств на основе систем сканирования и полунатурного моделирования. *Russ. Technol. J*. 2024;12(4):23–39. https://doi.org/10.32362/2500-316X-2024-12-4-23-39

Прозрачность финансовой деятельности: Авторы не имеют финансовой заинтересованности в представленных материалах или методах.

Авторы заявляют об отсутствии конфликта интересов.

INTRODUCTION

Hardware vulnerability is an error in the technical implementation of hardware which can allow malicious intruders to gain access to a system or its application. Advanced hardware vulnerabilities can have serious security implications for computer systems, including compromising sensitive data, disruption of systems, and potential threat to human life and health, if vulnerabilities in medical devices or automotive equipment are exploited.[1]

Hardware vulnerabilities can be diverse and include bugs in various computer components: processor, chips, memory, hardware modules, and drivers. They are also contained in other hardware complex function blocks (CF-blocks). Hardware vulnerabilities can occur as a result of interaction with software, particularly drivers, databases, and other applications that contain bugs or malicious code.

Checking for vulnerabilities is a complex process and requires the involvement of information security experts.[2] Hardware vulnerabilities can be identified by scanning the system under investigation, in order to find problem areas and then fix them [1]. One option for finding vulnerabilities in existing computing devices is to use specialized software and tools. For example, many utilities and applications for searching and analyzing vulnerabilities can also be used to check the security of network devices, etc. A comprehensive approach of model comparison in the form of *OpenOCD*[3] binding and a software model of the device obtained using *Verilator* [2] from hardware description languages[4] can also be applied.

Analysis and reverse engineering techniques are also used to find vulnerabilities. These methods can be used to find vulnerabilities in hardware and software systems, operating systems, device drivers, and other computing systems [3].

Each vulnerability has certain attributes which can be used to detect it. This paper describes the attributes of hardware vulnerabilities, methods of their detection, and risk assessment. Attributes of hardware vulnerabilities are considered in accordance with the accepted taxonomy proposed in a number of works which categorize the identification of hardware vulnerabilities and assessment of their risk or severity [4]. This taxonomy identifies four multi-parametric attributes (vectors) corresponding to hardware vulnerability identification, hardware vulnerability detection identification, hardware vulnerability risk or severity, and hardware vulnerability detection efficiency.

[1] Zantout S. *Hardware Trojan Detection in FPGA through Side-Channel Power Analysis and Machine Learning*. MSc Thesis. University of California, Irvine. 2018. https://escholarship.org/uc/item/7hk8x6rb. Accessed May 15, 2023.

[2] Oberg J. *Testing Hardware Security Properties and Identifying Timing Channels*. UC San Diego. 2014. P. 5–38. https://escholarship.org/uc/item/8b530988. Accessed May 15, 2023.

[3] Documentation regarding OpenOCD RISC-V Debug Configuration Commands. https://openocd.org/doc/html/Architecture-and-Core-Commands.html#RISC_002dV-Debug-Configuration-Commands. Accessed May 15, 2023.

[4] Andrianov A.V. *Realization of possibility of step-by-step debugging at debugging of test scenarios on VLSI SonC model*. https://www.module.ru/uploads/media/1534156062-2018-833a272aac.pdf (in Russ.). Accessed May 15, 2023.

TASK STATEMENT. TAXONOMY OF HARDWARE BOOKMARKS

Each hardware vulnerability has a number of attributes, so methods have been developed to perform their detection by means of some or all of the attributes. Information about vectors and attributes is further needed to select methods for vulnerability detection.

Attributes in each category may be ranked based on their importance, uniqueness, weighting, or other criteria determined by the specific Trojan detection project or task. A hardware Trojan is a malicious module embedded in an integrated circuit or a malicious modification of the circuit to alter its operation or add additional functionality, for example, to organize an information leakage channel.

A TI (Trojan Identification) vector includes attributes that are used to identify Trojans, such as Trojan size, location in the circuitry, defense mechanisms used by the Trojan, and other characteristics that may be unique to a particular Trojan.

TDI (Trojan Detection Identification) vector includes attributes that can be detected by a particular Trojan detection method, such as changes in Trojan signatures, anomalies in Trojan behavior, attack features used by the Trojan, and other attributes that can be detected by a particular method.

TR vector (Trojan Risk or Severity) includes attributes that assess the risk or severity of a Trojan, such as the ability of the Trojan to cause harm, how stealthy the Trojan is, how likely it is to spread, the potential consequences of its actions, and other factors that may affect the severity of the Trojan.

TDE vector (Trojan Detection Effectiveness) includes attributes that evaluate the effectiveness of a particular Trojan detection method, such as detection accuracy, false positives and false negatives of the method, detection rate, complexity of the method implementation, and other factors that may affect the effectiveness of the method.

These vectors can be used to evaluate Trojans and select the most effective method of detecting it, identifying it, and assessing its risk or severity.

A combination of TI, TDI, CR, and TDE vectors can be used to select the most effective Trojan detection method based on certain criteria and requirements of a project or task. For example, a method with high values of the TDI and TDE vectors indicating a high Trojan detection capability and method effectiveness may be preferred over a method with lower values in these vectors. Attributes in the TR vector can also be used to assess the severity of a Trojan and its priority when selecting a detection method.

Attributes in each category are used to identify Trojans and assess their risk or severity. They can also be used to identify Trojan detection methods and evaluate their effectiveness. Two vectors TI and TR are assigned to each Trojan. The former identifies the corresponding attributes and the latter represents the attributes in terms of their risk or severity. Each Trojan detection method also has two vectors TDI and TDE. TDI identifies the attributes that can be detected and TDE represents the attributes in terms of the effectiveness of the method. Thus, there are four vectors corresponding to: 1) TI Trojan identification, 2) TDI Trojan detection identification, 3) TR Trojan risk or severity, 4) TDE Trojan detection effectiveness [5].

The proposed approach based on ranking the attributes of Trojans in each category and using TI, TR, TDI, and TDE vectors can be a useful tool for identification and risk assessment of Trojans, as well as for selecting effective detection methods when developing more robust security and defense against attacks.

However, it should be noted that the proposed Trojan attribute ranking system may be limited because new types of Trojans and their attributes may emerge as a result of evolving technologies and attack methods. Therefore, the database of Trojan attributes and detection methods need to be continuously updated and supplemented, in order to better protect against them.

Detecting vulnerabilities is only the first step. Steps must also be taken to remediate the vulnerabilities and prevent potential attacks. In this process, tools such as computer-aided design (CAD) systems can play an important role in verifying devices and detecting vulnerabilities early in the design process. A typical example of such a system is the CAD tool suite of Cadence Design Systems [6]. In general, security is a critical aspect in the development of computing systems, detection and protection against hardware vulnerabilities should be considered at all stages of the development and operation process.

In addition to the implemented function, the vulnerability can be upgraded for remote interaction. Here it is necessary to program the ability to access the network card and go online. In addition, the bookmark can be configured to corrupt not only the output data at a given time, but also to modify already recorded data. To do this, the bookmark must have access to memory storages, as well as the ability to detect certain data or the ability to change all data by a certain amount. Writing and modernizing a bookmark is limited only by the skills of the attacker and the size of the bookmark [7–9].

HARDWARE BOOKMARK IMPLEMENTATION EXAMPLE

An important aspect of the methodology for identifying hardware bookmarks is the procedure for creating possible examples. Usually, the main difficulty

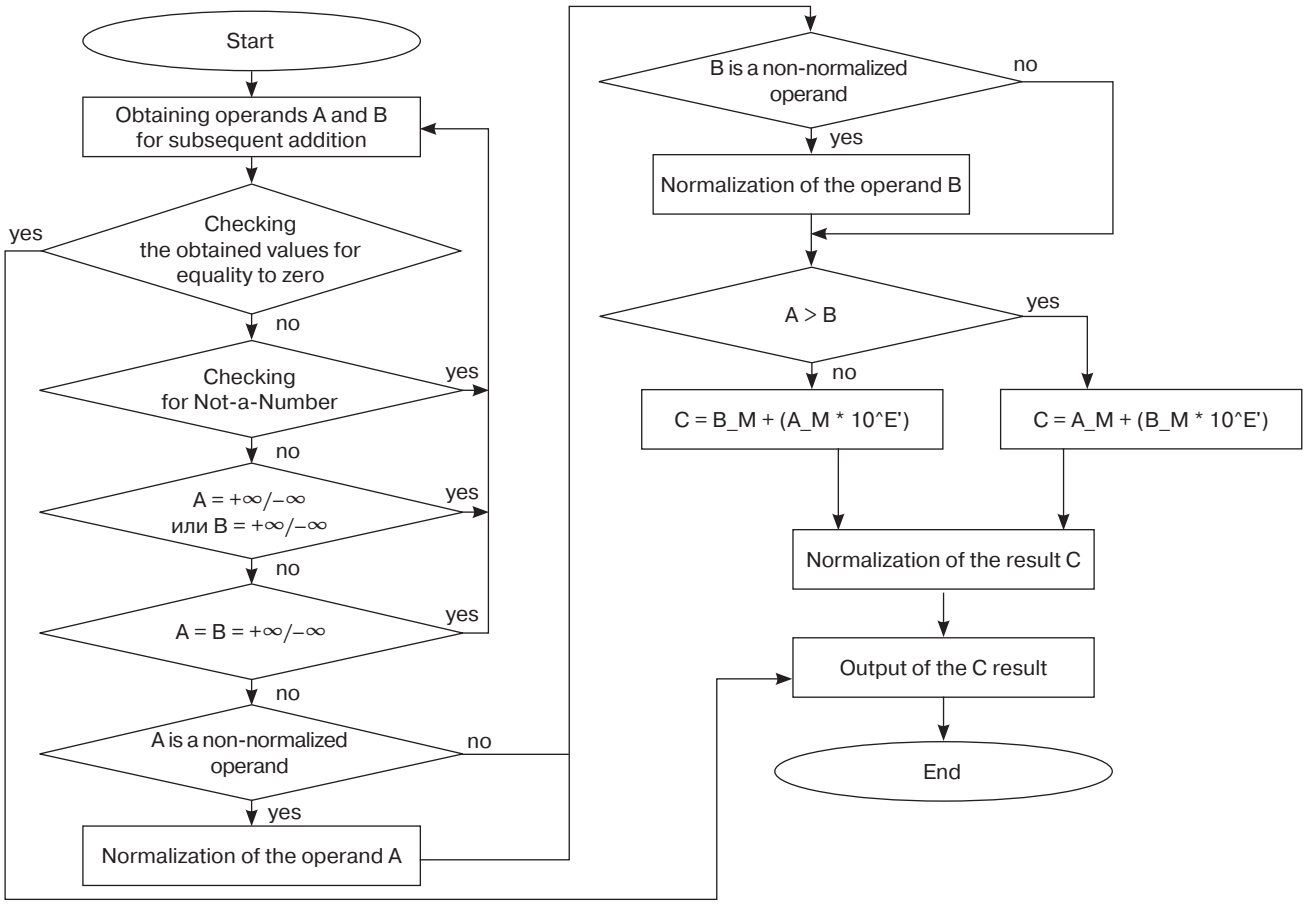

Fig. 1. Algorithm of adder operation

arises with regard to what exactly to show and how to present it. The example can be useful for developers of computer security devices during design in terms of identifying possible vulnerabilities.

Let us consider hardware bookmarks which violate the accuracy of calculations in the kernels, also known as the hardware gas pedal of mathematical calculations. When adding real numbers at the adder, multiplier or divider, you can create a hardware bookmark that violates the correctness of calculations. Let us introduce the bookmark into the addition algorithm and adder code using a separate module and synthesize the resulting computation block.

This module performs the following procedure: when the adder receives a certain number, the bookmark triggers and replaces this number with the one needed by the intruder. It then passes this number directly to the summation. If the bookmark has not received the number necessary for its transition, it remains inactive. Thus, the bookmark spoils output data, while giving its appearance at a particular moment of receipt of a certain number at the input. Figure 1 shows the algorithm of the adder block operation for practicing the skills of introducing and detecting bookmarks in the most common nodes of digital computer systems.

A hardware tab in the presence of the fractional part in the result will change its value, and affect calculation accuracy. The presence of a fractional part in a number in the encoded 32-bit IEEE 754 standard format[5] can be detected by the presence of units in the digits of the number:

$$s + e + \exp + 1 \le n, \quad (1)$$

where s is the number of bits allocated to the sign of the number, e is the number of bits allocated to the shifted exponent of the number, exp is the exponent of the number, and n is the total number of bits.

In the 32-bit representation (1) can be written as:

$$10 + \exp \le 32. \quad (2)$$

If the number has a fractional part, then we invert the digit $s + e + \exp + 2$. In other words, the number $5.5_{10} = 101.1\mathbf{0}0_2$ after inverting this digit will become equal to $5.75_{10} = 101.1\mathbf{1}0_2$.

[5] 2754-2019 IEEE Standard for Floating-Point Arithmetic. July 22, 2019. Electronic ISBN 978-1-5044-5924-2. https://ieeexplore.ieee.org/document/8766229. Accessed May 15, 2023.

Block diagram of the hardware bookmarking algorithm is shown in Fig. 2 [10, 11].

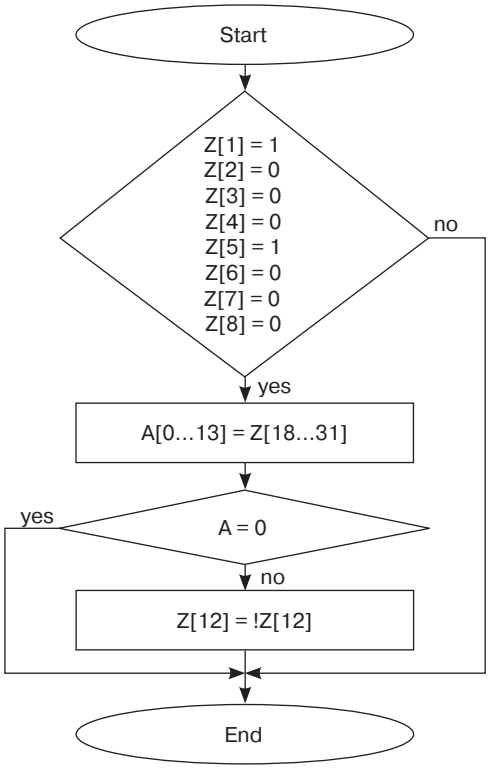

Fig. 2. Block diagram of the hardware bookmarking algorithm

In order to reduce the frequency of this event which triggers a hardware tab, we will take only numbers that, in addition to having a fractional part, have values only in the range $512 \le x < 1024$. The prerequisite for this condition can be met from the value of the exponent of the binary number. If the exponent of the binary number is equal to $9_{10} = 1001_2$, which corresponds to the shifted exponent 10001000_2, then this number lies in the interval $512 \le x < 1024$.

As a result, this hardware Trojan will change the result on the adder only if this result belongs to the interval $512 \le x < 1024$ and has a fractional part.

Since we have determined the order of numbers required for distortion to be equal to 9_{10}, the previously described step of finding the right digit in a number to check whether the number has a fractional part is no longer required. Any 32-bit IEEE 754 numbers lying in the interval $512 \le x < 1024$ with one in any of $18 \le n \le 31$ digits will have a fractional part according to formulas (1) and (2):

$$1 + 8 + 9 + 1 = 19 \le n.$$

The encoded fractional part of the number will be located in the interval from 19 digits to 32 digits, and the encoded integer part of the number is located in digits 9 to 17. Therefore, in order to check whether the number has a fractional part, at least one unit in digits 18–31 needs to be found.

From the adder result bus, the value of the resulting encoded number is read into register Z of the hardware Trojan. If the shifted exponent of the number is equal to 10001000_2, then the remainder of the mantissa of the encoded number is written to register A of the hardware tab. Further, if this register A is non-empty, then in register Z the z value of the 12th digit is inverted, corresponding to the second digit of the fractional part of the number. As a result, the number is either increased by 0.25 if there is 0 in this digit, or decreased by 0.25 if there is 1 in this digit. The developed hardware Trojan can be embedded into the real number adder core of a hardware math gas pedal. The developed bookmark is described in the Verilog language [12].

After the successful development of a hardware Trojan, verification must be performed. This is required, in order to determine whether the hardware tab works correctly depending on the specified conditions. For the purpose of this verification, we define several possible events. Each of the events must be verified both with and without the presence of the hardware Trojan.

1. Result of the adder lies in the interval $512 \le x < 1024$.
   a) result has a fractional part;
   b) result has no fractional part.
2. Result of the adder does not belong to the interval $512 \le x < 1024$.
   a) result is less than 512 and has a fractional part;
   b) result is less than 512 and has no fractional part;
   c) result is greater than or equal to 1024 and has a fractional part;
   d) result is greater than or equal to 1024 and has no fractional part.
3. The adder result is an exceptional number.
   a) result is equal to 0;
   b) result is equal to $+\infty$;
   c) result is equal to $-\infty$.

Such hardware vulnerability can be detected using the following methods.

1. **Anomalous behavior analysis.** The presence of a bookmark can lead to abnormal behavior of the floating-point unit (FPU), such as unexpected calculation errors, incorrect results, or unusual activity during mathematical operations.
2. **Application of Linpack performance test** [13]. A hardware tab introduced into FPU is difficult to detect using this test because its size has a negligible effect on performance. However, this method will be effective, if it is possible to compare two hardware blocks: with and without the bookmark. One model has an intentionally introduced hardware vulnerability and is loaded into a programmable logic integrated circuit (PLIC). The other model

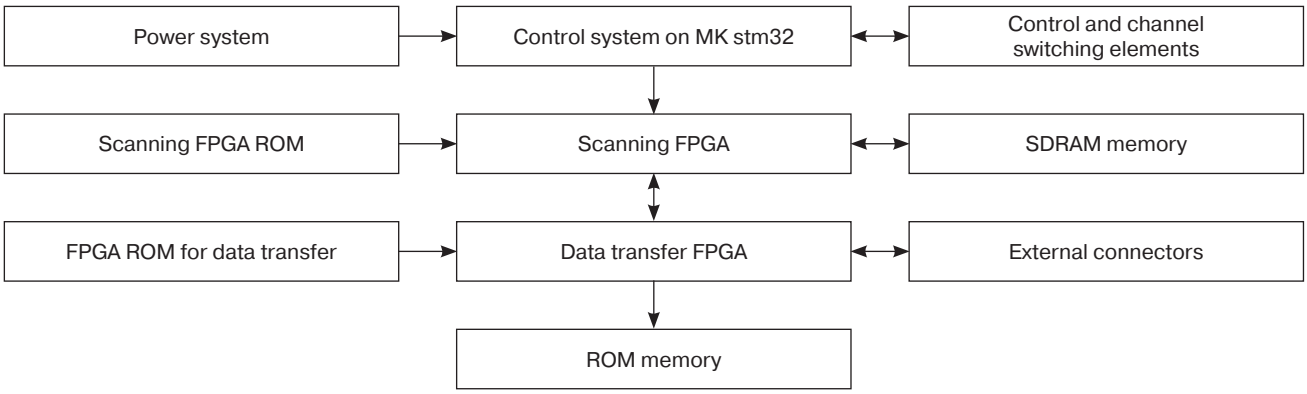

Fig. 3. The structure of the bench for conducting experiments to identify hardware vulnerabilities. ROM, read-only memory; SDRAM, synchronous dynamic random access memory; MK stm32, STM32 microcontroller

is behavioral and is implemented with some simplifications in a simulator on a computer using special CAD tools for integrated circuits, such as Cadence Design Systems tools.

3. **Checking the instruction set** inside the processor using the Joint Test Action Group (JTAG) interface[6] and the Remote Bitbang protocol-based scanning system. Specifically, this meant auditing the FPU microcode for unusual or suspicious instructions which may indicate the presence of a hardware bookmark.

   The Remote Bitbang protocol is a protocol used in *OpenOCD* (an open source program for debugging embedded systems) which allows data to be transferred between *OpenOCD* and a device that is connected to the debug port. The Remote Bitbang protocol is used to control I/O and other device interfaces.

   The Remote Bitbang protocol uses asynchronous data transfer, represented as a simple message format. Commands sent through this protocol are of two types: write commands and read commands. Write commands allow you to control pins, transfer data, and set interface modes, while read commands allow you to receive data from the device via inputs.

   Remote Bitbang protocol is used in conjunction with protocols such as JTAG, in order to enable full debugging and programming of embedded systems. This protocol can be used to scan registers on a remote device connected to *OpenOCD*, and in the automation of testing, fault diagnosis, and device programming in production environments [14–16].

4. **The use of specialized tools** (microcode analyzers and specialized stands for detecting hardware bookmarks) which can be useful in detecting such threats. However, their use requires specialized knowledge and experience.

[6] https://ru.wikipedia.org/wiki/JTAG (in Russ.). Accessed May 15, 2023.

SEMI-NATURAL SIMULATION BENCH

When developing a stand designed to detect hardware vulnerabilities, it needs to ensure the reliability of the results obtained and fulfill the following functions:

1. Ability to test various types of hardware, including processors, chipsets, I/O controllers, network cards, and other components.
2. Ability to use a variety of tools to detect vulnerabilities in hardware, including vulnerability scanners, debuggers, emulators, and other tools.
3. Ability to experiment in a variety of scenarios, including malware attacks on hardware, memory and peripheral manipulation, and vulnerability exploits.
4. Ensue security and data protection during experiments, including protection against leakage of confidential information and ensuring confidentiality of test results.
5. Ensure that test results can be reproduced and all steps of the experiment can be documented, including test automation and tools for analyzing results.

The structural diagram of the stand is shown in Fig. 3.

The feature is a special FPGA structure that enables verification for the repeated firmware in order to ensure that there are no changes to the complex programmable logic device (CPLD) circuit. It is also possible to use the FPGA's built-in resources for basic firmware verification using built-in controls.

Verification of the Verilog code used to generate the firmware file (bitstream) can be performed using various methods and tools such as simulation, formal verification, and emulation on hardware.

1. **Simulation.** After creating test vectors which represent different bitstream loading scenarios in the FPGA, the Verilog simulator should be used to perform a simulation of these test vectors. As a result, the signal values within the bitstream comparison circuitry can be analyzed and compared to the expected values. This enables error detection

and verification that the bitstream comparison methods are working correctly.

2. **Formal verification** is a method of verifying the correctness of Verilog code based on mathematical algorithms. Formal verification tools, such as Model Checking or Equivalence Checking, can be used to verify that bitstream comparison methods work correctly. This can include checking the correctness of the comparison logic, detecting potential errors, and finding unexpected execution paths.
3. **Emulation on hardware.** Load the bitstream into the FPGA and run it on a physical device. Test vectors and physical signals can then be used to verify that the bitstream comparison methods work correctly in real time. This can help identify possible problems when running on the real hardware.
4. **Manual validation.** The code of bitstream comparison methods can be carefully analyzed and manual validation performed against requirements and expected behavior. This can include analyzing logic, checking boundary conditions, and testing different bitstream loading scenarios.

Another feature of the semi-natural simulation bench architecture is the ability to load into internal memory via the internal FPGA reconfiguration interface. If such an interface is not available, the standard external reconfiguration interface can be used. In order to avoid problems when verifying and loading into memory from the FIFO (first in, first out) buffer, verification blocks need to be placed in strictly allocated FPGA cells when writing the configuration and layout on-chip. In addition, this module has multi-stage verification to detect threats, report them, and eliminate possible negative effects. A report of the validation results is saved and can be used to further analyze and improve the module's performance.

Since FPGA architectures can vary from model to model and manufacturer to manufacturer, this structure enables the verification algorithms to be adapted to different architectures and manufacturers. Compared to the closest analogs, this module is more relevant because it has the ability to connect to various external devices. This provides for its versatility and the possibility of it being used as a master device in information switching systems, as well as in systems with high-performance processors [17, 18].

Before scanning, device operation modes need to be selected which will allow you to identify possible vulnerabilities in the RS-485 data transmission system. For example, you can configure the device to send malicious commands or to intercept and analyze data transmitted over the network. It should be taken into account that such actions can lead to disruption of the device or the network as a whole. Therefore, the experiments should be conducted in a controlled environment and with prior coordination with those responsible for the operation of the system [1, 19].

An example of implementation of the semi-natural simulation stand is shown in Fig. 4.

Fig. 4. Implementation of semi-natural simulation bench

A configuration according to the target model is loaded into the data transfer FPGA, describing the expected results of the device. Then the process begins of obtaining readings from the external interfaces of the unit under investigation, such as RS-485 or Ethernet[7], and comparing them with the target model. If the results do not correspond to the expected results, an error is generated and recorded in the report. Then the indicator on the device signals the occurrence of the error[8].

When connecting the bench and debugging the FPGA firmware, in order to obtain the necessary data for comparison with the target model deployed on a computer, it is important to note that the connection scheme of the JTAG programmer to the FPGA may differ depending on the specific model of the programmer and FPGA, as well as the task to be solved by this connection[9, 10, 11]. In this case, if additional peripherals

[7] Andrianov A.V. *Realization of possibility of step-by-step debugging at debugging of test scenarios on VLSI SonC model*. https://www.module.ru/uploads/media/1534156062-2018-833a272aac.pdf (in Russ.). Accessed May 15, 2023.

[8] Fern N.C. *Verification Techniques for Hardware Security*: Ph.D. Thesis (Comput.). USA: UC Santa Barbara; 2016. P. 10–25. https://escholarship.org/uc/item/2ch6f44s. Accessed May 15, 2023.

[9] Cadence documentation. https://www.cadence.com/content/cadence-www/global/en_US/home/support/documentation.html. Accessed May 15, 2023.

[10] Yang P. *Assessing VeSFET Monolithic 3D Technology in Physical Design, Dynamic Reconfigurable Computing, and Hardware Security*: Ph.D. Thesis (Comput.). USA: UC Santa Barbara; 2017. P. 62–81. https://escholarship.org/uc/item/5s9833kz. Accessed May 15, 2023.

[11] Farinholt B.R. *Understanding the Remote Access Trojan malware ecosystem through the lens of the infamous DarkComet RAT*: Ph.D. Thesis (Comput.). USA: UC San Diego; 2019. P. 17–29. https://escholarship.org/uc/item/3vv544n5. Accessed May 15, 2023.

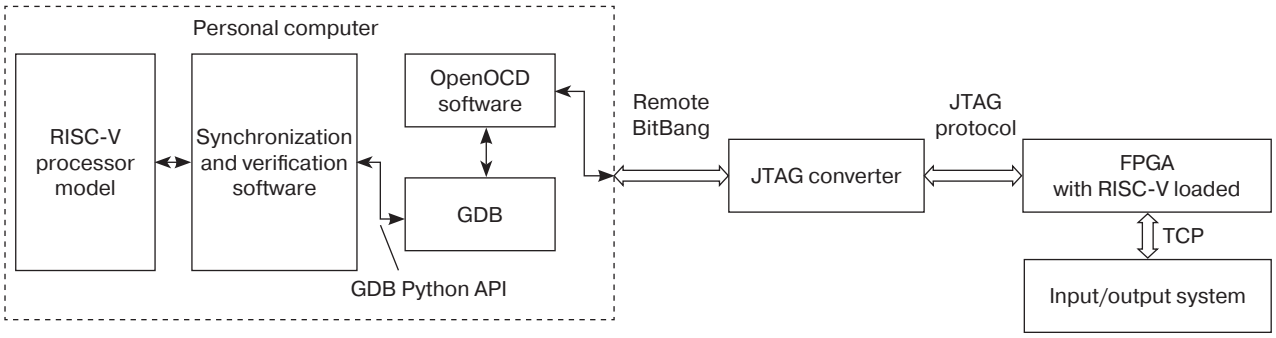

Fig. 5. A model for finding vulnerabilities in a RISC-V processor-based system. API, application programming interface; TCP, transmission control protocol; GVB, Gnu DeBugger, open source debugger

need to be connected to the FPGA, for example, to debug a system containing a microcontroller, a special debug module may also need to be connected.

EXPERIMENTAL

A semi-natural simulation test bench is performed on the basis of verification of a processor design, e.g., RISC-V,[12] in whose behavioral description in the Verilog language code of an intentional hardware vulnerability is introduced. This vulnerability can be represented as a modified SF block ready to be embedded into a system with RISC-V architecture for hardware vulnerability detection experiments[13] [20].

After implementing the modified hardware NF block, the performance needs to be compared, and the node with vulnerability first identified using error detection software. Then, using virtual model analysis, analysis needs to be performed on the FPGA using a combination of Remote Bitbang and JTAG protocols, as well as *OpenOCD* software. Then the results need to be compared and possible deviations from the behavioral model of the device identified. The general concept of the scanning idea is presented in Fig. 5.

The device behavioral model is an abstract model which describes the functional behavior of a device and its interaction with other system components. It describes how a particular unit should behave under certain input signals and conditions. It does not specify the internal implementation of the device, and how this behavior is reflected in the overall picture of the device's interaction with external sources of information.

A description in unified modeling language, used to describe the behavior of the entire device, should be used for verification, but other options are possible.

You can use automated security checkers to check Verilog code for vulnerabilities or hardware flaws. These systems analyze the code for bugs and look for possible vulnerabilities. Third-party tools such as *Verilator* and *VeriSim*[14] can also be used to analyze and check Verilog code for vulnerabilities.

Verilator is an open source translator from Verilog to C/C++ which generates files for profiling and debugging. It allows users to analyze code for hardware bookmarks and vulnerabilities. This tool can be used to automatically check Verilog code for bugs.

VeriSim is an another tool for analyzing and verifying Verilog code. It allows users to analyze code using simulation and profiling. It also enables identification of hardware bookmarks and vulnerabilities in Verilog code.

Alternative tools for analyzing and inspecting Verilog code for hardware bookmarks and vulnerabilities include *Vivado HLS*[15], *Synopsys VCS*[16], and *Mentor Questa*[17].

Automated vulnerability scanning tools such as *SonarQube*[18] and *Coverity*[19] can be used to find

[12] RISC-V is an extensible open and free instruction system and processor architecture based on the RISC (reduced instruction set computer) concept for processor/microcontroller design and software development.

[13] Li C. *Securing Computer Systems Through Cyber Attack Detection at the Hardware Level*: Ph.D. Thesis (Comput.). USA: UC Irvine; 2020. P. 13–26. https://escholarship.org/uc/item/8vr8f0dq. Accessed May 15, 2023.

[14] Wei S. *Minimizing Leakage Energy in FPGAs Using Intentional Post-Silicon Device Aging*: Master Sci. Thesis. USA: UC Los Angeles; 2013. P. 16–35. https://escholarship.org/uc/item/75h4m6qb. Accessed May 15, 2023.

[15] https://docs.xilinx.com/r/en-US/ug949-vivado-design-methodology/Vivado-Design-Suite-User-and-Reference-Guides. Accessed May 15, 2023.

[16] https://users.ece.utexas.edu/~patt/10s.382N/handouts/vcs.pdf. Accessed May 15, 2023.

[17] https://www.orcada.ru/product/mentor-graphics/proektirovanie-zakaznyh-ims/products_106.html (in Russ.). Accessed May 15, 2023.

[18] https://www.sonarsource.com/products/sonarqube/. Accessed May 15, 2023.

[19] https://devguide.python.org/development-tools/coverity/. Accessed May 15, 2023.

vulnerabilities in SystemC program code. These tools enable automated scanning of the source code for vulnerabilities. If vulnerabilities or hardware bookmarks are not found, there is a risk that the application will be vulnerable to attack by malicious attackers who can exploit the vulnerability to make unwanted changes to the code or gain access to data[20, 21, 22, 23, 24] [21, 22].

In order to perform synchronization between a virtual processor and a real processor undergoing debugging, *OpenOCD* capabilities can be used. *OpenOCD* needs to be connected to the debug interface of the real processor. This can be done, for example, via the JTAG interface *OpenOCD* must then be configured to work with a virtual processor undergoing debugging, such as a processor emulated in *QEMU* [23] or through the Functional Safety Simulator[25].

Next, synchronization between the virtual and real processor must be performed. This can be done with the resume command which allows execution of the process on the virtual processor to be continued while synchronizing it with the real processor. Thus, it is possible to debug the virtual processor while being able to monitor its operation in real time.

For correct synchronization the correct *OpenOCD* configuration is needed, in order to work with a specific virtual processor and debugging interface of a real processor. The particular features of working with certain types of processors and debug interfaces also need to be taken into account.

In order to build a project for testing for hardware vulnerabilities, the cross-platform automatic build system *CMake* can be used. This allows you to create, test and package a build system for source code, as well as freely distributed compilers[26].

Figure 6 shows a code fragment of building a test program using *CMake* for the RISC-V processor. In order to execute the procedure, you need to install *CMake* and RISC-V compiler. To do this, you can use the operating system package manager or download them from the official websites.

To start it, the commands 'mkdir build && cd build && cmake ... && make' need to be executed. Then the project will be built, and the result of the build will be loaded into the stand and the virtual testing system, the code description of which is given in Fig. 7.

Since a hardware vulnerability in the FPU compute unit is under consideration here, one option for identifying vulnerabilities is to directly stress test systems related to floating-point computing.

Identifying hardware vulnerabilities by means of stress testing can be quite complex, unproductive, and depends on the type of vulnerability. However, the following approaches can be distinguished:

1. Changing operating conditions: stress testing can be used to identify vulnerabilities associated with prolonged operation of the device under high load conditions. For example, you can increase the number of requests to the device, increase the duration of operation, or change the temperature, humidity, or other operating parameters.
2. Attack simulation: with stress testing, attacks on the device can be simulated.
3. Congestion testing: stress testing can be used to test the device's resistance to congestion, for example, to check how the device handles high traffic or a situation where the number of users on the network increases dramatically.
4. Use of random test data: by generating random test data, the robustness of the device against data errors can be tested, e.g., data transmission errors or data storage errors.

It is important to realize that stress testing can only help identify specific hardware vulnerabilities. For a complete check, a combination of different methods and tests must be used, and the security recommendations of the device manufacturer must be followed. An evolution of this concept is the identification of vulnerabilities through software scanners.

The creation of a stand for identifying hardware vulnerabilities, as well as the technology of working with it, can be considered as one result of this research. This is because the available scientific literature provides no clear definition and description of the steps required to create similar hardware and developing examples for practicing possible vulnerable situations.

[20] Architecture and Core Commands. https://openocd.org/doc/html/Architecture-and-Core-Commands.html#RISC_002dV-Authentication-Commands. Accessed May 15, 2023.

[21] Verilog-Mode Help. https://veripool.org/verilog-mode/help/. Accessed May 15, 2023.

[22] Shepherd C., Markantonakis K. *Vulnerabilities analysis and attack scenarios description.* 2021. https://exfiles.eu/wp-content/uploads/2022/07/EXFILES-D5.1-Vulnerabilities-analysis-and-attack-scenarios-description-PU-M06.pdf. Accessed May 15, 2023.

[23] Wang B. *Improving and Securing Machine Learning Systems*: Ph.D. Thesis (Comput.). USA: UC Santa Barbara; 2019. P. 10–14. https://escholarship.org/uc/item/1nv8m9nb. Accessed May 15, 2023.

[24] Guo Z. *Security of Internet of Things Devices and Networks*: Ph.D. Thesis (Comput.). USA: UC Irvine; 2016. P. 1–30. https://escholarship.org/uc/item/4rq8s4jx. Accessed May 15, 2023.

[25] Spear Ch. *System Verilog for Verification: A Guide to Learning the Testbench Language Features*. Springer. 2018. https://3ec1218usm.files.wordpress.com/2016/12/book_systemverilog_for_verification.pdf. Accessed May 15, 2023.

[26] Qualys platform. https://www.qualys.com/solutions/pci-compliance/. Accessed May 15, 2023.

```
set(MCU_RISCV RISCV)
set(START_FILE startup.s) # Startup file s

add_compile_options(-Wall -Wextra)
add_compile_options(-O2 -ggdb)
add_link_options(-mthumb -mfpu=fpv4-sp-dl6 -mfloat-abi=hard
                 -T${RISCV_LDSCRIPT} --specs=nosys.specs --specs=nano.spec

# set the project name
project(Test_firs_prj VERSION 0.1)

include_directories(
                    "${PROJECT_BINARY_DIR}"
                    "${PROJECT_SOURCE_DIR}/inc"
                    "${PROJECT_SOURCE_DIR}/library/CMSIS"
                     )

set_property(SOURCE ${START_FILE} PROPERTY LANGUAGE C)

add_subdirectory(library/CMSIS)

configure_file(inc/version.h.in inc/version.h)

list(APPEND TARGET_SOURCE ${PROJECT_SOURCE_DIR}/inc/main.h)
list(APPEND TARGET_SOURCE ${PROJECT_SOURCE_DIR}/src/main.c)
```

Fig. 6. Example of program test assembly system

```
    delay_lms(100);
    printf("linpackc test \r\n");
    rtc_print_current_time();
    printf("Start >> linpackc test \r\n");

    rtc_print_current_time();
    printf("Stop >> linpackc test \r\n");

    while(1) {
        time_start = rtc_get_subsecond();
        linpackc_test();
        uint16_t real_len = read_string(test_string, TEST_STR_SIZE);
        printf("len read data = %d \r\n",real_len);

        if(real_len){
            printf("read data = %s \r\n",test_string);
            memset(test_string, 0, TEST_STR_SIZE);
        }

        time_stop = rtc_get_subsecond();
        uint64_t runtime = (uint64_t)time_stop-(uint64_t)time_start;
        printf("runtime = %ld \r\n",(uint32_t)runtime);
        rtc_print_current_time();
    }
}
```

Fig. 7. Code for running a stress test to verify the RISC-V behavioral description

IDENTIFYING VULNERABILITIES THROUGH SOFTWARE VULNERABILITY SCANNERS

A comparison of the most commonly used software vulnerability scanning systems is shown in the table below.

One of the tools specializing in searching for errors and vulnerabilities in C, C++, C#, and Java code is *PVS-Studio*, static code analyzer. However, for a more complete C code scanning you may need other tools such as *Gitleaks*, *Trivy*[27], *Burp Suite*[28], and *MobSF*[29]. Here is a brief description of these tools and their capabilities for detecting vulnerabilities in C code.

1. *Gitleaks* is a tool for finding sensitive data in Git repositories which can be used to scan C code stored in Git.
2. *Trivy* is a tool for scanning Docker containers and images for vulnerabilities in the packages and dependencies used. It can be used to scan Docker images containing C code.
3. *Burp Suite* is a popular web application security testing tool used to scan web applications written in the C language.
4. *MobSF* is a mobile application vulnerability scanning tool used to scan mobile applications written in C language (e.g., using Native Development Kit).

Table. Comparison of different software vulnerability scanning systems

No.	Scanner Name	Open code	C/C++ support	Main purpose
1	*Sn1per*[30]	no	no	It is used to scan for vulnerabilities in web applications, ports, and network devices, supports dictionary brute force scanning and allows you to customize various scanning parameters
2	*Wapiti3*[31]	yes	no	It is a vulnerability scanner for web applications that is open source and can automatically search for vulnerabilities in various parts of a web application such as URL parameters, forms, headers, and scripts
3	*Nikto*[32]	yes	no	It performs database and extensible script-based vulnerability scanning, enables scanning various vulnerabilities such as cross-site scripting (XSS), SQL-injections, header spoofing, unauthorized access, etc.
4	*OWASP ZAP*[33]	yes	no	It provides automatic or manual scanning and penetration tests. It is used to search for vulnerabilities such as SQL injection, XSS, cross-site request forgery, invalid authorization, etc.
5	*Sqlmap*[34]	yes	no	It is a tool for automatic scanning of SQL injection vulnerabilities in web applications. It supports multiple databases including *MySQL, Oracle*, *PostgreSQL*, *Microsoft SQL Server*, etc.
6	*Acunetix WVS*[35]	no	no	It is a web application vulnerability scanning tool that provides automatic or manual scanning options. It supports detection of vulnerabilities such as XSS, SQL injection, information leaks, file security breaches, etc.

[27] https://trivy.dev/. Accessed May 15, 2023.
[28] https://portswigger.net/burp. Accessed May 15, 2023.
[29] https://github.com/MobSF/Mobile-Security-Framework-MobSF. Accessed May 15, 2023.
[30] https://github.com/1N3/Sn1per/releases. Accessed May 15, 2023.
[31] https://pypi.org/project/wapiti3/ (in Russ.). Accessed May 15, 2023.
[32] https://github.com/sullo/nikto. Accessed May 15, 2023.
[33] https://www.zaproxy.org/docs/. Accessed May 15, 2023.
[34] https://sqlmap.org/. Accessed May 15, 2023.
[35] https://allsoft.ru/software/vendors/acunetix/acunetix-web-vulnerability-scanner-/ (in Russ.). Accessed May 15, 2023.

Table. Continued

No.	Scanner Name	Open code	C/C++ support	Main purpose
7	*Vega*[36]	yes	no	It is a tool for scanning vulnerabilities in web applications. It supports dictionary brute-force scanning and provides penetration tests and enables detection of vulnerabilities such as XSS, SQL-injections
8	*PVS-Studio*[37]	no	yes	A static code analyzer in C, C++, C#, and Java designed to search for errors and vulnerabilities
9	*Gitleaks*[38]	no	yes	It is a tool for scanning open source Git repositories for sensitive information and other security vulnerabilities. It operates by analyzing source code, commits, and change history in the repository for lines of code containing sensitive information such as passwords, secure shell keys, access tokens, API secrets
10	*QARK*[39]	yes	no	Java application scanner for Android and IOS

Each of these tools is designed to detect vulnerabilities in different areas. When combined, they can provide more comprehensive code security coverage.

However, it should be noted that most of the scanners on the list can be used to scan code in a variety of programming languages, including C. However, depending on your specific needs and the type of vulnerabilities you need to detect, a combination of several tools may need to be used.

CONCLUSIONS

The research carried out herein has shown that the proposed approach based on scanning systems and semi-natural modeling can successfully identify the hardware vulnerabilities of digital systems when other methods prove ineffective and the analysis of the results is difficult to interpret. Only in a synthetic experiment using semi-natural modeling is it possible to narrow the search area and identify a system with embedded malicious code with a vulnerability. The results of the experiments allowed us to develop a methodology and define a set of tools for identifying vulnerabilities in digital devices of computing systems, as well as to create a library of ready-made solutions for implementing an optimal solution.

The results obtained and the stand we developed for conducting experiments can be used in perspective projects linked to the creation of digital devices on a modern element base. It offers the possibility of transition to new technologies for detection of hardware vulnerabilities. Hardware security should be considered as a priority task in various industries and spheres of activity. The detection and elimination of vulnerabilities of digital components of devices should be carried out both at early stages of development and at the stage of operation.

[36] https://subgraph.com/vega/. Accessed May 15, 2023.
[37] https://pvs-studio.ru/ru/pvs-studio/ (in Russ.). Accessed May 15, 2023.
[38] https://github.com/gitleaks/gitleaks. Accessed May 15, 2023.
[39] https://github.com/linkedin/qark. Accessed May 15, 2023.

ACKNOWLEDGMENTS

This work was supported by the Ministry of Science and Higher Education of the Russian Federation (State task for universities No. FGFZ-2023-0005) and using the equipment of the Center for Collective Use of RTU MIREA (agreement dated September 01, 2021, No. 075-15-2021-689, unique identification number 2296.61321X0010).

Authors' contributions

E.F. Pevtsov—the research idea, consultations on research issues, writing the text of the article.

T.A. Demenkova—the research idea, research planning, scientific editing of the article.

A.O. Indrishenok—the research idea, conducting research, writing the text of the article, interpretation and generalization of the results.

V.V. Filimonov—consultations on research issues, writing the text of the article.

REFERENCES

1. Smetana D. FPGA-Enabled Trusted Boot Is Part of Building Security into Every Aspect of Trusted Computing Architectures. *Military & Aerospace Electronics Journal*. September 25, 2019. Available from URL: https://www.militaryaerospace.com/trusted-computing/article/14040672/trustedcomputing-embedded-computing-realworld
2. Sesin I.Yu., Bolbakov R.G. Comparative analysis of software optimization methods in context of branch predication on GPUs. *Russ. Technol. J.* 2021;9(6):7–15 (in Russ.). https://doi.org/10.32362/2500-316X-2021-9-6-7-15
3. Shayan M., Basu K., Karri R. Hardware Trojans Inspired Hardware IP Watermarks. *IEEE Design & Test*. 2019;36(6):72–79. https://doi.org/10.1109/MDAT.2019.2929116
4. Hennessy J.L., Patterson D.A. A new golden age for computer architecture: Domain-specific hardware/software co-design, enhanced security, open instruction sets, and agile chip development. In: *Proceedings of the 2018 ACM/IEEE 45th Annual International Symposium on Computer Architecture* (*ISCA*). IEEE; 2018. https://doi.org/10.1109/ISCA.2018.00011
5. Li D., Zhang Q., Zhao D., Li L., He J., Yuan Y., Zhao Y. Hardware Trojan Detection Using Effective Property-Checking Method. *Electronics*. 2022;11(17):2649. https://doi.org/10.3390/electronics11172649
6. Alekhin V.A. Designing electronic systems using SystemC and SystemC-AMS. *Russ. Technol. J.* 2020;8(4):79–95 (in Russ.). https://doi.org/10.32362/2500-316X-2020-8-4-79-95
7. Yang K., Zhang K., Ren J., Shen X. Security and privacy in mobile crowdsourcing: Challenges and opportunities. *IEEE Commun. Mag*. 2015;53(8):75–81. https://doi.org/10.1109/MCOM.2015.7180511
8. Lou X., Zhang T., Jiang J., Zhang Y. *A Survey of Microarchitectural Side-channel Vulnerabilities, Attacks and Defenses in Cryptography*. Vol. 1. No. 1. March 2021. Available from URL: https://arxiv.org/pdf/2103.14244
9. Skorobogatov S., Woods C. Breakthrough Silicon Scanning Discovers Backdoor in Military Chip. In: Prouff E., Schaumont P. (Eds.). *Cryptographic Hardware and Embedded Systems – CHES 2012*. *Lecture Notes in Computer Science*. 2012. V. 7428. Berlin, Heidelberg: Springer. https://doi.org/10.1007/978-3-642-33027-8_2
10. Tasiran S., Keutzer K. Coverage metrics for functional validation of hardware designs. *IEEE Des. Test. Comput.* 2001;18(4):36–45. https://doi.org/10.1109/54.936247
11. Mukhopadhyay D., Chakraborty R.S. *Hardware Security: Design, Threats, and Safeguards*. CRC Press; 2014. 542 p. ISBN 978-1-4398-9584-9
12. Tarasov I.E. *PLIS Xilinx. Yazyki opisaniya apparatury VHDL i Verilog, SAPR, priemy proektirovaniya* (*FPGA Xilinx. Hardware Description Languages VHDL and Verilog, CAD, Design Techniques*). Moscow: Goryachaya liniya – Telekom; 2024. 538 p. (in Russ.). ISBN 978-5-9912-0802-4
13. Turkington K., Masseios K., Constantinides G.A., Leong P. FPGA Based Acceleration of the Linpack Benchmark: A High Level Code Transformation Approach. In: *2006 International Conference on Field Programmable Logic and Applications*. IEEE; 2007. INSPEC Accession Number: 9604301. https://doi.org/10.1109/FPL.2006.311240
14. Tamuly S., Joseph A. Chandrasekharan J. Deep Learning Model for Image Classification. In: Smys S., Tavares J., Balas V., Iliyasu A. (Eds.). *Computational Vision and Bio-Inspired Computing. ICCVBIC 2019. Advances in Intelligent Systems and Computing*. Springer, Cham; 2019. V. 1108. P. 312–320. https://doi.org/10.1007/978-3-030-37218-7_36
15. Majeric F., Gonzalvo B., Bossuet L. JTAG Fault Injection Attack. *IEEE Embed. Syst. Lett.* 2018;10(3):65–68. https://doi.org/10.1109/LES.2017.2771206
16. Abdalhag B., Awad A., Hawash A. A fast Binary Decision Diagram (BDD)-based reversible logic optimization engine driven by recent meta-heuristic reordering algorithms. *Microelectron. Reliab*. 2021;123:114168. https://doi.org/10.1016/j.microrel.2021.114168
17. Pevtsov E.F., Demenkova T.A., Shnyakin A.A. Design for Testability of Integrated Circuits and Project Protection Difficulties. *Russ. Technol. J*. 2019;7(4):60–70 (in Russ.). https://doi.org/10.32362/2500-316X-2019-7-4-60-70

18. Kuo M.-H., Hu Ch.-M., Lee K.-J. Time-Related Hardware Trojan Attacks on Processor Cores. In: *IEEE International Test Conference in Asia* (*ITC-Asia*). IEEE; 2019. https://doi.org/10.1109/ITC-Asia.2019.00021
19. Komolov D., Zolotukho R. Using special memory chips to ensure FPGA copy protection. *Komponenty i tekhnologii = Components & Technologies*. 2008;12:24–26 (in Russ.). Available from URL: https://kit-e.ru/wp-content/uploads/2008_12_24.pdf
20. Becker A., Hu W., Tai Y., Brisk P., Kastner R., Ienne P. Arbitrary Precision and Complexity Tradeoffs for Gate-Level Information Flow Tracking. In: *Proceedings of the 54th ACM/EDAC/IEEE Design Automation Conference* (*DAC*). IEEE, 2017. Part 128280. https://doi.org/10.1145/3061639.3062203
21. Polychronou N.F., Thevenon P.H., Puys M., Beroulle V. A Comprehensive Survey of Attacks without Physical Access Targeting Hardware Vulnerabilities in IoT/IIoT Devices, and Their Detection Mechanisms. *ACM Trans. Design Automat. Electron. Syst*. 2022;27(1):1–35. https://doi.org/10.1145/3471936
22. Erata F., Deng Sh., Zaghloul F., Xiong W., Demir O., Szefer J. Survey of Approaches and Techniques for Security Verification of Computer Systems. *ACM J. Emerg. Technol. Comput. Syst.* 2022;1(1):Article 1. https://doi.org/10.1145/3564785
23. Yang X., Zhao D., Jiang Y., Zhang X., Yuan Y. Fault Simulation and Formal Analysis in Functional Safety CPU FMEDA Campaign. *J. Phys.: Conf. Ser*. 2021;1769:012061. https://doi.org/10.1088/1742-6596/1769/1/012061

СПИСОК ЛИТЕРАТУРЫ

1. Smetana D. FPGA-Enabled Trusted Boot Is Part of Building Security into Every Aspect of Trusted Computing Architectures. *Military & Aerospace Electronics Journal*. September 25, 2019. URL: https://www.militaryaerospace.com/trusted-computing/article/14040672/trustedcomputing-embedded-computing-realworld
2. Сесин И.Ю., Болбаков Р.Г. Сравнительный анализ методов оптимизации программного обеспечения для борьбы с предикацией ветвлений на графических процессорах. *Russ. Technol. J*. 2021;9(6):7–15. https://doi.org/10.32362/2500-316X-2021-9-6-7-15
3. Shayan M., Basu K., Karri R. Hardware Trojans Inspired Hardware IP Watermarks. *IEEE Design & Test*. 2019;36(6):72–79. https://doi.org/10.1109/MDAT.2019.2929116
4. Hennessy J.L., Patterson D.A. A new golden age for computer architecture: Domain-specific hardware/software co-design, enhanced security, open instruction sets, and agile chip development. In: *Proceedings of the 2018 ACM/IEEE 45th Annual International Symposium on Computer Architecture* (*ISCA*). IEEE; 2018. https://doi.org/10.1109/ISCA.2018.00011
5. Li D., Zhang Q., Zhao D., Li L., He J., Yuan Y., Zhao Y. Hardware Trojan Detection Using Effective Property-Checking Method. *Electronics*. 2022;11(17):2649. https://doi.org/10.3390/electronics11172649
6. Алехин В.А. Проектирование электронных систем с использованием SystemC и SystemC–AMS. *Russ. Technol. J*. 2020;8(4):79–95. https://doi.org/10.32362/2500-316X-2020-8-4-79-95
7. Yang K., Zhang K., Ren J., Shen X. Security and privacy in mobile crowdsourcing: Challenges and opportunities. *IEEE Commun. Mag*. 2015;53(8):75–81. https://doi.org/10.1109/MCOM.2015.7180511
8. Lou X., Zhang T., Jiang J., Zhang Y. *A Survey of Microarchitectural Side-channel Vulnerabilities, Attacks and Defenses in Cryptography*. Vol. 1. No. 1. March 2021. URL: https://arxiv.org/pdf/2103.14244
9. Skorobogatov S., Woods C. Breakthrough Silicon Scanning Discovers Backdoor in Military Chip. In: Prouff E., Schaumont P. (Eds.). *Cryptographic Hardware and Embedded Systems – CHES 2012*. *Lecture Notes in Computer Science*. 2012. V. 7428. Berlin, Heidelberg: Springer. https://doi.org/10.1007/978-3-642-33027-8_2
10. Tasiran S., Keutzer K. Coverage metrics for functional validation of hardware designs. *IEEE Des. Test. Comput.* 2001;18(4):36–45. https://doi.org/10.1109/54.936247
11. Mukhopadhyay D., Chakraborty R.S. *Hardware Security: Design, Threats, and Safeguards.* CRC Press; 2014. 542 p. ISBN 978-1-4398-9584-9
12. Тарасов И.Е. *ПЛИС Xilinx. Языки описания аппаратуры VHDL и Verilog, САПР, приемы проектирования.* М.: Горячая линия – Телеком; 2024. 538 с. ISBN 978-5-9912-0802-4
13. Turkington K., Masseios K., Constantinides G.A., Leong P. FPGA Based Acceleration of the Linpack Benchmark: A High Level Code Transformation Approach. In: *2006 International Conference on Field Programmable Logic and Applications*. IEEE; 2007. https://doi.org/10.1109/FPL.2006.311240
14. Tamuly S., Joseph A. Chandrasekharan J. Deep Learning Model for Image Classification. In: Smys S., Tavares J., Balas V., Iliyasu A. (Eds.). *Computational Vision and Bio-Inspired Computing. ICCVBIC 2019. Advances in Intelligent Systems and Computing*. Springer, Cham; 2019. V. 1108. P. 312–320. https://doi.org/10.1007/978-3-030-37218-7_36
15. Majeric F., Gonzalvo B., Bossuet L. JTAG Fault Injection Attack. *IEEE Embed. Syst. Lett.* 2018;10(3):65–68. https://doi.org/10.1109/LES.2017.2771206
16. Abdalhag B., Awad A., Hawash A. A fast Binary Decision Diagram (BDD)-based reversible logic optimization engine driven by recent meta-heuristic reordering algorithms. *Microelectron. Reliab*. 2021;123:114168. https://doi.org/10.1016/j.microrel.2021.114168
17. Певцов Е.Ф., Деменкова Т.А., Шнякин А.А. Тестопригодное проектирование интегральных схем и проблемы защиты проектов. *Russ. Technol. J*. 2019;7(4):60–70. https://doi.org/10.32362/2500-316X-2019-7-4-60-70
18. Kuo M.-H., Hu Ch.-M., Lee K.-J. Time-Related Hardware Trojan Attacks on Processor Cores. In: *IEEE International Test Conference in Asia* (*ITC-Asia*). IEEE; 2019. https://doi.org/10.1109/ITC-Asia.2019.00021

19. Комолов Д., Золотухо Р. Использование микросхем специальной памяти для обеспечения защиты ПЛИС FPGA от копирования. *Компоненты и технологии*. 2008;12:24–26. URL: https://kit-e.ru/wp-content/uploads/2008_12_24.pdf
20. Becker A., Hu W., Tai Y., Brisk P., Kastner R., Ienne P. Arbitrary Precision and Complexity Tradeoffs for Gate-Level Information Flow Tracking. In: *Proceedings of the 54th ACM/EDAC/IEEE Design Automation Conference* (*DAC*). IEEE, 2017. Part 128280. https://doi.org/10.1145/3061639.3062203
21. Polychronou N.F., Thevenon P.H., Puys M., Beroulle V. A Comprehensive Survey of Attacks without Physical Access Targeting Hardware Vulnerabilities in IoT/IIoT Devices, and Their Detection Mechanisms. *ACM Trans. Design Automat. Electron. Syst*. 2022;27(1):1–35. https://doi.org/10.1145/3471936
22. Erata F., Deng Sh., Zaghloul F., Xiong W., Demir O., Szefer J. Survey of Approaches and Techniques for Security Verification of Computer Systems. *ACM J. Emerg. Technol. Comput. Syst.* 2022;1(1):Article 1. https://doi.org/10.1145/3564785
23. Yang X., Zhao D., Jiang Y., Zhang X., Yuan Y. Fault Simulation and Formal Analysis in Functional Safety CPU FMEDA Campaign. *J. Phys.: Conf. Ser*. 2021;1769:012061. https://doi.org/10.1088/1742-6596/1769/1/012061

About the authors

Evgeniy F. Pevtsov, Cand. Sci. (Eng.), Director of Center for the Design of Integrated Circuits, Nanoelectronics Devices and Microsystems, MIREA – Russian Technological University (78, Vernadskogo pr., Moscow, 119454 Russia). E-mail: pevtsov@mirea.ru. Scopus Author ID 6602652601. ResearcherID M-2709-2016, RSCI SPIN-code 1410-2483, http://orcid.org/0000-0001-6264-1231

Tatyana A. Demenkova, Cand. Sci. (Eng.), Associated Professor, Computer Technology Department, Institute of Information Technologies, MIREA – Russian Technological University (78, Vernadskogo pr., Moscow, 119454 Russia). E-mail: demenkova@mirea.ru. Scopus Author ID 57192958412, ResearcherID AAB-3937-2020, RSCI SPIN-code 3424-7489, http://orcid.org/0000-0003-3519-6683

Alexander O. Indrishenok, Postgraduate Student, Computer Technology Department, Institute of Information Technologies, MIREA – Russian Technological University (78, Vernadskogo pr., Moscow, 119454 Russia). E-mail: indrishenoksasha@mail.ru. RSCI SPIN-code 2308-7140, http://orcid.org/0000-0003-1471-9043

Vladimir V. Filimonov, Senior Lecturer, Department of Physics and Technical Mechanics, Institute for Advanced Technologies and Industrial Programming, MIREA – Russian Technological University (78, Vernadskogo pr., Moscow, 119454 Russia). E-mail: filimonov@mirea.ru. Scopus Author ID 7102525379. http://orcid.org/0000-0003-1118-6608

Об авторах

Певцов Евгений Филиппович, к.т.н., директор структурного подразделения «Центр проектирования интегральных схем, устройств наноэлектроники и микросистем», ФГБОУ ВО «МИРЭА – Российский технологический университет» (119454, Россия, Москва, пр-т Вернадского, д. 78). E-mail: pevtsov@mirea.ru. Scopus Author ID 6602652601. ResearcherID M-2709-2016, SPIN-код РИНЦ 1410-2483, http://orcid.org/0000-0001-6264-1231

Деменкова Татьяна Александровна, к.т.н., доцент, кафедра вычислительной техники, Институт информационных технологий, ФГБОУ ВО «МИРЭА – Российский технологический университет» (119454, Россия, Москва, пр-т Вернадского, д. 78). E-mail: demenkova@mirea.ru. Scopus Author ID 57192958412, ResearcherID AAB-3937-2020, SPIN-код РИНЦ 3424-7489, http://orcid.org/0000-0003-3519-6683

Индришенок Александр Олегович, аспирант, кафедра вычислительной техники, Институт информационных технологий, ФГБОУ ВО «МИРЭА – Российский технологический университет» (119454, Россия, Москва, пр-т Вернадского, д. 78). E-mail: indrishenoksasha@mail.ru. SPIN-код РИНЦ 2308-7140, http://orcid.org/0000-0003-1471-9043

Филимонов Владимир Викторович, старший преподаватель, кафедра физики и технической механики, Институт перспективных технологий и индустриального программирования, ФГБОУ ВО «МИРЭА – Российский технологический университет» (119454, Россия, Москва, пр-т Вернадского, д. 78). E-mail: filimonov@mirea.ru. Scopus Author ID 7102525379, http://orcid.org/0000-0003-1118-6608

Translated from Russian into English by Lyudmila O. Bychkova
Edited for English language and spelling by Dr. David Mossop

Multiple robots (robotic centers) and systems. Remote sensing and non-destructive testing

Роботизированные комплексы и системы.
Технологии дистанционного зондирования неразрушающего контроля

UDC 004.31
https://doi.org/10.32362/2500-316X-2024-12-4-40-50
EDN ECAQGY

RESEARCH ARTICLE

Calculation of the main operational characteristics of a tethered high-altitude ship-based system

Igor I. Dawlyud @

Admiral F.F. Ushakov Baltic Higher Naval School, Kaliningrad, 236022 Russia
@ *Corresponding author, e-mail: sawefew2@yandex.ru*

Abstract

Objectives. Currently, UAVs are actively used in many military and civilian fields such as object surveillance, telecommunications, radar, photography, video recording, and mapping, etc. The main disadvantage of autonomous UAVs is their limited operating time. The long-term operation of UAVs on ships can be ensured by tethered high-altitude systems in which the power supply of engines and equipment is provided from the onboard energy source through a thin cable tether. This paper aims to select and justify the appearance of such system, as well as to calculate the required performance characteristics.

Methods. The study used methods of systemic and functional analysis of tethered system parameters, as well as methods and models of the theory of relations and measurement.

Results. The issues of design and implementation of new generation tethered high-altitude ship-based systems were considered. A rational type of aerodynamic design for unmanned aerial vehicles was determined based on existing tethered platforms. The optimal architecture of the tethered system was defined and justified. The paper presents the appearance and solution for placement onboard the ship, and describes its operation. The main initial parameters for designing high-altitude systems such as take-off weight, optimal lift altitude, maximum power required for operation, structure of the energy transfer system, as well as deployment and lift time to the design altitude were selected and calculated.

Conclusions. The methodology for calculating the necessary characteristics described in the paper can be used for developing and evaluating tethered high-altitude systems. These systems are capable of performing a wide range of tasks, without requiring a separate storage and launch location, which is especially important in the ship environment. The system presented herein possesses significant advantages over well-known analogues.

Keywords: tethered high-altitude platform, unmanned aerial vehicle, power, energy transfer, ship, transport and launch container

• **Submitted:** 23.11.2023 • **Revised:** 04.03.2024 • **Accepted:** 24.05.2024

For citation: Dawlyud I.I. Calculation of the main operational characteristics of a tethered high-altitude ship-based system. *Russ. Technol. J*. 2024;12(4):40–50. https://doi.org/10.32362/2500-316X-2024-12-4-40-50

Financial disclosure: The author has no a financial or property interest in any material or method mentioned.

The author declares no conflicts of interest.

НАУЧНАЯ СТАТЬЯ

Расчет основных эксплуатационных характеристик привязной высотной системы корабельного базирования

И.И. Давлюд [@]

Балтийское высшее военно-морское училище имени Ф.Ф. Ушакова, Калининград, 236022 Россия
[@] *Автор для переписки, e-mail: sawefew2@yandex.ru*

Резюме

Цели. Беспилотные летательные аппараты (БПЛА) активно применяются во многих военных и гражданских областях: мониторинг критических объектов, телекоммуникации, радиолокация, фото- и видеосъемка, картографирование и др. Основным недостатком автономных БПЛА является ограниченное время функционирования. Длительное функционирование БПЛА на кораблях могут обеспечить привязные высотные системы (ПВС), в которых электропитание двигателей и аппаратуры полезной нагрузки осуществляется от бортового источника энергии по тонкому кабель-тросу. Цель работы – выбор и обоснование облика ПВС, расчет необходимых эксплуатационных характеристик.

Методы. В работе используются методы системного и функционального анализа параметров привязной системы, методы и модели теории отношений и измерения.

Результаты. Рассмотрены вопросы проектирования и реализации нового поколения ПВС корабельного базирования. На основе существующих привязных платформ определен рациональный тип аэродинамической схемы БПЛА. Определена и обоснована оптимальная архитектура привязной системы, представлен ее облик и решение по размещению на корабле, а также описана ее работа. Выбраны и рассчитаны основные исходные параметры для проектирования высотных систем, такие как взлетная масса, оптимальная высота подъема, максимальная необходимая мощность для функционирования, структура системы передачи энергии, время развертывания и подъема на расчетную высоту.

Выводы. Представленная в статье методология расчета необходимых характеристик позволяет использовать ее для разработки и оценки ПВС. Данные системы способны выполнять различный спектр задач, при этом не требуя отдельного места хранения и запуска, что особенно актуально в корабельных условиях. Представленная система имеет значительные преимущества перед известными аналогами.

Ключевые слова: привязная высотная платформа, беспилотный аппарат, мощность, передача энергии, корабль, транспортно-пусковой контейнер

• **Поступила:** 23.11.2023 • **Доработана:** 04.03.2024 • **Принята к опубликованию:** 24.05.2024

Для цитирования: Давлюд И.И. Расчет основных эксплуатационных характеристик привязной высотной системы корабельного базирования. *Russ. Technol. J.* 2024;12(4):40–50. https://doi.org/10.32362/2500-316X-2024-12-4-40-50

Прозрачность финансовой деятельности: Автор не имеет финансовой заинтересованности в представленных материалах или методах.

Автор заявляет об отсутствии конфликта интересов.

INTRODUCTION

Today, multirotor unmanned aerial vehicles (UAVs) have become widespread and intensely developed. UAVs have many irrefutable advantages including simple and inexpensive designs in contrast to large aircraft systems, as well as safety, low maintenance, absence of the need for special launch sites, and efficiency. The main disadvantage of the UAV is low (limited) flight autonomy due to the insufficient battery capacity of UAVs equipped with electric motors [1].

Long-term UAV operation can be ensured by a continuous power supply using tethered high-altitude systems (THAS). In such systems, high power energy is transferred to UAV while the UAV is maintained at a certain altitude by means of a thin cable tether [2]. At the same time, THAS enables the precise landing of the UAV at the designated location. It can also be used in places with barriers (obstacles), e.g., on the deck of a ship.

In the Russian Navy (Navy), THAS is used for video surveillance, target designation, communication, and electronic warfare, etc. However, the mass use of THAS on ships is currently difficult due to the lack of specialized storage sites, as well as simple and reliable launch and landing systems [3].

DESIGN AND CALCULATION OF THAS PERFORMANCE CHARACTERISTICS

The following activities are required for the development of ship-based THAS:

- defining the operating architecture, appearance, and THAS storage and launch sites;
- calculating the basic tactical and operational characteristics;
- calculating the parameters of tolerance to external disturbances.

At the present time, the Navy is searching for the optimal placement of the THAS storage, take-off, and landing sites along with their operation and maintenance facilities on ships. In most cases, this is due to the need for a significant change in the external and internal architecture of the ship in order to find the necessary space [3]. This approach is unacceptable for a warship since it may cause significant changes in its operational and technical characteristics. Therefore, the solution to the problem of storing, launching, and landing THAS should be reduced to the need for searching for other ways using special means.

In architectural terms, advanced THAS is a system consisting of airborne (UAV) and shipborne modules connected to each other by a flexible link (cable tether) and placed in a standard transporter-launcher container (TLC) for vertical launching systems (VLS) located below the upper deck (Fig. 1).

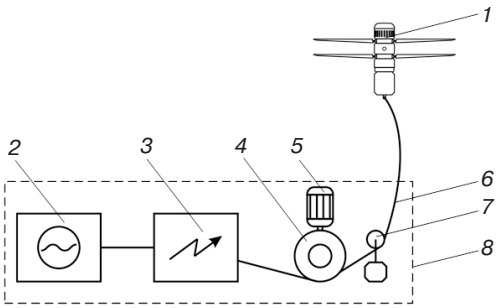

Fig. 1. Ship-based tethered high-altitude system: *1* air module (UAV), *2* alternating current source, *3* voltage converter and winch control system, *4* winch, *5* winch drive, *6* cable tether, *7* cable tether tension sensor, and *8* shipborne module

The unmanned aerial vehicle holds the payload on board at a given point above sea level. The UAV is mechanically linked to the shipborne module by a cable tether. The ship module includes an AC voltage source, voltage converter, winch control system, winch drive, and a cable tether tension sensor. The appearance of the THAS located in TLC is shown in Fig. 2.

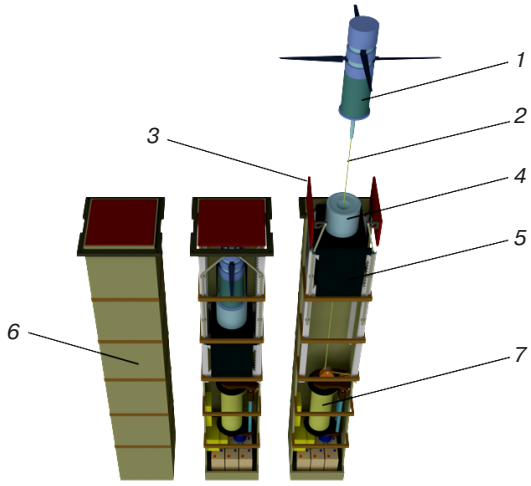

Fig. 2. THAS located in TLC: *1* UAV, *2* cable tether, *3* lid flaps, *4* cup, *5* pedestal, *6* TLC, and *7* winch

When selecting the type of UAV, its specific operating features should be taken into account [4] along with operating conditions. The UAV's dependence for spatial orientation on the force and direction of the wind load should be minimized. Therefore, three aerodynamic schemes can be used for THAS: single-rotor UAV with several steering devices (steering propellers) symmetrically located relative to the axis of the main rotor; coaxial; and a multi-rotor one with four or more propellers located symmetrically relative to the UAV center.

All types of UAV have their own advantages and disadvantages. However, despite the relative complexity of the design, a coaxial scheme is selected for THAS. Its heading orientation is slightly dependent on wind

direction. This UAV type is simpler to store and launch from a container: a rational solution under given conditions.

The following are the main initial designed parameters when developing THAS:

- the UAV take-off weight, including the weight of UAV itself, payload weight, and cable tether weight;
- optimal UAV flying altitude;
- maximum power required for UAV operation;
- the system structure for transferring power to UAV;
- UAV deployment and lift time to the set altitude.

THAS operates as follows. In the storage base, the UAV is equipped with the payload required for specific missions. The TLC is loaded into VLS (Fig. 2). Prior to using the device, the VLS lid is opened. Then, the TLC lid flaps are opened using the drive. This is followed by lifting the cup which is rigidly fixed on the pedestal.

Once the pedestal is lifted to the highest position, the propellers of the UAV are started. They are driven by at least two electric motors powered through the cable tether. The UAV begins to rise vertically. The control system generates the voltage necessary for the winch drive which rotates, in order to unwind the cable tether connected to the UAV's pin via the tension sensor, roller system, and cable laying equipment. A tension sensor is required for maintaining a set tension force of the cable tether and preventing emergencies by generating signals for the control system. During operation (rising and hovering at a certain altitude), the UAV is supplied with high voltage from the control system through the cable tether, reduced by the onboard converter to the value required for operating the UAV with the payload installed on it.

After gaining altitude, the UAV is stabilized relative to the horizon and heading with the specified accuracy. It is maintained in this position during the entire operation. UAV stabilization during operation is carried out automatically by a system of sensors: gyroscope, accelerometer, barometric altimeter (altimeter), and three-component magnetometer. The control laws are formed using a microprocessor to stabilize heading, roll, and pitch, as well as to resist wind disturbances. The UAV drift due to wind or ship motion is compensated by the global navigation system receiver and accelerometers. The vertical movements caused by wave action are compensated by changing the length of the cable tether in response to signals from onboard sensors and the control system.

In the event of an emergency or a lack of power supply from the onboard source, the UAV is powered by batteries located in the bottom part of the TLC. In the case of a cable tether breakage, the UAV is provided with an automatic emergency landing mode using the onboard battery energy.

Landing is performed in the reverse sequence. In this case, the constant tension of the cable tether ensures UAV leveling over the cup. The deployment, take-off, landing, and rollback of the onboard tethered high-altitude system are performed automatically.

TAKE-OFF WEIGHT

In UAV design, an important parameter is the maximum take-off weight of the UAV. This means the UAV weight with the payload installed and the weight of the cable tether of the maximum possible length:

$$m_{TO} = m_{UAV} + m_{PL} + m_{CT}h, \quad (1)$$

where m_{UAV} is UAV weight, m_{PL} is the payload weight, m_{CT} is the cable tether weight per unit length, and h is UAV altitude.

In Eq. (1), the unknown quantity is the last summand dependent on the cable tether used and the UAV altitude. The cable tether may consist of either the cable with support tether or the cable attached to support tether separately (Fig. 3).

(a) (b)

Fig. 3. Cable tether versions: (a) CPVLS[1] power cable, (b) UTP[2] cable tether

The first version is preferable since it has a more compact and easy-to-use design. The cable tether production technology implies using the insulated power cable in its center, and the insulated wires with copper conductive conductors of round cross-section around it. The cable tether outer protective sheath consists of insulating material. Inside the cable outer sheath, there are voids filled with low density material which provide the system with crush resistance.

The main materials used in producing cable tether are copper, kevlar, fiber optics, and plastics. The cable weight per unit length is determined by the following equation:

$$m_{CT} = \rho_K S_{Teth} + \rho_{Cu} S_{Cu} u_{Cu} n + \\ + \rho_{Ins} S_{Ins} + \rho_{Sh} S_{Sh} + \rho_{Fill} S_{Fill} + \rho_{OF} S_{OF}, \quad (2)$$

where ρ_K, ρ_{Cu}, ρ_{Ins}, ρ_{Sh}, ρ_{Fill}, and ρ_{OF} are densities of kevlar, copper, insulation, sheath, filling material,

[1] C is control cable, P is polyethylene core insulation, V is polyvinyl chloride plastic sheath, L is lifting cable, and S means with load-carrying tether made of synthetic threads.

[2] UTP is the unshielded twisted pair.

and optical fiber, respectively; u_{Cu} is the coefficient accounting for twisting of wires in the conductive core; S_{Teth}, S_{Cu}, S_{Ins}, S_{Sh}, S_{Fill}, and S_{OF} are cross-sectional areas of the tether, copper conductor, insulation, sheath, filling, and optical fiber, respectively; and n is number of copper conductors.

For further calculations, the following constraints are assumed:

- the optical fiber is homogeneous over the entire cross-section;
- the outer sheath has a circular cross-section;
- thickness and insulation material of all cores and cable are the same;
- all cores have the same cross-section.

A simplified version of the cross-section of a cable tether with two copper conductors and optical fiber is shown in Fig. 4.

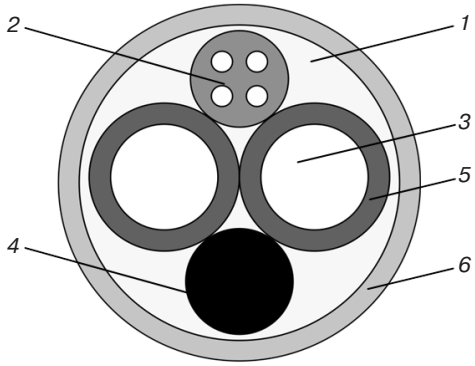

Fig. 4. Cross section of a cable tether: *1* filling material, *2* optical fiber, *3* copper core, *4* kevlar tether, *5* insulation, and *6* sheath

The insulation area S_{Ins} is calculated by means of the following formula:

$$S_{Ins} = 2\pi k_{Ins}(r_{Cond} - k_{Ins}/2)(n+1), \quad (3)$$

where k_{Ins} is the insulation thickness, r_{Cond} is the conductor radius.

The area of the sheath is determined as follows:

$$S_{Sh} = 2\pi k_{Sh}(r_{CT} - k_{Sh}/2), \quad (4)$$

where k_{Sh} is thickness of the sheath, r_{CT} is radius of the cable tether.

The radius of the considered cable tether is determined by means of the following formula:

$$r_{CT} = k_{Sh} + 3k_{Ins} + 2r_{Cu} + r_{Teth}, \quad (5)$$

where r_{Teth} is the tether radius, r_{Cu} is the copper core radius.

The cross-section of the filling material has a complex shape, so its area is determined by means of the following expression:

$$S_{Fill} = \pi r_{CT}^2 - \pi(r_{Teth}^2 u_{Teth} + r_{Cu}^2 u_{Cu} n + 2k_{Ins}(r_{Cond} - k_{Ins}/2)(n+1) + r_{OF}^2 + 2k_{Sh}(r_{CT} - k_{Sh}/2)), \quad (6)$$

where r_{OF} is the optical fiber radius.

After transforming expression (6), the following is obtained:

$$S_{Fill} = \pi((r_{CT} - k_{Sh})^2 - ((r_{Teth} + k_{Ins})^2 u_{Teth} + r_{Cond}^2 u_{Cu} n + r_{OF}^2)). \quad (7)$$

By substituting equations (3), (4), and (7) into (2), we obtain the following:

$$\begin{aligned} m_{CT} = {} & \rho_K \pi r_{Teth}^2 + \\ & + \rho_{Cu} \pi r_{Cu}^2 u_{Cu} n + \\ & + \rho_{Ins} 2\pi k_{Ins}(r_{Cond} - k_{Ins}/2)(n+1) + \\ & + \rho_{Sh} 2\pi k_{Sh}(r_{CT} - k_{Sh}/2) + \\ & + \rho_{Fill}(\pi((r_{CT} - k_{Sh})^2 - \\ & - ((r_{Teth} + k_{Ins})^2 u_{Teth} + r_{Cond}^2 u_{Cu} n + r_{OF}^2))) + \\ & + \rho_{OF} \pi r_{OF}^2. \end{aligned} \quad (8)$$

Assuming r_{Teth} = 0.0015 m, r_{Cu} = 0.00075 m, r_{OF} = 0.001 m, r_{Cond} = 0.00155 m, and $r_{Ins} = k_{Sh}$ = 0.0008 m, we obtain m_{CT} = 0.09 kg. Thus, the UAV weight with cable tether increases by 9 kg at an altitude of 100 m.

OPTIMAL UAV LIFT ALTITUDE

The UAV lift altitude directly affects the operating efficiency of THAS suspended equipment: the higher the altitude, the greater the view.

Maximum radar range is limited by the line of sight to the target whose value (in km) is determined by the following commonly known formula (derived from the basic radar equation [5]):

$$L_{max} \approx 4.12\left(\sqrt{h_a} + \sqrt{h_{Tgt}}\right), \quad (9)$$

where h_a is the antenna height (UAV lift altitude), h_{Tgt} is the target height.

At target height h_{Tgt} = 0 (e.g., small-sized surface target) and target surveillance from the upper deck of the ship ($h_a \approx 10$ m), the radar track acquisition range is $L_{max} \approx 13$ km. However, when elevating the means of surveillance to $h_a \approx 100$ m, the maximum range increases more than 3 times up to $L_{max} \approx 41$ km. Dependence of the horizon visibility range on the surveillance height is presented in Fig. 5.

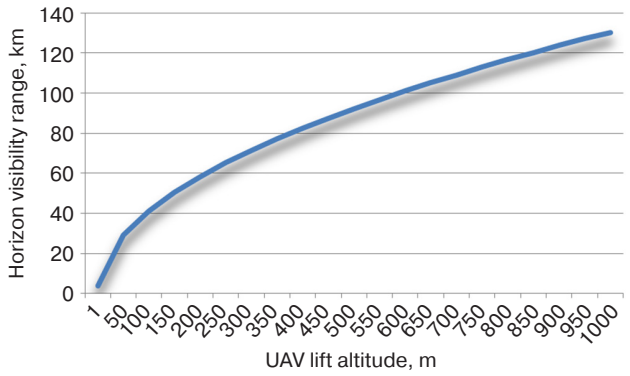

Fig. 5. Dependence of horizon visibility range on surveillance height

However, increasing UAV lift altitude results in increasing its power consumption and wind speed [6]. Comparing the simulation results of THAS application conditions [7, 8], it can be concluded that the rational lift altitude is about 100 m.

MAXIMUM POWER REQUIRED FOR UAV OPERATION

The suspended UAV and the forces acting on it are shown in Fig. 6, where F_g is gravity force, F_t is thrust force of UAV engines, F_{WR} is wind resistance force, and F_{CT} is cable tether tension force.

The modulus of all forces acting on UAV is calculated using the following formula [6]:

$$|\mathbf{F}_t| = \sqrt{(|\mathbf{F}_g| + |\mathbf{F}_{CT}|\cos\alpha)^2 + (|\mathbf{F}_{WR}| + |\mathbf{F}_{CT}|\sin\alpha)^2}, \quad (10)$$

where α is the vector angle of the cable tether tension force to the vertical.

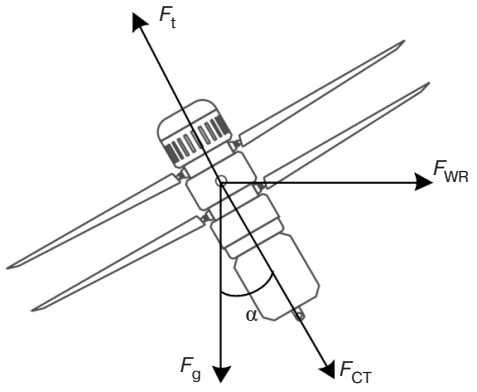

Fig. 6. UAV with forces acting on it

The gravity force is determined by the UAV take-off weight, as follows:

$$F_g = m_{UAV}g + m_{PL}g + m_{CT}g, \quad (11)$$

where g is gravity acceleration.

The wind resistance force is determined by the following equation[3]:

$$F_{WR} = C\rho S v^2 = CqS, \quad (12)$$

where C is the aerodynamic coefficient, S is the UAV area projection onto the direction perpendicular to the oncoming flow, v is oncoming air flow velocity, ρ is the air density, and q is the wind pressure.

As follows from (12), the UAV geometric characteristics, the velocity head, and the aerodynamic coefficient need to be known, in order to determine the wind effect. The known values are geometric characteristics and aerodynamic coefficient.

We consider aerodynamic loads under wind effect as operating and limiting. Under the operating wind effect, the UAV may be used without limiting conditions. Under the limiting wind effect, the UAV should retain its strength and stability, as well as provide other performance requirements.

Specified parameters for operational wind effect are the estimated maximum value of the average (with a two-minute averaging period) wind speed at an altitude of 10 m from the ground surface and the minimum ambient temperature at which UAV operation is allowed.

The estimated velocity head at operating effect is determined by the following equation:

$$q_{est} = \frac{\rho v_{est}^2}{2}, \quad (13)$$

where v_{est} is the estimated average wind speed under operational impact.

When calculating the wind load on a moving ship, its speed should be taken into account whenever it exceeds $0.025v_{est}$. In this case, for a given average wind speed, the estimated velocity head when traveling against the wind is determined by means of the following equation:

$$q_{est} = \frac{\rho(v_{est} + v_{max})^2}{2}, \quad (14)$$

where v_{max} is the maximum speed of the ship.

Based on the limiting value of the standard average velocity head q_{LV}, the estimated velocity head for the limiting wind effect is determined as follows:

$$q_{est} = q_{LV}\mu, \quad (15)$$

where μ is the overload factor taken equal to 1.0–1.3.

[3] OST 92–9249–80. Industry standard. *Units of special purpose. Calculation methodology for wind loads*. 1980 (in Russ.).

The coefficient C_i depends on angle α, wind direction, and UAV profile.[4]

The engine power required to hold the UAV at a given point, after determining the resultant force modulus, is calculated using the following equation:

$$P = \frac{|\mathbf{F}_t|}{k \times g}, \quad (16)$$

where $|\mathbf{F}_t|/g$ is the total thrust of the UAV engines; k is the efficiency factor of the propeller group which characterizes the ratio of the engine total thrust to its power.

As is known from the practical implementation of THAS, and propeller group selection, k = 10 kg/kW and higher is considered a good value for the efficiency factor. This implies the ability to lift 10 kg of load for every kilowatt of energy expended. The efficiency factor depends largely on the engine type and traction propeller characteristics. For THAS, as the altitude rises, the load weight increases (due to the increasing tension force of the cable tether). Consequently, the propeller motor group efficiency decreases.[5]

The calculation of the tension force (F_{CT}) acting on THAS due to the cable tether is described in [9]. It represents a differential equation system: one being a linear differential equation of the first order; while the other two being nonlinear differential equations of the second order. It should be noted that the system of differential equations obtained coincides with the flexible thread position equation [10] for a tethered flying object:

$$\begin{cases} \dfrac{dF_{CT}}{dz} - \rho_{CT} g = 0, \\ F_{CT} \dfrac{d^2x}{dz^2} + \rho_{CT} g \dfrac{dx}{dz}\left(1 + \left(\dfrac{dx}{dz}\right)^2 + \left(\dfrac{dy}{dz}\right)^2\right) + \\ + A\sqrt{v_x^2(z) + v_y^2(z) + \left(v_x(z)\dfrac{dy}{dz} - v_y(z)\dfrac{dx}{dz}\right)^2} \times \\ \times v_x(z)\sqrt{1 + \left(\dfrac{dx}{dz}\right)^2 + \left(\dfrac{dy}{dz}\right)^2} = 0, \\ F_{CT} \dfrac{d^2y}{dz^2} + \rho_{CT} g \dfrac{dy}{dz}\left(1 + \left(\dfrac{dx}{dz}\right)^2 + \left(\dfrac{dy}{dz}\right)^2\right) + \\ + A\sqrt{v_x^2(z) + v_y^2(z) + \left(v_x(z)\dfrac{dy}{dz} - v_y(z)\dfrac{dx}{dz}\right)^2} \times \\ \times v_y(z)\sqrt{1 + \left(\dfrac{dx}{dz}\right)^2 + \left(\dfrac{dy}{dz}\right)^2} = 0, \end{cases} \quad (17)$$

where A is the aerodynamic drag factor; ρ_{CT} is the cable tether linear density; x, y, z is the rectangular coordinate system; v_x, v_y, v_z are the projections of wind velocity onto corresponding axes of the rectangular coordinate system.

The problem under consideration is complicated by the need to resolve not the Cauchy problem but the boundary problem, when the conditions are set at different values for argument z [11].

Given (10), (11), (16), and (17), the required power for operating THAS is defined as follows:

$$P = \frac{\sqrt{(m_{UAV} g + m_{PL} g + |\mathbf{F}_{CT}| \sin\alpha)^2 + (|\mathbf{F}_{WR}| + |\mathbf{F}_{CT}| \cos\alpha)^2}}{k \times g}. \quad (18)$$

The work of A.M. Shirvanyan[6] presents the calculation of the required power for operating THAS of 25 kg and 35 kg in weight at an altitude of 75 m under tension force F_{CT} = 10 H and 30 H (Fig. 7). From this, it can be concluded that a high wind speed and ship motion have a significant effect on the required power. When wind speed (and/or ship motion) increases, slope angle α of the cable-tether tension force action F_{CT} on THAS increases, thus increasing the horizontal component of the tension force. In addition, changing the cable tether tension force by the winch will change its profile and length significantly.

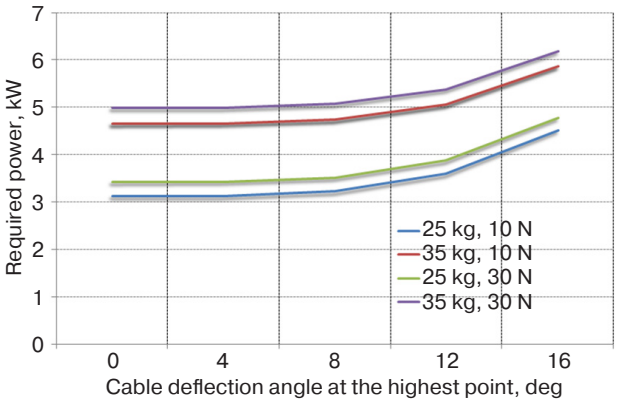

Fig. 7. Dependence of THAS required power on the wind speed at different weight and tension force of the cable tether

For the cable winch drive control system, a balance needs to be found between the tension force of the cable tether at the winch and the UAV power consumption. Weak winch tension may trigger a large cable tether release which is unsafe in a shipboard environment.

[4] Albisser M. *Identification of Aerodynamic Coefficients from Free-Flight Data*. Université de Lorraine, Nancy, France, Ph.D. Thesis, 2015.

[5] XRotor 8 Series Power Combo for Agricultural Drones. https://www.hobbywing.com/en/products/xrotor-6-series-power-combo-for-agriculutral-drones226.html. Accessed May 11, 2023.

[6] Shirvanyan A.M. *Development and research for the mathematical model of the tethered high-altitude unmanned telecommunication platforms functioning at wind loads*. Cand. Sci. Thesis (Eng.). Moscow, 2020, 116 p. (in Russ.).

Strong winch tension makes the cable profile nearly vertical. However, this significantly increases the UAV power required for operating.

The findings are significant for estimating the maximum payload weight and the required electrical power transferred from the ship to the UAV under conditions of wind loads and ship motion, as well as for designing the THAS positioning control system.

THE SYSTEM STRUCTURE FOR TRANSFERRING POWER TO UAV

The efficient UAV operation requires a high power supply. Currently, there are effective UAV power supply systems based on high-frequency direct or alternating current (AC). A large number of studies [12–15] deal with selecting the type of current supply for suspended systems. In the case of an AC power supply, a relatively high efficiency and smaller conductor cross-sectional area can be obtained, when compared to direct current (DC). However, in a long supply line, wave processes consisting in the occurrence of a reflected wave inevitably occur. This results in an increase in voltage on some parts of the cable-rope. In the coiled state (around the winch drum), the cable tether reel represents an inductive resistance, which also prevents the transmission of alternating current. At the same time, power transfer at industrial frequency results in the need for conversion, thus reducing the payload weight.

For the same level of power, the cross-sectional area of the conductor decreases with the increasing supply voltage. Thus high voltage needs to be transmitted through the cable tether for the UAV power supply. The structure of the power supply circuit is shown in Fig. 8.

The maximum power transmitted through the cable tether depends on the type of current. In order to calculate the maximum transmitted power, the wire diameter (cross-sectional area), current density, interwire voltage (for DC), and wave impedance (for AC) need to be determined.

The DC power is determined by means of the following equation:

$$P_{DC} = IU = \pi \frac{d_{Cu}^2}{4} JU, \quad (19)$$

where I is the current strength, d_{Cu} is the diameter of the copper conductor, J is the current density, and U is the interwire voltage.

Losses per unit length in wires are determined by means of the following equation [16]:

$$\Delta_{DC} = 2S_{Cu} J^2 \sigma, \quad (20)$$

where σ stands for the conducting material conductivity.

When building an AC power system, reflected waves transfer energy from the point of the line connection to the load backward to the power source. Equality of the line wave impedance to the line load impedance is the condition for maximum AC power transfer efficiency. The maximum transmitted power is determined as follows:

$$P_{AC} = I^2 \tilde{R} = I^2 \frac{120}{\sqrt{\varepsilon}} \ln \frac{l_{Cu}}{r_{Cu}}, \quad (21)$$

where $\tilde{R}$ is the wave impedance for a two-conductor line, l_{Cu} is the distance between centers of two

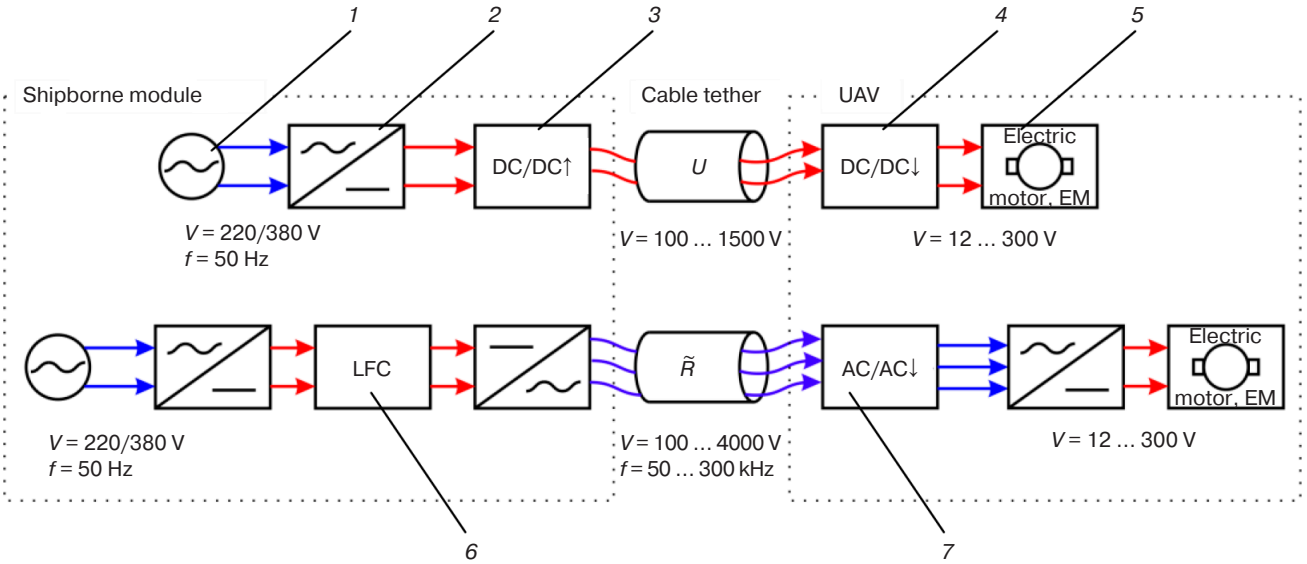

Fig. 8. THAS power circuit structure: *1* AC voltage source, *2* rectifier, *3* direct current boost converter, *4* DC-DC voltage converter, *5* UAV and payload consumer, *6* low frequency converter, *7* alternating current buck converter. *V* is a voltage, *f* is a frequency

conductors, ε is the dielectric permeability of the medium between conductors.

The AC power losses are determined by means of the following equations:

$$\Delta_{AC} = 2S_{Cu}\sigma(K_s J)^2, \quad (22)$$

where K_s is the section utilization factor.

Thus, a comparison of (20) and (22) shows that power losses in AC transmission are lower than those in DC transmission due to the skin effect. When using a cable with $d_{Cu} > 6$ mm, the maximum possible AC power increases significantly. For example, at $d_{Cu} = 8$ mm and 1200 V voltage, it is possible to transmit 48 kW DC, whereas 135 kW AC.

Nguen et al. [17] determines that a slight increase in the radius of the conductive core r_{Cu} results in a large increase in the transmitted power, reducing the share of the cost required to lift and hold the cable tether. In the case of a smaller conductive core radius, the maximum power depends insignificantly on the type of current. Thus, the transmission of high power (over 14 kW) is preferable to AC, while DC is more appropriate for lower power.

DEPLOYMENT TIME AND UAV LIFTING TO THE SET ALTITUDE

In addition to its obvious advantages, the placement of the THAS in TLC has a significant disadvantage. The transporter-launcher container is loaded into a vertical launcher which contains certain means of destruction of various types and purposes. Since there may be THAS or UAV cable tethers on their trajectory, the operation of deployed THAS prevents the use of these means either partially or completely. Therefore, the calculation of deployment (redeployment) time is of great importance when operating THAS on Navy ships. The deployment time is calculated using the following equation:

$$t_{Dep} = t_{ad} + h / v_{da}, \quad (23)$$

where t_{ad} is the ascent (descent) time of the platform with UAV in TLC, v_{da} is the speed of UAV descent (ascent).

At $t_{ad} = 5$ s and $v_{da} = 4$ m/s, the redeployment time from an altitude of 100 m amounts to 30 s.

For comparison, the tethered ETOP UAV (Israel Aerospace Industries, Israel) with 20 kg maximum payload and 100 m altitude has a comparable deployment time [17].

CONCLUSIONS

Implementing the principles of THAS construction under consideration in this study allows the creation of a complex capable of performing various tasks with a high level of efficiency. The proposed THAS has significant advantages over known platforms. They include: container storage and launch, high-power energy transmission system via low-section cable tether (low weight per unit length), and stabilization of UAV with payload by altitude. At the same time, the advanced THAS provides payload lifting to an altitude of 100 m with a long operational life, only limited by THAS reliability characteristics.

REFERENCES

1. Khofiyah N.A., Maret S., Sutopo W., Nugroho B.D.A. Goldsmith's Commercialization Model for Feasibility Study of Technology Lithium Battery Pack Drone. In: *2018 5th International Conference on Electric Vehicular Technology* (*ICEVT*). IEEE; 2018. P. 147–151. https://doi.org/10.1109/ICEVT.2018.8628439
2. Zikou L., Papachristos C., Tzes A. The Power-over-Tether system for powering small UAVs: Tethering-line tension control synthesis. In: *Proceedings of the 2015 23rd Mediterranean Conference on Control and Automation* (*MED*). IEEE; 2015. P. 681–687. https://doi.org/10.1109/MED.2015.7158825
3. Solovyeva V.V., Sharov S.N. Shipping take-off and alighting gears of unmanned flying vehicles. *Morskoy Vestnik.* 2015;1(53):65–69 (in Russ.). Available from URL: https://www.elibrary.ru/tjxpif
4. Vishnevskii V.M. Methods and algorithms for designing tethered high-altitude unmanned telecommunication platforms. In: *The 13th All-Russian Conference on Management Problems: Collection of Proceedings.* (*VSPU 2019*). Moscow: Institute of Control Science RAS; 2019. P. 40–42 (in Russ.). Available from URL: https://vspu2019.ipu.ru/proceedings/0040.pdf
5. Botov M.I., Vyakhirev V.A. *Osnovy teorii radiolokatsionnykh sistem i kompleksov* (*Fundamentals of the Theory of Radar Systems and Complexes*). Krasnoyarsk: Siberian Federal University; 2013. 530 p. (in Russ.). Available from URL: https://vii.sfu-kras.ru/images/libs/Osnovi_teorii.pdf
6. Vishnevsky V.M., Shirvanyan A.M., Bryashko N.N. Calculation of the required power for the operation of a tethered unmanned platform in a turbulent atmosphere. *Informatsionnye tekhnologii i vychislitel'nye sistemy = Journal of Information Technologies and Computing Systems.* 2020;3:71–84 (in Russ.). https://doi.org/10.14357/20718632200307
7. Lopukhov A.A., Osipov YU.N., Ershov V.I., Simanov S.E. Formation features of effective load and technical characteristics of unmanned aircraft system of signal retranslation for ground-robotic systems control. *Aktual'nye voprosy pozharnoi bezopasnosti = Current Fire Safety Issues.* 2022;2(12):33–40 (in Russ.). https://doi.org/10.37657/vniipo.avpb.2022.40.70.004

8. Wang G., Samarathunga W., Wang S. Uninterruptible Power Supply Design for Heavy Payload Tethered Hexaroters. *Int. J. Emerging Eng. Res. Technol*. 2016;4(2):16–21.
9. Vishnevsky V.M., Shirvanyan A.M., Tumchenok D.A. Mathematical model of the dynamics of functioning of a tethered high-altitude telecommunications platform in a turbulent atmosphere. In: *Distributed Computer and Communication Networks: Control, Computation, Communications. Proceedings of the 21st International Scientific Conference DCCN 2018.* Moscow: RUDN University*;* 2018. P. 402–414 (in Russ.).
10. Merkin D.R. *Vvedenie v mekhaniku gibkoi niti* (*Introduction to Flexible Filament Mechanics*). Moscow: Nauka; 1980. 240 p. (in Russ.).
11. Tognon M., Franchi A. *Theory and Applications for Control of Aerial Robots in Physical Interaction Through Tethers.* Part of the book series: *Springer Tracts in Advanced Robotics.* (STAR, vol. 140). Cham, Switzerland: Springer; 2021. 156 p.
12. Vishnevsky V.M., Tumchenok D.A., Shirvanyan A.M.M. Optimal structure of a high-voltage cable for transmitting energy from the ground to a tethered high-altitude unmanned telecommunications platform. In: *Distributed Computer and Communication Networks: Control, Computation, Communications. Proceedings of the 20 International Scientific Conference DCCN 2017.* Moscow: Tekhnosfera; 2017. P. 197–205 (in Russ.).
13. Gerasimov V.A., Komlev A.V., Naidenko N.A., Filozhenko A.Yu. Research and development of an energy supply system for a tethered underwater robot with an upgraded power source. *Podvodnye issledovaniya i robototekhnika = Underwater Investigations and Robotics*. 2021;3(37):82–89 (in Russ.). https://doi.org/10.37102/1992-4429_2021_37_03_08
14. Masyukov M.V., Lukashov P.P. *Tethered Monitoring Platform with Power System*: RF Pat. 2724509. Publ. 2020.06.23 (in Russ.).
15. Akhobadze G.N. *Electrical Supply System for Tethered Aircraft*: RF Pat. 2782805. Publ. 2022.11.02 (in Russ.).
16. Vishnevsky V.M., Tereshchenko B.N., Tumchenok D.A., Shirvanyan A.M. Comparative analysis of options for constructing a wired ground-to-air power transmission system for tethered high-altitude telecommunication platforms. In: *Distributed Computer and Communication Networks: Control, Computation, Communications. Proceedings of the 21st International Scientific Conference DCCN 2018.* Moscow: RUDN University*;* 2018. P. 387–401 (in Russ.).
17. Nguen T.L., Kuzin N.A., Yurkov N.K. On the problem of forming the appearance of promising unmanned aerial vehicles. *Nadezhnost' i kachestvo slozhnykh system = Reliability and Quality of Complex Systems*. 2022;1(37):55–66 (in Russ.). https://doi.org/10.21685/2307-4205-2022-1-7

СПИСОК ЛИТЕРАТУРЫ

1. Khofiyah N.A., Maret S., Sutopo W., Nugroho B.D.A. Goldsmith's Commercialization Model for Feasibility Study of Technology Lithium Battery Pack Drone. In: *2018 5th International Conference on Electric Vehicular Technology* (*ICEVT*). IEEE; 2018. P. 147–151. https://doi.org/10.1109/ICEVT.2018.8628439
2. Zikou L., Papachristos C., Tzes A. The Power-over-Tether system for powering small UAVs: Tethering-line tension control synthesis. In: *Proceedings of the 2015 23rd Mediterranean Conference on Control and Automation* (*MED*). IEEE; 2015. P. 681–687. https://doi.org/10.1109/MED.2015.7158825
3. Соловьева В.В., Шаров С.Н. Судовые взлетные и посадочные устройства беспилотных летательных аппаратов. *Морской вестник*. 2015;1(53):65–69. URL: https://www.elibrary.ru/tjxpif
4. Вишневский В.М. Методы и алгоритмы проектирования и реализации привязных высотных беспилотных телекоммуникационных платформ. В сб.: *XIII Всероссийское совещание по проблемам управления: Сборник трудов*. (*ВСПУ – 2019*). М.: Институт проблем управления; 2019. С. 40–42. URL: https://vspu2019.ipu.ru/proceedings/0040.pdf
5. Ботов М.И., Вяхирев В.А. *Основы теории радиолокационных систем и комплексов*. Красноярск: Сиб. федер. ун-т; 2013. 530 с. URL: https://vii.sfu-kras.ru/images/libs/Osnovi_teorii.pdf
6. Вишневский В.М., Ширванян А.М., Бряшко Н.Н. Расчет необходимой мощности для функционирования привязной беспилотной платформы в условиях турбулентной атмосферы. *Информационные технологии и вычислительные системы*. 2020;3:71–84. https://doi.org/10.14357/20718632200307
7. Лопухов А.А., Осипов Ю.Н., Ершов В.И., Симанов С.Е. Особенности формирования полезной нагрузки и технического облика беспилотной авиационной системы ретрансляции сигналов управления для наземных робототехнических комплексов. *Актуальные вопросы пожарной безопасности*. 2022;2(12):33–40. https://doi.org/10.37657/vniipo.avpb.2022.40.70.004
8. Wang G., Samarathunga W., Wang S. Uninterruptible Power Supply Design for Heavy Payload Tethered Hexaroters. *Int. J. Emerging Eng. Res. Technol*. 2016;4(2):16–21.
9. Вишневский В.М., Ширванян А.М., Тумченок Д.А. Математическая модель динамики функционирования привязной высотной телекоммуникационной платформы в условиях турбулентной атмосферы. В сб.: *Распределительные компьютерные и телекоммуникационные сети: управление, вычисление, связь*. *Материалы 21 Международной научной конференции DCCN-2018*. М.: РУДН; 2018. С. 402–414.
10. Меркин Д.Р. *Введение в механику гибкой нити.* М.: Наука; 1980. 240 с.
11. Tognon M., Franchi A. Theory and Applications for Control of Aerial Robots in Physical Interaction Through Tethers. Part of the book series: *Springer Tracts in Advanced Robotics.* (STAR, vol. 140). Cham, Switzerland: Springer; 2021. 156 p.

12. Вишневский В.М., Тумченок Д.А., Ширванян А.М. Оптимальная структура высоковольтного кабеля для передачи энергии с земли на борт привязной высотной беспилотной телекоммуникационной платформы. В сб.: *Распределительные компьютерные и телекоммуникационные сети: управление, вычисление, связь. Материалы 20 Международной научной конференции DCCN-2017*. М.: Техносфера; 2017. С. 197–205.
13. Герасимов В.А., Комлев А.В., Найденко Н.А., Филоженко А.Ю. Исследование и разработка системы энергообеспечения привязного подводного робота с модернизированным источником электропитания. *Подводные исследования и робототехника*. 2021;3(37):82–89. https://doi.org/10.37102/1992-4429_2021_37_03_08
14. Масюков М.В., Лукашов П.П. *Привязная мониторинговая платформа с системой питания*: пат. № 2724509 РФ. Заявка № 2019106709; заявл. 11.03.2019: опубл. 23.06.2020.
15. Ахобадзе Г.Н. *Система электроснабжения привязного летательного аппарата*: пат. № 2782805 РФ. Заявка № 2022116012: заявл. 14.06.2022: опубл. 02.11.2022.
16. Вишневский В.М., Терещенко Б.Н., Тумченок Д.А., Ширванян А.М. Сравнительный анализ вариантов построения проводной системы передачи энергии земля–борт для привязных высотных телекоммуникационных платформ. В сб.: *Распределительные компьютерные и телекоммуникационные сети: управление, вычисление, связь. Материалы 21 Международной научной конференции DCCN-2018*. М.: РУДН; 2018. С. 387–401.
17. Нгуен Т.Л., Кузин Н.А., Юрков Н.К. К проблеме формирования облика перспективных беспилотных летательных аппаратов. *Надежность и качество сложных систем.* 2022;1(37):55–66. https://doi.org/10.21685/2307-4205-2022-1-7

About the author

Igor I. Dawlyud, Cand. Sci. (Eng.), Doctoral Student, Department of Artillery and Anti-Aircraft Missile Armament of Surface Ships, Admiral F.F. Ushakov Baltic Higher Naval School (82, Sovetsky pr., Kaliningrad, 236022 Russia). E-mail: sawefew2@yandex.ru. https://orcid.org/0009-0003-2926-718X

Об авторе

Давлюд Игорь Игоревич, к.т.н., докторант, кафедра артиллерийского и зенитного ракетного вооружения надводных кораблей, Балтийское высшее военно-морское училище имени адмирала Ф.Ф. Ушакова (236022, Калининград, Советский пр-т, 82). E-mail: sawefew2@yandex.ru. https://orcid.org/0009-0003-2926-718X

Translated from Russian into English by K. Nazarov
Edited for English language and spelling by Dr. David Mossop

Multiple robots (robotic centers) and systems. Remote sensing and non-destructive testing

Роботизированные комплексы и системы.
Технологии дистанционного зондирования неразрушающего контроля

UDC 620.179.15
https://doi.org/10.32362/2500-316X-2024-12-4-51-58
EDN VOQEBL

RESEARCH ARTICLE

Tomographic task solution using a dichotomous discretization scheme in polar coordinates and partial system matrices invariant to rotations

Alexey A. Manushkin [1, @],
Nikolay N. Potrachov [2],
Alexander V. Stepanov [1],
Evgeny Yu. Usachev [1]

[1] *Diagnostika-M, Moscow, 109316 Russia*
[2] *Saint Petersburg Electrotechnical University (ETU "LETI"), St. Petersburg, 197022 Russia*
[@] *Corresponding author, e-mail: manushkinaa@mail.ru*

Abstract

Objectives. The purpose of this work was to create an effective iterative algorithm for the tomographic reconstruction of objects with large volumes of initial data. Unlike the convolutional projection algorithm, widely used in commercial industrial and medical tomographic devices, algebraic iterative reconstruction methods use significant amounts of memory and typically involve long reconstruction times. At the same time, iterative methods enable a wider range of diagnostic tasks to be resolved where greater accuracy of reconstruction is required, as well as in cases where a limited amount of data is used for sparse-view angle shooting or shooting with a limited angular range.

Methods. A feature of the algorithm thus created is the use of a polar coordinate system in which the projection system matrices are invariant with respect to the rotation of the object. This enables a signification reduction of the amount of memory required for system matrices storage and the use of graphics processors for reconstruction. Unlike the simple polar coordinate system used earlier, we used a coordinate system with a dichotomous division of the reconstruction field enabling us to ensure invariance to rotations and at the same time a fairly uniform distribution of spatial resolution over the reconstruction field.

Results. A reconstruction algorithm was developed on the basis of the use of partial system matrices corresponding to the dichotomous division of the image field into partial annular reconstruction regions. A 2D and 3D digital phantom was used to show the features of the proposed reconstruction algorithm and its applicability to solving tomographic problems.

Conclusions. The proposed algorithm allows algebraic image reconstruction to be implemented using standard libraries for working with sparse matrices based on desktop computers with graphics processors.

Keywords: nondestructive technics, X-ray computed tomography, iterative algorithm, system matrix

• **Submitted:** 11.12.2023 • **Revised:** 06.03.2024 • **Accepted:** 22.05.2024

For citation: Manushkin A.A., Potrachov N.N., Stepanov A.V., Usachev E.Yu. Tomographic task solution using a dichotomous discretization scheme in polar coordinates and partial system matrices invariant to rotations. *Russ. Technol. J.* 2024;12(4):51–58. https://doi.org/10.32362/2500-316X-2024-12-4-51-58

Financial disclosure: The authors have no a financial or property interest in any material or method mentioned.

The authors declare no conflicts of interest.

НАУЧНАЯ СТАТЬЯ

Решение томографической задачи с использованием дихотомической схемы дискретизации в полярных координатах и парциальных системных матриц, инвариантных к вращениям

А.А. Манушкин [1, @], Н.Н. Потрахов [2], А.В. Степанов [1], Е.Ю. Усачев [1]

[1] *Диагностика-М, Москва, 109316 Россия*
[2] *СПбГЭТУ «ЛЭТИ», Санкт-Петербург, 197022 Россия*
[@] *Автор для переписки, e-mail: manushkinaa@mail.ru*

Резюме

Цели. Цель работы состояла в создании эффективного итерационного алгоритма для томографической реконструкции объектов с большими объемами исходных данных. В отличие от сверточного алгоритма проецирования, широко используемого в коммерческих промышленных и медицинских томографах, алгебраические итерационные методы реконструкции используют значительные объемы памяти и характеризуются большими временными затратами на реконструкцию. В то же время итерационные методы позволяют решать более широкий круг диагностических задач, где требуется большая точность реконструкции, а также в случаях использования ограниченного объема данных при малоракурсной съемке или съемке с ограниченным угловым диапазоном.

Методы. Особенностью созданного алгоритма является использование полярной системы координат, в которой проекционные системные матрицы инвариантны по отношению к вращению объекта. Это дает возможность значительно сократить объемы памяти для хранения проекционных матриц и использовать для реконструкции графические процессоры. В отличие от простой полярной системы координат, используемой ранее, нами была использована система координат с дихотомическим делением поля реконструкции, что позволяет обеспечить инвариантность к вращениям и в тоже время достаточно равномерное распределение пространственного разрешения по полю реконструкции.

Результаты. Был разработан алгоритм реконструкции, основанный на использовании парциальных системных матриц, соответствующих дихотомическому делению поля изображения на парциальные кольцевые области реконструкции. С использованием цифровых фантомов Шеппа – Логана и Де Фриза были исследованы особенности работы предложенного алгоритма реконструкции и показана его применимость для решения томографических задач.

Выводы. Предложенный алгоритм дает возможность реализовать алгебраическую реконструкцию изображения с использованием стандартных библиотек для работы с разреженными матрицами на базе настольных компьютеров с графическими процессорами.

Ключевые слова: неразрушающий контроль, компьютерная томография, итерационный алгоритм, системная матрица

• **Поступила:** 11.12.2023 • **Доработана:** 06.03.2024 • **Принята к опубликованию:** 22.05.2024

Для цитирования: Манушкин А.А., Потрахов Н.Н., Степанов А.В., Усачев Е.Ю. Решение томографической задачи с использованием дихотомической схемы дискретизации в полярных координатах и парциальных системных матриц, инвариантных к вращениям. *Russ. Technol. J*. 2024;12(4):51–58. https://doi.org/10.32362/2500-316X-2024-12-4-51-58

Прозрачность финансовой деятельности: Авторы не имеют финансовой заинтересованности в представленных материалах или методах.

Авторы заявляют об отсутствии конфликта интересов.

INTRODUCTION

There are two main approaches for resolving tomographic tasks of object reconstruction from projection data. The first approach is based on the application of analytical reconstruction formulation in a fan beam for 2D or a cone beam for 3D geometry [1–3]. This assumes the acquisition of a complete data set in the scanning angular range larger than 180° with a small angular scanning step. The second approach involves the use of a matrix formulation of the tomographic task using regularizing functionals and iterative reconstruction algorithms.

The advantage of the second approach consists in the possibility of using an incomplete dataset for tomosynthesis tasks with limited angular range [4, 5], or for resolving tomography tasks with a limited number of projections [6–11]. Another advantage of algebraic reconstruction is the ability to reduce the influence of metallic artifacts. This is achieved by allowing incorrect tomographic data to be excluded from the reconstruction without the need to find a suitable interpolation to replace them [12].

At present, graphic processors are widely used for tomographic reconstruction, accelerating calculations by dozens of times. In the case of 3D tomography, the use of a system matrix in a Cartesian coordinate system, containing all information about the survey geometry, is difficult. This is due to the huge data volume, which makes its storage in the graphics processor memory impossible. Therefore, in iterative reconstruction, multiple ray tracing is applied online using special means of programming parallel computational threads of the graphics processor, as, for example, in *TIGRE* software package [13].

When using the system matrix, optimized libraries of sparse matrix computations can be used on a graphics processor, greatly simplifying software development. The development of software tools for image processing and artificial intelligence tasks is based on libraries of algebraic procedures for working with matrices and vectors. They are constantly updated to work on various stationary and mobile computing platforms.

A number of industrial 3D tomographs utilize a circular imaging geometry in which the object, located between the X-ray source and the high-resolution matrix detector, rotates on a stage. If we use a polar coordinate system centered on the object's rotation axis, it can easily be seen that by proper selection of the radial line pitch corresponding to the angular rotation pitch, the imaging geometry and its corresponding system matrix become invariant with respect to rotation with discrete pitch. This enables the use of a single system matrix computed for only one angular position, instead of computing anew for tens or hundreds of different angular positions in the case of a Cartesian coordinate system. Thus, the system matrix can be entered into the limited memory of the graphics processor and accelerate calculations.

RESEARCH METHODS

In order to calculate the system matrix in the polar coordinate system, we used the Siddon algorithm [14]. Here the lengths of the segments of its intersection with the coordinate lines are calculated for each ray. A disadvantage of the conventional polar coordinate system is that the azimuthal size of the voxel increases as it moves away from the center of rotation. In order to minimize this undesirable effect, a dichotomous division of the image reconstruction field was used in accordance with Fig. 1.

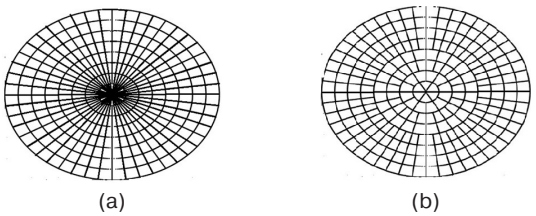

Fig. 1. Simple polar (a) and dichotomous (b) schemes for discretization of the reconstruction area

In the dichotomous image discretization scheme, each doubling of the radius of polar lines doubles the number of azimuthal lines. Thus, the object image is constructed from a consecutive series of circular segments with indices $ind = 0, 1, 2, \ldots, N$, the outer radius R_{ind} of which is given by the formula:

$$R_{ind} = 2^{ind} R_0,$$

where R_0 is the radius of the central segment with zero index.

In each ring segment, pixels are indexed by two indices, the polar string index i:

$$i = 1, \ldots, m,$$

$$m = 2^{ind} - 2^{(ind-1)},$$

and azimuthal column index j:

$$j = 1, \ldots, n,$$

$$n = 6 \times 2^{ind}.$$

In accordance with known system matrix formalism, two-dimensional indexing is replaced by a one-dimensional one using the column index J given by the formula:

$$J = (j - 1)m + i.$$

Thus, in this discretization scheme, each image can be represented as a set of concentric ring images, each of which is a matrix vectorizable in the above-mentioned way. As a result, each image can be represented as a vector $\mathbf{X}$ composed of vectors $\mathbf{X}_{ind}$, for each of which there is a different matrix $\mathbf{A}_{ind}$ partial matrix of direct projection of the fan bundle, carried out using the formula:

$$\mathbf{B}_{ind} = \mathbf{A}_{ind}\mathbf{X}_{ind},$$

where $\mathbf{B}_{ind}$ is the partial projection. The resulting tomographic projection $\mathbf{B}$ is the sum of projections from all annular segments:

$$\mathbf{B} = \Sigma\mathbf{B}_{ind}.$$

$$\mathbf{B} = \mathbf{A}\mathbf{X},$$

where the resulting projection matrix $\mathbf{A}$ is a horizontal concatenation of the matrices $\mathbf{A}_{ind}$:

$$\mathbf{A} = [\mathbf{A}_1\ \mathbf{A}_2\ \ldots\ \mathbf{A}_N].$$

The vector $\mathbf{X}$, respectively, is the vertical concatenation of the vectors $\mathbf{X}_{ind}$:

$$\mathbf{X} = \begin{matrix} \mathbf{X}_1 \\ \ldots \\ \mathbf{X}_N \end{matrix}.$$

In order to take angular scanning into account, the total system matrix needs to be vertically increased, and, accordingly the partial matrices according to the number of selected angles. In this case, there is no need to create new partial matrices if the radial lines of the corresponding partial annular segment coincide during angular rotation by a discrete angle $\Delta\theta$. If the angle of alternation of the radial lines of the ring segment coincides with the angle $\Delta\theta$ of the scanning step, a single partial matrix is sufficient. For example, a 1° step scan over a 360° interval using Cartesian discretization would require at least 90 different partial matrices for each angular position of the object. Thus, in the case of polar discretization, the memory size required to store a single system matrix would be reduced by almost 2 orders of magnitude. When moving to previous ring segments of smaller radius, the number of partial matrices grows dichotomously. However, it can easily be seen that the number of columns of these matrices corresponding to the number of elements of the ring segment decreases proportionally to the degree of number 4. Based on this, we can conclude that when using dichotomous polar discretization of the object, the memory size required to store the system matrix in comparison with Cartesian discretization decreases in proportion to the number of the aspect views.

RESEARCH RESULTS

The standard Shepp–Logan phantom was chosen for the numerical experiment. Due to the distinct features of the dichotomous division of the image radius, the phantom size in Cartesian pixels was chosen as 512 × 512. In terms of matching their information capacity, the size of the reconstruction area in pixels roughly corresponds to the format of digital panel detectors. Using this phantom and the equal-angle distribution of 780 rays in the fan beam, projection data were generated for $6 \times 2^7 = 768$ projections at Cartesian pixel partitioning of the phantom. Then, partial system matrices for 8 segments were generated and used to iteratively reconstruct the object in the polar coordinate system using the classical Landweber algorithm for gradient descent on a quadratic inviscid functional [15]. The iterative procedure was accelerated using the method of moments.

Figure 2 shows the reconstructed images of the digital phantom for different number of iterations. Reconstruction in the dichotomous system provides an acceptable image quality. However, the reconstructed

image shows ring artifacts caused by the fact that during iterations the ring regions have different convergence rates to their limit. Increasing the number of iterations from 50 to 500 made the artifacts almost indistinguishable.

(a) (b)

Fig. 2. Phantom reconstructions: (a) 50 iterations, (b) 500 iterations

In order to verify the possibility of using the dichotomous scheme for 3D tomographic reconstruction with a large volume of data, a numerical experiment was performed using the de Vries digital phantom, used in modeling volumetric reconstruction with a wide conical beam. The modeling was performed in *MATLAB*[1] environment for circular imaging geometry. The parameters are specified in the table below.

Reconstruction results of the de Vries digital phantom are shown in Fig. 3.

A comparison of the original and reconstructed phantoms shows that reconstruction by the algebraic method, as well as Feldkamp's algorithm, does not fully restore the shape of the outermost disks. This is apparently due to the violation of the Kirillov–Tuy condition, occurring in circular imaging geometry with a wide cone beam [16].

Accelerated gradient descent using Nesterov's method of moments was used for image reconstruction. In total, 40 iterations and 440 s were required for their implementation in *MATLAB* environment when using GeForce RTX 2080 graphics card (NVIDIA, USA). Analysis of the reconstruction program operation showed that the distinct features of the *MATLAB* environment interpreter are associated with large calculation time required to organize the iterative process independently of the user. This can include *MATLAB* system procedures in addition to computational iterative procedures. In our case, the operation of projecting a vector by a partial matrix with the maximum index takes 0.0004 s. At optimal organization of the computational process, one iteration should take no more than 2 s. For 40 iterations, the total reconstruction time should not exceed 2 min which is comparable to the reconstruction time of this

[1] https://www.mathworks.com/products/matlab.html. Accessed June 14, 2024.

Table. Shooting geometry parameters for digital phantom

Distance from the radiation source to the center of rotation, mm	300
Distance from the center of rotation to the detector, mm	138
Registration field size on the flat panel detector, mm^2	600 × 220
Detector pixels size, mm^2	1 × 1
Reconstruction field size, mm^3 (length × width × height)	256 × 256 × 128
Angular range of rotation, °	0–359
Number of rotation steps	768
Phantom size, mm^3 (length × width × height)	256 × 256 × 128

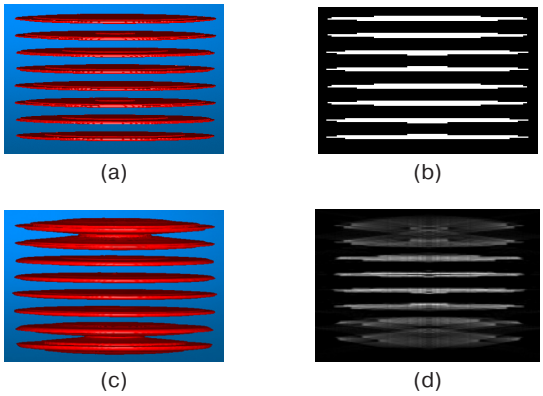

(a) (b) (c) (d)

Fig. 3. De Vries phantom: (a) volumetric image, (b) cross-section and its reconstruction result (c) volumetric image, (d) cross-section

digital phantom by the conjugate gradient method using the *TIGRE* package.

When implementing the proposed algorithm at a lower level in C++ with CUDA extension, a 32-bit data storage format is acceptable instead of the 64-bit representation allowed in *MATLAB* for sparse matrices. Moreover, top gaming video cards have 24 GB of allocated graphics memory. If we take into account that algebraic reconstruction enables the use of less data volume for reconstruction, we can conclude that the proposed algorithm enables applying computational capabilities of a personal computer for solving a wide range of tomographic tasks. Based on this algorithm, desktop computing systems can feasibly be created for training and modeling the operation of CT scanners in order to optimize their parameters [17, 18].

Thus, the paper proposes a workable discretization scheme combining the advantages of the polar system (invariance to rotations) and the Cartesian system (approximately equal pixel density). The application

of the polar coordinate system without dichotomous pixel division used in [19] can result in a different correspondence between the number of pixels of the ring segments and the number of pixels of their corresponding detector segments. While this correspondence will be correct for the outer segments, i.e., the number of corresponding pixels will be approximately the same, the information capacity for the inner regions of the corresponding detector region will be insufficient. This will lead to underdetermination of the system of linear equations, and consequently to the need to use regularization, in order to avoid the appearance of various artifacts typical for tomography with limited data. On the other hand, if the number of corresponding detector pixels for the inner regions is sufficient, the number of data for the outer regions will be excessive. In this case binning must be used for the outer regions of the detector, in order to save memory and speed up reconstruction.

CONCLUSIONS

When using a desktop computer with modern video cards, the use of a dichotomous polar scheme of image division into pixels creates possibilities of iterative algebraic image reconstruction with minimal memory consumption. Applied to a range of tasks of X-ray nondestructive testing, these possibilities will be investigated in numerical simulations on digital phantoms and experimental studies on a desktop microtomograph with a microfocus X-ray source and a large-format digital detector.[2]

ACKNOWLEDGMENTS

The work was financially supported by the Ministry of Education and Science of the Russian Federation (Agreement with the Ministry of Education and Science of the Russian Federation dated February 09, 2023, No. 075-11-2023-006, State Contract Identifier 000000S407523Q6V0002).

Authors' contributions

A.A. Manushkin—conceptualization and research design, computer simulation, working with graphic material, and writing the text of the manuscript.

N.N. Potrachov—project administration, writing and editing original draft, critical review. Analysis and systematization of the results obtained. Conducting comparative analysis. Generalization of research results. Formulation of conclusions.

A.V. Stepanov—supervision, monitoring research activities.

E.Yu. Usachev—conceptualization, funding acquisition.

REFERENCES

1. Feldkamp L.A., Davis L.C., Kress J.W. Practical cone-beam algorithm *J. Opt. Soc. Am. A.* 1984;1(6):612–619. https://doi.org/10.1364/JOSAA.1.000612
2. Zou Y., Pan X. Image reconstruction on PI-lines by use of filtered backprojection in helical cone-beam CT. *Phys. Med. Biol.* 2004;49:2717–2731. https://doi.org/10.1088/0031-9155/49/12/017
3. Parker D.L. Optimal short scan convolution reconstruction for fan-beam CT. *Med. Phys.* 1982;9(2):245–257. https://doi.org/10.1118/1.595078
4. Chen Z., Jin X., Li L., Wang G. A limited-angle CT reconstruction method based on anisotropic TV minimization. *Phys. Med. Biol.* 2013;58:2119–2141. https://doi.org/10.1088/0031-9155/58/7/2119
5. Wang C., Tao M., Nagy J.G., Lou Y. Limited-angle CT reconstruction via the L_1/L_2 minimization**.** *SIAM Journal on Imaging Sciences.* 2021;14(2):749–777. https://doi.org/10.1137/20M1341490
6. Li M., Zhang C., Peng C., Guan Y., Xu P., Sun M., Zheng J. Smoothed l_0 norm regularization for sparse-view X-ray CT reconstruction. *BioMed Res. Int.* 2016;2016:Article ID 2180457. https://doi.org/10.1155/2016/2180457
7. Sun Y., Chen H., Tao J., Lei L. Computed tomography image reconstruction from few views via Log-norm total variation minimization. *Digital Signal Processing.* 2019;88:172–181. https://doi.org/10.1016/j.dsp.2019.02.009
8. Sun Y., Tao J. Few views image reconstruction using alternating direction method via ℓ_0-norm minimization. *Int. J. Syst. Technol.* 2014;24(3):215–223. https://doi.org/10.1002/ima.22097
9. Xu Z., Chang X., Xu F., Zhang H. $L_{1/2}$ regularization: A thresholding representation theory and a fast solver. *IEEE Trans. Neural Networks Learn. Syst.* 2012;23(7):1013–1027. https://doi.org/10.1109/TNNLS.2012.2197412
10. Wang C., Yan M., Rahimi Y., Lou Y. Accelerated schemes for L_1/L_2 minimization. *IEEE Trans. Signal Processing.* 2020;68:2660–2669. https://doi.org/10.1109/TSP.2020.2985298
11. Jumanazarov D., Koo J., Kehres, J., Poulsen H.F., Olsen U.L., Iovea M. Material classification from sparse spectral X-ray CT using vectorial total variation based on L infinity norm. *Mater. Charact*. 2022;187:111864. https://doi.org/10.1016/j.matchar.2022.111864
12. Hegazy M.A.A., Cho M.H., Cho M.H., Lee S.Y. Metal artifact reduction in dental CBCT Images using direct sinogram correction combined with metal path-length weighting. *Sensors.* 2023;23(3):1288. https://doi.org/10.3390/s23031288

[2] https://eltech-med.com/ru/service/tomogram (in Russ.). Accessed June 14, 2024.

13. Bigury A., Dosanjh M., Hancock S., Soleimani M. Tigre: A MATLAB-GPU toolbox for CBCT image reconstruction. *Biomed. Phys. Eng. Express*. 2016;2(5):055010. http://doi.org/10.1088/2057-1976/2/5/055010
14. Siddon R.L. Fast calculation of the exact radiological path for a three-dimensional CT array. *Med. Phys.* 1985;12(2):252–255. https://doi.org/10.1118/1.595715
15. Landweber L. An iteration formula for Fredholm integral equations of the first kind. *Am. J. Math.* 1951;73(3):615–624. https://doi.org/10.2307/2372313
16. Tuy H.K. An inversion formula for cone-beam reconstruction. *SIAM. J. Appl. Math.* 1983;43(3):546–552. https://doi.org/10.1137/0143035
17. Osipov S.P., Chakhlov S.V., Zhvyrblia V.Y., Sednev D.A., Osipov O.S., Usachev E.Y. The Nature of Metal Artifacts in X-ray Computed Tomography and Their Reduction by Optimization of Tomography Systems Parameters. *Appl. Sci.* 2023;13(4):2666. https://doi.org/10.3390/app13042666
18. Hashem N., Pryor M., Haas D., Hunter J. Design of a Computed Tomography Automation Architecture. *Appl. Sci.* 2021;11(6):2858. https://doi.org/10.3390/app11062858
19. Jian L., Litao L., Peng C., Qi S., Zhifang W. Rotating polar-coordinate ART applied in industrial CT image reconstruction. *NDT&E International.* 2007;40(4):333–336. https://doi.org/10.1016/j.ndteint.2006.11.005

About the authors

Alexey A. Manushkin, Cand. Sci. (Phys.-Math.), Leading Researcher, Diagnostika-M (42, Volgogradskii pr., Moscow, 109316 Россия). E-mail: manushkinaa@mail.ru. Scopus Author ID 6507658966, https://orcid.org/0009-0009-8428-9588

Nikolay N. Potrachov, Dr. Sci. (Eng.), Head of the Department of Electronic Instruments and Devices; Chief Researcher, Saint Petersburg Electrotechnical University LETI (5, ul. Professora Popova, St. Petersburg, 197022 Russia). E-mail: nnpotrahov@epu.ru. Scopus Author ID 8689381700, SPIN-код РИНЦ 8875-7322, https://orcid.org/0000-0001-8806-0603

Alexander V. Stepanov, Cand. Sci. (Eng.), Head of the Department of Industrial Introscopy and Diagnostics, Diagnostika-M (42, Volgogradskii pr., Moscow, 109316 Russia). E-mail: stepanov_a@x-ray.ru. RSCI SPIN-code 3806-5336, https://orcid.org/0009-0000-0760-6222

Evgeny Yu. Usachev, Cand. Sci. (Eng.), Founder, Diagnostika-M (42, Volgogradskii pr., Moscow, 109316 Russia). E-mail: usachev_e@x-ray.ru. Scopus Author ID 55193172600, RSCI SPIN-code 6504-4959, https://orcid.org/0000-0001-5197-2465

Об авторах

Манушкин Алексей Анатольевич, к.ф.-м.н., ведущий научный сотрудник, ООО «Диагностика-М» (109316, Россия, Москва, Волгоградский просп., д. 42). E-mail: manushkinaa@mail.ru. Scopus Author ID 6507658966, https://orcid.org/0009-0009-8428-9588

Потрахов Николай Николаевич, д.т.н., заведующий кафедрой электронных приборов и устройств; главный научный сотрудник, ФГАОУ ВО «Санкт-Петербургский государственный электротехнический университет «ЛЭТИ» им. В.И. Ульянова (Ленина) (СПбГЭТУ «ЛЭТИ») (197022, Россия, Санкт-Петербург, ул. Профессора Попова, д. 5, литера Ф). E-mail: nnpotrahov@epu.ru. Scopus Author ID 8689381700, SPIN-код РИНЦ 8875-7322, https://orcid.org/0000-0001-8806-0603

Степанов Александр Вячеславович, к.т.н., начальник отдела промышленной интроскопии и диагностики, ООО «Диагностика-М» (109316, Россия, Москва, Волгоградский просп., д. 42). E-mail: stepanov_a@x-ray.ru. SPIN-код РИНЦ 3806-5336, https://orcid.org/0009-0000-0760-6222

Усачев Евгений Юрьевич, к.т.н., учредитель ООО «Диагностика-М» (109316, Россия, Москва, Волгоградский просп., д. 42). E-mail: usachev_e@x-ray.ru. Scopus Author ID 55193172600, SPIN-код РИНЦ 6504-4959, https://orcid.org/0000-0001-5197-2465

Translated from Russian into English by Lyudmila O. Bychkova
Edited for English language and spelling by Dr. David Mossop

Modern radio engineering and telecommunication systems

Современные радиотехнические и телекоммуникационные системы

UDC 537.874:537.877:621.37
https://doi.org/10.32362/2500-316X-2024-12-4-59-69
EDN PYJISU

RESEARCH ARTICLE

Digital technologies for signal radio vision and radio monitoring

Mihail S. Kostin [@], **Konstantin A. Boikov**

MIREA – Russian Technological University, Moscow, 119454 Russia
[@] *Corresponding author, e-mail: kostin_m@mirea.ru*

Abstract

Objectives. Radiophysical processes involving the electrodynamic formation of signal radio images diffusely scattered by the signature of small-sized objects or induced by the near field of radio devices are relevant for identifying radiogenomic (cumulant) features of objects in the microwave range in the development of neuroimaging ultra-short pulse (USP) signal radio vision systems, telemonitoring, and near-radio detection. The paper sets out to develop methods and algorithms for vector analysis of radio wave deformation of nonstationary fields forming a signal radio image based on radiophysical and topological characteristics of small-sized objects; to develop software and hardware for registration and neural network recognition of signal radio images, including methods for the synthesis and extraction of signal radiogenomes using digital twins of objects obtained through vector electrodynamic modeling; and to analyze signal radio images induced by elements of printed topology of electronic devices.

Methods. The study is based on statistical radiophysics methods, time-frequency approaches for wavelet transformation of USP radio images, numerical electrodynamic methods for creating digital twins of small-sized objects, as well as neural network authentication algorithms based on the cumulant theory of pole-genetic and resonant physically unclonable functions used in identifying signal radio images.

Results. The results of fundamental research on electrodynamic effects of vector-wave deformation of nonstationary fields of sub-nanosecond configuration are presented as a means of identifying and authenticating signal radio images. Neural network techniques for cumulant formation of radio genomes of signal radio images are proposed on the basis of pole-genetic and resonant functions.

Conclusions. A radiogenome, representing the unique authenticator of a radio image, is shown to be formed on the basis of physically unclonable functions determined by the structure and set of radiophysical parameters of the image. Cumulant features of signal radio images identified on the basis of pole-genetic and physically unclonable resonant functions of small-sized objects are revealed.

Keywords: signal radiovision, radiogenome, radio image, physically unclonable function, cumulant, pole-genetic functions

• **Submitted:** 28.01.2024 • **Revised:** 21.02.2024 • **Accepted:** 19.05.2024

For citation: Kostin M.S., Boikov K.A. Digital technologies for signal radio vision and radio monitoring. *Russ. Technol. J.* 2024;12(4):59–69. https://doi.org/10.32362/2500-316X-2024-12-4-59-69

Financial disclosure: The authors have no a financial or property interest in any material or method mentioned.

The authors declare no conflicts of interest.

НАУЧНАЯ СТАТЬЯ

Цифровые технологии сигнального радиовидения и радиомониторинга

М.С. Костин [@], **К.А. Бойков**

МИРЭА – Российский технологический университет, Москва, 119454 Россия
[@] *Автор для переписки, e-mail: kostin_m@mirea.ru*

Резюме

Цели. Цель работы – разработка методов и алгоритмов векторного анализа радиоволновой деформации нестационарных полей, образующих сигнальное радиоизображение, определяемое радиофизическими и топологическими признаками малоразмерных объектов; создание программно-аппаратных средств регистрации и нейросетевого распознавания сигнальных радиоизображений, в т.ч. методов синтеза и экстракции сигнальных радиогеномов при помощи цифровых двойников объектов, полученных посредством векторного электродинамического моделирования; анализ сигнальных радиоизображений, наводимых элементами печатной топологии электронных устройств.

Методы. Использованы методы статистической радиофизики, частотно-временные методы вейвлет-преобразования финитных во времени сигнальных радиоизображений, численные методы электродинамики при создании цифровых двойников малоразмерных объектов, а также нейросетевые алгоритмы аутентификации, основанные на кумулянтной теории полюсно-генетических и резонансных физически неклонируемых функций (ФНФ), используемых при распознавании сигнальных радиоизображений.

Результаты. Приведены научные результаты фундаментальных исследований электродинамических эффектов векторно-волновой деформации нестационарных полей субнаносекундной конфигурации, представляющие интерес при распознавании и аутентификации сигнальных радиоизображений. Предложены нейросетевые методы кумулянтного формирования радиогеномов сигнальных радиоизображений на базе полюсно-генетических и резонансных функций.

Выводы. Показано, что радиогеном – уникальный аутентификатор радиоизображения – формируется в базисе ФНФ, определяемых структурой и набором радиофизических параметров объекта. Выявлены кумулянтные признаки распознавания сигнальных радиоизображений в базисе полюсно-генетических и резонансных ФНФ малоразмерных объектов.

Ключевые слова: сигнальное радиовидение, радиогеном, радиоизображение, физически неклонируемая функция, кумулянта, полюсно-генетические функции

• **Поступила:** 28.01.2024 • **Доработана:** 21.02.2024 • **Принята к опубликованию:** 19.05.2024

Для цитирования: Костин М.С., Бойков К.А. Цифровые технологии сигнального радиовидения и радиомониторинга. *Russ. Technol. J*. 2024;12(4):59–69. https://doi.org/10.32362/2500-316X-2024-12-4-59-69

Прозрачность финансовой деятельности: Авторы не имеют финансовой заинтересованности в представленных материалах или методах.

Авторы заявляют об отсутствии конфликта интересов.

INTRODUCTION

Signal radio vision is a field of radiophysics that studies methods for forming, processing, and authenticating vector radio images of objects in the superhigh frequency (SHF) range, which result from the diffuse scattering by the object signature of an ultra-short pulse (USP) object or USP induced by electronic devices during transients on their components and distributed topology reactivities [1, 2]. Signal radio vision technology is based on the electrodynamic effect of vector-wave deformation of nonstationary fields of subnanosecond configuration. For ultra-wideband radio monitoring tasks, this can be used to obtain not only a vector radio image in the form of a signal radio profile (SRP) but also information about the radiophysical parameters of the irradiated object, including synthesizing a time-spectral radiogenome or unique authenticator on the basis of physical unclonable functions (PUF) [1–9]. Indeed, radiometric authenticators of objects (including radioelectronic devices) determined by the parametric distribution of reference element characteristics and inhomogeneities composing their structure (signature, topology, architecture, etc.) are hidden in wave deformations (dispersive, dissipative, polarization, time-frequency, and phase-dynamic) of the electromagnetic field scattered or induced into the USP space [10–14]. In order to identify radiogenomic features of small-sized objects in the SHF range, a neural network approach for authenticating radio images via cumulants on the basis of pole-genetic and resonant PUF synthesized using digital twin technology (numerical methods of electrodynamic modeling) [3, 10] is proposed.

On the basis of previously published research results in the field of signal radio imaging, including those presented in [1, 2, and 12], it can be shown that authenticators of different objects defined by the PUF reference basis are hidden in wave deformations of the USP field. Due to the quasi-identical envelopes of wave profiles of signal radio images of dissimilar objects, restrictions are imposed on their identification by means of USP envelopes. As a consequence, it becomes relevant to practically implement radio wave technologies of subnanosecond resolution.

1. FORMATION AND AUTHENTICATION OF SIGNAL RADIO IMAGES DIFFUSELY SCATTERED BY SIGNATURE OF SMALL-SIZED OBJECTS

The time-frequency authentication of signal radio images is determined on the basis of a priori research data on electrodynamic features of the radio wave processes of non-stationary fields, which are scattered on the impedance inhomogeneities of an irradiated object. This involves the development of adaptive algorithms for analyzing USP based on singular-statistical methods for obtaining reference frames (radiogenomes) in the time profiles of signal radio images, forming the most complete representation of the object structure in the SHF range (Fig. 1) [1, 2, and 9].

Neural network algorithms have been developed on the basis of cumulant theory of pole-genetic and resonant functions for finding and identifying reference frames in a radio signal image, which can be achieved by experimentally synthesizing specified impulse responses (IR) or using digital twin technology [1, 2, 9]. A neural network used for identifying signal radio images with an ultra-precise ConvNet architecture consisting of three layers is based on an Intel Neural Compute Stick 2 16-core USB computing module (Intel Corporation, USA), which uses backpropagation while training to minimize error probability when identifying the signature of a small-sized object.

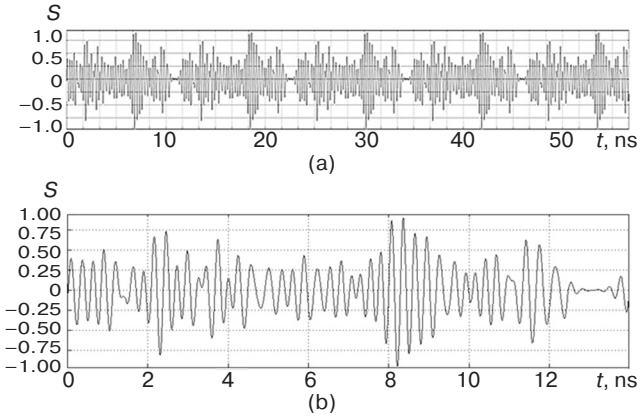

Fig. 1. Reduced signal radio image of a small-size UAV object: (a) USP periodicity on the equivalent time interval; (b) reference frame of the signal radio image. *S* is scale reduced to the USP power maximum (dimensionless); *t* is equivalent time of stroboscopic transformation

Analyzing the time-frequency distribution of diffusely scattered USP implies a preliminary wavelet transformation of the complete radio response, whose signal radio image concentrates the signature radio genome of the small-sized object's equivalent inhomogeneity, which is formed by its instantaneous effective scattering area (ESA). This influences the nature of the spectral formant superposition produced by the electrodynamic process of wave deformations of the nonstationary field *E*,*H*-components [1–10]. In this case, decomposition of the signal radio response of the object in the coordinated mode can also be achieved by discrete formation of the USP power spectral density function in time [10]. This provides a unique opportunity to create a library of signal radio genomes of small-sized objects of the "unmanned aerial vehicle" (UAV) type by specified signatures for generating a priori information about USP radio images [1, 2, and 10]. Indeed, in

case of USP diffuse scattering by a small-sized object with dynamic ESA, the wavelet transform at the time set by a given windowed frame function permits the radiophysical behavior of USP wave deformations $s(t)$ to be localized and even identified when interacting with the signature. Thus, the functional character of the USP signal change $y(t)$ is shown to be completely determined by IR properties $h(t)$ of the propagation medium and the family of local IR of the object, as follows:

$$y(t) = H\left[s(t)\right] = \int_{-\infty}^{\infty} s(\tau)h(t-\tau)d\tau,$$

where H is the USP wave deformation operator determined by radiophysical and topological properties of the object signature.

At the same time, the singular-statistical evaluation of radio image reproducibility shows that the beat interference generation conditioned by multipath copies of $y(t)$ significantly affects ambiguity when identifying pole-genetic functions of the radiogenome [3]. At the same time, wavelet cepstral postprocessing of the form

$$C(q) = \frac{1}{2\pi}\int_{-\omega_{\text{bdry}}}^{+\omega_{\text{bdry}}} \ln\left[S(\omega)\right]^2 e^{j\omega q_t}\, d\omega,$$

which is the most effective approach when decomposing signal radio images by pole-genetic functions, can be used to compensate for the impact of Rician interference [1, 2]. Here, $S(\omega)$ is USP amplitude spectrum $s(t)$; $\pm\omega_{\text{bdry}}$ is boundary frequencies of integration; $\ln\left[S(\omega)\right]^2$ is logospectrum; and q_t is cepstral time variable.

Considering the case when the radio image of an object can be represented by the difference in its intrinsic IR of the same signature shifted by the USP duration, the radio genome of the small-sized object is defined by complex basis of intrinsic resonant frequencies ω_m, $m = 1, 2, ..., N$, while the evaluation of the small-sized object IR is reduced to finding its pole functions

$$Q_m(\omega) = \frac{\dot{C}_m^*}{\omega + \dot{q}_m^*} - \frac{\dot{C}_m}{\omega - \dot{q}_m}, \dot{q}_m = \omega_m + j\gamma_m,$$

concentrated in the frequency-to-time mapping (FTM) of the scattered USP radio response. Here, it is assumed that each of basic functions $Q_m(\omega)$ with complex amplitude $\dot{C}_m$ contains pole cumulant $\dot{q}_m$ with frequency ω_m and dissipation coefficient γ_m set as a priori information when constructing a recurrent neural network for identifying signal radio images.

The vector radio images of the baseline signatures of the radiogenome of small-sized UAV-type objects and their corresponding pole functions at signal-to-noise ratio (SNR) equal to 12 dB shown in Fig. 2 include those used to determine the functional relationship between the change of the object signature in time and its radiogenome [1, 2–8, and 10].

The object signature PUFs (reference identifiers) can also be resonant frequencies (resonant cumulants) characterizing the set of reference elements and object signature inhomogeneities forming the superposition of resonators.

The nature of the PUF distribution comprises two elements, a "forced" component due to the influence of polarization, field strength distribution rate, direction

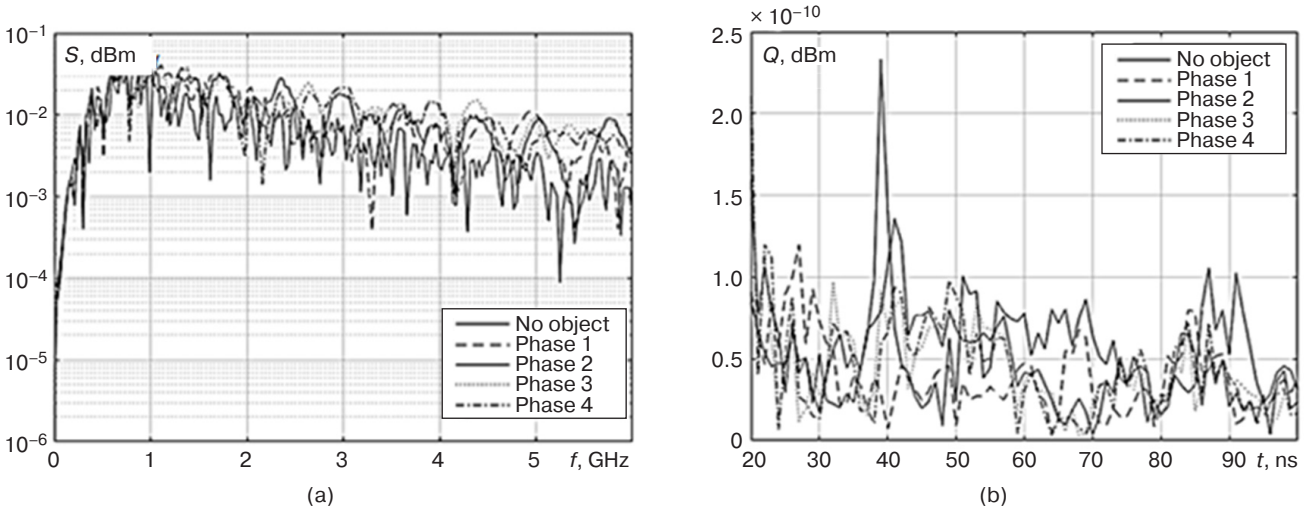

Fig. 2. UAV vector radio images (a) and their corresponding pole functions (b) obtained at periodic time phases of 10 ns; f is linear frequency ($\omega = 2\pi f$)

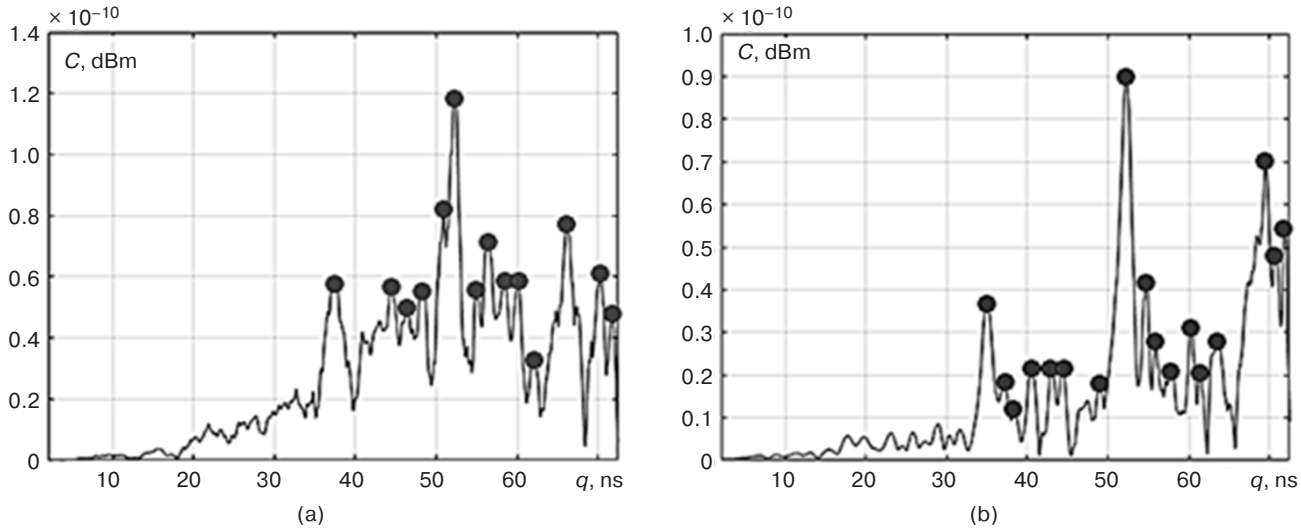

Fig. 3. Cepstral representation of the resonant components of the UAV signal radio image for two orthogonal signatures of a small-sized object: (a) angular position at 0°, (b) angular position at 90°

and conditions of the USP propagation medium, etc., and a "mode" component associated with USP diffuse scattering on resonant and selective structures of the object signature. Thus, in order to extract the mode component on the basis of a priori information on resonant frequencies obtained, for example, when irradiating a digital twin (electrodynamic model) of a small-sized object, a discriminative (anti-resonant) signal $d_e(t)$ of finite duration T_e fitted to the radio image compensates for resonances in scattered USP $s(t)$, at which convolution

$$\chi(t) = d_e s(t) = \int_0^{T_e} d_e(\tau) s(t-\tau) d\tau$$

for $t \geq T_e$ tends to zero.

Figure 3 shows cepstral functions $C(q)$ of resonant cumulants and the mode component comprising the radio genome of the UAV signal radio image [7, 10], whose vector radio image of pole functions is shown in Fig. 2.

According to published research, at SNR equal to 12 dB and a discriminative difference of 10 dB between scattered USP and reference PUF, the reproducibility of radio image identification by resonant responses may reach 0.95. In other words, since the singularization of radio images of small-sized objects in a given basis of resonant frequencies (radiogenomic features) used as cumulants of the neural network does not require a priori information about the complete time-spectral function of the object radio image, the probability of identifying object radio images by reference identifiers can be increased [9, 7, 10–12].

2. FORMING AND MONITORING SIGNAL RADIO IMAGES INDUCED BY PRINTING TOPOLOGY ELEMENTS OF ELECTRONIC DEVICES

Signal processes on reactive components of electronic devices (ED) are generally accompanied by the energy redistribution between capacitive and inductive elements (hereinafter referred to as accumulators) determined for a multiparameter system by stochastically oscillating electromagnetic radiation induced into space, forming SRP or a unique ED radiometric image. In this case, parasitic reactivities in conducting lines distributed as electronic circuit parameters that include interlayer topology elements can result in signal distortions related to the steepness of signal edges and impedance over-reflections [11]. This typically results in a lowered maximum frequency of digital devices or reduced capacity of microcircuit power outputs. At the same time, the supply line in the ED printing module topology accumulates electric and magnetic energy, combining inductances, capacitances, and ohmic losses whose values depend on the line topology and material properties. When analyzing SRP formation in the ED module with radiating circuit architecture (topology), the relationship between consumer loads and accumulators should be taken into account. These interrelations are determined by the values of roots of the secular equation set up for the ED radiating circuit architecture. The radiation in the ED fragment topology results in the energy redistribution between reactive accumulators. The general solution of this equation is the oscillation free component (U_{fr}) with complex-conjugate roots $\dot{p}_{1,2} = -\delta \pm j\omega$. The ED node usually comprises a group of components forming the

electrical circuit architecture. The total operating field of an electronic circuit node is a superposition of emissions of input and output circuits constituting it. At time instants corresponding to the arrival of an actuating pulse (supply voltage, mode switching, or clocking), these components emit free damped oscillations described by the following expression:

$$U(t)=\sum_{i=1}^{N}U_{\text{fr}i}(t)=\sum_{i=1}^{N}U_{0i}\mathrm{e}^{-\delta_i(t-t_{0i})}\sin\left[2\pi f_i(t-t_{0i})\right],$$

here, N is the number of components; $U_{\text{fr}i}$ is the reduced value of the free component of ith oscillation; U_{0i} is the reduced amplitude of the first half-wave of ith oscillation; δ_i s the damping factor of ith oscillation; t is the current time; t_{0i} is the radiation time of ith oscillation; and f_i is the frequency of ith oscillation.

The ED SRP decomposition with decomposition into formant components is shown in Fig. 4.

Analyzing the curves shown in Fig. 4b, it can be seen that signal parameters of SRP N-formant components carry information about the electronic node [12–15]. The number of sources of damped oscillations can be obtained from the N value to estimate whether all node elements of interest participate in radiation. Since not all emitters participate in the SRP formation, fewer emitters than in the reference SRP (received from a functioning original ED) means that ED malfunction (or unoriginality) has been detected. A number of emitters exceeding the reference value indicates incorrect measurement or that interference occurred during measurement. The amplitude of the first half-wave of oscillations U_{0i} (Fig. 4b) depends on the radiation power of the considered node components. The power of this radiation is proportional to the voltage drop across the emitter and inversely proportional to double the wave impedance of emitter Z [16]. Since the wave impedance of the emitter does not depend on electrical characteristics of the investigated radioelectronic node, the reduced amplitude of the first half-wave of the oscillation can be used to estimate the electrical potential at the emitter. The oscillation the damping factor δ determined by inductance and ohmic resistance shows the energy dissipation rate. While parasitic and concentrated inductances are not significantly dependent on changes in external factors, the equivalent ohmic resistance significantly depends on temperature. The biggest changes are in specific resistances of supply conductors ρ and conducting regions of semiconductor devices $\frac{d\rho}{dT}=\alpha_\rho\rho$, where α_ρ is the temperature coefficient of conductor specific resistance (for copper, $\alpha_\rho = 4.1 \cdot 10^{-3}$ 1/K). Thus, the damping factor essentially indicates the temperature difference between the radiating node and the temperature at which the SRP reference measurement has been taken.

At equivalent capacitance values of the order of tens picofarads and equivalent ohmic resistances measured in tenths of 1 ohm, oscillation frequency f contains information about the quality of gate dielectrics of metal-oxide-semiconductor structures or modes of operation of p-n-junctions of ED radiating radioelectronic nodes. Here, oscillation frequencies are informative provided that there is a reference signal with previously extracted parameters. In this case, the radiation start time t_0 reflects the transmission rate of the disturbing influence and characterizes the response rate of the node. By comparing the measured value of this parameter with the reference value, the conclusion can be made about the change in the responsiveness of the considered ED components.

The physically unclonable function obtained by registering the electrical component of the electromagnetic radiation of ED electronic components defines physical parameters of the item taking into

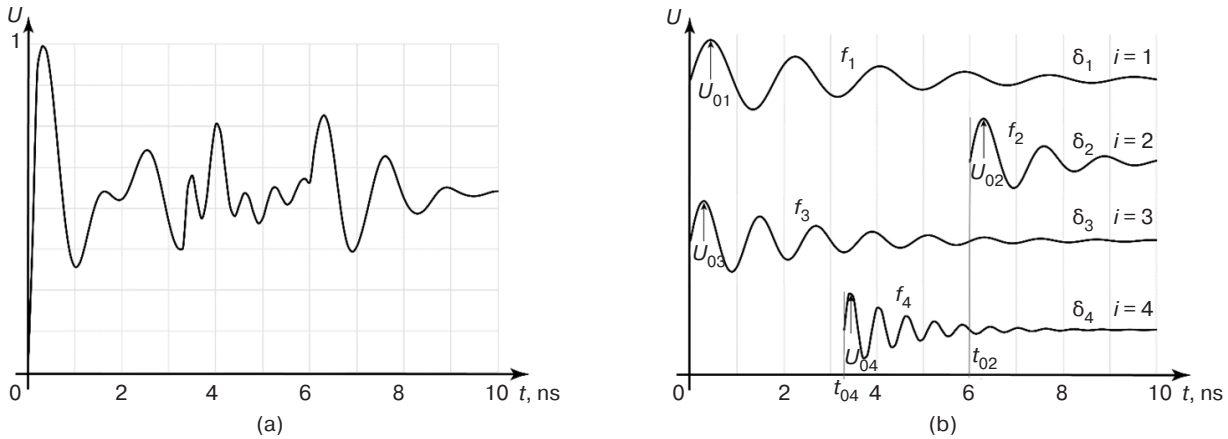

Fig. 4. SRP time representation:
(a) superposition of radiations, (b) SRP components

account the scatter of technological tolerances on component parameters. Reconstruction and analysis of this PUF by cross-correlation with the reference accepted by ED manufacturer, as well as comparison of the parameters obtained by the complex PUF decomposition allow evaluating the originality of the radioelectronic item remotely [17].

For recording SRP in laboratory research, sensitive ultrabroadband antennas, oscilloscopes with memory (or data transmission) function, and low-noise power preamplifiers providing a bandwidth of several gigahertz can be used. The detail of SRP research and the possibility of estimating the device radiometric characteristics depend on the bandwidth and sampling frequency. Due to its flexibility, the software-defined radio system for receiving and processing SRP opens up new opportunities in fields of nondestructive testing (NDT) and determining ED authenticity [18].

The total operating field in digital ED is emitted while applying the supply voltage to generate signals for controlling internal and external periphery at changes of power consumption mode. In the case of analog circuits, SRP is emitted only at the moment of supply voltage application.

In order to obtain the damping factor and the elementary radiation phase, the windowed Fourier transform is used. This method can be used to obtain the spectrum of damped oscillations with corresponding bias for each discrete quantity. For visualizing data in the form of samples, a three-dimensional dependence of the reduced value of signal energy X on frequency f and window position t is plotted (Fig. 5).

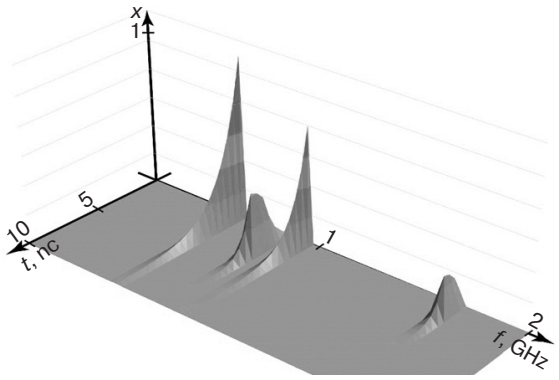

Fig. 5. SRP three-dimensional spectrum

When the amplitude value reduced to frequency increases or does not change with increasing time, the absence of radiation at this readout is indicated. A decrease in amplitude indicates the presence of radiation induction. The starting point of radiation is defined by the moment of transition from increasing amplitude to decay (peak point). The damping of the reduced energy value corresponds to the dumped oscillation law with the same factors $X_i = X_{0i}e^{-\delta_i t}$, where X_{0i} is the amplitude spectrum of ith oscillation at the start point. Correct SRP decomposition with parameter extraction is possible at SNR more than 18 dB.

For ED authentication, the compliance matrix is created (Fig. 6), where "1" stands for the transmitter parameter falling within the confidence interval determined by simulation results or experimental data.

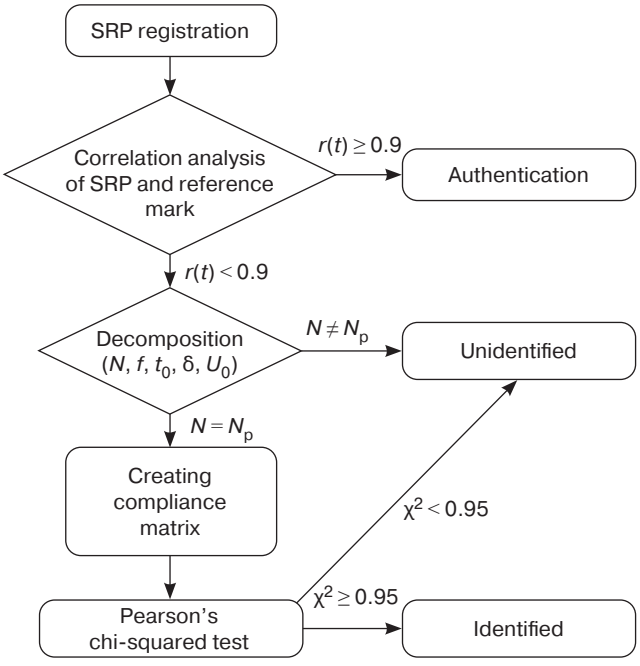

Parameters \ Emitters	1	2	3	4
f	1	1	1	0
δ	1	0	1	1
t_0	1	1	1	1
U_0	1	1	0	1

Fig. 6. Architectural algorithmics of ED authentication by SRP. N_p is the number of desired emitters, while $r(t)$ is the correlation between the received SPR and the reference mark

Taking into account that during ED authentication the sample of SRP parameters is expected to fall into the confidence interval (Fig. 6) determined for each emitter experimentally, the Pearson's chi-squared test may be determined, as follows:

$$\chi^2 = \sum_{j=1}^{k} \frac{(u_j - e_j)^2}{e_j},$$

where u_j is the observed frequency of the feature in jth group and e_j is the theoretical frequency of the feature in jth group.

The analysis based on the experimental data show that for $\chi^2 \geq 0.95$, the ED authentication reliability is determined to be at least 95% [19, 20].

CONCLUSIONS

The radiogenome formed on the basis of PUF determined by the structure and the set of radiophysical parameters of the object serves as a unique radio image authenticator to obtain information about radiophysical parameters of both irradiated and radiating SRP of the object. Radiometric authenticators of objects including ED determined by parametric distribution of characteristics of reference elements and inhomogeneities constituting their structure (signature, topology, architecture, etc.) are hidden in wave deformations (dispersive, dissipative, polarization, frequency-time, and phase-dynamic ones) of the electromagnetic field scattered or induced into the USP space. The vector-wave deformation of nonstationary fields of subnanosecond configuration can be used to identify and authenticate objects according to signal radio images or so-called radio genomes on the basis of synthesized pole-genetic and resonant PUFs using neural network algorithms. The extraction of SRP parameters using floating "window" provides new opportunities in identifying ED radio-physical parameters, including the development of new SHF technologies for signal radio vision, telemonitoring, and short-range radio detection. Further development of signal radio vision technology will involve creating an algorithm for identifying radio wave images based on vector analysis, as well as the adaptation and emulation of a neural network for identifying signal radio images with ultra-precise ConvNet architecture on a single-board module, and the formation and extraction of a database of radiogenomes of small-sized objects and ED in order to create a prototype of an autonomous neuroimaging hardware and software system for short-range radio detection.

ACKNOWLEDGMENTS

The study was carried out within the framework of the 170-IRI initiative research project on the topic "Microwave technologies for signal radio vision, telemonitoring and short-range radio detection." Scientific and practical results of recording radio images were obtained using control and measuring equipment from Rohde & Schwarz[1] in the laboratory of "Radio wave processes and microwave modules" of the TESLA educational and scientific center of the Department of Radio Wave Processes and Technologies of the Institute of Radio Electronics and Informatics of RTU MIREA.

Authors' contributions

M.S. Kostin—formulation of the problem, conducting the experiment, analyzing the results obtained, formulating conclusions, and writing the text of the article.

K.A. Boikov—conducting the experiment, analyzing the results, formulating conclusions, and writing the text of the article.

REFERENCES

1. Kostin M.S., Boikov K.A. *Radiovolnovye tekhnologii subnanosekundnogo razresheniya:* monografiya (*Radio Wave Technologies of Subnanosecond Resolution: monograph*). Moscow: RTU MIREA; 2021. 142 p. (in Russ.). ISBN 978-5-7339-1565-4
2. Kostin M.S., Boikov K.A. *Signal'no-arkhitekturnyi reinzhiniring i radiosensornoe raspoznavanie elektronnykh sredstv* (*Signal-Architectural Reengineering and Radiosensor Recognition of Electronic Devices:* textbook). Moscow; Vologda: Infra-Inzheneriya; 2024. 152 p. (in Russ.). ISBN 978-5-9729-1832-4
3. Shadinov S.S. Spatial ultra-wideband visualization of probed near-field surveillance objects. *Zhurnal Radioelektroniki = J. Radio Electronics*. 2020;7 (in Russ.). https://doi.org/10.30898/1684-1719.2020.7.8. Available from URL: http://jre.cplire.ru/jre/jul20/8/text.pdf
4. Nerukh A., Benson T. *Non-stationary Electromagnetics*. USA: Jenny Stanford Publishing; 2012. 616 p. https://doi.org/10.1201/b13058
5. Allen B., Dohler M., Okon E.E., et al. *Ultra-Wideband Antennas and Propagation for Communications, Radar and Imaging*. USA: John Wiley & Sons; 2007. 475 p.

[1] https://www.rsh-tech.ru/ (in Russ.). Accessed January 31, 2024.

6. Mahafza B.R. *Radar Signal Analysis and Processing Using Matlab*. USA: CRC Press; 2016. 504 p.
7. Carrer L., Yarovoy A.G. Concealed weapon detection using UWB 3-D radar imaging and automatic target recognition. In: *The 8th European Conference on Antennas and Propagation* (*EuCAP*). 2014. P. 2786–2790. https://doi.org/10.1109/EuCAP.2014.6902403
8. Günther L. *Electromagnetic Field Theory for Engineers and Physicists*. Berlin, Heidelberg: Springer; 2010. 659 p.
9. Oppermann I., Hämäläinen M., Iinatti J. *UWB: Theory and Applications*. John Wiley & Sons; 2004. 248 p.
10. Taylor J.D. (Ed.). *Advanced Ultrawideband Radar. Signals, Targets, and Advanced Ultrawideband Radar Systems*. Boca Raton, USA: CRC Press; 2016. 494 p.
11. Wang X., Dinh A., Teng D. Radar Sensing Using Ultra Wideband – Design and Implementation. In: Matin M.A. (Ed.). *Ultra Wideband – Current Status and Future Trends*. 2013;11:41–63. https://dx.doi.org/10.5772/48587
12. Shadinov S.S., Kostin M.S., Konyashkin G.V., et al. Vector *S*-Parametric Analysis of Signal Phase Dynamic Radio Images. *Dokl. Phys.* 2023;68(9):311–318. https://doi.org/10.1134/S1028335823090057
[Original Russian Text: Shadinov S.S., Kostin M.S., Konyashkin G.V., Korchagin A.S., Romanovskii M.Yu., Gusein-zade N.G. Vector *S*-parametric analysis of signal phase dynamic radio images. *Doklady Rossiiskoi akademii nauk. Fizika, tekhnicheskie nauki.* 2023;512(1):78–86 (in Russ.). https://doi.org/10.31857/S2686740023050115]
13. Boikov K.A. Determination of parameters of electronic devices by the method of passive radio-sensor technical diagnostics. *Izvestiya vysshikh uchebnykh zavedenii Rossii. Radioelektronika = Journal of the Russian Universities. Radioelectronics*. 2021;24(6):63–70 (in Russ.). https://doi.org/10.32603/1993-8985-2021-24-6-63-70
14. Lebedev E.F., Ostashev V.E., Ulyanov A.V. Means for generating ultra-wideband radio frequency emissions with semiconductor field generators. *Vestnik Kontserna VKO Almaz-Antei = Bulletin of Concern VKO Almaz-Antey*. 2018;1(24):35–42 (in Russ.).
15. Boikov K.A., Shamin A.E. Software Analysis of the Signal Radio Profile during Passive Radio-Sensor Technical Diagnostics. *J. Commun. Technol. Electron*. 2022;67(11):1337–1344. https://doi.org/10.1134/S1064226922110018
16. Astakhov N.V., Bashkirov A.V., Zhurilova O.E., Makarov O.Yu. Time-frequency analysis of non-stationary signals by wavelet transform and windowed Fourier transform. *Radiotekhnika = Radioengineering*. 2019;83(6-8):109–112 (in Russ.).
17. Herder C., Ren L., van Dijk M., Yu M.-D., Devadas S. Trapdoor Computational Fuzzy Extractors and Cryptographically-Secure Physical Unclonable Functions. *IEEE Transactions on Dependable and Secure Computing*. 2017;14(1):65–82. https://doi.org/10.1109/TDSC.2016.2536609
18. Lukyanchikov A.V., Lyzlov A.V. Radio broadcast monitoring system using SDR technology. *SVCh-tekhnika i telekommunikatsionnye tekhnologii = Microwave and Telecommunication Technology*. 2021;3:69–70 (in Russ.). Available from URL: https://elibrary.ru/dxiqdb
19. Huang R., Cui H. Consistency of chi-squared test with varying number of classes. *J. Syst. Sci. Complex*. 2015;28(2):439–450. https://doi.org/10.1007/s11424-015-3051-2
20. Liu Y., Mu Y., Chen K., et al. Daily Activity Feature Selection in Smart Homes Based on Pearson Correlation Coefficient. *Neural Process. Lett*. 2020;51(2):1771–1787. https://doi.org/10.1007/s11063-019-10185-8

СПИСОК ЛИТЕРАТУРЫ

1. Костин М.С., Бойков К.А. *Радиоволновые технологии субнаносекундного разрешения:* монография. М.: РТУ МИРЭА; 2021. 142 с. ISBN 978-5-7339-1565-4
2. Костин М.С., Бойков К.А. *Сигнально-архитектурный реинжиниринг и радиосенсорное распознавание электронных средств:* учебник. М.: Вологда: Инфра-Инженерия; 2024. 152 с. ISBN 978-5-9729-1832-4
3. Шадинов С.С. Пространственная сверхширокополосная визуализация зондируемых объектов ближнего радионаблюдения. *Журнал радиоэлектроники*. 2020;7. https://doi.org/10.30898/1684-1719.2020.7.8. URL: http://jre.cplire.ru/jre/jul20/8/text.pdf
4. Nerukh A., Benson T. *Non-stationary Electromagnetics*. USA: Jenny Stanford Publishing; 2012. 616 p. https://doi.org/10.1201/b13058
5. Allen B., Dohler M., Okon E.E., et al. *Ultra-Wideband Antennas and Propagation for Communications, Radar and Imaging*. USA: John Wiley & Sons; 2007. 475 p.
6. Mahafza B.R. *Radar Signal Analysis and Processing Using Matlab*. USA: CRC Press; 2016. 504 p.
7. Carrer L., Yarovoy A.G. Concealed weapon detection using UWB 3-D radar imaging and automatic target recognition. In: *The 8th European Conference on Antennas and Propagation* (*EuCAP*). 2014. P. 2786–2790. https://doi.org/10.1109/EuCAP.2014.6902403
8. Günther L. *Electromagnetic Field Theory for Engineers and Physicists*. Berlin, Heidelberg: Springer; 2010. 659 p.
9. Oppermann I., Hämäläinen M., Iinatti J. *UWB: Theory and Applications*. John Wiley & Sons; 2004. 248 p.
10. Taylor J.D. (Ed.). *Advanced Ultrawideband Radar. Signals, Targets, and Advanced Ultrawideband Radar Systems*. Boca Raton, USA: CRC Press; 2016. 494 p.
11. Wang X., Dinh A., Teng D. Radar Sensing Using Ultra Wideband – Design and Implementation. In: Matin M.A. (Ed.). *Ultra Wideband – Current Status and Future Trends*. 2013;11:41–63. https://dx.doi.org/10.5772/48587
12. Шадинов С.С., Костин М.С., Коняшкин Г.В., Корчагин А.С., Романовский М.Ю., Гусейн-заде Н.Г. Векторный *S*-параметрический анализ сигнальных фазодинамических радиоизображений. *Доклады Российской академии наук. Физика, технические науки*. 2023;512(1):78–86. https://doi.org/10.31857/S2686740023050115

13. Бойков К.А. Определение параметров электронных устройств методом пассивной радиосенсорной технической диагностики. *Известия высших учебных заведений России. Радиоэлектроника.* 2021;24(6):63–70. https://doi.org/10.32603/1993-8985-2021-24-6-63-70
14. Лебедев Е.Ф., Осташев В.Е., Ульянов А.В. Устройства генерирования сверхширокополосных излучений радиочастотного диапазона с генераторами возбуждения полупроводникового типа. *Вестник Концерна ВКО «Алмаз – Антей».* 2018;1(24):35–42.
15. Boikov K.A., Shamin A.E. Software Analysis of the Signal Radio Profile during Passive Radio-Sensor Technical Diagnostics. *J. Commun. Technol. Electron*. 2022;67(11):1337–1344. https://doi.org/10.1134/S1064226922110018
16. Астахов Н.В., Башкиров А.В., Журилова О.Е., Макаров О.Ю. Частотно-временной анализ нестационарных сигналов методами вейвлет-преобразования и оконного преобразования Фурье. *Радиотехника*. 2019;83(6–8):109–112.
17. Herder C., Ren L., van Dijk M., Yu M.-D., Devadas S. Trapdoor Computational Fuzzy Extractors and Cryptographically-Secure Physical Unclonable Functions. *IEEE Transactions on Dependable and Secure Computing*. 2017;14(1):65–82. https://doi.org/10.1109/TDSC.2016.2536609
18. Лукьянчиков А.В., Лызлов А.В. Система мониторинга радио эфира с использованием технологии SDR. *СВЧ-техника и телекоммуникационные технологии*. 2021;3:69–70. URL: https://elibrary.ru/dxiqdb
19. Huang R., Cui H. Consistency of chi-squared test with varying number of classes. *J. Syst. Sci. Complex*. 2015;28(2):439–450. https://doi.org/10.1007/s11424-015-3051-2
20. Liu Y., Mu Y., Chen K., et al. Daily Activity Feature Selection in Smart Homes Based on Pearson Correlation Coefficient. *Neural Process. Lett*. 2020;51(2):1771–1787. https://doi.org/10.1007/s11063-019-10185-8

About the authors

Mihail S. Kostin, Dr. Sci. (Eng.), Associate Professor, Head of the Department of Radio Wave Processes and Technologies, Deputy Director, Institute of Radio Electronics and Informatics, MIREA – Russian Technological University (78, Vernadskogo pr., Moscow, 119454 Russia). E-mail: kostin_m@mirea.ru. Scopus Author ID 57208434671, RSCI SPIN-code 5819-2178, http://orcid.org/0000-0002-5232-5478

Konstantin A. Boikov, Dr. Sci. (Eng.), Associate Professor, Department of Radio Wave Processes and Technologies, Institute of Radio Electronics and Informatics, MIREA – Russian Technological University (78, Vernadskogo pr., Moscow, 119454 Russia). E-mail: bojkov_k@mirea.ru. Scopus Author ID 57208926258, RSCI SPIN-code 2014-6951, http://orcid.org/0000-0003-0213-7337

Об авторах

Костин Михаил Сергеевич, д.т.н., доцент, заведующий кафедрой радиоволновых процессов и технологий, заместитель директора Института радиоэлектроники и информатики, ФГБОУ ВО «МИРЭА – Российский технологический университет» (119454, Россия, Москва, пр-т Вернадского, д. 78). E-mail: kostin_m@mirea.ru. Scopus Author ID 57208434671, SPIN-код РИНЦ 5819-2178, http://orcid.org/0000-0002-5232-5478

Бойков Константин Анатольевич, д.т.н., доцент, кафедра радиоволновых процессов и технологий, Институт радиоэлектроники и информатики, ФГБОУ ВО «МИРЭА – Российский технологический университет» (119454, Россия, Москва, пр-т Вернадского, д. 78). E-mail: bojkov_k@mirea.ru. Scopus Author ID 57208926258, SPIN-код РИНЦ 2014-6951, http://orcid.org/0000-0003-0213-7337

Translated from Russian into English by K. Nazarov
Edited for English language and spelling by Thomas A. Beavitt

Modern radio engineering and telecommunication systems

Современные радиотехнические и телекоммуникационные системы

UDC 621.396.969
https://doi.org/10.32362/2500-316X-2024-12-4-70-83
EDN QDYIBS

RESEARCH ARTICLE

Principles of construction of nanosatellite radar systems based on global navigation satellite system reflectometry

Alexander V. Ksendzuk [1, @], Vyacheslav F. Fateev [2]

[1] *MIREA – Russian Technological University, Moscow, 119454 Russia*
[2] *Scientific and Technical Center of Metrology in Gravimetry, VNIIFTRI, Solnechnogorsk, Moscow oblast, 141570 Russia*
[@] *Corresponding author, e-mail: ks_alex@mail.ru*

Abstract

Objectives. The development of radar remote sensing systems based on the reception of signals of navigation satellite systems reflected from the surface enables a constellation of nanosatellites to be deployed, in order to perform radar surveying of the Earth's surface. The aim of this work is to develop the principles of construction of onboard bistatic remote sensing systems on nanosatellites, in order to assess the energy potential and possibilities for its increase.

Methods. The optimal processing method in onboard bistatic radar systems is a development of known analytical methods of optimal processing in monostatic systems. The calculation of the energy potential is based on the experimental data obtained by other authors.

Results. The utilization of signals from navigation satellite systems for surface sensing is a promising and developing area. The USA and China have deployed satellite constellations to perform remote sensing using reflected signals of navigation satellites. An algorithm for optimal processing in such systems, which realizes the principle of aperture synthesis, was developed, and the energy potential of bistatic synthetic aperture radar was calculated. In order to achieve this processing, the proposed scheme uses a standard navigation receiver to form reference signals.

Conclusions. The application of optimal processing methods in bistatic radar enables a synthetic aperture based on scattered satellite navigation system signals. In order to improve the accuracy of estimates, the signal-to-noise ratio needs to be increased by combining coherent accumulation (aperture synthesis) and incoherent accumulation (aggregating measurements from different spacecraft). The signal processing methods and receiver structure proposed in this work onboard nanosatellites allow aperture synthesis to be achieved with realizable hardware requirements.

Keywords: bistatic radar, synthetic aperture, navigation satellite, optimal processing

• **Submitted:** 29.11.2023 • **Revised:** 02.02.2024 • **Accepted:** 24.05.2024

For citation: Ksendzuk A.V., Fateev V.F. Principles of construction of nanosatellite radar systems based on global navigation satellite system reflectometry. *Russ. Technol. J*. 2024;12(4):70–83. https://doi.org/10.32362/2500-316X-2024-12-4-70-83

Financial disclosure: The authors have no a financial or property interest in any material or method mentioned.

The authors declare no conflicts of interest.

НАУЧНАЯ СТАТЬЯ

Принципы построения бортовых радиолокационных систем наноспутников, основанных на приеме отраженных сигналов спутниковых навигационных систем

А.В. Ксендзук [1, @],
В.Ф. Фатеев [2]

[1] *МИРЭА – Российский технологический университет, Москва, 119454 Россия*
[2] *Всероссийский научно-исследовательский институт физико-технических и радиотехнических измерений, Солнечногорск, Московская область, 141570 Россия*
[@] *Автор для переписки, e-mail: ks_alex@mail.ru*

Резюме

Цели. Создание радиолокационных систем дистанционного зондирования, основанных на приеме отраженных от поверхности Земли сигналов навигационных спутниковых систем, позволяет развернуть группировку наноспутников радиолокационного обзора земной поверхности. Целью работы является развитие принципов построения бортовых бистатических систем дистанционного зондирования на сверхмалых космических аппаратах, оценка энергетического потенциала и возможностей его увеличения.

Методы. Оптимальный метод обработки в бортовых бистатических радиолокационных системах (ББРЛС) является развитием известных аналитических методов оптимальной обработки в моностатических системах. Расчет энергетического потенциала основывается на исходных данных, полученных в ходе экспериментальных исследований других авторов.

Результаты. Использование сигналов навигационных спутниковых систем для зондирования поверхности является перспективным, развивающимся направлением. США и Китаем развернуты спутниковые группировки, осуществляющие дистанционное зондирование по отраженным сигналам навигационных спутников. Разработан алгоритм оптимальной обработки в таких системах, реализующий принцип синтезирования апертуры, рассчитан энергетический потенциал бистатической радиолокационной системы с синтезированием апертуры антенны. Для реализации обработки предложена схема с использованием стандартного навигационного приемника, который используется для формирования опорных сигналов.

Выводы. Применение методов оптимальной обработки в ББРЛС позволяет синтезировать радиолокационное изображение по сигналам космических навигационных аппаратов. Для повышения точности оценок необходимо увеличить отношение сигнал/шум за счет сочетания когерентного накопления (синтез апертуры) и некогерентного накопления (комплексирование измерений по разным космическим аппаратам). Предложенные в работе методы обработки сигналов и структура приемника на борту сверхмалого космического аппарата позволяют реализовать синтезирование апертуры при реализуемых требованиях к аппаратной части.

Ключевые слова: бистатическая радиолокационная система, синтез апертуры, навигационный спутник, оптимальная обработка

• **Поступила:** 29.11.2023 • **Доработана:** 02.02.2024 • **Принята к опубликованию:** 24.05.2024

Для цитирования: Ксендзук А.В., Фатеев В.Ф. Принципы построения бортовых радиолокационных систем наноспутников, основанных на приеме отраженных сигналов спутниковых навигационных систем. *Russ. Technol. J*. 2024;12(4):70–83. https://doi.org/10.32362/2500-316X-2024-12-4-70-83

Прозрачность финансовой деятельности: Авторы не имеют финансовой заинтересованности в представленных материалах или методах.

Авторы заявляют об отсутствии конфликта интересов.

INTRODUCTION

Space-based Earth remote sensing (ERS) radiolocation systems (radars) make it possible to monitor the Earth's surface and objects located on it regardless of weather conditions and time of day.

The possibility of recording large areas, incl. in hard-to-reach areas, high efficiency, operation at any time of the day and in any weather, have led to the deployment of satellite constellations (more than 80 spacecrafts (SC) at the end of 2023). Their objective is to resolve the following tasks: constructing radar images of the surface, detecting stationary and moving objects, construction of surface relief maps, assessment of the state of the water surface (currents, near-shore wind, wave intensity), monitoring of hurricanes and tsunamis, monitoring and forecasting of ice conditions, incl. in the Arctic zone, etc. [1].

Currently, most spaceborne remote sensing radars are monostatic radars with radar antenna aperture synthesis (synthetic-aperture radar (SAR)). The bistatic configuration has been achieved only in the form of TanDem-X (EADS Astrium, Germany) [1].

In active SAR, the possibilities of reducing the size, mass, and power consumption are limited by the parameters of the transmitter which must generate sufficient power to obtain high-quality images. For example, for a modern constellation of 27 ICEYE SAR spacecrafts (ICEYE, Finland), the peak radiated power is 3.2 kW.[1]

For this reason, non-radiating systems are considered to be a separate area of space radar development. In such systems, the role of a transmitter is performed by existing (third-party) satellites. The most elaborated of these is the option of using global navigation satellite systems (GNSS) as transmitters. In foreign literature this option has received its own name: GNSS reflectometry (GNSS-R) [2, 3]. This option was used, among other things, for altimetry of the sea surface [4]. Russian scientists have also proposed options for creating remote sensing equipment based on the use of GLONASS signals[2] in terms of building multi-position systems [5, 6], methods of signal processing in the aperture synthesis mode [7], the use of ground-based signal reception system for determining surface parameters [8], the use of aircraft for receiving and processing signals [9]. However, only one project has been realized in practical terms [10].

The results of ship detection on the background of water surface using GNSS signals as presented in [10–12] show that such detection is only possible when the aperture synthesis algorithm is implemented. [13, 14] also published data on successful detection of river vessels from GNSS signals using aperture synthesis.

In 2014, the TechDemoSat-1 satellite (SSTL, United Kingdom) was launched. It carries equipment to receive GNSS signals reflected from the sea surface and to determine wind speeds and the boundaries between the water surface and ice.

On September 28, 2015, the European Space Agency launched Spire nanosatellites (Spire Global, Scotland). It generates radar data for water, sea surface, ice cover, and also enable estimating ionosphere parameters using GNSS signals [15].

The NASA Cyclone Global Navigation Satellite System (CYGNSS) satellite constellation launched in December 2016 consists of 8 satellites and provides resolution in coherent accumulation mode up to 3.5 × 0.5 km with estimation of water and land surface parameters.[3]

GNSS-R satellites were also launched. They include: FSSCat [16], Chinese BuFeng-1 (BF-1) A/B satellites [17], Surrey Satellite Technology Ltd (SSTL) DoT-1 satellite [18], Fengyun-3E satellite [19]. The People's Republic of China launched the Jilin-1 Kuanfu 01C satellite on May 8, 2023, which receives GNSS signals reflected from the Earth's surface to determine average sea surface height, wave height, ice cover characteristics, surface wind parameters, and sea salinity.[4]

The Spire nanosatellite network is the most modern. It has more than 165 3U/6U microsatellites launched on the LEMUR platform. GNSS-R satellites on this platform collect 4 GB of data daily, which are received by more than thirty ground stations.[5]

Remote sensing based on reflected GNSS signals is being developed in such projects as PRETTY[6], HydroGNSS[7], SNOOPI[8], etc.

1. TASK STATEMENT

The task of 24/7 monitoring of the Earth's surface under any weather conditions needs to be resolved through the creation of a constellation of bistatic radars with a receiver on the spacecraft. In order to create such

[1] https://earth.esa.int/eogateway/missions/iceye. Accessed March 20, 2024.

[2] https://glonass-iac.ru/ (in Russ.). Accessed March 20, 2024.

[3] https://podaac.jpl.nasa.gov/CYGNSS. Accessed 20.03.2024.

[4] https://news.cgtn.com/news/2022-05-08/China-launches-first-bipolar-GNSS-R-ocean-survey-payload-19RYzG3bmCs/index.html. Accessed March 20, 2024.

[5] https://spirespaceservices.spire.com/. Accessed March 20, 2024.

[6] https://space.oscar.wmo.int/satellites/view/pretty. Accessed March 20, 2024.

[7] https://www.eoportal.org/satellite-missions/hydrognss. Accessed March 20, 2024.

[8] https://esto.nasa.gov/invest/snoopi. Accessed March 20, 2024.

promising Russian satellites, in order to resolve the task of building radar images of the Earth's surface, measure geoid height, detect broken ice fields, etc. based on the results of reception and processing of GNSS signals reflected from the surface, the method of optimal processing of reflected signals, signal energy, the structure of data reception and processing equipment, need to be defined, including the parameters of the antenna system.

We synthesized an algorithm for radar image formation in space bistatic SAR in the mode of receiving reflected GNSS satellite signals. This enabled us to obtain radar images of the disturbed surface near mirror reflection points. We will form an algorithm for an additive model of the observation equation including a useful signal $S(t)$ at the antenna input and noise $n(t)$, where t is time. In this case, we will assume that the mutual interference of signals is insignificant and can be accounted for in the receiver noise.

Let us distinguish an arbitrary bistatic pair ith receiver–kth transmitter (Fig. 1).

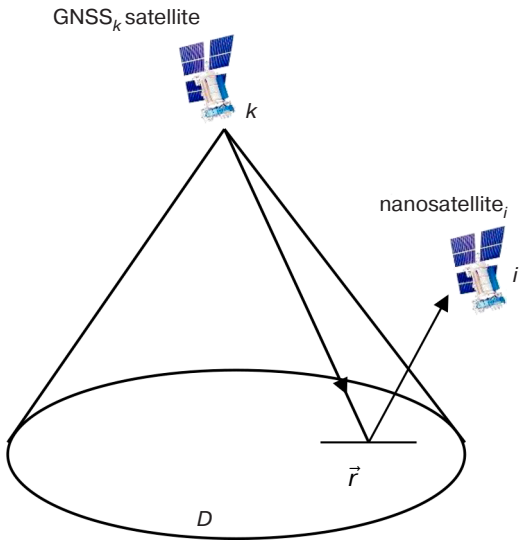

Fig. 1. Observation geometry. $\vec{r}$ is the reflecting point within the probed surface D

The signal of the kth GNSS satellite, reflected from the surface and received by the ith receiving antenna, after reflection from the surface point with coordinates are defined by the expression:

$$\begin{aligned}\dot{S}_{ik}(t,\vec{r}) &= \dot{K}_k(t,\vec{r})\dot{K}_i(t,\vec{r})\times \\ &\times \dot{G}_k(t,\vec{r})\dot{G}_i(t,\vec{r})\dot{F}_{ik}[t,\vec{r},\vec{\lambda}(\vec{r})]\times \\ &\times \dot{S}_{0k}[t-\tau_k(t,\vec{r})-\tau_i(t,\vec{r})]\times \\ &\times \exp\{j\omega_{0k}[t-\tau_k(t,\vec{r})-\tau_i(t,\vec{r})]\},\end{aligned} \quad (1)$$

where $\dot{S}_{ik}(t,\vec{r})$ is the trajectory signal; $\dot{K}_k(t,\vec{r})$ and $\dot{K}_i(t,\vec{r})$ are the coefficients which take into account signal attenuation and distortion during propagation through the atmosphere from the transmitting antenna to the surface point $\vec{r}$ and from the surface point $\vec{r}$ to the receiving antenna, respectively. $\dot{G}_k(t,\vec{r})$, $\dot{G}_i(t,\vec{r})$ are the complex functions which take into account the influence of the directivity diagram of the transmitting and receiving antennas. $\dot{F}_{ik}[t,\vec{r},\vec{\lambda}(\vec{r})]$ is the complex reflection coefficient of the element $\vec{r}$, depending on its electrophysical parameters $\vec{\lambda}(\vec{r})$ for the bistatic pair ik. $\dot{S}_{0k}(t)\exp(j\omega_{0k}t)$ is the signal emitted by the kth satellite, and $\omega_{0k}=2\pi f_{0k}$ is the carrier frequency of the emitted signal of the kth transmitter. Further, $\tau_k(t,\vec{r})$ and $\tau_i(t,\vec{r})$ is the delay time associated with the signal path from the transmitting antenna to the surface point with coordinates $\vec{r}$ and from the surface point to the receiving antenna, respectively.

For practical calculations of the reference functions in synthesizing the aperture in bistatic SAR, the change of the functions $\dot{G}(t,\vec{r})$ and $\dot{K}(t,\vec{r})$ for the time of pulse propagation can reasonably be neglected. The function $\dot{F}[t,\vec{\lambda}(t,\vec{r})]=\dot{F}[\vec{r},\vec{\lambda}(\vec{r})]$ will be considered constant over the observation interval. As a result, the signal $S_{Dik}(t)$ reflected from the probed surface D will be a real part of the limit value of the sum of signals reflected from its individual elements $\dot{S}_{ik}(t,\vec{r})$:

$$\begin{aligned}S_{Dik}(t) &= \\ &= \mathrm{Re}\int_D \dot{F}_{ik}[\vec{r},\vec{\lambda}(\vec{r})]\dot{K}_{ik}[t,\vec{r}]\dot{G}_{ik}[t,\vec{r}]\dot{S}_{0k}[t-\tau_{ik}(t,\vec{r})]\times \\ &\times \exp\{j\omega_{0k}[t-\tau_{ik}(t,\vec{r})]\}d\vec{r},\end{aligned} \quad (2)$$

where, for the convenience of perception, the products of the functions depending on the transmitter and receiver parameters are combined into one function with indices $(\cdot)_{ik}$.

Although reflection occurs from all surface elements for which the traces of the directivity diagrams of the transmitting and receiving antennas intersect, the greatest contribution will be made by components near the point of specular reflection [20].

A particular feature of the processing mode (2) is the determination of the difference of course between the direct and reflected signal. The processing of the direct GNSS signal and the signal reflected from the mirror area enables not only the surface parameters to be estimated, but also the current height of the geoid at this point to be calculated. The number of such mirror reflection points coincides with the number of visible GNSS satellites. The points themselves move in space with the mutual movement of the transmitter and receiver relative to the underlying surface.

Both foreign and Russian researchers [21–23] have demonstrated the possibility of resolving the task of

altitude measurement. The use of high-precision GNSS ephemerides allows us to resolve the task of altimetry with a high level of accuracy. For example, the motion parameters of the center of mass of the GLONASS GNSS satellites are determined with errors (at a probability level of 0.997) of no more than 0.5 m along the orbit, 0.2 m along the binormal to the orbit, and 0.1 m along the radius-vector.[9]

2. OPTIMAL SIGNAL PROCESSING IN BISTATIC SPACEBORNE RADAR SYSTEM

Without a loss of generality of the results, let us assume that the useful signal emitted by the navigation satellite, reflected from the Earth's surface and received on board the nanosatellite $\mathrm{Re}\,\dot{S}_{Dik}(t)$, is observed against the background of additive normal white noise $n_{ik}(t)$. The statistical characteristics thereof can be assumed to be the same for all pairs *i*th receiver–*k*th transmitter:

$$u_{ik}(t) = \mathrm{Re}\,\dot{S}_{Dik}(t) + n_{ik}(t). \tag{3}$$

Optimal estimates of surface $\vec{\lambda}(\vec{r})$ parameters contained in the reflected signal, for functionally-deterministic surface models can be found in the framework of the maximum likelihood method by means of the maximum of the functional:

$$p\left[u_{ik}(t) / \dot{F}_{ik}[\vec{r},\vec{\lambda}(\vec{r})]\right] = \\ = C\exp\left\{-\frac{1}{N_{0_{ik}}}\int_0^T [u_{ik}(t) - \mathrm{Re}\int_D \dot{F}_{ik}[\vec{r},\vec{\lambda}(\vec{r})]\dot{S}_{ik}(t,\vec{r})d\vec{r}]^2 dt\right\}, \tag{4}$$

where $N_{0_{ik}}$ is the additive noise power spectral density, T is the observation interval (aperture synthesis), C is the normalizing multiplier.

Let one of the parameters $\lambda(\vec{r})$ be estimated, if there is no a priori information about it or if it is distributed with maximum entropy (uniformly in the area Λ, $\lambda \in \Lambda$), then the optimal estimates are to be found from the solution of the variational equation $\frac{\delta\left\{p[u_{ik}(t) / \dot{F}_{ik}[\vec{r},\lambda(\vec{r})]]\right\}}{\delta\lambda(\vec{r})} = 0$. The variational equation occurs due to the fact that it is not a constant value of the parameter estimated, but a function of spatial coordinates $\dot{F}_{ik}[\vec{r},\lambda(\vec{r})]$.

After a number of calculations, the solution of Eq. (4), which defines the principle of aperture synthesis in bistatic radar system, can be written in compact form as follows:

$$\dot{Y}_{ik}(\vec{r}) = \int_0^T u_{ik}(t)\dot{S}^*_{ik}(t,\vec{r})dt = \\ = \int_D \dot{F}_{ik}[\vec{r},\vec{\lambda}(\vec{r})]\dot{\Psi}_{ik}(\vec{r},\vec{r}_1)d\vec{r}_1, \tag{5}$$

where $\dot{Y}_{ik}(\vec{r}) = \int_0^T u_{ik}(t)\dot{S}^*_{ik}(t,\vec{r})dt$ is the optimal output effect in a given bistatic pair, $\dot{\Psi}_{ik}(\vec{r},\vec{r}_1) = \int_0^T \dot{S}_{ik}(t,\vec{r})\dot{S}^*_{ik}(t,\vec{r}_1)dt$ is the spatial uncertainty function of bistatic SAR.

Processing result (5) is a radar image of the surface which contains information about its electrophysical parameters.

The formation of independent estimates for all bistatic pairs allows us to obtain $N = N_{\mathrm{KA}}N_{\mathrm{S}}$ measurements (4), wherein N_{KA} is the number of visible GNSS SC, N_{S} is the number of emitted (quasi)-orthogonal signals. For GNSS GLONASS[10] the signals L1OF, L1OC (L1OCd и L1OCp), L2q (L2OCd, L2OCp), L2OF, L3OC (L3OCd и L3OCp) at visibility of 10 navigation satellites enable us to obtain 80 values of $\dot{Y}_{ik}(\vec{r})$ (see the table).

As a result of processing (5), the output will be an additive mixture of four components:

- signal part for a specific signal of a given transmitter $\dot{S}_{ik}(t,\vec{r})$

$$\dot{Y}_{S_{ik}}(\vec{r}) = \int_D \dot{F}_{ik}[\vec{r},\vec{\lambda}(\vec{r})]\dot{\Psi}_{ik}(\vec{r},\vec{r}_1)d\vec{r}_1; \tag{6}$$

- noise component

$$\dot{Y}n_{ik}(\vec{r}) = \int_0^T n_{ik}(t)\dot{S}^*_{ik}(t,\vec{r})dt; \tag{7}$$

- interference component for the same satellite emitting M signals $\dot{S}^*_{imk}(t,\vec{r}_1)$ which do not coincide with $\dot{S}_{ik}(t,\vec{r})$:

$$\dot{Y}_{IS_{ik}}(\vec{r}) = \\ = \sum_{m=1\ldots M}\int_D \dot{F}_{ik}[\vec{r},\vec{\lambda}(\vec{r})]\int_0^T \dot{S}_{ik}(t,\vec{r})\dot{S}^*_{imk}(t,\vec{r}_1)dtd\vec{r}_1; \tag{8}$$

- inter-satellite interference component caused by the reception of signals from other GNSS satellites irradiating the D surface area:

[9] http://www.glonass-svoevp.ru/index.php?lang=ru (in Russ.). Accessed March 20, 2024.

[10] https://russianspacesystems.ru/bussines/navigation/glonass/interfeysnyy-kontrolnyy-dokument/ (in Russ.). Accessed March 20, 2024.

Table. Characteristics of GLONASS signals. *I* and *Q* are in-phase and quadrature components of the signal, respectively

Carrier frequency f_0, MHz	1602 + 0.5625k $k = -7 \ldots +6$		1600.995			1248.06			1246 + 0.4375k $k = -7 \ldots +6$		1202.025	
I/Q	Q	I	Q		I	Q		I	Q	I	Q	I
Type	L1OF (L1 CT)	L1SF (Ll BT)	L1OC [L1OCd]	L1OC [LOCp]	L1SC	L2q (L2OC) [L2KCИ (L2OCd)]	L2q (L2OC) [L2OCp]	L2SC	L2OF (L2 CT)	L2SF (L2 BT)	L3OC [L3OCp	L3OC [L3OCd]]
Strip, MHz	1.022	–	2.046	4.092	–	2.046	4.092	–	1.022	–	20.46	20.46
Average signal power $\bar{A}$, dBW	−161	–	−161.5	−161.5	–	−161.5	−161.5	–	−161	–	−101.5	−101.5

$$\dot{Y}_{in_{ik}}(\vec{r}) = \sum_{n=1\ldots N} \int_D \dot{F}_{ik}[\vec{r},\vec{\lambda}(\vec{r})] \int_0^T \dot{S}_{ik}(t,\vec{r})\dot{S}^*_{in}(t,\vec{r}_1)dtd\vec{r}_1. \quad (9)$$

The study of the influence of quasi-orthogonal signals, including the different trajectories of GNSS satellite motion, can be performed both numerically and experimentally. The experiment enables the statistical characteristics of noise and interference components to be estimated when comparing the effects at the correlator output obtained in an anechoic chamber for a single simulated GNSS satellite signal and the same effects when working on the signals of real GNSS satellites. Such an experiment, conducted at the All-Russian Research Institute of Physical-Technical and Radio-Technical Measurements[11] [24], showed that, in accordance with the law of large numbers, the combined effect (8)–(9) can be approximated by a normal random process. Consequently, these components can be accounted for using the simplified model (3) with a 1–2 dB increase in noise level.

3. ENERGY POTENTIAL OF BISTATIC SAR WITH THE RECEPTION OF REFLECTED GNSS SIGNALS

When calculating the energy parameters, we will assume that the receiver of the multi-position SAR performs optimal processing—matched filtering in accordance with (5). Then at the output of the processing system, two components will be formed: signal $\dot{Q}_s$ and noise $\dot{Q}_n$ components.

[11] https://www.vniiftri.ru/ (in Russ.). Accessed March 20, 2024.

Let us write down the power of the signal component P_s in the following form:

$$P_s = \frac{\lambda^2}{(4\pi)^3} \cdot \frac{P_{av} G_T}{R_1^2} \cdot \frac{G_R T_{Rs}}{R_2^2} \sigma^o \Delta s, \quad (10)$$

where P_{av} is the average power of the signal emitted by the transmitter. T_{Rs} is the time of receiver synthesis. R_1, R_2 is the distance from the reflecting point to the transmitter and receiver, respectively. G_T, G_R are the gain coefficients of the transmitting and receiving antenna, respectively, σ^o is the specific effective scattering area (SESA) of the surface, Δs is the resolution area size on the probed surface.

When surface specular reflection is used, the trace on the surface of the spatial uncertainty function of the navigation signal $\dot{\Psi}_{ik}(\vec{r},\vec{r}_1)$ should be used as the size of the area.

The noise component of the output effect (4) $\dot{Q}_n$ is determined by the interference power spectral density at the receiver input N_0:

$$N_0 = t_A k T_0, \quad (11)$$

where t_A is the relative noise temperature of the antenna, $k = 1.38 \cdot 10^{-23}$ J/K is the Boltzmann constant, T_0 is the antenna temperature.

In Eq. (10), the main parameters are determined by the observation geometry and the characteristics of the transmitters, i.e. the navigation satellites. Additionally, the specific effective surface scattering surface needs to be defined.

The mathematical model of reflection from the agitated sea surface is based on the two-scale surface model [25]. In order to describe the reflection of the navigation signal from the sea surface, the BA-PTSM

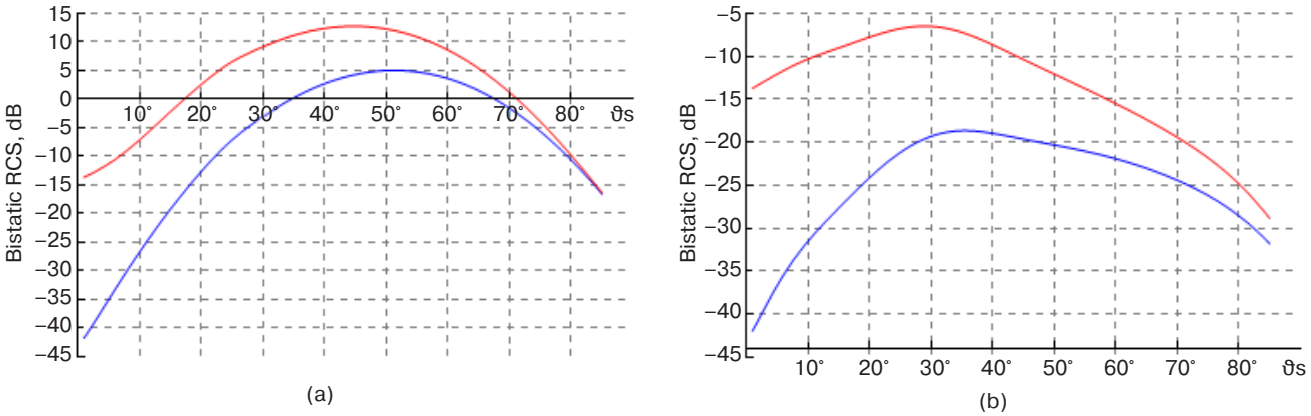

Fig. 2. Dependence of the SESA value at reception of the reflected signal with right circular polarization (red line) and left circular polarization (blue line) on the vertical scattering angle ϑs for the signal with frequency 1.58 GHz at the coinciding vertical projection of bistatic observation angle 45° and horizontal projection of bistatic angle 0° (a) and 30° (b) [26]

model [26] is proposed. This model takes into account the polarization of the signals and at the same time provides higher calculation speed while matching the results with the two-scale model. For this model, the results of calculating the SESA for the circular polarization of the GNSS satellite signal are shown in Fig. 2.

Experimentally obtained data can be used to estimate the energy parameters (Figs. 3 and 4).

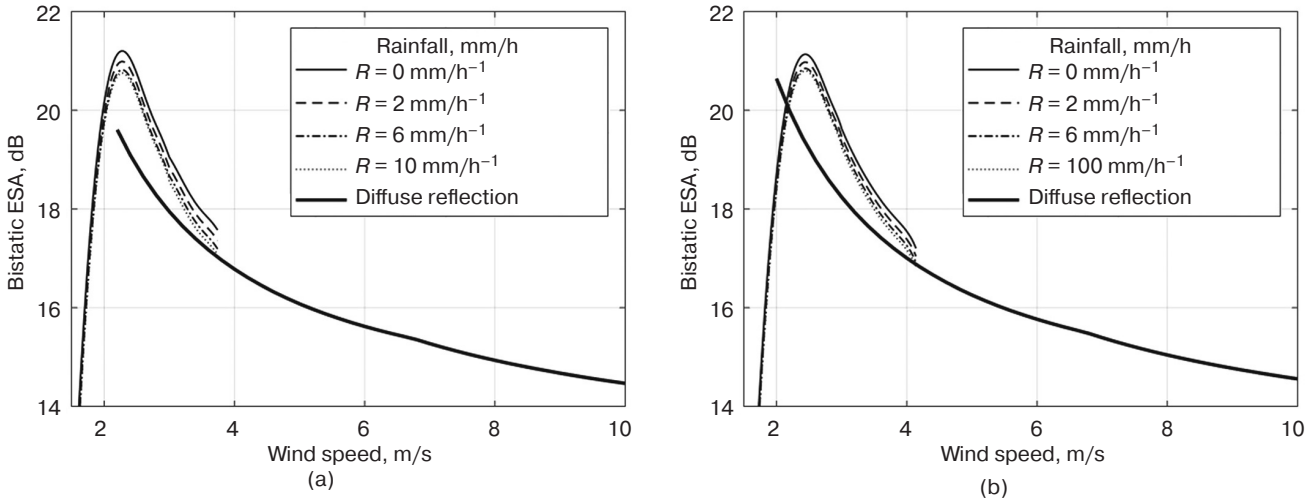

Fig. 3. Dependence of bistatic ESA of GPS[12] L1 signal for sea surface on the driving wind speed at different precipitation level *R* for the horizontal projection of bistatic angle 0° (a) and 30° (b), according to data [27]

The results of calculation (9) using data from [28] show that using an antenna with a gain of 14 dBi, it is possible to provide a signal-to-noise ratio of 4 dB for an accumulation time of 1 ms in regions up to 10° relative to the mirror reflection region. The results obtained are close to those obtained experimentally at wind speeds less than 5 m/s [29] (Fig. 5).

The optimum aperture synthesis time is limited by two factors. On the one hand, the signal accumulation needs to be achieved with a level sufficient to ensure the required accuracy of estimates of surface parameters and geoid height (at least 10 ms). On the other hand, the surface parameters should not change significantly during the synthesis time, in order that the complex reflection coefficient in Eq. (3) does not become a function of time. When placed on an ultra-small cubesat[13], the antenna gain will be no more than 10–16 dBi (size of the antenna corresponds to one face of the 3U-6U spacecraft), unless a design with an unfolding antenna is used, i.e. as on the SPIRE spacecraft. Taking into account the possibility of co-processing over visible satellites which may produce an additional 4–7 dB increase in signal-to-noise ratio, the aperture synthesis time can be reduced to 100 ms. This will greatly simplify the implementation of aperture synthesis on board.

[12] https://www.gps.gov/. Accessed March 20, 2024.
[13] https://www.nasa.gov/wp-content/uploads/2018/01/cubesatdesignspecificationrev14_12022-02-09.pdf. Accessed March 20, 2024.

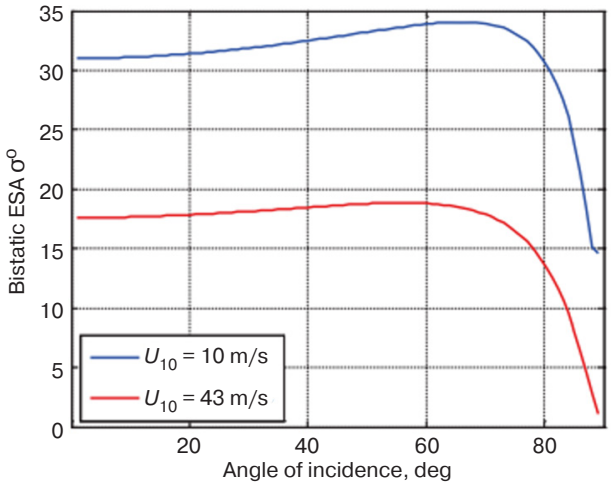

Fig. 4. Dependence of the bistatic ESA of the GPS L1 signal for the sea surface in the specular reflection region on the scattering angle for two driving wind speeds U_{10}, according to σ° [26][14]

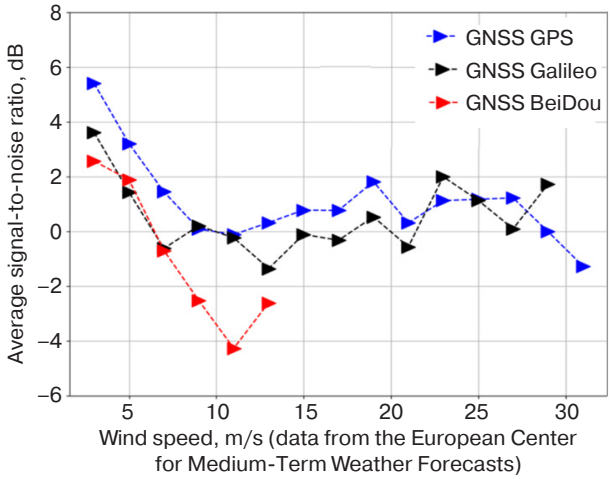

Fig. 5. Average values of signal-to-noise ratio at different wind speeds (for GNSS GPS, Galileo[15], BeiDou[16]) [29]

4. STRUCTURE OF ON-BOARD BISTATIC RADAR SYSTEM

For correct signal processing, the on-board radar must contain (Fig. 6):

- antenna system to receive the direct GNSS signal needed to form the reference signal (standard navigation antenna);
- antenna system for signal reception with left circular polarization, polarization separation not worse than 20 dB, gain not less than 10 dBi;
- software-defined receiver;
- standard spaceborne GNSS receiver with the ability to provide coordinate information for spacecraft position control. This information is used in the correlator to form reference functions, which will significantly reduce the requirements for onboard processing;
- data transmission channel with data storage device for data transmission to ground stations.

In order to increase signal-to-noise ratio, a patch antenna can reasonably be used. The size of the proposed antenna is larger than that used in CYGNSS (6 patch elements). The elements are arranged in a mosaic, but they can also be arranged in parallel, as in foreign GNSS-R, and thus reduce the size of the antenna on the satellite (Fig. 7).

[14] *Cyclone global navigation satellite system* (*CYGNSS*). Algorithm Theoretical Basis DocumentLevel 2 Wind Speed Retrieval. https://cygnss.engin.umich.edu/wp-content/uploads/sites/534/2021/07/148-0138-ATBD-L2-Wind-Speed-Retrieval-R6_release.pdf. Accessed March 20, 2024.

[15] https://galileognss.eu/. Accessed March 20, 2024.

[16] https://glonass-iac.ru/guide/gnss/beidou.php (in Russ.). Accessed March 20, 2024.

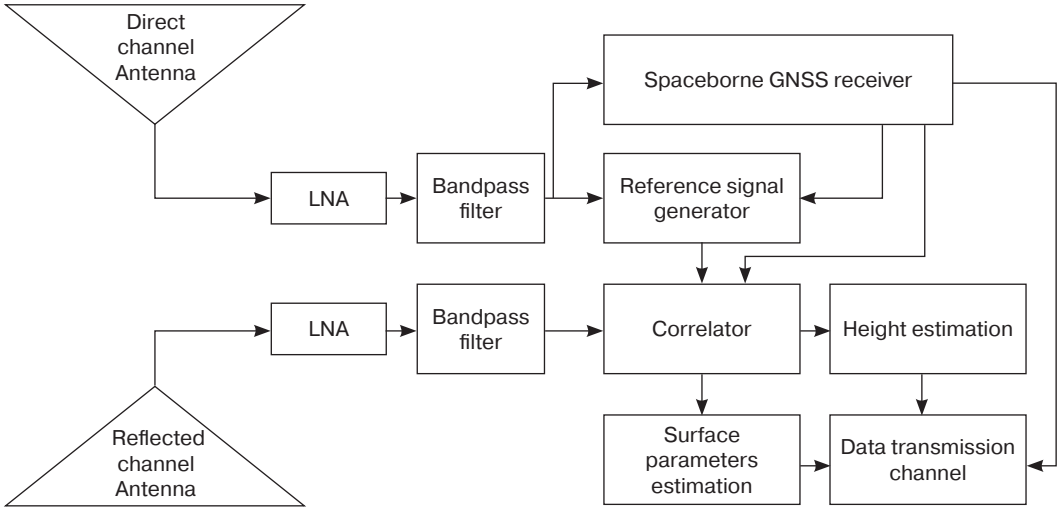

Fig. 6. Proposed structure of bistatic radar operating on GNSS signals reflected from the surface. LNA—low noise amplifier

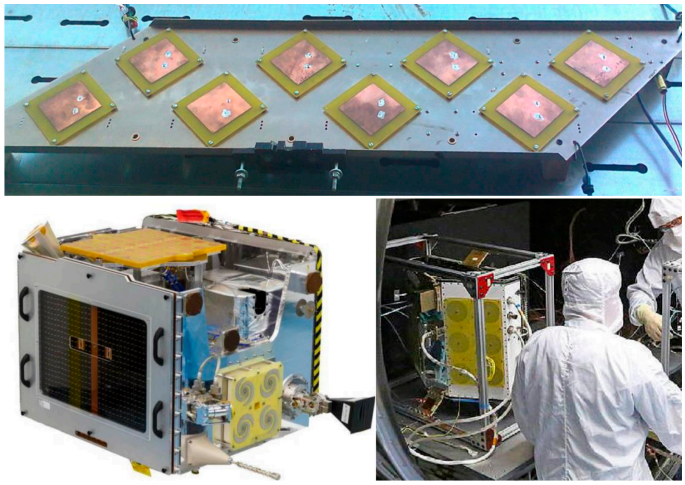

Fig. 7. Proposed patch antenna array model (top) [14], TDS-1 satellite antenna (bottom left) [11] and CYGNSS (bottom right)[17] [28]

It is advisable to have two antennas for receivers on spacecraft. They are directed to the left and right of the sub-satellite point at an angle of 30° relative to the vertical, in order to enable signals to be processed to the left and right of the track of the receiving spacecraft. In this case, the scheme in Fig. 6 adds one more receiving channel of the GNSS signal reflected from the surface.

5. WAYS TO INCREASE THE ENERGY POTENTIAL OF BISTATIC SAR

The main disadvantage of non-radiating radar is that the power of the transmitters is relatively low. In CYGNSS, the simplest method of providing the required power is to process the signal in the mirror reflection region. This provides a 15–30 dB increase in signal strength relative to other regions. The size of the region which makes the main contribution to the reflected signal depends not only on the observation geometry, but also on the characteristics of the underlying surface (Fig. 8) [30]. Sea ice, lake surface and swampy terrain are characterized by a small reflection area in the delay–Doppler shift coordinates due to specular reflection. Vegetation cover and open sea are characterized by a wide reflection area. Consequently, information about the type of reflecting surface is contained not only in the absolute value of the reflected signal power, but also in its distribution in the delay–Doppler shift coordinates. This makes it possible for new methods to be created for analyzing radar images to determine the water-ice situation.

[17] https://www.eoportal.org/satellite-missions/techdemosat-1#spacecraft. Accessed March 20, 2024.

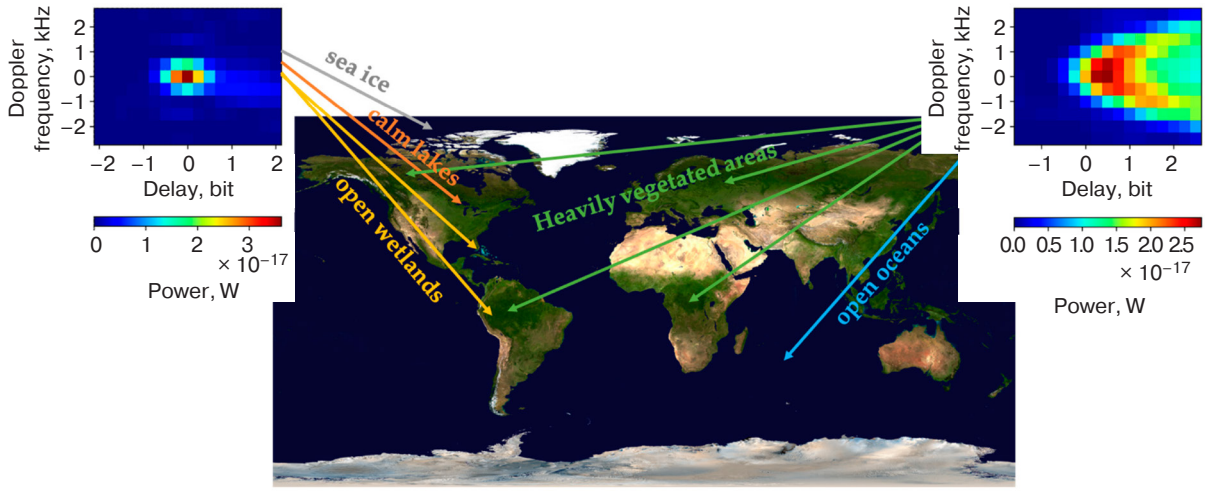

Fig. 8. Two example images in delay–Doppler shift coordinates for two different types of surfaces [30]

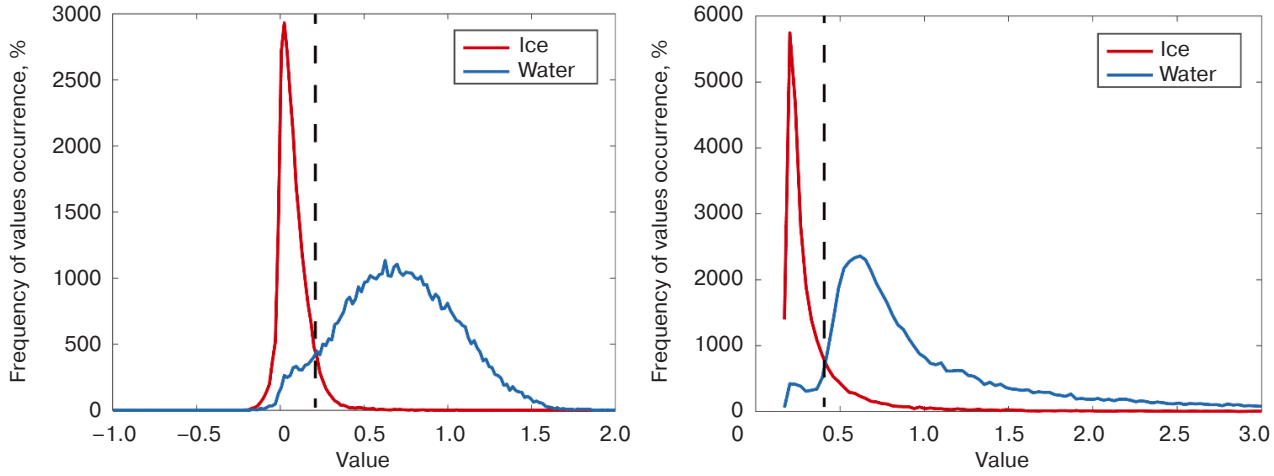

Fig. 9. Histograms of reflection power distribution in the range–Doppler shift coordinates (left) and the leading edge of the reflected pulse (right)

Another indication of distinguishing the GNSS signal reflected from water and ice can be a histogram of the level of the reflected signal from the type of surface (Fig. 9) [31].

The synthesis of the optimal co-processing algorithm is performed by taking into account the electrodynamic models of the surface when it is observed at different angles and at different carrier frequencies [32].

In order to increase the signal-to-noise ratio, required in order to improve the quality of estimates, we propose the use of coherent signal accumulation (in the mode of synthesizing the antenna aperture). This will make it possible to observe and equalize the spatial resolution in the range and azimuthal directions in a wide range of angles.

Additional opportunities are provided by receiving the signals of all visible GNSS satellites, their separate processing (aperture synthesis) and subsequent aggregation of measurements at the stage of secondary processing (estimation of surface parameters, object detection and radar imaging).

In contrast to the methods of processing the reflected GNSS signals described in the literature, signals at all carrier frequencies need to be processed. This makes it possible to generate independent data on the surface reflectivity and correct ionospheric distortions. This is particularly important when determining the geoid height for a sub-satellite point or a specular reflection point.

CONCLUSIONS

The study analyzed systems of remote sensing of the Earth surface by reflected signals of navigation satellites. It also showed that foreign constellations of such satellites operate in orbit, thus resolving the tasks of determining the parameters of the water surface and soil. Data from these satellites is publicly available and can be analyzed. Taking into account the limited capabilities for creating meteorological satellite constellations, satellites for water surface monitoring and geoid height determination, based

on reception of reflected signals of satellite navigation systems, enable a number of important scientific and practical tasks to be resolved. This paper presents an algorithm for the optimal processing of reflected signals of navigation systems, and takes into account the particular features of GNSS satellite operation, including the presence of interference component. The numerically calculated values of the energy potential of bistatic SAR for circular polarization signals coincide with the experimental values given in foreign literature.

The study proposes a choice of aperture synthesis time of the order of 100 ms. This takes into account the constancy of the reflecting surface parameters. A further increase of signal-to-noise ratio can be achieved by means of joint processing over the whole visible constellation.

The paper also proposes a structure of onboard bistatic radar, which, unlike known analogs, uses a navigation receiver to form a reference signal. The use of delays and Doppler frequency shifts calculated in the navigation equipment allows us to simplify the signal correlator. This also enables the load on the software-defined receiver to be reduced while maintaining the required quality of estimates.

ACKNOWLEDGMENTS

The study was financially supported by the Russian Science Foundation, grant No. 23-67-10007.

Authors' contributions

A.V. Ksendzuk—developing aims and objectives, theoretical background, processing methods, and energy potential.

V.F. Fateev—the research idea, developing the structure of on-board bistatic radar system, and formulating the conclusions.

REFERENCES

1. Krieger G., Moreira A., Fiedler H., et al. TanDEM-X: A satellite formation for high-resolution SAR interferometry. *IEEE Trans. Geosci. Remote Sens*. 2007;45(11):3317–3341. https://doi.org/10.1109/TGRS.2007.900693
2. Hall C.D., Cordey R.A. Multistatic scatterometry. In: *International Geoscience and Remote Sensing Symposium, 'Remote Sensing: Moving Toward the 21st Century'*. IEEE. 1988. V. 1. P. 561–562. https://doi.org/10.1109/IGARSS.1988.570200
3. Cardellach E., Fabra F., Nogués-Correig O., et al. GNSS-R ground-based and airborne campaigns for ocean, land, ice, and snow techniques: Application to the GOLD-RTR data sets. *Radio Sci*. 2011;46(6):RS0C04. http://doi.org/10.1029/2011RS004683
4. Martin-Neira M. A passive reflectometry and interferometry system (PARIS): Application to ocean altimetry. *ESA J*. 1993;17(4):331–355.
5. Ksendzuk A.V. Use of GLONASS/GPS satellite navigation systems for remote surface sensing. *Elektromagnitnye volny i elektronnye sistemy = Electromagnetic Waves and Electronic Systems*. 2003;8(5):8–15 (in Russ.).
6. Fateev V.F., Sakhno I.V. Application of navigating space vehicles GPS/GLONASS in structure multi-position radar the review of a terrestrial surface. *Izvestiya vysshikh uchebnykh zavedenii. Priborostroenie = J. Instrument Eng.* 2004;47(3):27–30 (in Russ.).
7. Fateev V.F., Sakhno I.V. *Method for Producing Radiolocation Image of Earth Surface by Means of Using Multi-Positional Radiolocation System with Synthesized Aperture of Antenna*: RF Pat. 2278398. Publ. 20.06.2006 (in Russ.).
8. Fateev V.F., Ksendzuk A.V. *Ground-Space Radar System*: RF Pat. 113022. Publ. 27.01.2012 (in Russ.).
9. Baholdin V.S., Gavril D.A., Shaldaev A.V. Algorithms of pattern SAR images of the Earth surface with the use of GLONASS signals. *Izvestiya vysshikh uchebnykh zavedenii. Priborostroenie = J. Instrument Eng.* 2012;55(9):24–29 (in Russ.).
10. Ksendzuk A.V., Fateev V.F., Gerasimov P.A., Novikov V.A. Multiposition radar coprocessing techniques. Experimental results. In: *Radar Research of Natural Environments*: *Proceedings of the 28th All-Russian Symposium*. St. Petersburg: Mozhaisky Military Space Academy. 2013;10(2):218–222 (in Russ.).
11. Di Simone A., Park H., Riccio D., Camps A. Sea target detection using spaceborne GNSS-R delay-Doppler maps: Theory and experimental proof of concept using TDS-1 data. *IEEE Journal of Selected Topics in Applied Earth Observations and Remote Sensing*. 2017;10(9):4237–4255. https://doi.org/10.1109/JSTARS.2017.2705350
12. Hu C., Benson C.R., Park H., et al. Detecting targets above the Earth's surface using GNSS-R delay Doppler maps: Results from TDS-1. *Remote Sens*. 2019;11(19):2327. https://doi.org/10.3390/rs11192327
13. Fateev V.F., Ksendzuk A.V., Obukhov P.S., et al. Multi-position non-radiating SAR with GNSS GLONASS transmitters. *Elektromagnitnye volny i elektronnye sistemy = Electromagnetic Waves and Electronic Systems*. 2012;17(5):62–68 (in Russ.).
14. Fateev V.F., Ksendzuk A.V., Obukhov P.S., et al. Experimental bistatic radar complex. *Elektromagnitnye volny i elektronnye sistemy = Electromagnetic Waves and Electronic Systems*. 2012;17(5):58–61 (in Russ.).
15. Freeman V., Masters D., Jales P., et al. Earth Surface Monitoring with Spire's New GNSS Reflectometry (GNSS-R) CubeSats. In: *22nd EGU General Assembly Conference Abstracts*. 2020. id. 13766. https://doi.org/10.5194/egusphere-egu2020-13766
16. Camps A., Golkar A., Gutierrez A., et al. Fsscat, the 2017 Copernicus Masters' "Esa Sentinel Small Satellite Challenge" Winner: A federated polar and soil moisture tandem mission based on 6U Cubesats. In: *IGARSS 2018 IEEE International Geoscience and Remote Sensing Symposium.* IEEE; 2018. P. 8285–8287. https://doi.org/10.1109/IGARSS.2018.8518405
17. Jing C., Niu X., Duan C., et al. Sea surface wind speed retrieval from the first Chinese GNSS-R mission: Technique and preliminary results. *Remote Sens*. 2019;11(24):3013. https://doi.org/10.3390/rs11243013

18. Unwin M., Rawinson J., King L., et al. GNSS-reflectometry activities on the DoT-1 microsatellite in preparation for the hydrognss mission. In: *2021 IEEE International Geoscience and Remote Sensing Symposium IGARSS*. IEEE; 2021. P. 1288–1290. https://doi.org/10.1109/IGARSS47720.2021.9554352
19. Xia J., Bai W., Sun Y., et al. Calibration and wind speed retrieval for the Fengyun-3 E Meteorological Satellite GNSS-R Mission. In: *2021 IEEE Specialist Meeting on Reflectometry using GNSS and other Signals of Opportunity* (*GNSS+R*). IEEE; 2021. P. 25–28. https://doi.org/10.1109/GNSSR53802.2021.9617699
20. Cheng Z., Jin T., Chang X., et al. Evaluation of spaceborne GNSS-R based sea surface altimetry using multiple constellation signals. *Front. Earth Sci*. 2023;10:1079255. https://doi.org/10.3389/feart.2022.1079255
21. Munoz-Martin J.F., Portero A.P., Camps A., et al. Snow and ice thickness retrievals using GNSS-R: Preliminary results of the MOSAiC experiment. *Remote Sens*. 2020;12(24):4038. https://doi.org/10.3390/rs12244038
22. Nogués O.C., Munoz-Martin J.F., Park H., et al. Improved GNSS-R altimetry methods: Theory and experimental demonstration using airborne dual frequency data from the microwave interferometric reflectometer (MIR). *Remote Sens*. 2021;13(20):4186. https://doi.org/10.3390/rs13204186
23. Fateev V.F., Lopatin V.P. Space bistatic radar to monitor the ocean surface profile based on GNSS signals. *Izvestiya vysshikh uchebnykh zavedenii. Priborostroenie = J. Instrument Eng.* 2019;62(5):484–491 (in Russ.). https://doi.org/10.17586/0021-3454-2019-62-5-484-491
24. Lopatin V.P., Fateev V.F. Study of a bistatic radiolocation system on the basis of GPS/GLONASS signals in echo-free camera. *Proceedings of the Mozhaisky Military Aerospace Academy*. 2019;670:64–68 (in Russ.).
25. Volosyuk V.K., Kravchenko V.F. *Statisticheskaya teoriya radiotekhnicheskikh sistem distantsionnogo zondirovaniya i radiolokatsii* (*Statistical Theory of Radio-engineering Systems of Remote Sensing and Radiolocation*). Moscow: Fizmatlit; 2008. 351 p. (in Russ.).
26. Di Martino G., Di Simone A., Iodice A., Riccio D. Bistatic scattering from anisotropic rough surfaces via a closed-form two-scale model. *IEEE Trans. Geosci. Remote Sens*. 2020;59(5):3656–3671. https://doi.org/10.1109/TGRS.2020.3021784
27. Asgarimehr M., Zavorotny V.U., Wickert J., Reich S. Can GNSS reflectometry detect precipitation over oceans? *Geophys. Res. Lett.* 2018;45(22):12,585–12,592. https://doi.org/10.1029/2018GL079708
28. Gleason S., Ruf C.S., O'Brien A.J., McKague D.S. The CYGNSS Level 1 calibration algorithm and error analysis based on on-orbit measurements. *IEEE Journal of Selected Topics in Applied Earth Observations and Remote Sensing*. 2019;12(1):37–49. https://doi.org/10.1109/JSTARS.2018.2832981
29. Nan Y., Ye S., Liu J., et al. Signal-to-noise ratio analyses of spaceborne GNSS-reflectometry from Galileo and BeiDou satellites. *Remote Sens*. 2022;14(1):35. https://doi.org/10.3390/rs14010035
30. Rodriguez-Alvarez N., Munoz-Martin J.F., Morris M. Latest Advances in the Global Navigation Satellite System—Reflectometry (GNSS-R) Field. *Remote Sens*. 2023;15(8):2157. https://doi.org/10.3390/rs15082157
31. Cartwright J., Banks Ch.J., Srokosz M. Sea Ice Detection Using GNSS-R Data From TechDemoSat-1. *JGR Oceans*. 2019. V. 124. Iss. 8. P. 5801–5810. https://doi.org/10.1029/2019JC015327
32. Potapov A.A., Kuznetsov V.A., Alikulov E.A. Methods for Complexing Images Formed by Multi-Band Synthetic Aperture Radars. *Izvestiya vysshikh uchebnykh zavedenii Rossii. Radioelektronika = Journal of the Russian Universities. Radioelectronics*. 2021;24(3):6–21 (in Russ.). https://doi.org/10.32603/1993-8985-2021-24-3-6-21

СПИСОК ЛИТЕРАТУРЫ

1. Krieger G., Moreira A., Fiedler H., et al. TanDEM-X: A satellite formation for high-resolution SAR interferometry. *IEEE Trans. Geosci. Remote Sens*. 2007;45(11):3317–3341. https://doi.org/10.1109/TGRS.2007.900693
2. Hall C.D., Cordey R.A. Multistatic scatterometry. In: *International Geoscience and Remote Sensing Symposium, 'Remote Sensing: Moving Toward the 21st Century'*. IEEE. 1988. V. 1. P. 561–562. https://doi.org/10.1109/IGARSS.1988.570200
3. Cardellach E., Fabra F., Nogués-Correig O., et al. GNSS-R ground-based and airborne campaigns for ocean, land, ice, and snow techniques: Application to the GOLD-RTR data sets. *Radio Sci*. 2011;46(6):RS0C04. http://doi.org/10.1029/2011RS004683
4. Martin-Neira M. A passive reflectometry and interferometry system (PARIS): Application to ocean altimetry. *ESA J*. 1993;17(4):331–355.
5. Ксендзук А.В. Использование спутниковых навигационных систем ГЛОНАСС/GPS для дистанционного зондирования поверхности. *Электромагнитные волны и электронные системы.* 2003;8(5):8–15.
6. Фатеев В.Ф., Сахно И.В. Применение навигационных КА GPS/ГЛОНАСС в составе многопозиционных РЛС обзора земной поверхности. *Известия высших учебных заведений. Приборостроение.* 2004;47(3):27–30.
7. Фатеев В.Ф., Сахно И.В. *Способ получения радиолокационного изображения земной поверхности при помощи многопозиционной радиолокационной системы с синтезированной апертурой антенны*: пат. № 2278398 РФ. Заявка № 2004121076/092006; заявл. 06.07.2004; опубл. 20.06.2006.
8. Фатеев В.Ф., Ксендзук А.В. *Наземно-космическая радиолокационная система*: пат. № 113022 РФ. Заявка № 2010154058/07; заявл. 29.12.20104; опубл. 27.01.2012.
9. Бахолдин В.С., Гаврил Д.А., Шалдаев А.В. Алгоритмы формирования радиолокационных изображений земной поверхности при использовании сигналов ГЛОНАСС. *Известия высших учебных заведений. Приборостроение*. 2012;55(9):24–29.

10. Ксендзук А.В., Фатеев В.Ф., Герасимов П.А., Новиков В.А. Совместная обработка в многопозиционных РСА. Результаты экспериментальных исследований. В сб.: *Радиолокационное исследование природных сред: труды XXVIII Всероссийского симпозиума*. СПб.: ВКА имени А.Ф. Можайского. 2013;10(2):218–222.
11. Di Simone A., Park H., Riccio D., Camps A. Sea target detection using spaceborne GNSS-R delay-Doppler maps: Theory and experimental proof of concept using TDS-1 data. *IEEE Journal of Selected Topics in Applied Earth Observations and Remote Sensing*. 2017;10(9):4237–4255. https://doi.org/10.1109/JSTARS.2017.2705350
12. Hu C., Benson C.R., Park H., et al. Detecting targets above the Earth's surface using GNSS-R delay Doppler maps: Results from TDS-1. *Remote Sens*. 2019;11(19):2327. https://doi.org/10.3390/rs11192327
13. Фатеев В.Ф., Ксендзук А.В., Обухов П.С., Крапивкин Г.И., Тимошенко Г.В., Король Г.Н., Фатеев О.В., Новиков В.А., Герасимов П.А., Шахалов К.С. Многопозиционная радиолокационная система с синтезированием апертуры антенны по отраженным сигналам ГНСС «ГЛОНАСС». *Электромагнитные волны и электронные системы*. 2012;17(5):62–68.
14. Фатеев В.Ф., Ксендзук А.В., Обухов П.С., Крапивкин Г.И., Тимошенко Г.В., Король Г.Н., Новиков В.А., Герасимов П.А., Шахалов К.С. Экспериментальный бистатический радиолокационный комплекс. *Электромагнитные волны и электронные системы*. 2012;17(5):58–61.
15. Freeman V., Masters D., Jales P., et al. Earth Surface Monitoring with Spire's New GNSS Reflectometry (GNSS-R) CubeSats. In: *22nd EGU General Assembly Conference Abstracts*. 2020. id. 13766. https://doi.org/10.5194/egusphere-egu2020-13766
16. Camps A., Golkar A., Gutierrez A., et al. Fsscat, the 2017 Copernicus Masters' "Esa Sentinel Small Satellite Challenge" Winner: A federated polar and soil moisture tandem mission based on 6U Cubesats. In: *IGARSS 2018 IEEE International Geoscience and Remote Sensing Symposium.* IEEE; 2018. P. 8285–8287. https://doi.org/10.1109/IGARSS.2018.8518405
17. Jing C., Niu X., Duan C., et al. Sea surface wind speed retrieval from the first Chinese GNSS-R mission: Technique and preliminary results. *Remote Sens*. 2019;11(24):3013. https://doi.org/10.3390/rs11243013
18. Unwin M., Rawinson J., King L., et al. GNSS-reflectometry activities on the DoT-1 microsatellite in preparation for the hydrognss mission. In: *2021 IEEE International Geoscience and Remote Sensing Symposium IGARSS*. IEEE; 2021. P. 1288–1290. https://doi.org/10.1109/IGARSS47720.2021.9554352
19. Xia J., Bai W., Sun Y., et al. Calibration and wind speed retrieval for the Fengyun-3 E Meteorological Satellite GNSS-R Mission. In: *2021 IEEE Specialist Meeting on Reflectometry using GNSS and other Signals of Opportunity* (*GNSS+R*). IEEE; 2021. P. 25–28. https://doi.org/10.1109/GNSSR53802.2021.9617699
20. Cheng Z., Jin T., Chang X., et al. Evaluation of spaceborne GNSS-R based sea surface altimetry using multiple constellation signals. *Front. Earth Sci*. 2023;10:1079255. https://doi.org/10.3389/feart.2022.1079255
21. Munoz-Martin J.F., Portero A.P., Camps A., et al. Snow and ice thickness retrievals using GNSS-R: Preliminary results of the MOSAiC experiment. *Remote Sens*. 2020;12(24):4038. https://doi.org/10.3390/rs12244038
22. Nogués O.C., Munoz-Martin J.F., Park H., et al. Improved GNSS-R altimetry methods: Theory and experimental demonstration using airborne dual frequency data from the microwave interferometric reflectometer (MIR). *Remote Sens*. 2021;13(20):4186. https://doi.org/10.3390/rs13204186
23. Фатеев В.Ф., Лопатин В.П. Космический бистатический радиолокатор контроля профиля поверхности океана на основе сигналов ГНСС. *Известия высших учебных заведений. Приборостроение.* 2019;62(5):484–491. https://doi.org/10.17586/0021-3454-2019-62-5-484-491
24. Лопатин В.П., Фатеев В.Ф. Исследование бистатической радиолокационной системы на основе сигналов GPS/ГЛОНАСС в безэховой камере. *Труды Военно-космической академии имени А.Ф. Можайского*. 2019;670:64–68.
25. Волосюк В.К., Кравченко В.Ф. *Статистическая теория радиотехнических систем дистанционного зондирования и радиолокации.* М.: Физматлит; 2008. 351 с.
26. Di Martino G., Di Simone A., Iodice A., Riccio D. Bistatic scattering from anisotropic rough surfaces via a closed-form two-scale model. *IEEE Trans. Geosci. Remote Sens*. 2020;59(5):3656–3671. https://doi.org/10.1109/TGRS.2020.3021784
27. Asgarimehr M., Zavorotny V.U., Wickert J., Reich S. Can GNSS reflectometry detect precipitation over oceans? *Geophys. Res. Lett.* 2018;45(22):12585–12592. https://doi.org/10.1029/2018GL079708
28. Gleason S., Ruf C.S., O'Brien A.J., McKague D.S. The CYGNSS Level 1 calibration algorithm and error analysis based on on-orbit measurements. *IEEE Journal of Selected Topics in Applied Earth Observations and Remote Sensing*. 2019;12(1):37–49. https://doi.org/10.1109/JSTARS.2018.2832981
29. Nan Y., Ye S., Liu J., et al. Signal-to-noise ratio analyses of spaceborne GNSS-reflectometry from Galileo and BeiDou satellites. *Remote Sens*. 2022;14(1):35. https://doi.org/10.3390/rs14010035
30. Rodriguez-Alvarez N., Munoz-Martin J.F., Morris M. Latest Advances in the Global Navigation Satellite System—Reflectometry (GNSS-R) Field. *Remote Sens*. 2023;15(8):2157. https://doi.org/10.3390/rs15082157
31. Cartwright J., Banks Ch.J., Srokosz M. Sea Ice Detection Using GNSS-R Data From TechDemoSat-1. *JGR Oceans*. 2019. V. 124. Iss. 8. P. 5801–5810. https://doi.org/10.1029/2019JC015327
32. Потапов А.А., Кузнецов В.А., Аликулов Е.А. Анализ способов комплексирования изображений, формируемых многодиапазонными радиолокационными станциями с синтезированной апертурой. *Известия высших учебных заведений России. Радиоэлектроника*. 2021;24(3):6–21. https://doi.org/10.32603/1993-8985-2021-24-3-6-21

About the authors

Alexander V. Ksendzuk, Dr. Sci. (Eng.), Head of Department Radioelectronic systems, Institute of Radio Electronics and Informatics, MIREA – Russian Technological University (78, Vernadskogo pr., Moscow, 119454 Russia). E-mail: ks_alex@mail.ru. Scopus Author ID 56628472300, RSCI SPIN-code 2389-6036, https://orcid.org/0009-0001-7084-1433, https://www.researchgate.net/profile/Alexander-Ksendzuk-2

Vyacheslav F. Fateev, Dr. Sci. (Eng.), Professor, Honored Scientist of the Russian Federation, Head of Scientific and Technical Center for Metrological Support of Ground and Space Gravimetry, Russian Metrological Institute of Technical Physics and Radioengineering (VNIIFTRI) (industrial zone of VNIIFTRI, settlement Mendeleevo, Solnechnogorsk, Moscow oblast, 141570 Russia). E-mail: office@vniiftri.ru. Scopus Author ID 56442213300, RSCI SPIN-code 5385-8126, https://orcid.org/0000-0001-7902-0212

Об авторах

Ксендзук Александр Владимирович, д.т.н., заведующий базовой кафедрой № 346 – радиоэлектронных систем, Институт радиоэлектроники и информатики, ФГБОУ ВО «МИРЭА – Российский технологический университет» (119454, Россия, Москва, пр-т Вернадского, д. 78). E-mail: ks_alex@mail.ru. Scopus Author ID 56628472300, SPIN-код РИНЦ 2389-6036, https://orcid.org/0009-0001-7084-1433, https://www.researchgate.net/profile/Alexander-Ksendzuk-2

Фатеев Вячеслав Филиппович, д.т.н., профессор, Заслуженный деятель науки РФ, начальник научно-технического центра «Метрологического обеспечения наземной и космической гравиметрии», ФГУП «Всероссийский научно-исследовательский институт физико-технических и радиотехнических измерений» (ФГУП «ВНИИФТРИ») (141570, Россия, Московская область, г. Солнечногорск, рабочий поселок Менделеево (промзона ВНИИФТРИ). E-mail: office@vniiftri.ru. Scopus Author ID 56442213300, SPIN-код РИНЦ 5385-8126, https://orcid.org/0000-0001-7902-0212

Translated from Russian into English by Lyudmila O. Bychkova
Edited for English language and spelling by Dr. David Mossop

Modern radio engineering and telecommunication systems

Современные радиотехнические и телекоммуникационные системы

UDC 621.391.072
https://doi.org/10.32362/2500-316X-2024-12-4-84-95
EDN OJGGRP

RESEARCH ARTICLE

Studying the influence of correction codes on coherent reception of M-PSK signals in the presence of noise and harmonic interference

Van D. Nguyen @

Le Quy Don Technical University, Ha Noi, Vietnam
@ *Corresponding author, e-mail: nguyenvandungvtdt@lqdtu.edu.vn*

Abstract

Objectives. Signals with multiple phase shift keying (M-PSK) exhibiting good spectral and energy characteristics are successfully used in many information transmission systems. These include satellite communication systems, GPS, GLONASS, DVB/DVB-S2, and a set of IEEE 802.11 wireless communication standards. In radio communication channels, the useful signal is affected by various interferences in addition to noise. One of these is harmonic interference. As a result, high intensity harmonic interference practically destroys the reception of M-PSK signals. One of the important requirements for the quality of data transmission is the system error tolerance. There are different ways of improving the quality of information transmission. One of these is the use of corrective encoding technology. The aim of the paper is to assess the noise immunity of a coherent demodulator of M-PSK signals using Hamming codes (7,4) and (15,11), and convolutional encoding with Viterbi decoding algorithm (7,5) when receiving M-PSK signals under noise and harmonic interference in the communication channel.

Methods. The methods of statistical radio engineering, optimal signal reception theory and computer simulation modeling were used.

Results. Experimental dependencies of the bit error rate on the signal-to-noise ratio and on the intensity of harmonic interference of coherent reception of M-PSK signals in a channel with noise and harmonic interference were obtained using computer simulation modeling. This was done without using correction codes and with Hamming code (7.4) and (15.11) and convolutional encoding with Viterbi decoding algorithm (7,5).

Conclusions. It is shown that the application of the correction codes effectively corrects errors in the presence of noise and harmonic interference with lower intensity. The correction is ineffective in the presence of high intensity interference. These results can provide important guidance in designing the reliable and energy efficient system.

Keywords: multiple phase shift keying, correction codes, Hamming code, convolutional encoding, Viterbi decoding algorithm, noise immunity, bit error rate, harmonic interference

• **Submitted:** 19.11.2023 • **Revised:** 11.02.2024 • **Accepted:** 22.05.2024

For citation: Nguyen V.D. Studying the influence of correction codes on coherent reception of M-PSK signals in the presence of noise and harmonic interference. *Russ. Technol. J*. 2024;12(4):84–95. https://doi.org/10.32362/2500-316X-2024-12-4-84-95

Financial disclosure: The author has no a financial or property interest in any material or method mentioned.

The author declares no conflicts of interest.

НАУЧНАЯ СТАТЬЯ

Исследование влияния корректирующих кодов на когерентный прием сигналов с многопозиционной фазовой манипуляцией при наличии шумовой и гармонической помех

В.З. Нгуен [@]

Вьетнамский государственный технический университет им. Ле Куй Дона, Ханой, Вьетнам
[@] *Автор для переписки, e-mail: nguyenvandungvtdt@lqdtu.edu.vn*

Резюме

Цели. Сигналы с многопозиционной фазовой манипуляцией (М-ФМ), обладающие хорошими спектральными и энергетическими характеристиками, успешно применяются во многих системах передачи информации, таких, как системы спутниковой связи, GPS, ГЛОНАСС, DVB/DVB-S2, в наборе стандартов беспроводной связи IEEE 802.11. В каналах радиосвязи на полезный сигнал действуют, кроме шумовой, разные помехи, одной из них является гармоническая, которая при большой интенсивности практически разрушает прием сигналов М-ФМ. Одним из важных требований, предъявляемых к качеству передачи данных, является устойчивость системы к ошибкам. Существуют разные способы повышения качества передачи информации, один из которых – применение технологии корректирующего кодирования. Цель статьи – оценка помехоустойчивости когерентного демодулятора сигналов М-ФМ с применением кодов Хэмминга (7,4) и (15,11) и сверточного кодирования с алгоритмом декодирования Витерби (7,5) при приеме сигналов М-ФМ в условиях воздействия в канале связи шумовой и гармонической помех.

Методы. Использованы методы статистической радиотехники, теории оптимального приема сигналов и компьютерного имитационного моделирования.

Результаты. С помощью компьютерного имитационного моделирования получены экспериментальные зависимости вероятности битовой ошибки от отношения сигнал/шум и от интенсивности гармонической помехи для когерентного приема сигналов М-ФМ в канале с шумовой и гармонической помехами без применения корректирующих кодов и с применением кодов Хэмминга (7,4) и (15,11), сверточного кодирования с алгоритмом декодирования Витерби (7,5).

Выводы. Показано, что применение корректирующих кодов позволяет эффективно исправлять ошибки при наличии шумовой и гармонической помех с малой интенсивностью. При большой интенсивности помехи коррекция неэффективна. Результаты могут служить важным руководством при проектировании надежных и энергоэффективных систем передачи информации.

Ключевые слова: многопозиционная фазовая манипуляция, корректирующие коды, код Хэмминга, сверточный код, алгоритм декодирования Витерби, помехоустойчивость, вероятность битовой ошибки, гармоническая помеха

• **Поступила:** 19.11.2023 • **Доработана:** 11.02.2024 • **Принята к опубликованию:** 22.05.2024

Для цитирования: Нгуен В.З. Исследование влияния корректирующих кодов на когерентный прием сигналов с многопозиционной фазовой манипуляцией при наличии шумовой и гармонической помех. *Russ. Technol. J.* 2024;12(4):84–95. https://doi.org/10.32362/2500-316X-2024-12-4-84-95

Прозрачность финансовой деятельности: Автор не имеет финансовой заинтересованности в представленных материалах или методах.

Автор заявляет об отсутствии конфликта интересов.

INTRODUCTION

Many studies have examined the impact of encoding on the noise immunity of multivariable signal reception when only white Gaussian noise operates in radio communication channels. In [1–13], the authors define the effectiveness of different correction codes used in encoding channels with different modulation techniques. Table 1 presents the energy gain from using such codes by the particular example of Hamming code and convolutional encoding with Viterbi decoding algorithm.

Figure 1 shows the theoretical dependencies of the bit error rate (BER) P_{eb} on the signal-to-noise ratio (SNR) E_b/N_0 (E_b is average bit energy, N_0 is noise power spectral density) for receiving signals with multiple phase shift keying (M-PSK) in the channel with additive white Gaussian noise. The solid lines correspond to BER without using correction codes. The dashed lines refer to BER using Hamming code (7,4), the dash-dotted lines stand for using Hamming code (15,11), and dotted lines correspond to BER using convolutional encoding with Viterbi decoding algorithm (7,5) [14].

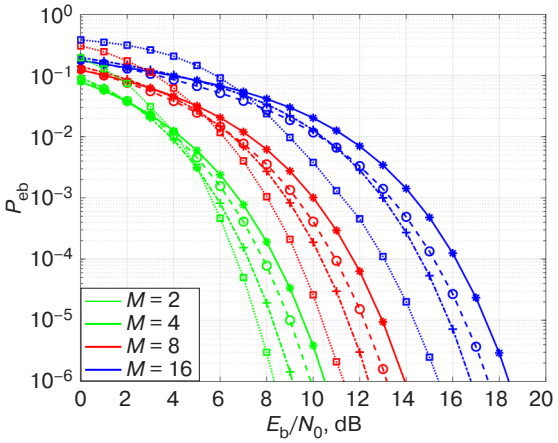

Fig. 1. Theoretical dependencies of the BER P_{eb} on SNR E_b/N_0 for receiving M-PSK signals in the channel with additive white Gaussian noise

In [15–18], the impact of harmonic interference in the reception of signals with multi-position shift keying is analyzed. Harmonic interference is shown to be the most dangerous in the event that its frequency coincides with the useful signal frequency. As a result of its impact, the noise immunity is greatly reduced.

The most important contribution to resolving this problem is made by the noise-resistant coding theory. The aim of the paper is to evaluate the noise immunity for the coherent demodulator of M-PSK signals using Hamming codes (7,4) and (15,11) as well as convolutional encoding with Viterbi decoding algorithm (7,5) when receiving M-PSK signals under the noise and harmonic interference in the communication channel.

1. MODEL OF THE DIGITAL INFORMATION TRANSMISSION SYSTEM

Figure 2 shows the structural diagram of the digital information transmission system. The encoding and decoding algorithm using Hamming code or Viterbi algorithm is implemented in units of channel encoder and channel decoder. The M-PSK signal shaping scheme is based on the universal quadrature modulator, while the receiving scheme is implemented on the basis of a multichannel coherent demodulator which is optimal according to the maximum likelihood criterion (Fig. 3) [19, 20].

2. MATHEMATICAL MODELS OF M-PSK SIGNALS, NOISE AND HARMONIC INTERFERENCE

Mathematical models of M-PSK signals, noise, and harmonic interference may be described as follows:

a) Mathematical model of M-PSK signals

The M-PSK signal at timing period T_s equal to the duration of the channel symbol carrying information about $k = \log_2 M$ information bits can take one of M possible values:

$$s_i(t) = A_0 \cos(\omega_0 t + \varphi_i + \varphi_s),$$
$$\varphi_i = \frac{i2\pi}{M}, t \in (0, T_s], i = \overline{0, M-1},$$

where $A_0 = \sqrt{2E_s / T_s}$ is signal amplitude; $E_s = kE_b$ is channel symbol energy; ω_0 is carrier frequency; φ_s is initial PSK of the signal constellation.

Table 1. Energy gain in SNR (dB) at $P_{eb} = 10^{-5}$

Modulation modes	Hamming code (7,4)	Hamming code (15,11)	Convolutional encoding with Viterbi decoding algorithm (7,5)
BPSK, QPSK	0.56	1.31	1.99
8-PSK	0.78	1.49	2.59
16-PSK	0.91	1.57	3.07

Note: BPSK—binary phase shift keying, QPSK—quadrature phase shift keying.

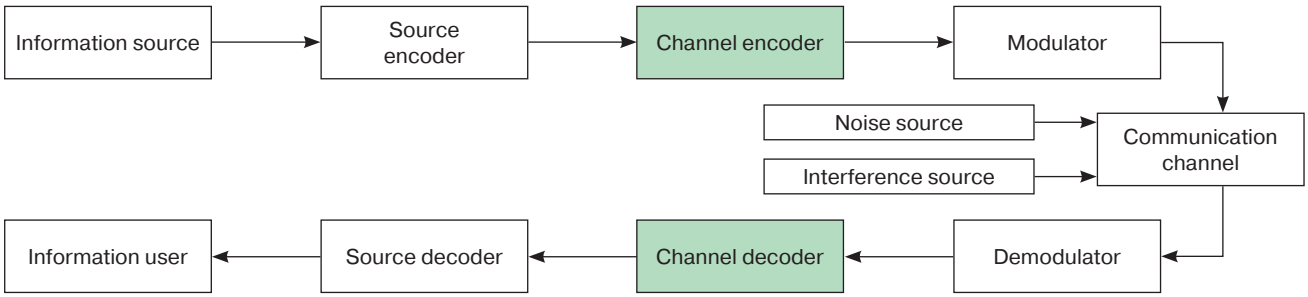

Fig. 2. Structural diagram of the digital information transmission system

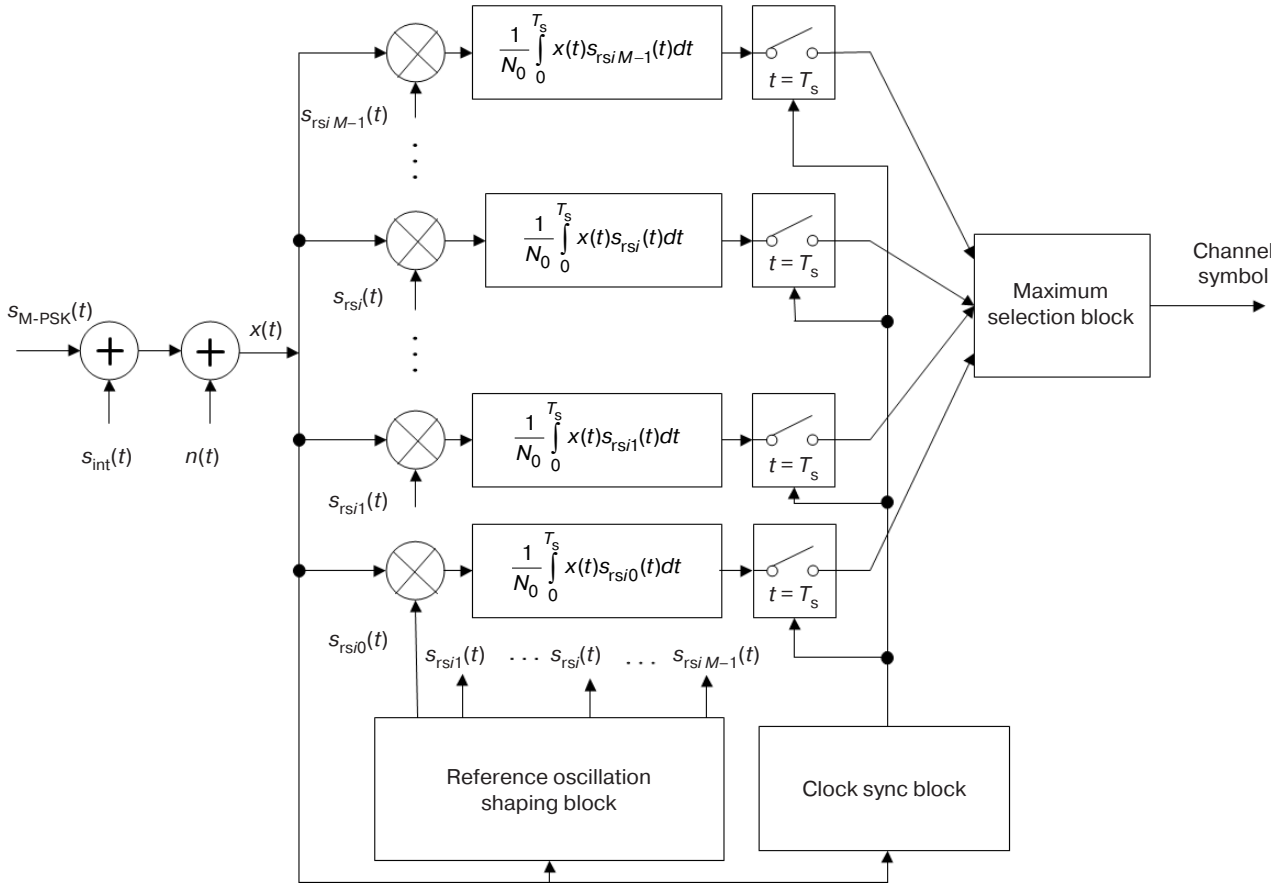

Fig. 3. Structural diagram of the M-PSK coherent demodulator:
t is time; $x(t)$ is input process; $s_{rsi}(t)$ is reference signals

The M-PSK signal constellations using Gray encoding are shown in Fig. 4. Here the signal points corresponding to channel symbols are marked, and the decision boundaries are shown as dotted lines.

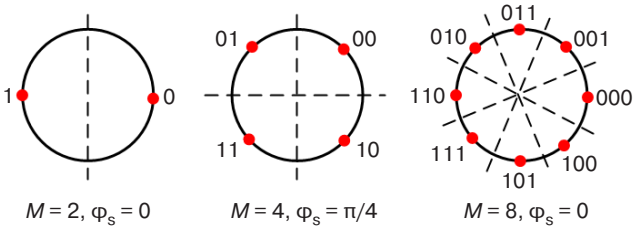

Fig. 4. M-PSK signal constellations

b) Noise interference model

A stationary random process $n(t)$ of the "white Gaussian noise" type with correlation delta function and zero mean is considered as a noise interference.

c) Harmonic interference model

$$s_{int}(t) = \mu A_0 \cos[(\omega_0 + \Delta\omega_{int})t + \varphi_{int}],$$

where μ is relative intensity; φ_{int} is random initial phase of interference uniformly distributed on the half-interval $(-\pi, +\pi]$; $\Delta\omega_{int}$ is interference detuning relative to the center frequency of the spectrum of the useful signal ω_0.

3. HAMMING CODES (7,4) AND (15,11)

The Venn diagrams for the relationship between parity check bits and data bits in Hamming codes are shown in Fig. 5.

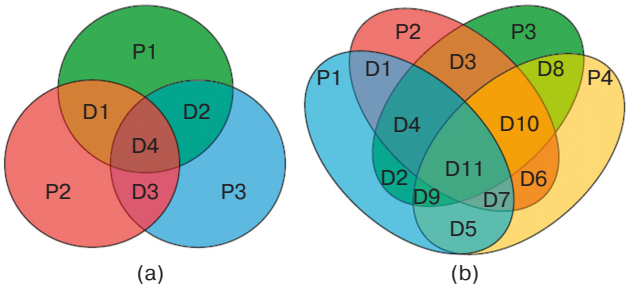

Fig. 5. Venn diagrams describing parity check bits and data bits: (a) Hamming code (7,4), (b) Hamming code (15,11) [21]

There is a certain set of Hamming code parameters:

- number of characters for checking m ($m \geq 3$),
- number of code message symbols $n = 2^m - 1$,
- number of informational symbols $k = 2^m - m - 1$,
- error correction capability $t = 1$ ($d_{min} = 3$),
- code rate $R = k/n$.

The code parameters used in the paper are given in Table 2.

Table 2. Hamming code parameters

Parameters	Hamming code (7,4)	Hamming code (15,11)
m	3	4
n	7	15
k	4	11
R	4/7	11/15

4. CONVOLUTIONAL ENCODING WITH VITERBI DECODING ALGORITHM (7,5)

Figure 6 shows the convolutional encoder scheme with rate 1/2, $K = 3$, generator polynomial is [7,5], octal.

There is a certain set of convolution code parameters:

- number of information symbols k,
- number of symbols transmitted into the communication channel for one clock cycle of information symbol n arriving at the encoder,
- relative code rate $R = k/n$,
- constraint length K,
- number of convolution code states $2^K - 1$.

The convolution code parameters used in the paper are given in Table 3.

Table 3. Convolution code parameters

Parameters	Value
n	1
k	2
K	3
R	1/2

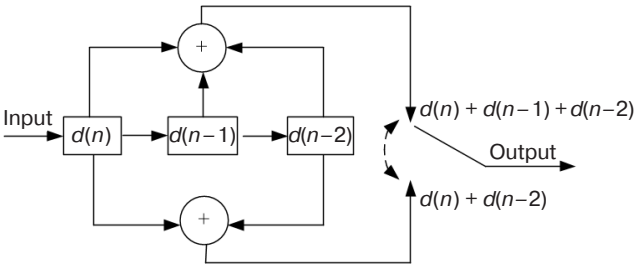

Fig. 6. Convolutional encoder scheme

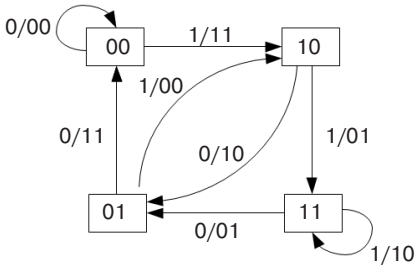

Fig. 7. Convolutional encoding state diagram

5. MODELING AND RESULTS

5.1. Modeling

The information transmission channel is modeled with the parameters presented in Table 4.

The block diagram of the modeling algorithm is shown in Fig. 8.

The relationship between SNRs with and without encoding is taken into account in modeling.

$$\frac{E_{cb}}{N_0} = \frac{E_b}{N_0} + 10\lg\left(\frac{k}{n}\right) \text{(dB)}.$$

5.2. Simulation modeling results

Figure 9 shows the experimental dependencies of BER P_{eb} on SNR E_b/N_0 and on the relative intensity of harmonic interference μ at coherent reception of M-PSK signals using Hamming codes for different code rates. The solid lines correspond to BER without using Hamming code, while the dashed lines refer to BER using Hamming code (7,4), and dash-dotted lines stand for the use of Hamming code (15,11).

Figure 10 shows the experimental dependencies of BER P_{eb} on SNR E_b/N_0 and on the relative intensity of harmonic interference μ at coherent reception of M-PSK signals using convolutional encoding with Viterbi decoding algorithm. The solid lines correspond to BER without encoding, while the dashed lines stand for BER using convolutional encoding with Viterbi decoding algorithm (7,5).

Table 4. Modeling parameters

Parameters	Value
SNR	E_b/N_0 = 0–25 dB
Communication channel	Additive Gaussian white noise, Harmonic interference
Relative interference intensity	μ = 0–1
Interference initial phase	φ = 0–2π
Ratio of sampling frequency to carrier frequency	$f_s/f_0 = 20$, $f_0 = \omega_0/2\pi$
Number of information bits	N = 1080000
Modulation modes	BPSK, QPSK, 8-PSK, 16-PSK
Code types	Hamming code (7,4), Hamming code (15,11), convolutional encoding with Viterbi decoding algorithm (7,5)

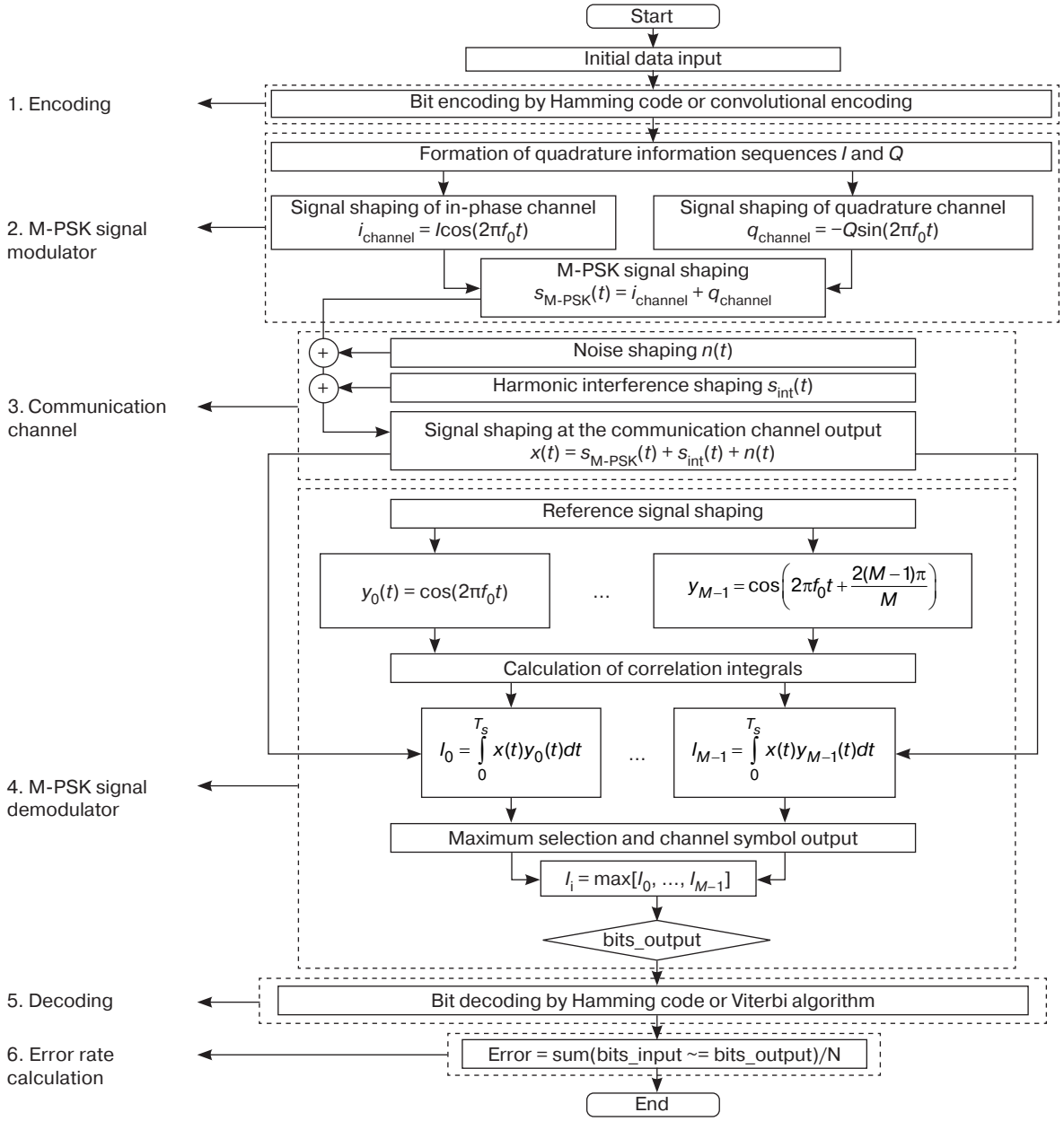

Fig. 8. Block diagram of the modeling algorithm

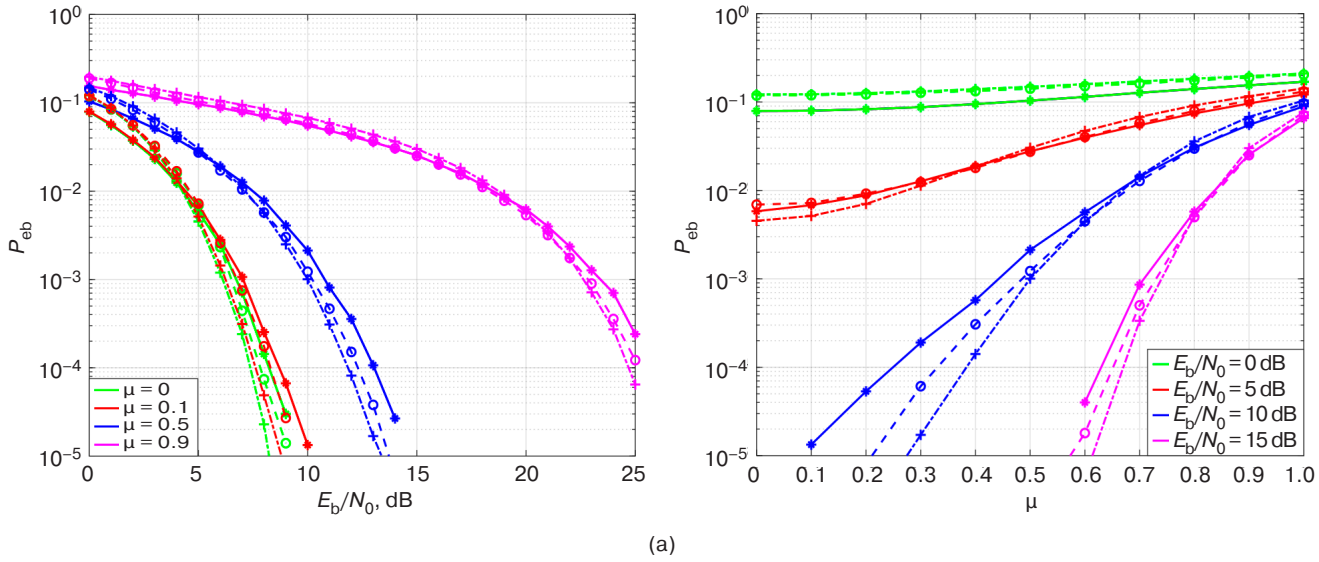

(a)

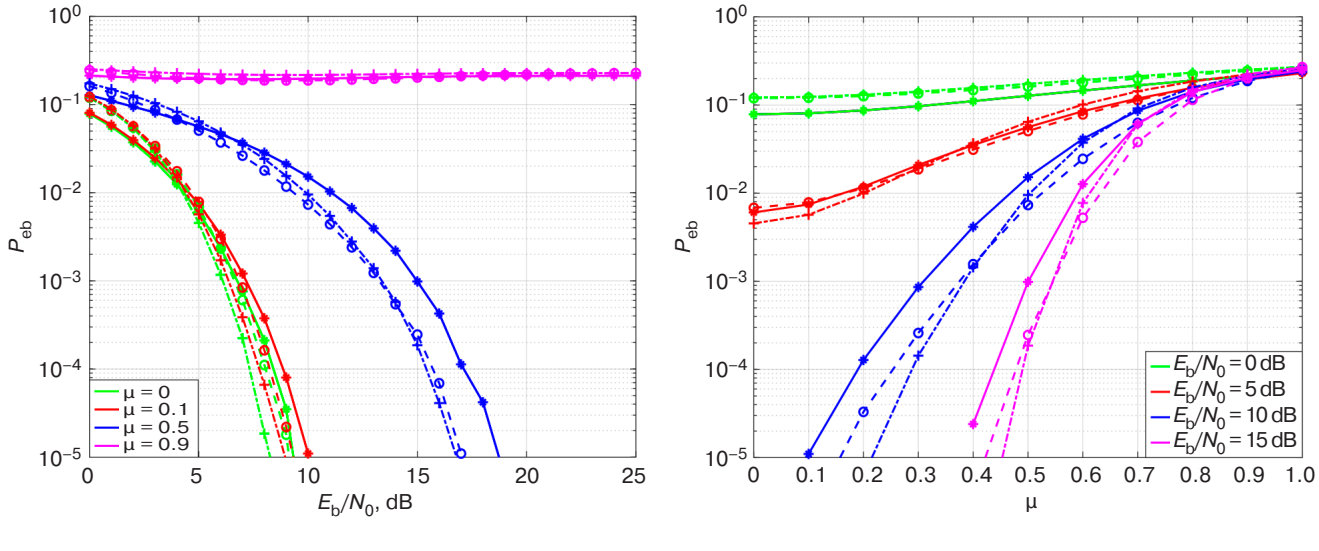

(b)

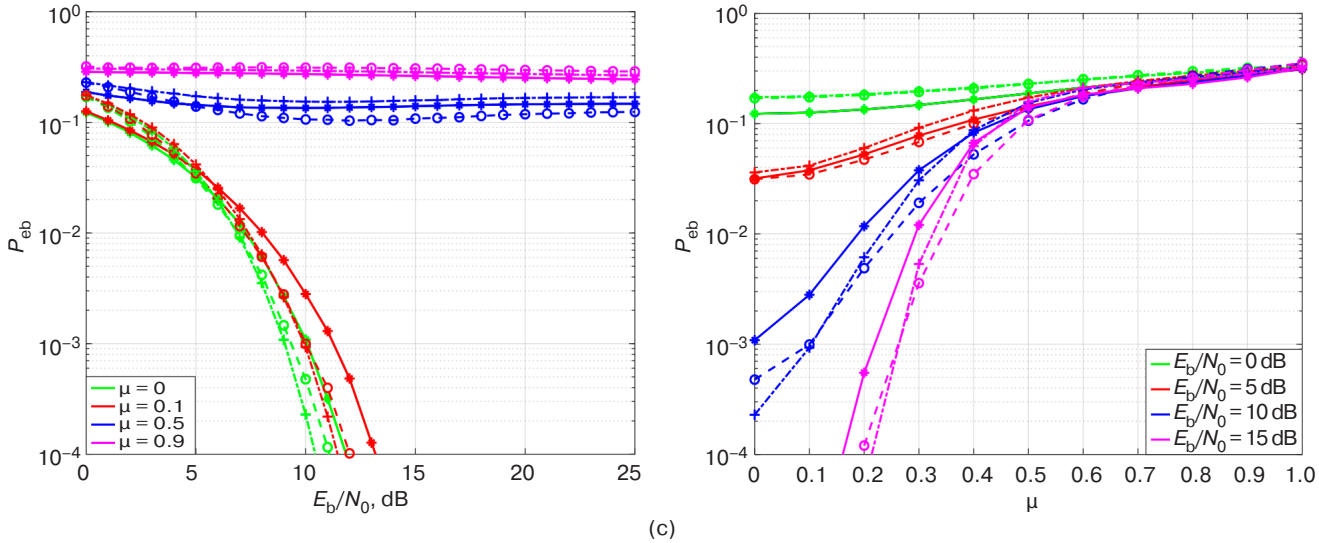

(c)

Fig. 9 (*start*). Experimental dependencies of BER P_{eb}
on SNR E_b/N_0 (left) and on the relative intensity of harmonic interference μ (right)
during coherent reception of M-PSK signals using Hamming codes:
(a) BPSK; (b) QPSK; (c) 8-PSK;

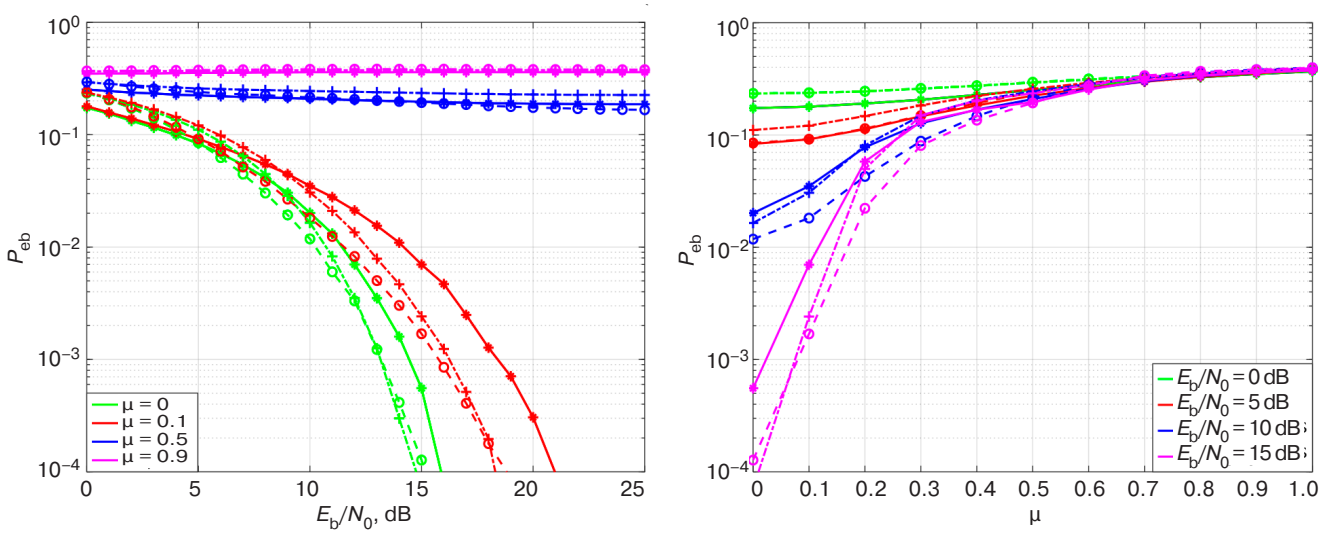

(d)

Fig. 9 (*end*). Experimental dependencies of BER P_{eb} on SNR E_b/N_0 (left) and on the relative intensity of harmonic interference μ (right) during coherent reception of M-PSK signals using Hamming codes: (d) 16-PSK

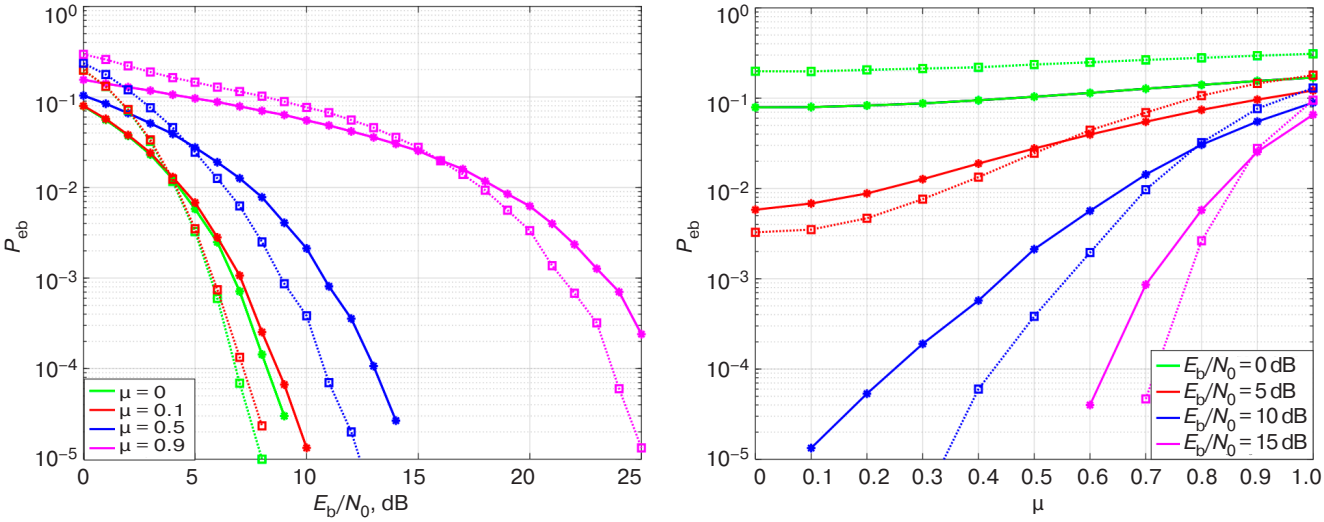

(a)

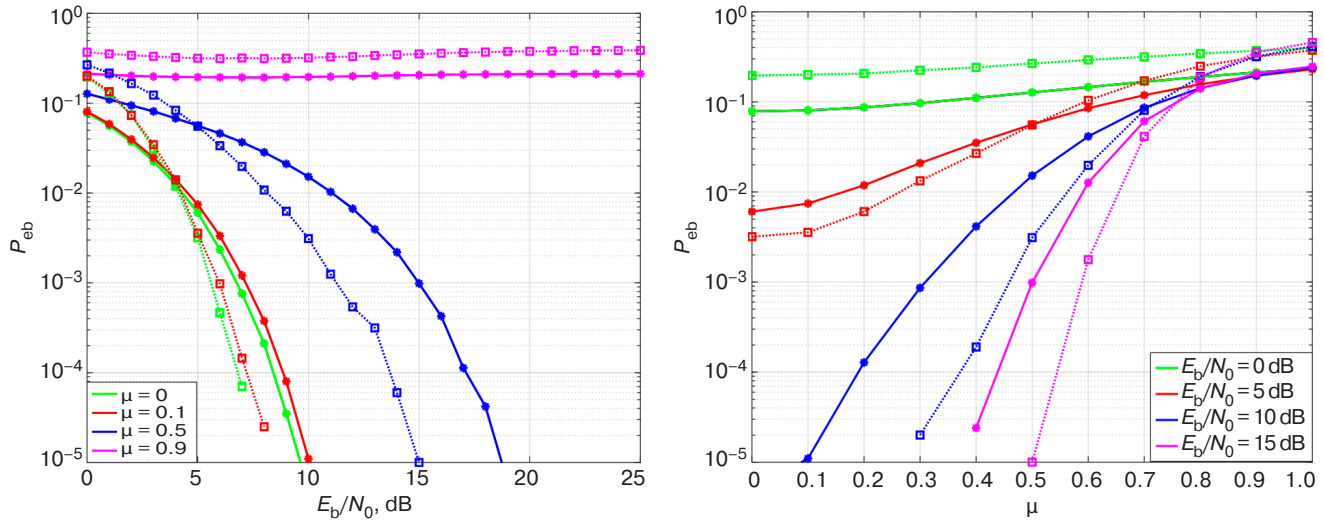

(b)

Fig. 10 (*start*). Experimental dependencies of BER P_{eb} on SNR E_b/N_0 (left) and on the relative intensity of harmonic interference μ (right) at coherent reception of M-PSK signals using convolutional encoding with Viterbi decoding algorithm: (a) BPSK; (b) QPSK;

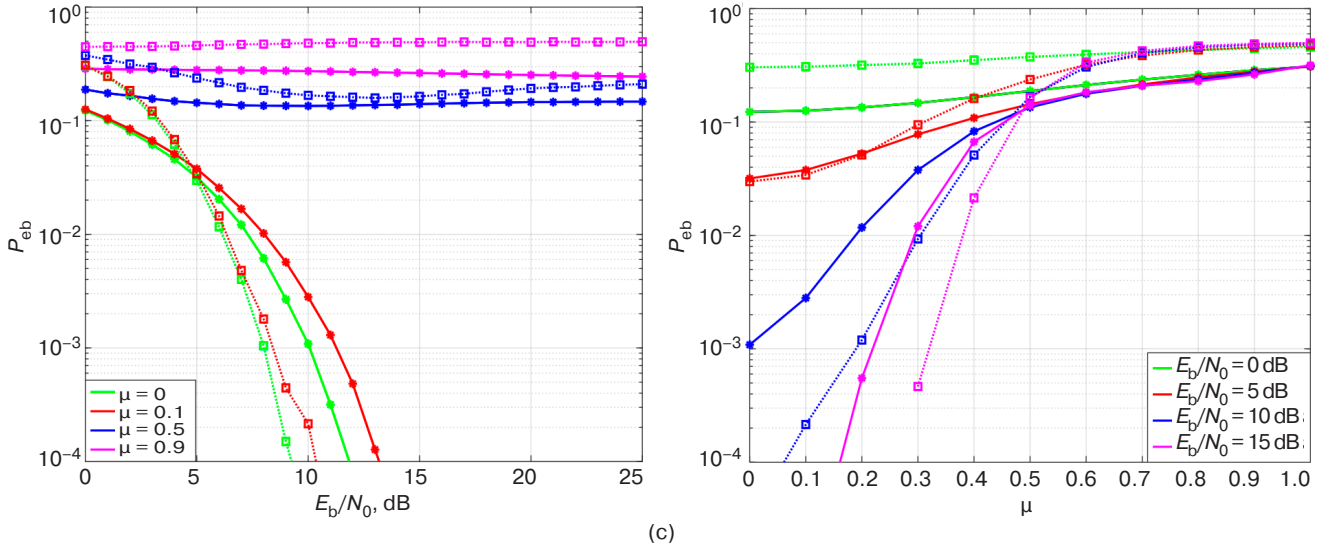

(c)

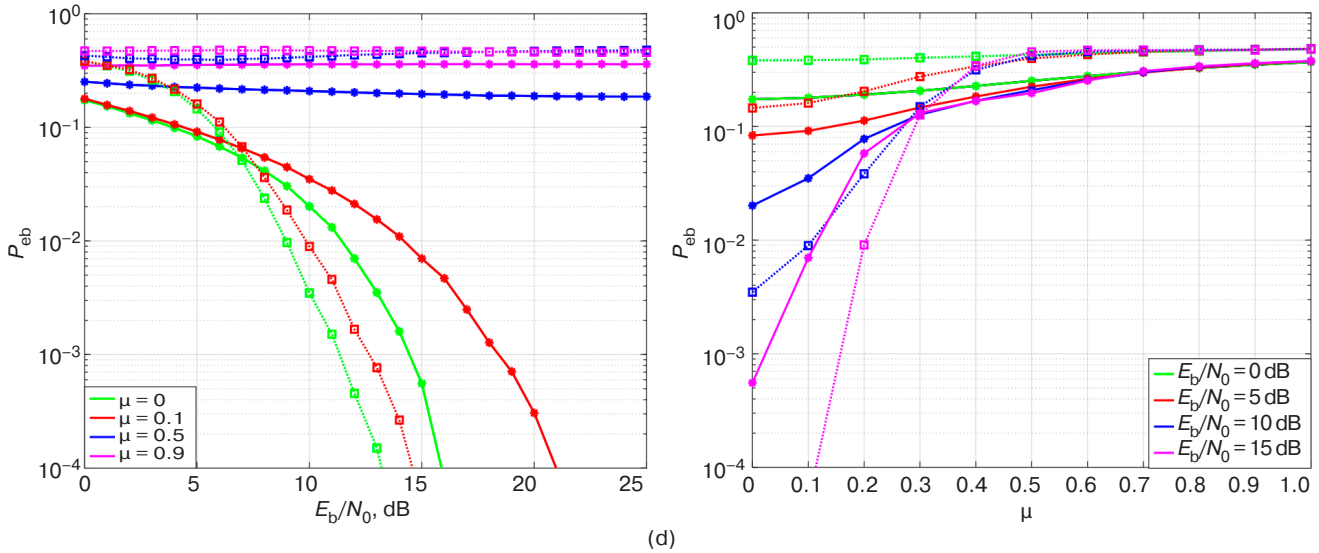

(d)

Fig. 10 (*end*). Experimental dependencies of BER P_{eb} on SNR E_b/N_0 (left) and on the relative intensity of harmonic interference μ (right) at coherent reception of M-PSK signals using convolutional encoding with Viterbi decoding algorithm: (c) 8-PSK; (d) 16-PSK

Figure 11 shows the comparative experimental dependencies of BER P_{eb} on SNR E_b/N_0 (μ = 0.3) and on the harmonic interference intensity (E_b/N_0 = 10 dB) at coherent reception of M-PSK signals using Hamming code and convolutional encoding with Viterbi decoding algorithm. The solid lines correspond to BER without using codes, while the dashed lines refer to using Hamming code (7,4), dash-dotted lines stand for using Hamming code (15,11), and the dotted lines correspond to using convolutional encoding with Viterbi decoding algorithm (7,5).

CONCLUSIONS

In this paper, simulation modeling is carried out to evaluate the efficiency of encoding by Hamming code and convolutional encoding with Viterbi decoding algorithm at coherent reception of M-PSK signals against noise and harmonic interference. The results allow the following conclusions to be made:

1. There is a significant gain from using correction codes in M-PSK signal demodulators in the presence of noise and harmonic interference with low intensity. For example, at μ = 0.3 and $P_{eb} = 10^{-4}$ for QPSK, the energy gain is 1.24 dB with Hamming code (7,4), 1.6 dB with Hamming code (15,11), and 2.69 dB with convolutional encoding and Viterbi decoding algorithm (7,5). At μ = 0.3 and $P_{eb} = 10^{-3}$ for 8-PSK, the energy gain is 2.89 dB with Hamming code (7,4), 2.54 dB with Hamming code (15,11), and 5.4 dB with convolutional encoding and Viterbi decoding algorithm (7,5).

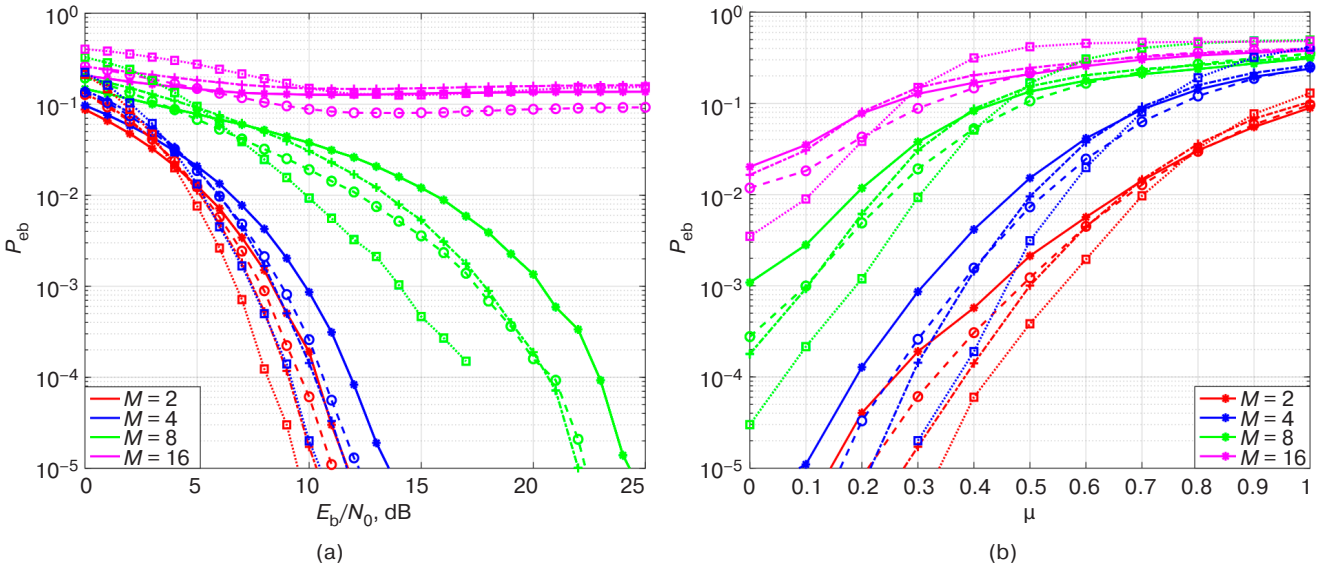

Fig. 11. Comparative dependencies of BER P_{eb} on SNR E_b/N_0 (a) and on the relative intensity of harmonic interference μ (b) at coherent reception of M-PSK signals for different encoding procedures

2. With increased positionality of M-PSK signals and a high intensity of harmonic interference, the use of convolutional encoding and Viterbi decoding algorithm decreases the BER of M-PSK signal reception error more than Hamming codes.
3. Hamming codes with higher code rates outperform codes with lower code rates at high SNR. For example, at $E_b/N_0 \geq 14$ dB, μ = 0.5, and $P_{eb} = 10^{-4}$ for QPSK, the energy gain is 1.4 dB with Hamming code (7,4) and 1.7 dB with Hamming code (15,11) At $E_b/N_0 \geq 20.5$ dB, μ = 0.3, and $P_{eb} = 10^{-4}$ for QPSK, the energy gain is 2 dB with Hamming code (7,4) and 2.3 dB with Hamming code (15,11).

REFERENCES

1. Abu-Baker A., Bani-Hani K., Khasawneh F., Jaradat A. The Impact of Hamming Code and Cyclic Code on MPSK and MQAM Systems over AWGN Channel: Performance Analysis. *Univers. J. Electr. Electron. Eng*. 2021;8(1):9–15. http://doi.org/10.13189/ujeee.2021.080102
2. Singh J., Bahel S. Comparative study of data transmission techniques of different block codes over AWGN channel using Simulink. *International Journal of Engineering Trends and Technology* (*IJETT*). 2014;9(12):609–615. http://doi.org/10.14445/22315381/IJETT-V9P316
3. Saraswat H., Sharma G., Mishra S.K. Performance evaluation and comparative analysis of various concatenated error correcting codes using BPSK modulation for AWGN channel. *International Journal of Electronics and Communication Engineering* (*IJECE*). 2012;5(3):235–244. Available from URL: https://www.ripublication.com/irph/ijece/ijecev5n3_01.pdf
4. Sarnin S.S., Kadri N., Mozi A.M., Ab Wahab N., Naim N.F. Performance analysis of BPSK and QPSK using errorcorrecting code through AWGN. In: *2010 International Conference on Networking and Information Technology*. IEEE; 2010. P. 178–182. https://doi.org/10.1109/ICNIT.2010.5508536
5. Pandey M., Pandey V.K. Comparative Performance Analysis of Block and Convolution Codes. *Int. J. Computer Appl*. 2015;119(24):43–47. http://doi.org/10.5120/21388-4398
6. Pushpa V., Ranganathan H., Palanivelan M. BER analysis of BPSK for block codes and convolution codes over AWGN channel. *Int. J. Pure Appl. Math*. 2017;114(11):221–230. Available from URL: https://acadpubl.eu/jsi/2017-114-7-ICPCIT-2017/articles/11/22.pdf
7. Chopra S.R., Kaur J., Monga H. Comparative Performance Analysis of Block and Convolution Codes. *Indian J. Sci. Technol*. 2016;9(47):1–5. http://doi.org/10.17485/ijst/2016/v9i47/106868
8. El Maammar N., Bri S., Foshi J. Convolutional Codes BPSK Modulation with Viterbi Decoder. In: Noreddine G., Kacprzyk J. (Eds.). *International Conference on Information Technology and Communication System. ITCS 2017. Advances in Intelligent Systems and Computing*. Springer; 2018. V. 640. P. 267–278. http://doi.org/10.1007/978-3-319-64719-7_23
9. Wang J., Huang H., Liu J., Li J. Joint Demodulation and Error Correcting Codes Recognition Using Convolutional Neural Network. *IEEE Access*. 2022;10:104844–104851. http://doi.org/10.1109/ACCESS.2022.3201354

10. Ar-Reyouchi E.M., Rattal S., Ghoumid K. A Survey on Error–Correcting Codes for Digital Video Broadcasting. *SN Comput. Sci.* 2022;3(2):105. https://doi.org/10.1007/s42979-021-00994-x
11. Serchenya A.A. Comparative assessment of noise-resistant coding using different types of codes. In: *Infocommunications*: *Materials of the 55th Anniversary Scientific Conference of Graduate Students, Undergraduates and Students*. Minsk; 2019. P. 49–50 (in Russ.). Available from URL: https://libeldoc.bsuir.by/bitstream/123456789/35911/1/Serchenya_Sravnitelnaya.pdf
12. Maglitskii B.N., Sergeeva A.S. *Otsenka vliyaniya iskazhenii i pomekh na kachestvennye pokazateli tsifrovykh sistem radiosvyazi metodom imitatsionnogo modelirovaniya* (*Assessment of the Influence of Distortions and Interference on the Quality Indicators of Digital Radio Communication Systems using Simulation Modeling*). Novosibirsk: SibGUTI; 2016. 129 p. (in Russ.).
13. Elishev V.V., Tikhonov Ya.E. Noise immunity of information transmission systems with fast pseudo-random tuning of the operating frequency and coding in noise interference conditions. *Scientific and Technical Conference of the A.S. Popov St. Petersburg NTO RES devoted to Radio Day*. 2021;1(76):163–166 (in Russ.). Available from URL: https://conf-ntores.etu.ru/assets/files/2021/cp/papers/163-166.pdf?ysclid=lvxmjjy9dr243257656
14. Golikov A.M. *Kodirovanie v telekommunikatsionnykh sistemakh* (*Coding in Telecommunication Systems*). Tomsk: TUSUR; 2018. 319 p. (in Russ.).
15. Kulikov G.V., Nguyen V.D., Nesterov A.V., Lelyukh A.A. Noise immunity of reception of signals with multiple phase shift keying in the presence of harmonic interference. *Naukoemkie tekhnologii = Science Intensive Technologies*. 2018;19(11):32–38 (in Russ.). Available from URL: https://www.elibrary.ru/item.asp?edn=vscalp&ysclid=lxirdr6ica649732959
16. Kulikov G.V. The effect of harmonic interference on the noise immunity of the correlating demodulator of the MSK signals. *Radiotekhnika = Radioengineering*. 2002;7:42–44 (in Russ.).
17. Kulikov G.V., Nesterov A.V., Lelyukh A.A. Interference immunity of reception of signals with quadrature amplitude shift keying in the presence of harmonic interference. *Zhurnal Radioelektroniki = J. Radio Electronics*. 2018;11:2 (in Russ.). https://doi.org/10.30898/1684-1719.2018.11.9
18. Kulikov G.V., Usmanov R.R., Trofimov D.S. Noise immunity analysis of amplitude and phase-shift keying signals reception in presence of harmonic interference. *Naukoemkie tekhnologii = Science Intensive Technologies*. 2020;21(1):22–29 (in Russ.). Available from URL: https://www.elibrary.ru/item.asp?edn=fdxmsn&ysclid=lxireoosth700939360
19. Proakis J.G. *Digital communications*. 4th ed. New York: McGraw-Hill; 2001. 1002 p.
20. Sklar B. *Digital Communication: Fundamentals and Application*. 2nd ed. Prentice Hall; 2001. 1079 p.
21. Hillier C., Balyan V. Error Detection and Correction On-Board Nanosatellites Using Hamming Codes. *J. Electr. Comput. Eng*. 2019;6:1–15. https://doi.org/10.1155/2019/3905094

СПИСОК ЛИТЕРАТУРЫ

1. Abu-Baker A., Bani-Hani K., Khasawneh F., Jaradat A. The Impact of Hamming Code and Cyclic Code on MPSK and MQAM Systems over AWGN Channel: Performance Analysis. *Univers. J. Electr. Electron. Eng*. 2021;8(1):9–15. http://doi.org/10.13189/ujeee.2021.080102
2. Singh J., Bahel S. Comparative study of data transmission techniques of different block codes over AWGN channel using Simulink. *International Journal of Engineering Trends and Technology* (*IJETT*). 2014;9(12):609–615. http://doi.org/10.14445/22315381/IJETT-V9P316
3. Saraswat H., Sharma G., Mishra S.K. Performance evaluation and comparative analysis of various concatenated error correcting codes using BPSK modulation for AWGN channel. *International Journal of Electronics and Communication Engineering* (*IJECE*). 2012;5(3):235–244. URL: https://www.ripublication.com/irph/ijece/ijecev5n3_01.pdf
4. Sarnin S.S., Kadri N., Mozi A.M., Ab Wahab N., Naim N.F. Performance analysis of BPSK and QPSK using errorcorrecting code through AWGN. In: *2010 International Conference on Networking and Information Technology*. IEEE; 2010. P. 178–182. https://doi.org/10.1109/ICNIT.2010.5508536
5. Pandey M., Pandey V.K. Comparative Performance Analysis of Block and Convolution Codes. *Int. J. Computer Appl*. 2015;119(24):43–47. http://doi.org/10.5120/21388-4398
6. Pushpa V., Ranganathan H., Palanivelan M. BER analysis of BPSK for block codes and convolution codes over AWGN channel. *Int. J. Pure Appl. Math*. 2017;114(11):221–230. URL: https://acadpubl.eu/jsi/2017-114-7-ICPCIT-2017/articles/11/22.pdf
7. Chopra S.R., Kaur J., Monga H. Comparative Performance Analysis of Block and Convolution Codes. *Indian J. Sci. Technol*. 2016;9(47):1–5. http://doi.org/10.17485/ijst/2016/v9i47/106868
8. El Maammar N., Bri S., Foshi J. Convolutional Codes BPSK Modulation with Viterbi Decoder. In: Noreddine G., Kacprzyk J. (Eds.). *International Conference on Information Technology and Communication System. ITCS 2017. Advances in Intelligent Systems and Computing*. Springer; 2018. V. 640. P. 267–278. http://doi.org/10.1007/978-3-319-64719-7_23
9. Wang J., Huang H., Liu J., Li J. Joint Demodulation and Error Correcting Codes Recognition Using Convolutional Neural Network. *IEEE Access.* 2022;10:104844–104851. http://doi.org/10.1109/ACCESS.2022.3201354
10. Ar-Reyouchi E.M., Rattal S., Ghoumid K. A Survey on Error–Correcting Codes for Digital Video Broadcasting. *SN Comput. Sci.* 2022;3(2):105. https://doi.org/10.1007/s42979-021-00994-x
11. Серченя А.А. Сравнительная оценка помехоустойчивого кодирования при использовании разных типов кодов. В сб.: *Инфокоммуникации*: *материалы 55-й юбилейной научной конференции аспирантов, магистрантов и студентов*. Минск; 2019. С. 49–50. URL: https://libeldoc.bsuir.by/bitstream/123456789/35911/1/Serchenya_Sravnitelnaya.pdf

12. Маглицкий Б.Н., Сергеева А.С. *Оценка влияния искажений и помех на качественные показатели цифровых систем радиосвязи методом имитационного моделирования*. Новосибирск: СибГУТИ; 2016. 129 с.
13. Елишев В.В., Тихонов Я.Е. Помехоустойчивость систем передачи информации с быстрой псевдослучайной перестройкой рабочей частоты и кодированием в условиях шумовых помех. *Научно-техническая конференция Санкт-Петербургского НТО РЭС им. А.С. Попова, посвященная Дню радио*. 2021;1(76):163–166. URL: https://conf-ntores.etu.ru/assets/files/2021/cp/papers/163-166.pdf?ysclid=lvxmjjy9dr243257656
14. Голиков А.М. *Кодирование в телекоммуникационных системах*. Томск: ТУСУР; 2018. 319 с.
15. Куликов Г.В., Нгуен В.З., Нестеров А.В., Лелюх А.А. Помехоустойчивость приема сигналов с многопозиционной фазовой манипуляцией в присутствии гармонической помехи. *Наукоемкие технологии*. 2018;19(11):32–38. URL: https://www.elibrary.ru/item.asp?edn=vscalp&ysclid=lxirdr6ica649732959
16. Куликов Г.В. Влияние гармонической помехи на помехоустойчивость корреляционного демодулятора сигналов МЧМ. *Радиотехника*. 2002;7:42–44.
17. Куликов Г.В., Нестеров А.В., Лелюх А.А. Помехоустойчивость приема сигналов с квадратурной амплитудной манипуляцией в присутствии гармонической помехи. *Журнал радиоэлектроники*. 2018;11:2. https://doi.org/10.30898/1684-1719.2018.11.9
18. Куликов Г.В., Усманов Р.Р., Трофимов Д.С. Анализ помехоустойчивости приема сигналов с многопозиционной амплитудно-фазовой манипуляцией в присутствии гармонической помехи. *Наукоемкие технологии*. 2020;21(1):22–29. URL: https://www.elibrary.ru/item.asp?edn=fdxmsn&ysclid=lxireoosth700939360
19. Proakis J.G. *Digital communications*. 4th ed. New York: McGraw-Hill; 2001. 1002 p.
20. Sklar B. *Digital Communication: Fundamentals and Application*. 2nd ed. Prentice Hall; 2001. 1079 p.
21. Hillier C., Balyan V. Error Detection and Correction On-Board Nanosatellites Using Hamming Codes. *J. Electr. Comput. Eng*. 2019;6:1–15. https://doi.org/10.1155/2019/3905094

About the author

Van D. Nguyen, Cand. Sci. (Eng.), Lecturer, Department of Circuit Theory – Measurement, Faculty of Radio-Electronic Engineering, Le Quy Don Technical University (236, Hoang Quoc Viet, Ha Noi, Vietnam). E-mail: nguyenvandungvtdt@lqdtu.edu.vn. https://orcid.org/0000-0002-2810-1204

Об авторе

Нгуен Ван Зунг, к.т.н., преподаватель, кафедра теории цепей – измерения, Факультет радиотехники и электроники, Вьетнамский государственный технический университет им. Ле Куй Дона (Вьетнам, Ханой, ул. Хоанг Куок Вьет, д. 236). E-mail: nguyenvandungvtdt@lqdtu.edu.vn. https://orcid.org/0000-0002-2810-1204

Translated from Russian into English by K. Nazarov
Edited for English language and spelling by Dr. David Mossop

Micro- and nanoelectronics. Condensed matter physics

Микро- и наноэлектроника. Физика конденсированного состояния

UDC 535.343.2
https://doi.org/10.32362/2500-316X-2024-12-4-96-105
EDN ZZDBRB

RESEARCH ARTICLE

Kretschmann configuration as a method to enhance optical absorption in two-dimensional graphene-like semiconductors

Andrey A. Guskov @,
Nikita V. Bezvikonnyi,
Sergey D. Lavrov

MIREA — Russian Technological University, Moscow, 119454 Russia
@ Corresponding author, e-mail: guskov@mirea.ru

Abstract

Objectives. The optical properties of two-dimensional semiconductor materials, specifically monolayered transition metal dichalcogenides, present new horizons in the field of nano- and optoelectronics. However, their practical application is hindered by the issue of low light absorption. When working with such thin structures, it is essential to consider numerous complex factors, such as resonance and plasmonic effects which can influence absorption efficiency. The aim of this study is the optimization of light absorption in a two-dimensional semiconductor in the Kretschmann configuration for future use in optoelectronic devices, considering the aforementioned phenomena.

Methods. A numerical modeling method was applied using the finite element method for solving Maxwell's equations. A parametric analysis was conducted focusing on three parameters: angle of light incidence, metallic layer thickness, and semiconductor layer thickness.

Results. Parameters were identified at which the maximum area of absorption peak was observed, including the metallic layer thickness and angle of light incidence. Based on the resulting graphs, optimal parameters were determined, in order to achieve the highest absorption percentages in the two-dimensional semiconductor film.

Conclusions. Based on numerical studies, it can be asserted that the optimal parameters for maximum absorption in the monolayer film are: Ag thickness <20 nm and angle of light incidence between 55° and 85°. The maximum absorption in the two-dimensional film was found only to account for a portion of the total absorption of the entire structure. Thus, a customized approach to parameter selection is necessary, in order to achieve maximum efficiency in certain optoelectronic applications.

Keywords: two-dimensional semiconductors, transition metal dichalcogenides, surface plasmon resonance, plasmon effects, nanostructured metal films

• **Submitted:** 26.09.2023 • **Revised:** 18.01.2024 • **Accepted:** 22.05.2024

For citation: Guskov A.A., Bezvikonnyi N.V., Lavrov S.D. Kretschmann configuration as a method to enhance optical absorption in two-dimensional graphene-like semiconductors. *Russ. Technol. J*. 2024;12(4):96–105. https://doi.org/10.32362/2500-316X-2024-12-4-96-105

Financial disclosure: The authors have no a financial or property interest in any material or method mentioned.

The authors declare no conflicts of interest.

НАУЧНАЯ СТАТЬЯ

Конфигурация Кречмана как метод увеличения оптического поглощения в двумерных графеноподобных полупроводниках

А.А. Гуськов [@], **Н.В. Безвиконный**, **С.Д. Лавров**

МИРЭА — Российский технологический университет, Москва, 119454 Россия
[@] *Автор для переписки, e-mail: guskov@mirea.ru*

Резюме

Цели. Оптические свойства двумерных полупроводниковых материалов, в частности монослойных дихалькогенидов переходных металлов, предоставляют новые возможности в области нано- и оптоэлектроники. Однако практическое применение этих материалов ограничено из-за низкой способности поглощать свет, вызванной их высокой прозрачностью. При работе с такими тонкими структурами возникает возможность использования множества физических механизмов, включая резонансные и плазмонные эффекты, которые можно настроить для улучшения эффективности поглощения света. Цель данной работы – оптимизация поглощения света в двумерном полупроводнике в конфигурации Кречмана с учетом указанных выше явлений для последующего применения в устройствах оптоэлектроники.

Методы. Для проведения моделирования использован метод конечных элементов решения уравнений Максвелла в структуре, представляющей стандартную конфигурацию Кречмана. Проведен параметрический анализ влияния трех параметров: угла падения света, толщины металлического слоя и толщины полупроводникового слоя.

Результаты. Проведено исследование конфигурации модели Кречмана с целью достижения максимального оптического поглощения в двумерной полупроводниковой пленке. Определены параметры, при которых наблюдается наибольшая «площадь» пика поглощения, включая толщину металлического слоя и угол падения излучения. На основе полученных результатов выявлены лучшие параметры для достижения наивысшей степени поглощения в двумерной пленке полупроводника.

Выводы. На основе численных исследований конфигурации модели Кречмана обнаружено, что оптимальными параметрами для максимального поглощения в монослойной пленке являются: толщина слоя серебра, не превышающая 20 нм, и угол падения света от 55° до 85°. Установлено, что максимальное поглощение в двумерной пленке составляет лишь часть от общего поглощения всей структуры. Таким образом, для достижения максимальной эффективности в определенных оптоэлектронных приложениях необходим индивидуальный подход к выбору параметров.

Ключевые слова: двумерные полупроводники, дихалькогениды переходных металлов, поверхностный плазмонный резонанс, плазмонные эффекты, наноструктурированные металлические пленки

• **Поступила:** 26.09.2023 • **Доработана:** 18.01.2024 • **Принята к опубликованию:** 22.05.2024

Для цитирования: Гуськов А.А., Безвиконный Н.В., Лавров С.Д. Конфигурация Кречмана как метод увеличения оптического поглощения в двумерных графеноподобных полупроводниках. *Russ. Technol. J.* 2024;12(4):96–105. https://doi.org/10.32362/2500-316X-2024-12-4-96-105

Прозрачность финансовой деятельности: Авторы не имеют финансовой заинтересованности в представленных материалах или методах.

Авторы заявляют об отсутствии конфликта интересов.

INTRODUCTION

Despite the unique properties of two-dimensional semiconductor materials, their integration into nano- and optoelectronics devices still remains a significant challenge. For example, monolayer transition metal dichalcogenides (TMD) such as MoS_2, $MoSe_2$, WS_2, WSe_2, and others, although being promising for application in optical detectors and photovoltaic elements, have a significant disadvantage that stems from their two-dimensionality, i.e., high optical transparency. In [1], it was demonstrated that the two-dimensional MoS_2 film absorbs no more than 10% of the incident light in the visible optical range. This is not sufficient for creating effective photosensitive elements on their basis. However, the most obvious solution to this problem, which consists in increasing the intrinsic thickness of the semiconductor, cannot be realized due to the almost instantaneous transition from direct-bandgap to indirect-bandgap semiconductor. This can lead to the subsequent loss of its efficiency as a photosensitive element.

At present, this problem can be solved using various approaches. These approaches can be conventionally divided into two main groups. The first group uses interference effects arising from the Fabry–Perot resonator [2–4], while the second group relies on the use of local or surface plasmon resonances [5–10].

Thus, the paper [3] shows that light absorption in a two-dimensional MoS_2 film can reach 70%, and in the WSe_2 75%. This is due to the inclusion of a layer of hexagonal boron nitride in the resonator. Paper [11] demonstrates a twofold theoretical and sixfold experimental increase in the absorption of a two-dimensional MoS_2 film in almost the entire visible spectrum when the structure is changed from $MoS_2/SiO_2/Si$ to $MoS_2/SiO_2/Au/Si$. This is due to the occurrence of interference due to multiple reflections from the air/SiO_2 и SiO_2/Au interfaces.

Despite the need for much more sophisticated technological methods and approaches to utilize plasmonic effects, they are often more effective. For example, in the use of nanoparticles or plasmonic antennas, there is a resonant amplification of the electromagnetic field at the metal/semiconductor interface, making it possible to concentrate light directly into two-dimensional structures [5]. Repeated attempts have been made over the past few years to enhance the photoluminescence signal in monolayers of TMD (e.g., such as MoS_2, WS_2, and WSe_2) by depositing single metallic nanoparticles or arrays of them on the surface of the TMD [6, 7]. Due to its relative simplicity compared to other technological methods for creating plasmonic structures, this method can be used to develop photosensitive devices [12, 13].

Many experimental and theoretical works are devoted to ordered plasmonic structures deposited on two-dimensional semiconductors [8–10]. One of their key advantages is the possibility of adjusting the performance characteristics of optical devices by modifying the shape and geometry of plasmonic elements [14, 15].

The possibility of combining plasmonic and interference techniques is also worth noting. This is confirmed by the results published in [16]. An absorption of 40% in the MoS_2 monolayer in the visible range was obtained using a combination of interference dielectric coating and nanoscale grooves. Also, [17] showed a method for creating ordered silver plasmonic structures on the surface of a waveguide. Nearly 95% total absorption in the entire structure (and 70% absorption in the MoS_2, monolayer in particular) was demonstrated by using a geometry that combines interference and plasmonic effects.

All the above-mentioned methods are based on the effect of local plasmon resonance, involving absorption in metallic plasmonic nanostructures, which is not optimal. Under certain conditions, surface plasmon resonance can be devoid of these drawbacks. To date, several papers have been presented which show the advantages of using surface plasmon resonance in Kretschmann geometry [18, 19]. In [20], high absorption in TMD (reaching almost 100%) was obtained by depositing a two-dimensional TMD film directly onto the dielectric surface. A standing plasmon wave propagates along the semiconductor/dielectric interface, due to which the incident radiation is localized in the TMD and its total absorption increases. It should be noted that in this work, high absorption is achieved not in the two-dimensional TMD film itself, but in the entire structure, including a periodic strip plasmonic lattice of gold.

However, to date, the use of Kretschmann geometry to enhance optical absorption in TMD has not yet been developed to an applied level. Since it is fundamentally technologically simpler than the creation of plasmonic structures by lithographic methods, its successful application requires more theoretical studies to optimize its use in combination with two-dimensional semiconductor films. In this case, the very physical mechanism of optical radiation detection in the structures described above is important. In these structures, the greatest contribution to the photocurrent is made by the photovoltaic effect and photoconductivity effect [21–23] which occur in the nanoscale layer of TMD itself. Thus, for the photosensitive elements created, the main role is played not by the total absorption in the created multilayer structures, but by the absorption in the TMD itself, which, obviously, can already be much lower. This work is devoted to the theoretical modeling of the application of Kretschmann geometry, in order to

estimate the possibility of increasing the absorption in a two-dimensional semiconductor layer rather than in the whole structure, which is especially relevant for photovoltaic applications.

METHODS AND APPROACHES

A simulated structure consisting of a glass prism with refractive index approximately equal to 1.5 [24, 25], onto which a thin metal layer and a two-dimensional TMD film were deposited (Fig. 1). Metals such as gold [26, 27], copper [28, 29], aluminum [30], or platinum [31] are commonly used in the Kretschmann configuration. In order to generate plasmon waves of the highest intensity, a material must be chosen with the largest modulo value of ε′ (real part of the dielectric constant) and small value of ε′′ (imaginary part of the dielectric constant) in the chosen visible optical range [30]. In this case, silver is the optimal choice. It should be noted that copper and gold show slightly lower efficiency in the selected wavelength range. However, the use of gold is not commercially feasible, while the surface of copper can be covered by an absorbing oxide layer, significantly reducing the efficiency of surface plasmons [32]. For this reason, silver was used as the metal in this work and its optical constants were taken from [33]. WSe_2 was used as the semiconductor film since it is one of the most studied two-dimensional semiconductors and its optical constants are well known for both monolayer and multilayer samples [34]. This approach can be applied to any type of TMD with known optical constants.

Simulation of optical radiation propagation in the structure under consideration was carried out using the *COMSOL Multiphysics*[1] software package in the Wave Optics extension module. The configuration being studied contains several key parameters which

[1] https://www.comsol.com/. Accessed June 01, 2023.

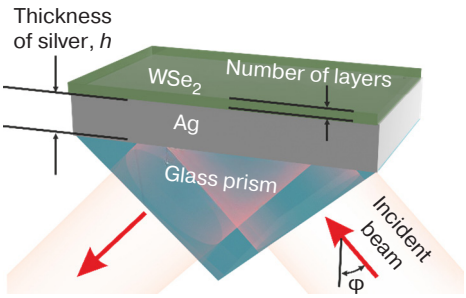

Fig. 1. Schematic diagram of the structure under study

contribute most to the simulation results. Parameters such as silver thickness and the number of TMD layers have technological limitations and can be chosen over a wide range of thicknesses. The angle of incidence of optical radiation at the metal/dielectric interface is also a variable parameter. At the same time, it is important for the Kretschmann geometry to use the transverse magnetic mode of the incident radiation. This is the necessary condition for the generation of surface plasmon waves. The wavelength of the incident optical radiation was equal to 740 nm, corresponding to the position of the exciton peak for WSe_2. Varying these parameters enables the distribution of electric and magnetic fields in the structure to be changed. This allows the parameters for the highest possible power density of optical electromagnetic radiation in the region of the two-dimensional semiconductor film to be defined.

RESULTS AND DISCUSSION

Figure 2 shows plots of the maximum absorption value as a function of the number of semiconductor film layers, the angle of light incidence, and the thickness of the silver layer. This value in this case means the maximum value among all other varying parameters.

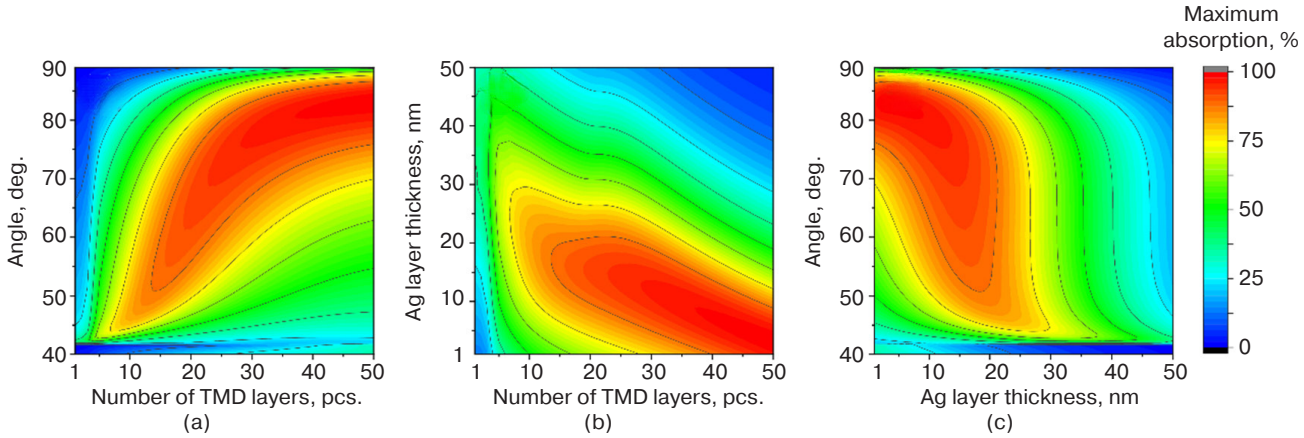

Fig. 2. Diagrams of dependence of the maximum absorption value in WSe_2 in the configuration with a homogeneous silver layer as a function of: (a) the angle of incidence of radiation and the number of TMD layers, (b) the thickness of the Ag layer and the number of TMD layers, (c) the angle of incidence of radiation and the thickness of the Ag layer

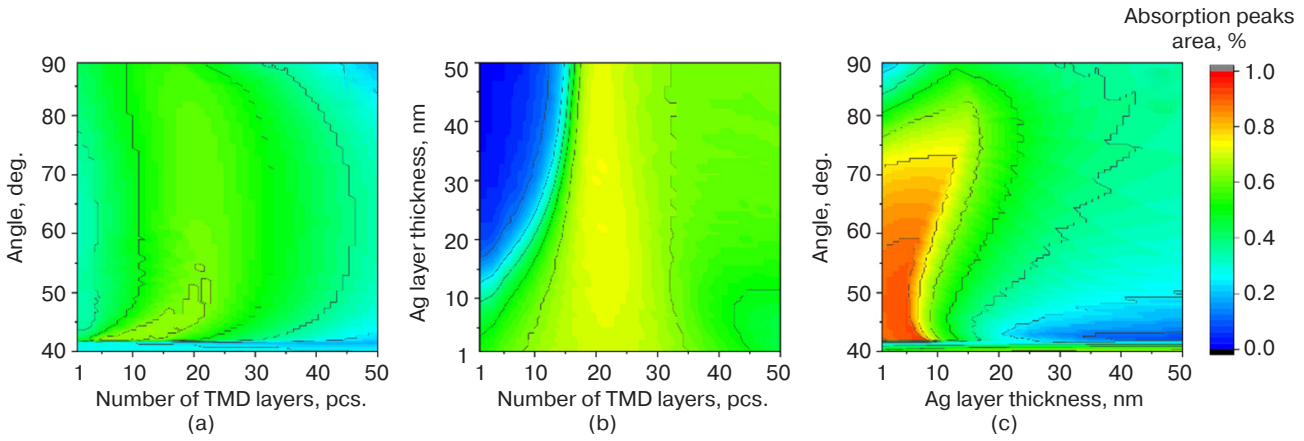

Fig. 3. Diagrams of the dependence of the area of absorption peaks in WSe_2 in the configuration with a flat silver layer as a function of: (a) the angle of incidence of radiation and the number of PDM layers, (b) the thickness of the Ag layer and the number of TMD layers, (c) the angle of incidence of incident radiation and the thickness of the Ag layer

In Fig. 2a, the maximum values for all other parameters (in this case, it is the thickness of the silver layer) are shown in the coordinates of the angle of incidence and the number of layers. The maximum absorption values for all values of the silver layer thickness were taken from among the sets of plots in the coordinates of the angle of incidence and the number of TMD layers. If the point with the maximum absorption value of 99% is taken (according to the coordinates of the number of TMD layers 40 and the angle of incidence 80°), then by any other graph (Figs. 2b and 2c) the value of the third coordinate can be defined: the thickness of the silver layer, at which this maximum value is achieved. So from Figs. 2b and 2c it is clear that this value of the silver layer thickness is ≈8 nm.

Figures 2a and 2b show that in such a configuration of the Kretschmann model, the maximum value of absorption in the TMD (close to 100%) can be achieved only with a large number of semiconductor layers (15 and more). Nevertheless, it shows that it is possible to achieve such a large percentage of absorption just in the semiconductor layer (which can be a conducting channel for optoelectronic devices), and not in the whole structure (as, for example, shown in the works analyzed in the introduction of this article).

In addition to the maximum optical absorption value, the area of the absorption peak is a characteristic value. This value must be taken into account because, for example, at different beam angles the maximum optical absorption values may be the same, while the areas of these absorption peaks may differ radically from each other. This fact can be decisive when selecting the configuration for the respective applications. Therefore, a plot of the absorption peak area as a function of the number of semiconductor film layers, the angle of light incidence, and the thickness of the silver layer was also calculated. The results of this calculation are shown in Fig. 3. The area of the peaks in this case refers to the number of points with a value above 68% (2σ, where σ is the standard deviation), of the absorption maximum. This analysis is also necessary because if the absorption peak is very narrow in some coordinates, it is technologically difficult to create a structure with such precise tolerances. It is thus important to determine not only the absorption maximum value, but also its area.

Figure 3c shows the specific parameters at which a large area of the absorption peaks is achievable. For example, it can be seen that a large area of the absorption peak is achieved with a silver layer thickness of up to 5 nm, and an angle of incidence of 42° to 60° (Fig. 2c shows that this peak roughly corresponds to an absorption value of 50%).

Figure 4 shows a diagram of the dependence of absorption in TMD on the thickness of the silver layer and the angle of incidence of light. The dotted white line in the inset shows the region with the maximum absorption value. It can be concluded that the use of monolayer TMD is not very advantageous in terms of achieving high optical absorption (Fig. 4 shows the maximum achievable absorption value of 40%). However, for nanoelectronics devices and other applications, energy-efficient semiconductors need to be used. Monolayer TMD specifically belong to this group, due to their direct bandgap. It can also be advantageous in terms of device integration and miniaturization. Hence, there is an obvious interest in finding methods to increase the name absorption in a monolayer film. It can be seen clearly from Fig. 4, that the optimal values of parameters for achieving maximum absorption in a monolayer film are: the thickness of the silver layer is 37 nm and the angle of incidence of incident radiation is 42.1°.

As mentioned above, the important quantity under study is the absorption by the semiconductor layer. In Fig. 5, the solid lines show the plots of absorption, reflection and transmittance of the whole structure as a function of the angle of incidence of light for different thicknesses of the silver layer, and the dashed line shows

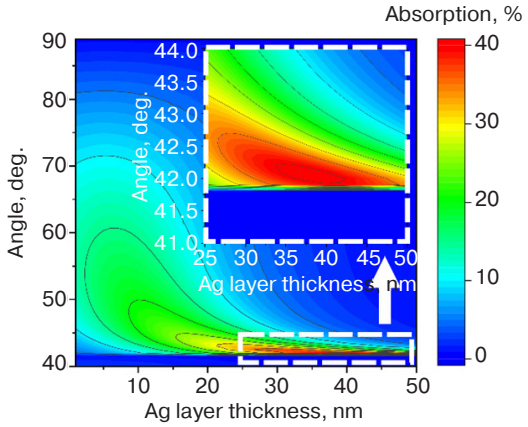

Fig. 4. Diagram of the absorption dependence in TMD as a function of the silver layer thickness and the angle of light incidence

the plots of absorption of as a function the semiconductor layer. These are typical plots that arise when using the Kretschmann geometry [35].

The width of the absorption peaks indicates the increase of absorption exactly due to plasmon resonance. Figure 5d shows a plot of the magnetic field distribution (H_z-component) in a structure with a silver thickness of 37 nm and a light incidence angle of 41.2°, i.e., the peak of plasmon resonance and absorption in Fig. 4. Here standing waves can be seen, the appearance of which is characteristic of surface plasmon resonance. It can also be seen that in this case, the absorption in the semiconductor film is only half of the total absorption of the structure.

Figure 6a shows the absorption map of the total structure as a function of silver layer thickness and

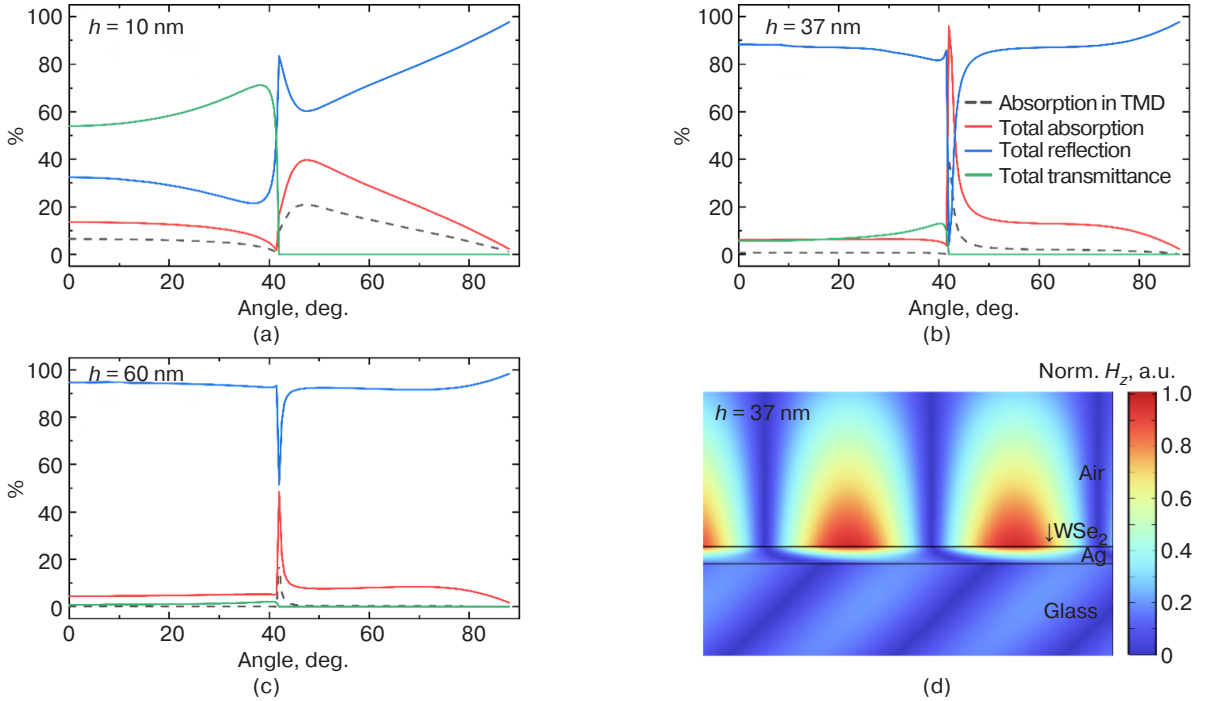

Fig. 5. Diagrams of absorption, reflection and transmittance as a function of the angle of incidence of light for structures with silver layer thicknesses of 10 (a), 37 (b), and 60 (c) nm and normalized graph (d) of magnetic field (H_z-component)

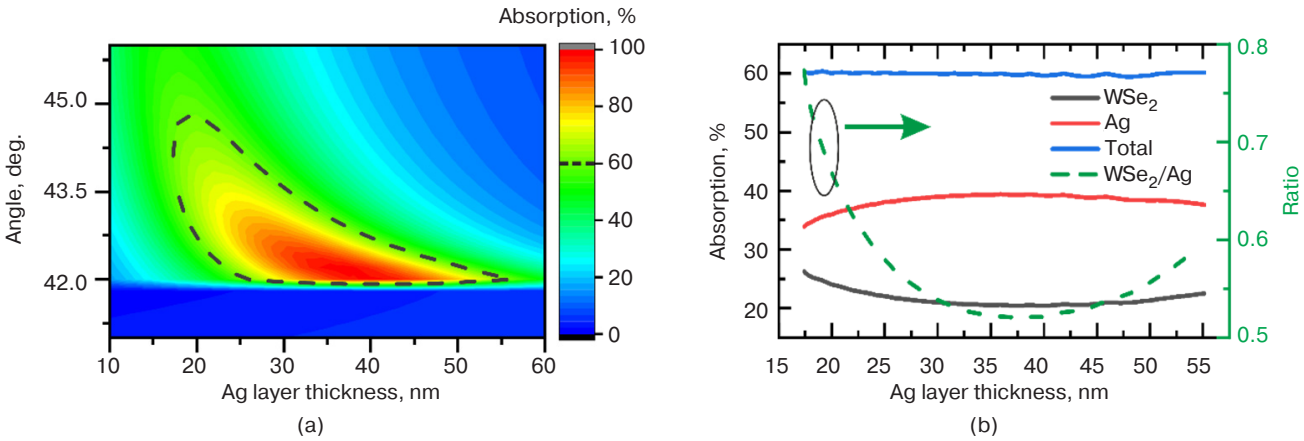

Fig. 6. Optical absorption map in the total structure as a function of silver layer thickness and beam angle of incidence (a) calculated absorption values in WSe_2 and Ag film separately as a function of Ag layer thickness (b)

angle of incidence (WSe_2 thickness is one monolayer). The contour of the graph with an absorption level of 60% (black dashed contour) was chosen as an example. As can be seen from the graph, an overall absorption equal to or greater than 60% can be achieved using different combinations of metal thickness and angle of incidence. However, this does not mean that the absorption in the TMD will be maximized. In order to demonstrate this effect, the absorption in the monolayer film, silver, was further calculated along the white line with arrows and the ratio of these absorptions was calculated (black, red, and dashed green lines in Fig. 6b). It can be clearly seen that the absorption of the total structure is 60% in the entire graph, but the absorption plots of the individual layers of the structure are not constant. The dotted green graph shows that the ratio of absorption in the semiconductor to absorption in the metal can vary from 0.7 to 0.5, i.e., differ almost by a factor of 1.5.

CONCLUSIONS

In the framework of this work, a theoretical study of optical absorption in a semiconductor WSe_2 film with Kretschmann configuration was conducted. The study took into account such parameters as the thickness of WSe_2, the thickness of the silver layer and the angle of light incidence. At the exciton peak wavelength (740 nm), a high absorption level (more than 80%) is achieved when the thickness of WSe_2 is 8 nm and above (corresponding to 15 monoatomic layers). In this case, the thickness of the silver layer is up to 20 nm and the angle of incidence in the range of 50° to 85°. In order to achieve 100% absorption, a WSe_2 thickness of about 22 nm or more (corresponding to 40 layers) is required. The Ag layer thickness value should be less than 10 nm, and the angle of incidence in the range of 55° to 85°.

The maximum achievable "area" of the absorption peak is observed at a silver layer thickness of up to 5 nm and an angle of incidence between 42° and 60°. For monolayer film, the optimum absorption values are achieved at a silver layer thickness of 37 nm and an incidence angle of 42.1°. Under these conditions, the total absorption in the structure is 100%, whereas the absorption in the monolayer film is 40%.

The importance of determining the optimal parameters for absorption directly in the semiconductor film needs to be emphasized. Despite the same absorption values throughout the structure, the absorption ratio between the WSe_2 semiconductor layer and the Ag metal layer can vary between 0.7 and 0.5. This information is of key importance for the development of nano- and optoelectronics devices such as phototransistors and photodetectors with a two-dimensional semiconductor channel.

ACKNOWLEDGMENTS

The main results obtained were supported by the Ministry of Science and Higher Education of the Russian Federation (State Assignment No. FSFZ-2023-0005). The authors thank RTU MIREA for the support (grant "For Young Scientists" NICh-55 "Polarization-sensitive optical detectors based on two-dimensional semiconductors") and the Foundation for Promotion of Innovations under the UMNIK program (contract No. 18383GU/2023 dated 09.08.2023).

Authors' contributions

A.A. Guskov—theoretical modeling, conducting numerical calculations using the finite element method to solve Maxwell's equations, and writing the text of the article.

N.V. Bezvikonnyi—visualization and systematization of results, creating graphs and diagrams illustrating key parameters and the dependence of light absorption efficiency on various factors.

S.D. Lavrov—overall project supervision, formulation of the research problem, strategic direction of the project, ensuring the achievement of set goals and high quality of the results.

REFERENCES

1. Liu J.-T., Wang T.-B., Li X.-J., Liu N.-H. Enhanced Absorption of Monolayer MoS_2 with Resonant Back Reflector. *J. Appl. Phys*. 2014;115:193511. https://doi.org/10.1063/1.4878700
2. Jeong H.Y., Kim U.J., Kim H., et al. Optical Gain in MoS_2 via Coupling with Nanostructured Substrate: Fabry–Perot Interference and Plasmonic Excitation. *ACS Nano*. 2016;10(9):8192–8198. https://doi.org/10.1021/acsnano.6b03237
3. Huang X., Feng X., Chen L., Wang L., Tan W.C., Huang L., Ang K.-W. Fabry-Perot Cavity Enhanced Light-Matter Interactions in Two-Dimensional van Der Waals Heterostructure. *Nano Energy*. 2019;62:667–673. https://doi.org/10.1016/j.nanoen.2019.05.090
4. Kumari S., Dalal J., Kumar V., Kumar A., Ohlan A. Emerging Two-Dimensional Materials for Electromagnetic Interference Shielding Application. *Int. J. Mol. Sci*. 2023;24(15):12267. https://doi.org/10.3390/ijms241512267
5. Gorbatova A.V., Khusyainov D.I., Yachmenev A.E., Khabibullin R.A., Ponomarev D.S., Buryakov A.M., Mishina E.D. A Photoconductive THz Detector Based on a Superlattice Heterostructure with Plasmonic Amplification. *Tech. Phys. Lett*. 2020;46(11):1111–1115. https://doi.org/10.1134/S1063785020110218

6. Yu L., Liu D., Qi X.-Z., Xiong X., Feng L.-T., Li M., Guo G.-P., Guo G.-C., Ren X.-F. Gap Plasmon-Enhanced Photoluminescence of Monolayer MoS_2 in Hybrid Nanostructure. *Chinese Phys. B*. 2018;27(4):047302. https://doi.org/10.1088/1674-1056/27/4/047302
7. Johnson A.D., Cheng F., Tsai Y., Shih C.K. Giant Enhancement of Defect-Bound Exciton Luminescence and Suppression of Band-Edge Luminescence in Monolayer WSe_2-Ag Plasmonic Hybrid Structures. *Nano Lett*. 2017;17(7):4317–4322. https://doi.org/10.1021/acs.nanolett.7b01364
8. Butun S., Tongay S., Aydin K. Enhanced Light Emission from Large-Area Monolayer MoS_2 Using Plasmonic Nanodisc Arrays. *Nano Lett.* 2015;15(4):2700–2704. https://doi.org/10.1021/acs.nanolett.5b00407
9. Su H., Wu S., Yang Y., Leng Q., Huang L., Fu J., Wang Q., Liu H., Zhou L. Surface Plasmon Polariton–Enhanced Photoluminescence of Monolayer MoS_2 on Suspended Periodic Metallic Structures. *Nanophotonics*. 2020;10(2):975. https://doi.org/10.1515/nanoph-2020-0545
10. Miao J., Hu W., Jing Y., Luo W., Liao L., Pan A., Wu S., Cheng J., Chen X., Lu W. Surface Plasmon-Enhanced Photodetection in Few Layer Mo_{S2} Phototransistors with Au Nanostructure Arrays. *Small*. 2015;11(20):2392–2398. https://doi.org/10.1002/smll.201403422
11. Xu H. Enhanced Light–Matter Interaction of a MoS_2 Monolayer with a Gold Mirror Layer. *RSC Adv*. 2017;7(37):23109–23113. https://doi.org/10.1039/C6RA27691A
12. Guo J., Li S., He Z., et al. Near-Infrared Photodetector Based on Few-Layer MoS_2 with Sensitivity Enhanced by Localized Surface Plasmon Resonance. *Appl. Surf. Sci.* 2019;483:1037–1043. https://doi.org/10.1016%2Fj.apsusc.2019.04.044
13. Li Y., DiStefano J.G., Murthy A.A., Cain J.D., et. al. Superior Plasmonic Photodetectors Based on Au@MoS_2 Core–Shell Heterostructures. *ACS Nano*. 2017;11(10):10321–10329. https://doi.org/10.1021/acsnano.7b05071
14. Kats M.A., Genevet P., Aoust G., et. al. Giant Birefringence in Optical Antenna Arrays with Widely Tailorable Optical Anisotropy. *Proc. Natl. Acad. Sci*. 2012;109(31):12364–12368. http://doi.org/10.1073/pnas.1210686109
15. Ross M.B., Blaber M.G., Schatz G.C. Using Nanoscale and Mesoscale Anisotropy to Engineer the Optical Response of Three-Dimensional Plasmonic Metamaterials. *Nat. Commun.* 2014;5(1):4090. https://doi.org/10.1038/ncomms5090
16. Li H.-J., Ren Y.-Z., Hu J.-G., Qin M., Wang L.-L. Wavelength-Selective Wide-Angle Light Absorption Enhancement in Monolayers of Transition-Metal Dichalcogenides. *J. Light. Technol.* 2018;36(16):3236–3241. https://doi.org/10.1109/JLT.2018.2840847
17. Bahauddin S.M., Robatjazi H., Thomann I. Broadband Absorption Engineering to Enhance Light Absorption in Monolayer MoS_2. *ACS Photonics*. 2016;3(5):853–862. http://doi.org/10.1021/acsphotonics.6b00081
18. Ouyang Q., Zeng S., Dinh X.-Q., Coquet P., Yong K.-T. Sensitivity Enhancement of MoS_2 Nanosheet Based Surface Plasmon Resonance Biosensor. *Procedia Eng*. 2016;140:134–139. https://doi.org/10.1016/j.proeng.2015.08.1114
19. Ouyang Q., Zeng S., Jiang L., et al. Sensitivity Enhancement of Transition Metal Dichalcogenides/Silicon Nanostructure-Based Surface Plasmon Resonance Biosensor. *Sci. Rep.* 2016;6(1):28190. https://doi.org/10.1038/srep28190
20. Oumekloul Z., Zeng S., Achaoui Y., Mir A., Akjouj A. Multi-Layer MoS_2-Based Plasmonic Gold Nanowires at Near-Perfect Absorption for Energy Harvesting. *Plasmonics*. 2021;16(5):1613–1621. https://doi.org/10.1007/s11468-021-01405-w
21. Furchi M.M., Polyushkin D.K., Pospischil A., Mueller T. Mechanisms of Photoconductivity in Atomically Thin MoS_2. *Nano Lett*. 2014;14(11):6165–6170. https://doi.org/10.1021/nl502339q
22. Di Bartolomeo A., Genovese L., Foller T., et al. Electrical Transport and Persistent Photoconductivity in Monolayer MoS_2 Phototransistors. *Nanotechnology*. 2017;28(11):214002. https://doi.org/10.1088/1361-6528/aa6d98
23. Huang Y., Zhuge F., Hou J., et al. Van Der Waals Coupled Organic Molecules with Monolayer MoS_2 for Fast Response Photodetectors with Gate-Tunable Responsivity. *ACS Nano*. 2018;12(4):4062–4073. https://doi.org/10.1021/acsnano.8b02380
24. Liu Y., Zhang H., Geng Y., et al. Long-Range Surface Plasmon Resonance Configuration for Enhancing SERS with an Adjustable Refractive Index Sample Buffer to Maintain the Symmetry Condition. *ACS Omega*. 2020;5(51):32951–32958. https://doi.org/10.1021/acsomega.0c03923
25. Borah R., Smets J., Ninakanti R., et al. Self-Assembled Ligand-Capped Plasmonic Au Nanoparticle Films in the Kretschmann Configuration for Sensing of Volatile Organic Compounds. *ACS Appl. Nano Mater.* 2022;5(8):11494–11505. http://doi.org/10.1021/acsanm.2c02524
26. Jamil N.A., Menon P.S., Said F.A., et al. Graphene-Based Surface Plasmon Resonance Urea Biosensor Using Kretschmann Configuration. In: *2017 IEEE Regional Symposium on Micro and Nanoelectronics* (*RSM*). IEEE; 2017. P. 112–115. https://doi.org/10.1109/RSM.2017.8069122
27. Shukla N., Chetri P., Boruah R., Gogoi A., Ahmed G.A. Surface Plasmon Resonance Biosensors Based on Kretschmann Configuration: Basic Instrumentation and Applications. In: Biswas R., Mazumder N. (Eds.). *Recent Advances in Plasmonic Probes. Lecture Notes in Nanoscale Science and Technology*. 2022. V. 33. P. 191–222. https://doi.org/10.1007/978-3-030-99491-4_6
28. Rodrigues E.P., Lima A.M.N., Oliveira L.C., et al. Surface Plasmon Resonance Features of Corrugatec Copper and Gold Films: Grating Mode Operation with Wavelength Interrogation. In: *2017 2nd International Symposium on Instrumentation Systems, Circuits and Transducers* (*INSCIT*). IEEE; 2017. https://doi.org/10.1109/INSCIT.2017.8103505
29. Maheswari P., Ravi V., Rajesh K.B., Rajan Jha. High Performance Bimetallic(Cu-Co) Surface Plasmon Resonance Sensor Using Hybrid Configuration of 2D Materials. *J. Environ. Nanotechnol*. 2022;11(3):01–10. https://doi.org/10.13074/jent.2022.09.223455

30. West P.R., Ishii S., Naik G.V., Emani N.K., Shalaev V.M., Boltasseva A. Searching for Better Plasmonic Materials. *Laser Photon*. Rev. 2010;4(6):795–808. https://doi.org/10.1002/lpor.200900055
31. Rycenga M., Cobley C.M., Zeng J., et al. Controlling the Synthesis and Assembly of Silver Nanostructures for Plasmonic Applications. *Chem. Rev*. 2011;111(6):3669–3712. https://doi.org/10.1021/cr100275d
32. Amendola V., Bakr O.M., Stellacci F. A Study of the Surface Plasmon Resonance of Silver Nanoparticles by the Discrete Dipole Approximation Method: Effect of Shape, Size, Structure, and Assembly. *Plasmonics*. 2010;5(1):85–97. http://doi.org/10.1007/s11468-009-9120-4
33. Rakić A.D., Djurišić A.B., Elazar J.M., Majewski M.L. Optical Properties of Metallic Films for Vertical-Cavity Optoelectronic Devices. *Appl. Opt.* 1998;37(22):5271. https://doi.org/10.1364/ao.37.005271
34. Gu H., Song B., Fang M., et al. Layer-Dependent Dielectric and Optical Properties of Centimeter-Scale 2D WSe_2: Evolution from a Single Layer to Few Layers. *Nanoscale*. 2019;11(47):22762–22771. http://doi.org/10.1039/C9NR04270A
35. Leong H.-S., Guo J., Lindquist R.G., Liu Q.H. Surface Plasmon Resonance in Nanostructured Metal Films under the Kretschmann Configuration. *J. Appl. Phys.* 2009;106(12):124314–124314-5. http://doi.org/10.1063/1.3273359

About the authors

Andrey A. Guskov, Research Intern, Department of Nanoelectronics, Institute for Advanced Technologies and Industrial Programming, MIREA – Russian Technological University (78, Vernadskogo pr., Moscow, 119454 Russia). E-mail: guskov@mirea.ru. Scopus Author ID 57225969940, ResearcherID AAE-2479-2022, RSCI SPIN-code 8000-3575, https://orcid.org/0000-0002-8462-5811

Nikita V. Bezvikonnyi, Research Intern, Department of Nanoelectronics, Institute for Advanced Technologies and Industrial Programming, MIREA – Russian Technological University (78, Vernadskogo pr., Moscow, 119454 Russia). E-mail: bezvikonnyj@mirea.ru. https://orcid.org/0000-0003-2222-4307

Sergey D. Lavrov, Cand. Sci. (Phys.-Math.), Associate Professor, Department of Nanoelectronics, Institute for Advanced Technologies and Industrial Programming, MIREA – Russian Technological University (78, Vernadskogo pr., Moscow, 119454 Russia). E-mail: lavrov_s@mirea.ru. Scopus Author ID 55453548100, ResearcherID G-2912-2016, RSCI SPIN-code 5918-8994, https://orcid.org/0000-0002-9432-860X

Об авторах

Гуськов Андрей Александрович, стажер-исследователь, кафедра наноэлектроники, Институт перспективных технологий и индустриального программирования, ФГБОУ ВО «МИРЭА – Российский технологический университет» (119454, Россия, Москва, пр-т Вернадского, д. 78). E-mail: guskov@mirea.ru. Scopus Author ID 57225969940, ResearcherID AAE-2479-2022, SPIN-код РИНЦ 8000-3575, https://orcid.org/0000-0002-8462-5811

Безвиконный Никита Владиславович, стажер-исследователь, кафедра наноэлектроники, Институт перспективных технологий и индустриального программирования, ФГБОУ ВО «МИРЭА – Российский технологический университет» (119454, Россия, Москва, пр-т Вернадского, д. 78). E-mail: bezvikonnyj@mirea.ru. https://orcid.org/0000-0003-2222-4307

Лавров Сергей Дмитриевич, к.ф.-м.н., доцент, кафедра наноэлектроники, Институт перспективных технологий и индустриального программирования, ФГБОУ ВО «МИРЭА – Российский технологический университет» (119454, Россия, Москва, пр-т Вернадского, д. 78). E-mail: lavrov_s@mirea.ru. Scopus Author ID 55453548100, ResearcherID G-2912-2016, SPIN-код РИНЦ 5918-8994, https://orcid.org/0000-0002-9432-860X

Translated from Russian into English by Lyudmila O. Bychkova
Edited for English language and spelling by Dr. David Mossop

Mathematical modeling

Математическое моделирование

UDC 330.4
https://doi.org/10.32362/2500-316X-2024-12-4-106-116
EDN WDYUFJ

RESEARCH ARTICLE

Neural network analysis in time series forecasting

Bakhtierzhon Pashshoev,
Denis A. Petrusevich @

MIREA — Russian Technological University, Moscow, 119454 Russia
@ *Corresponding author, e-mail: petrusevich@mirea.ru, petrdenis@mail.ru*

Abstract

Objectives. To build neural network models of time series (LSTM, GRU, RNN) and compare the results of forecasting with their mutual help and the results of standard models (ARIMA, ETS), in order to ascertain in which cases a certain group of models should be used.

Methods. The paper provides a review of neural network models and considers the structure of RNN, LSTM, and GRU models. They are used for modeling time series in Russian macroeconomic statistics. The quality of model adjustment to the data and the quality of forecasts are compared experimentally. Neural network and standard models can be used both for the entire series and for its parts (trend and seasonality). When building a forecast for several time intervals in the future, two approaches are considered: building a forecast for the entire interval at once, and step-by-step forecasting. In this way there are several combinations of models that can be used for forecasting. These approaches are analyzed in the computational experiment.

Results. Several experiments have been conducted in which standard (ARIMA, ETS, LOESS) and neural network models (LSTM, GRU, RNN) are built and compared in terms of proximity of the forecast to the series data in the test period.

Conclusions. In the case of seasonal time series, models based on neural networks surpassed the standard ARIMA and ETS models in terms of forecast accuracy for the test period. The single-step forecast is computationally less efficient than the integral forecast for the entire target period. However, it is not possible to accurately indicate which approach is the best in terms of quality for a given series. Combined models (neural networks for trend, ARIMA for seasonality) almost always give good results. When forecasting a non-seasonal heteroskedastic series of share price, the standard approaches (LOESS method and ETS model) showed the best results.

Keywords: dynamic series, macroeconomic statistics, GRU, LSTM, RNN, DNN, time series

• **Submitted:** 21.06.2023 • **Revised:** 15.02.2024 • **Accepted:** 26.05.2024

For citation: Pashshoev B., Petrusevich D.A. Neural network analysis in time series forecasting. *Russ. Technol. J.* 2024;12(4):106–116. https://doi.org/10.32362/2500-316X-2024-12-4-106-116

Financial disclosure: The authors have no a financial or property interest in any material or method mentioned.

The authors declare no conflicts of interest.

НАУЧНАЯ СТАТЬЯ

Анализ нейросетевых моделей для прогнозирования временных рядов

Б. Пашшоев,
Д.А. Петрусевич [@]

МИРЭА — Российский технологический университет, Москва, 119454 Россия
[@] *Автор для переписки, e-mail: petrusevich@mirea.ru, petrdenis@mail.ru*

Резюме

Цели. Основная цель работы – построить нейросетевые модели временных рядов (LSTM, GRU, RNN) и сравнить результаты прогнозирования с их помощью между собой и с результатами стандартных моделей (ARIMA, ETS), чтобы выяснить, в каких случаях следует пользоваться определенной группой моделей.

Методы. Проведен обзор нейросетевых моделей, рассмотрена структура моделей RNN, LSTM, GRU. Они используются для моделирования временных рядов российской макроэкономической статистики. Качество подстройки моделей под данные и качество прогнозов сравниваются в эксперименте. Нейросетевые и стандартные модели могут применяться как для всего ряда целиком, так и для его частей (тренд и сезонность). При построении прогноза на несколько временных промежутков вперед рассматриваются два подхода: построение прогноза сразу на весь промежуток и пошаговый прогноз. Так появляется несколько комбинаций моделей, которые могут использоваться для прогнозирования. Эти подходы проанализированы в вычислительном эксперименте.

Результаты. Проведено несколько экспериментов, в которых построены и сравниваются по близости прогноза к данным ряда в тестовом периоде стандартные (ARIMA, ETS, LOESS) и нейросетевые модели (LSTM, GRU, RNN).

Выводы. Для сезонных временных рядов модели на основе нейронных сетей превзошли по точности прогноза на тестовый период времени стандартные модели ARIMA, ETS. Одношаговый прогноз вычислительно менее эффективен, чем интегральный прогноз на весь целевой период, но точно указать, для каких рядов какой именно подход оказывается лучшим по качеству, не удается. Комбинированные модели (нейронные сети для тренда, ARIMA – для сезонности) почти всегда дают хороший результат. При прогнозировании несезонного гетероскедастичного ряда курса акций лучшие результаты показали стандартные подходы (метод LOESS и модель ETS).

Ключевые слова: динамические ряды, макроэкономическая статистика, GRU, LSTM, RNN, DNN, временные ряды

• **Поступила:** 21.06.2023 • **Доработана:** 15.02.2024 • **Принята к опубликованию:** 26.05.2024

Для цитирования: Пашшоев Б., Петрусевич Д.А. Анализ нейросетевых моделей для прогнозирования временных рядов. *Russ. Technol. J*. 2024;12(4):106–116. https://doi.org/10.32362/2500-316X-2024-12-4-106-116

Прозрачность финансовой деятельности: Авторы не имеют финансовой заинтересованности в представленных материалах или методах.

Авторы заявляют об отсутствии конфликта интересов.

INTRODUCTION

This article analyzes the application of common neural network models for time series forecasting. Much research has been devoted to the topic of time series forecasting. In fact, several off-the-shelf approaches are used in practice, such as: ARIMA (autoregressive integrated moving average) models, ETS (exponential smoothing) models [1, 2], construction of regressions reflecting dependencies between time-varying parameters. These can be referred to statistical models [3]. GARCH (generalized autoregressive conditional heteroskedasticity) models are used when establishing the phenomenon of heteroskedasticity [1, 2]. Ready-made neural network models LSTM (long short-term memory) and GRU (gated recurrent unit) can be trained using available time series data. There are many publications where several models of different types are built at once to describe a certain temporal process and their forecasts are used together (they are specified below in the description of models). Estimation of forecast accuracy when applying a combination of ARIMA models is discussed [4, 5]. Due to the availability of a multitude of models, the question of which of them should be used for modeling the time process depending on its properties becomes essential [6]. The experimental part of the work considers the representation of seasonal monthly time series of personal income (HHI), and the real agricultural production index (AGR).[1] Non-seasonal time series is represented by stock prices and stock indices (in particular, the SberBank stock price).[2] The main objective of the paper is to determine which models should be used for modeling time processes.

The experimental section considers the construction of time series models ARIMA, neural network models LSTM, GRU, recurrent neural networks (RNN), and full-connected neural networks. Their forecasts for the test period are compared. The quality of neural network models built on such data is compared with the quality of ARIMA/ETS statistical models by information criteria and the quality of forecasts for the test period.

CONSIDERED APPROACHES TO TIME SERIES SIMULATION

When forecasting a time series, a model can be built in many ways. In particular, it is possible to train a neural network or build a statistical model based on the initial values of the time series. However, on the other hand, it is possible to use the division of the series into a seasonal component and a trend.

Usually, the trend T_t is a deterministic part of the time series y_t with a seasonal component S_t (it may not exist), and noise R_t, where t is time. The series can be represented in an additive or multiplicative form:

$$y_t = S_t + T_t + R_t, \quad (1)$$

$$y_t = S_t \times T_t \times R_t. \quad (2)$$

These approaches are equivalent.

In this case, one of the most common models for describing a time series that does not rely on neural networks is ARIMA(p, d, q). This consists of the autoregressive part (for a model of order p the values of the series X are made dependent on p of their previous values):

$$X_t = c + \varphi_1 X_{t-1} + \ldots + \varphi_p X_{t-p},$$

where $\varphi_i, i = \overline{1, p}$ are the coefficients of the function; and from the moving average part of the order q [1]:

$$X_t = \varepsilon_t + \theta_1 \varepsilon_{t-1} + \ldots + \theta_q \varepsilon_{t-q}.$$

where $\theta_i, i = \overline{1, q}$ are the coefficients of the function. The order d denotes the number of differentiations of the series.

In fact, when building a model, the trend is overcome by switching to a stationary time difference (by repeatedly differentiating the series until the statistical test confirms stationarity) [1, 6]. The work is carried out with the transformed stationary time series. As part of the computational part of the study, we compare its results with the forecasts of the other models.

Since, according to decompositions (1), (2), the parts responsible for seasonal fluctuations and noise can be separated during modeling, the neural network can be trained both on the basis of original data and separately on the basis of trend. Because such separation is possible, several approaches to training data for neural network training are presented in the computational experiment. Neural network models enable forecasting both trend and seasonality, so trend and seasonality can be separately predicted using their own models and the results combined. In the second approach the data is not separated (used, for example, in ARIMA, ETS models). When modeling the trend, the time series is first separated into trend, seasonal component and noise. A neural network model is trained on the basis of trend data, except that the trend is predicted after training. Then the final forecast is collected from the trend forecast, as well as the seasonal component and noise models. The

[1] Unified archive of economic and sociological data. Dynamic series of macroeconomic statistics of the Russian Federation. Indices of wages, monetary incomes of the population; real volume of agricultural production. https://web.archive.org/web/20230317111717/http://sophist.hse.ru/hse/nindex.shtml (in Russ.). Accessed June 01, 2024.

[2] SberBank share price (SBER). https://www.moex.com/ru/issue.aspx?board=TQBR&code=SBER (in Russ.). Accessed June 01, 2024.

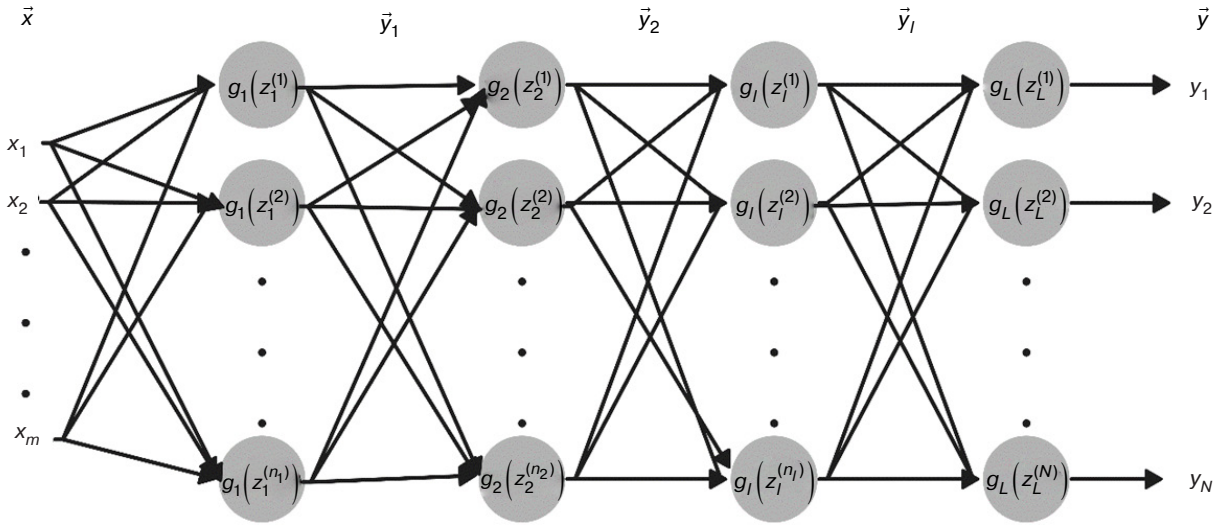

Fig. 1. DNN structure [8]. $\vec{x}$ is the input vector, $\vec{y}_i$ is the vector at the output of the *i*th layer of the network, $\vec{y}$ is the output vector of the entire network (result), $g(.)$ is the activation function, z_i^j is the input of the *j*th neuron in the *i*th layer is the weighted linear combination of the results of the previous layer (weights are adjusted during training)

separation into trend, noise and seasonality is done using LOESS (STL)[3] [1].

In addition, forecasting itself can also be done in two ways. Researchers are usually interested in forecasting not one step ahead, but for several or for the entire season (if the series is seasonal). In this way, it is possible to assess how well the model describes the data of the series. However, the forecast for several steps ahead can be made either at once (integral forecast) or one step at a time (one-step forecast). In the second case, each predicted value becomes a new part of the training sample, on the basis of which the model is constantly adjusted, while the forecast itself is made only one step ahead at each iteration. Both approaches are compared in a computational experiment in the form of single-step and multi-step forecasting.

Several models are involved in the computational experiment: dense neural networks (DNN), recurrent neural networks (RNN), long short-term memory networks (LSTM), and guided recurrent unit (GRU).

Fully connected neural networks are a widely known neural network architecture [7]. Each neuron receives a signal from all neurons of the previous layer (except for the network inputs), applies an activation function to their weighted combination and transmits the result to the neurons of the next layer. Various optimization methods are used to train fully-connected neural networks, such as gradient descent and its modifications. However, due to the large number of parameters, fully-connected networks can be prone to overtraining. Regularization methods such as L1 and L2 and dropout methods are used to combat overtraining. The structure of the network is shown in Fig. 1.

Recurrent neural networks RNN [9, 10] are used to simulate functional relationships between input features in the recent past, and the target variable in the future. As shown in Fig. 2, an RNN is periodically trained on a historical dataset, focusing on internal (hidden) state transitions from time state $t - 1$ to the cutoff t. The resulting model is defined by two weight matrices $\mathbf{W}_{xs}$ and $\mathbf{W}_y$, and two bias vectors $\mathbf{b}_s$ and $\mathbf{b}_y$. The output $\mathbf{y}_t$ depends on the internal state $\mathbf{S}_t$, which depends on both the current input $\mathbf{x}_t$ and the previous state $\mathbf{S}_{t-1}$:

$$\mathbf{S}_t = \text{th}[\mathbf{W}_{xs}(\mathbf{x}_t \oplus \mathbf{S}_{t-1}) + \mathbf{b}_s],$$
$$\mathbf{y}_t = \sigma(\mathbf{W}_y \mathbf{S}_t + \mathbf{b}_y).$$

Here $\mathbf{x}_t$ is the input vector at time t, $\sigma(\mathbf{x})$ is a sigmoid function, and the operation $\oplus$ is a concatenation. The main disadvantage of RNN is the problem of gradient decay, due to which the gradient becomes smaller over time. This is expressed by the fact that RNN memorizes information for only short periods of time.

Long Short Term Memory (LSTM) networks [11–26] are a variant of RNNs which partially resolve the fading gradient problem and learn longer term dependencies in time series. They are described at time t in terms of the internal (hidden) state $\mathbf{S}_t$ and the cell state $\mathbf{C}_t$. The state $\mathbf{C}_t$ depends on three parameters: the previous cell state $\mathbf{C}_{t-1}$; the previous internal state $\mathbf{S}_{t-1}$; and the input at the current time $\mathbf{x}_t$. The process depicted in Fig. 3, enables

[3] LOESS—locally estimated scatterplot smoothing; STL (seasonal and trend decomposition using LOESS)—method of decomposition of time series into trend, seasonality, and residuals.

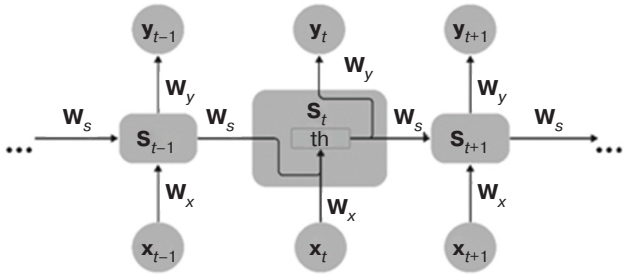

Fig. 2. RNN structure [8]

moving/filtering, multiplying/uniting, and adding information using forget, input, addition, and output gates implemented by the functions $\mathbf{x}_t$, $\mathbf{i}_t$, $\tilde{\mathbf{C}}_t$, and $\mathbf{O}_t$, respectively. This enables more precise control of learning long-term dependencies.

These functions are related as follows:

$$\mathbf{f}_t = \sigma(\mathbf{W}_f(\mathbf{x}_t \oplus \mathbf{S}_{t-1}) + \mathbf{b}_f),$$
$$\mathbf{i}_t = \sigma(\mathbf{W}_i(\mathbf{x}_t \oplus \mathbf{S}_{t-1}) + \mathbf{b}_i),$$
$$\tilde{\mathbf{C}}_t = \text{th}(\mathbf{W}_c(\mathbf{x}_t \oplus \mathbf{S}_{t-1}) + \mathbf{b}_c),$$
$$\mathbf{C}_t = \mathbf{f}_t\mathbf{C}_{t-1} + \mathbf{i}_t\tilde{\mathbf{C}}_t,$$
$$\mathbf{O}_t = \sigma(\mathbf{W}_O(\mathbf{x}_t \oplus \mathbf{S}_{t-1}) + \mathbf{b}_0),$$
$$\mathbf{S}_t = \mathbf{O}_t\text{th}(\mathbf{C}_t),$$
$$\mathbf{y}_t = \sigma(\mathbf{W}_y\mathbf{S}_t + \mathbf{b}_y),$$

where $\mathbf{W}_f$, $\mathbf{W}_i$, $\mathbf{W}_c$, $\mathbf{W}_O$, $\mathbf{W}_y$ are various weight matrices involved in the training. The functions are used for forecasting both independently (e.g., the spread of coronavirus in [12, 19, 26] is modeled based on LSTM) and in combination with other models in [14, 15]. A combination of the forecast of this model with the results of other models can be applied. In [12, 16, 24, 26], deep learning is used to tune LSTM-based models. In [11, 13, 19, 20], LSTM-based models are compared with other commonly used models in forecasting a certain time process.

Guided recurrence units (GRU) [13, 25, 27–29] are a variant of LSTM which can resolve the fading gradient problem even better. As can be seen from Fig. 4, the novelty of this method lies in the use of update, reset, and third gates implemented by functions $\mathbf{z}_t$, $\mathbf{r}_t$, $\tilde{\mathbf{S}}_t$ Each element has a different role in controlling the filtering, utilization, and merging of the previous information. The first term in the expression for the following state $(1-\mathbf{z}_t)\mathbf{S}_{t-1}$ enables configuration of what to keep from the past, while the element $\mathbf{z}_t\tilde{\mathbf{S}}_t$ determines what to use from current memory contents.

These functions are related as follows:

$$\mathbf{r}_t = \sigma(\mathbf{W}_r(\mathbf{x}_t \oplus \mathbf{S}_{t-1}) + \mathbf{b}_r),$$
$$\mathbf{z}_t = \sigma(\mathbf{W}_z(\mathbf{x}_t \oplus \mathbf{S}_{t-1}) + \mathbf{b}_z),$$
$$\tilde{\mathbf{S}}_t = \text{th}(\mathbf{W}_s(\mathbf{x}_t \oplus \mathbf{S}_{t-1}\mathbf{r}_t) + \mathbf{b}_s),$$
$$\mathbf{S}_t = (1-\mathbf{z}_t)\mathbf{S}_{t-1} + \mathbf{z}_t\tilde{\mathbf{S}}_t,$$
$$\mathbf{y}_t = \sigma(\mathbf{W}_y\mathbf{S}_t + \mathbf{b}_y).$$

Both applications of the GRU element connects with other neural networks (in [27, 28] with CNN networks [7]) and cascaded element construction [29] can be found in the literature.

COMPUTATIONAL EXPERIMENT

This work presents the results of three experiments on the representation of monthly time series: household income (HHI); the index of the real agricultural production (AGR) (the indices have dimensionless units); and the daily time series of the SberBank of the Russian Federation share price measured in rubles.

The fully connected neural network has the structure shown in the Table 1.

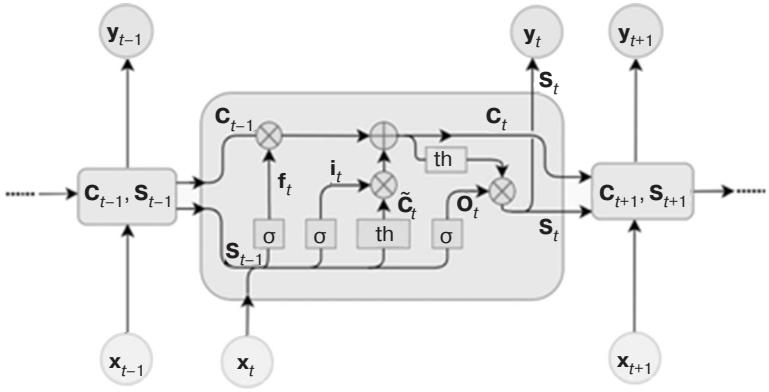

Fig. 3. LSTM structure [8]

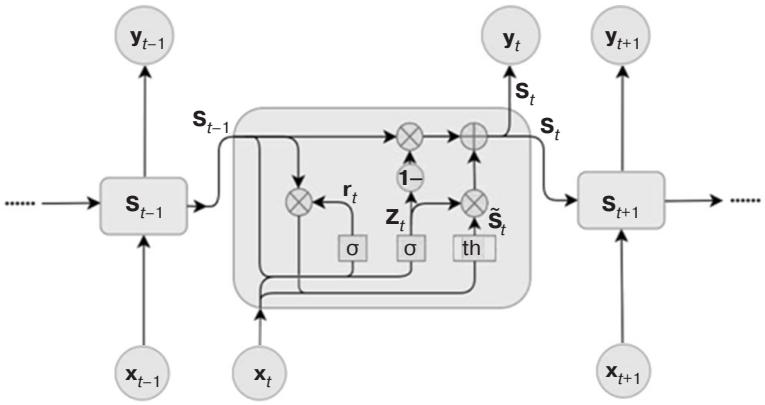

Fig. 4. GRU structure [8]

Table 1. Structure of a fully connected DNN neural network

Forecast type	Layer number	Number of neurons
Single-step	Input layer, 0	6
	Layers 1, 5	64
	Layers 2–4	128
	Output layer, 6	1
Integral (forecast for 12 time periods ahead)	Input layer, 0	24
	Layers 1, 5	64
	Layers 2–4	128
	Output layer, 6	12

In single-step forecasting, the network makes a forecast 1 step ahead. This data then becomes part of the training data, and the next step is made (one neuron in the output layer). In the integral approach, the forecast is made for 12 steps forward at once (for a year, since a series with annual seasonality is considered; there are 12 neurons in the output layer).

In order to evaluate model forecasts, measures of the closeness of the forecast vector and the vector of real values of the quantity are considered [1, 2]:

$$\mathrm{RMSE} = \sqrt{\frac{\sum_t (\tau(t) - ts(t))^2}{N}}, \qquad \mathrm{MAE} = \frac{\sum_t |\tau(t) - ts(t)|}{N}. \tag{3}$$

Here RMSE is a root mean square error; MAE is a mean absolute error; $\tau(t)$ are the real values of the time series; $ts(t)$ is the forecast of the mathematical model; N is the length of the forecasting segment (most often, it coincides with seasonality, and here we are talking about time series with annual seasonality, so $N = 12$).

The RNN network architecture chosen for integral trend forecasting with a step of 12 consists of three RNN layers (each containing 64 neurons), as well as a single layer of fully-connected neurons (i.e., 12 neurons in terms of the number of predicted values). A time window of size **w** is fed to the input of the model. As a result of experiments, it was found that a single layer is unable to detect seasonality. Adding more than three layers does not significantly improve the quality of the forecast. For this reason, three layers are chosen. The total number of trained parameters in the model is 21516.

A simpler model containing only one RNN layer with 64 neurons and an input layer with a single neuron was chosen for single-step trend forecast. This resulted in a significant reduction in the number of trained

parameters to 4289, since additional layers did not noticeably improve the forecast quality.

LSTM and GRU architectures were chosen to be identical in terms of the structure of the RNN network model described above. However, the number of trained parameters of LSTM for the two different architectures is 83724 and 16961, respectively, while for GRU it is 63564 and 12929.

The classical ARIMA and ETS models are involved in the experiments [1, 2]. In the LOESS method, a trend is extracted based on the STL decomposition. It is then forecast for the test period using the ARIMA model. A seasonality model is superimposed on the forecast for the test period. In addition, the trend was estimated using a polynomial. Seasonality was estimated using ARIMA, and the results were combined.

Experiment 1 considers the index of money income of the Russian population for 2000–2020. All the considered models were adapted for the 2000–2020 training period (the crisis years 2008 and 2014 were removed and the data agglomerated). The results of their forecasts for the test period (2021) are compared in Table 2.

Table 2. Money income index models according to macroeconomic statistics of the Russian Federation and their forecasts for the test period

Time series model	MAE	RMSE
Polynomial of degree 4 + seasonality ARIMA(1, 1, 2)	3.42	4.52
LOESS method	3.49	4.57
ARIMA(6, 1, 5) with the seasonality $(0, 1, 1)_{12}$	5.86	7.01
ETS	6.57	8.47
DNN model for trend, single-step forecast	4.21	5.58
DNN model for trend, integral forecast	3.88	4.58
DNN model for trend and seasonality, single-step forecast	2.44	3.06
DNN model for trend, ARIMA(1, 1, 2) for seasonality, single-step forecast	**1.73**	**1.97**
DNN model for trend and seasonality, integral forecast	2.48	3.36
DNN model for trend, ARIMA(1, 1, 2) model for seasonality, integral forecast	**2.29**	**2.62**
RNN model for trend, single-step forecast	6.25	7.68
RNN model for trend, integral forecast	4.65	5.86
RNN model for trend and seasonality, single-step forecast	4.32	4.72
RNN model for trend, ARIMA(1, 1, 2) model for seasonality, single-step forecast	2.82	3.3
RNN model for trend and seasonality, integral forecast	3.88	4.45
RNN model for trend, ARIMA(1, 1, 2) model for seasonality, integral forecast	**2.35**	**2.95**
LSTM model for trend, single-step forecast	23.43	30.68
LSTM model for trend, integral forecast	18.97	30.09
LSTM model for trend and seasonality, single-step forecast	3.83	4.25
LSTM model for trend, ARIMA(1, 1, 2) model for seasonality, single-step forecast	**2.42**	**2.79**
LSTM model for trend and seasonality, integral forecast	5.91	6.63
LSTM model for trend, ARIMA model for seasonality, integral forecast	5.03	5.40
GRU model for trend, single-step forecast	19.00	29.28
GRU model for trend, integral forecast	20.05	27.30
GRU model for trend and seasonality, single-step forecast	3.81	4.24
GRU model for trend, ARIMA(1, 1, 2) model for seasonality, single-step forecast	**2.40**	**2.76**
GRU model for trend and seasonality, integral forecast	3.94	4.36
GRU model for trend, ARIMA(1, 1, 2) model for seasonality, integral forecast	**2.41**	**2.89**

Table 3. Models of the index of real volume of agricultural production according to macroeconomic statistics of the Russian Federation and their forecasts for the test period

Time series model	MAE	RMSE
Polynomial of degree 1 + ARIMA(2, 0, 1) with seasonality $(2, 1, 1)_{12}$	67.04	77.76
Logarithmic function $y = a_0 + a_1 \ln x$	55.04	80.92
Exponential function $y = \exp(a_0 + a_1 x)$	53.00	90.48
ARIMA(3, 0, 1) with a seasonality $(2, 1, 2)_{12}$	13.24	18.51
ETS	17.22	25.40
DNN model for trend, single-step forecast	15.97	29.70
DNN model for trend, integral forecast	14.63	26.61
DNN model for trend and seasonality, single-step forecast	9.75	16.18
DNN model for trend, ARIMA(2, 0, 1) × $(2, 1, 1)_{12}$ model for seasonality, single-step forecast	8.71	11.94
DNN model for trend and seasonality, integral forecast	9.09	15.31
DNN model for trend, ARIMA(2, 0, 1) × $(2, 1, 1)_{12}$ model for seasonality, integral forecast	**6.81**	**10.90**
RNN model for trend, single-step forecast	17.02	23.72
RNN model for trend, integral forecast	13.94	16.66
RNN model for trend and seasonality, single-step forecast	8.37	14.67
RNN model for trend, ARIMA model for seasonality, single-step forecast	**6.72**	**10.53**
RNN model for trend and seasonality, integral forecast	10.51	16.17
RNN model for trend, модель ARIMA(2, 0, 1) × $(2, 1, 1)_{12}$ model for seasonality, single-step forecast	8.95	11.81
LSTM model for trend, single-step forecast	26.56	38.00
LSTM model for trend, integral forecast	23.35	31.07
LSTM model for trend and seasonality, single-step forecast	8.39	14.76
LSTM model for trend, ARIMA(2, 0, 1) × $(2, 1, 1)_{12}$ model for seasonality, single-step forecast	**6.87**	**10.58**
LSTM model for trend and seasonality, integral forecast	8.78	15.41
LSTM model for trend, ARIMA(2, 0, 1) × $(2, 1, 1)_{12}$ model for seasonality, integral forecast	7.30	11.13
GRU model for trend, single-step forecast	24.82	34.09
GRU model for trend, integral forecast	21.47	26.67
GRU model for trend and seasonality, single-step forecast	8.90	15.48
GRU model for trend, модель ARIMA(2, 0, 1) × $(2, 1, 1)_{12}$ model for seasonality, single-step forecast	7.88	11.24
GRU model for trend and seasonality, integral forecast	10.11	16.34
GRU model for trend, модель ARIMA(2, 0, 1) × $(2, 1, 1)_{12}$ model for seasonality, integral forecast	8.87	12.09

Based on an analysis of ACF/PACF[4] functions, a conclusion was drawn about the presence of seasonality in 12 months (which is confirmed by statistical tests) and ARIMA(p, d, q) mathematical models were selected. Their selection and analysis are detailed in [3, 30].

Note that the best forecasts are obtained for a combination of models (neural network model for trend, ARIMA for seasonality). Practically any model for the trend gives good results (the best results are obtained by the full-link network). The LSTM model performed better for single-step forecasts, the RNN and DNN models performed better for integral forecasts, while the GRU model worked well for both approaches. In this experiment, neural network models outperformed standard time series models.

Experiment 2 considers the index of real agricultural production in Russia for 2000–2020 (a detailed analysis of the series is presented in [30]). All the models considered were adapted for the 2000–2020 training period (the crisis years 2008 and 2014 were removed and the data agglomerated). The results of their forecasts for the test period (2021) are compared in Table 3.

[4] ACF—autocorrelation function; PCF—partial autocorrelation function.

According to ACF/PACF functions, it can be concluded that there is seasonality in 12 months (which is confirmed by statistical tests). Also, due to the presence of a spike in the PACF diagram, all ARIMA(p, d, q) models with orders p, q from 1 to 6 were tested. The ARIMA(2, 0, 1) model with annual seasonality of the form $(2, 1, 1)_{12}$ is used for a combination of models in which the standard ARIMA model is used to describe seasonality and the trend is specified using a neural network model or polynomial.

Note that the best forecasts are obtained for a combination of models (neural network model for trend, ARIMA for seasonality). At the same time, not all models give good results for the trend (RNN, DNN and LSTM give the best results). RNN and LSTM models performed better for single-step forecast, and DNN—for integral forecast. In this experiment, neural network models outperformed standard time series models.

Let us separately consider a series of exchange rate of exchange-traded shares: the shares of SberBank of the Russian Federation. It has heteroskedasticity: its mathematical expectation and dispersion change with time. This is confirmed by the McLeod–Li test (all components of the resultant vector are zero with an accuracy of 0.01) [31]. Due to the fact that it is non-seasonal, only two approaches are possible for each neural network system: to make a forecast for the entire test period at once (integral) or to make step-by-step forecasts, declaring each new step as part of the training sample, in order to move to the next point in time. They clearly indicate the absence of seasonality and the need to test second-order models. ARIMA(2, 1, 3) model was chosen for the series (the analysis of the series is given in [30]).

The forecasting results are presented in Table 4.

The best results are obtained by classical methods of series modeling: LOESS, ETS, and ARIMA models. Among neural network methods, the best result was shown by GRU model. In all cases, forecasts made one step ahead several times are better than a single forecast for a given period.

CONCLUSIONS

For seasonal time series, neural network-based models outperform standard models in terms of forecast accuracy for the test time period. The forecast accuracy of neural network models in all experiments was better than that of ARIMA/ETS models. The single-step forecast appears to be computationally less efficient than the integral forecast for the entire target period at once. However, it is not possible to specify precisely for which series the single-step or integral forecast is better in terms of quality.

Combined models, in which neural network models are used to model trend, and ARIMA model is used to model seasonality (when decomposed into trend, noise and seasonality, for example, using STL), almost always give a good result. More often than not, it is this model which provides the best result. At the same time, since the results are approximately equal, due to the lower complexity of construction and training, the RNN and full-link DNN models appear preferable.

When forecasting non-seasonal series, one-step forecasting is recommended (each predicted value is announced as part of the training sample to predict the next value). When forecasting the share price of SberBank of the Russian Federation, the best results were shown by the standard models and RNN.

Table 4. SberBank of the Russian Federation share price time series models

Time series model	MAE	RMSE
LOESS method	**0.004**	**0.006**
ARIMA (2, 1, 3)	**11.23**	**42.11**
ETS	**4.95**	**20.68**
DNN model for trend, single-step forecast	23.49	27.22
DNN model for trend, integral forecast	51.00	62.80
RNN model for trend, single-step forecast	16.42	21.69
RNN model for trend, integral forecast	80.53	86.39
LSTM model for trend, single-step forecast	49.74	59.32
LSTM model for trend, integral forecast	76.95	81.40
GRU model for trend, single-step forecast	**7.14**	**29.28**
GRU model for trend, integral forecast	24.66	85.05

When building neural networks modeling, the behavior of time series, several layers should be used (5–6 layers were used in this work). Networks with 1–2 layers do not extract features useful for forecasting even when the number of neurons in a layer is increased.

Authors' contribution. All authors equally contributed to the research work.

REFERENCES

1. Hyndman R.J., Athanasopoulos G. *Forecasting: principles and practice.* 3rd ed. OTexts; 2021. 442 p. ISBN-13 978-0987507136
2. Stock J.H., Watson M.W. *Introduction to Econometrics.* 3rd ed. Pearson; 2019. ISBN-13 978-9352863501
3. Kalugin T.R., Kim A.K., Petrusevich D.A. Analysis of the high order ADL(*p, q*) models used to describe connections between time series. *Russ. Technol. J*. 2020;8(2):7–22 (in Russ.). https://doi.org/10.32362/2500-316X-2020-8-2-7-22
4. Petrusevich D. Improvement of time series forecasting quality by means of multiple models prediction averaging. In: *Proceedings of the Third International Workshop on Modeling, Information Processing and Computing* (*MIP: Computing-2021*). 2021;2899:109–117. https://doi.org/10.47813/dnit-mip3/2021-2899-109-117
5. Beletskaya N., Petrusevich D. Linear combinations of time series models with minimal forecast variance. *J. Commun. Technol. Electron*. 2023;67(1):144–158. https://doi.org/10.1134/S1064226922130022
6. Box G., Jenkins G. *Time Series Analysis: Forecast and Management*. John Wiley & Sons; 2015. 712 p. ISBN 978-11185674918
7. Haykin S. *Neural Networks and Learning Machines*. Pearson Education; 2011. 936 p. ISBN 978-0133002553
8. Shi J., Jain M., Narasimhan G. *Time Series Forecasting* (*TSF*) *Using Various Deep Learning Models.* 2022. Available from URL: https://arxiv.org/abs/2204.11115v1, https://doi.org/10.48550/arXiv.2204.11115
9. Amalou I., Mouhni N., Abdali A. Multivariate time series prediction by RNN architectures for energy consumption forecasting. *Energy Rep*. 2022;8:1084–1091. https://doi.org/10.1016/j.egyr.2022.07.139
10. Aseeri A. Effective RNN-Based forecasting methodology design for improving short-term power load forecasts: application to large-scale power-grid time series. *J. Computational Sci*. 2023;68(4):101984. https://doi.org/10.1016/j.jocs.2023.101984
11. Ning Y., Kazemi H., Tahmasebi P. A comparative machine learning study for time series oil production forecasting: ARIMA, LSTM, and Prophet. *Comput. Geosci*. 2022;164(1):105126. https://doi.org/10.1016/j.cageo.2022.105126
12. Wang P., Zheng X., Ai G., Liu D., Zhu B. Time series prediction for the epidemic trends of COVID-19 using the improved LSTM deep learning method: Case studies in Russia, Peru and Iran. *Chaos, Solitons & Fractals*. 2020;140:110214. https://doi.org/10.1016/j.chaos.2020.110214
13. Arunkumar K.E., Kalaga D.V., Kumar M.S., Kawaji M., Brenza T.M. Comparative analysis of Gated Recurrent Units (GRU), long Short-Term memory (LSTM) cells, autoregressive Integrated moving average (ARIMA), seasonal autoregressive Integrated moving average (SARIMA) for forecasting COVID-19 trends. *Alexandria Eng. J*. 2022;61(10):7585–7603. https://doi.org/10.1016/j.aej.2022.01.011
14. Kumar B., Sunil, Yadav N. A novel hybrid model combining *βSARMA* and LSTM for time series forecasting. *Appl. Soft Comput*. 2023;134:110019. https://doi.org/10.1016/j.asoc.2023.110019
15. Abebe M., Noh Y., Kang Y.-J., Seo C., Kim D., Seo J. Ship trajectory planning for collision avoidance using hybrid ARIMA-LSTM models. *Ocean Eng*. 2022;256:111527. https://doi.org/10.1016/j.oceaneng.2022.111527
16. Cascone L., Sadiq S., Ullah S., Mirjalili S., Ur H., Siddiqui R., Umer M. Predicting household electric power consumption using multi-step time series with convolutional LSTM. *Big Data Res*. 2023;31:100360. https://doi.org/10.1016/j.bdr.2022.100360
17. Wang H., Zhang Y., Liang J., Liu L. DAFA-BiLSTM: Deep Autoregression Feature Augmented Bidirectional LSTM network for time series prediction. *Neural Netw*. 2023;157:240–256. https://doi.org/10.1016/j.neunet.2022.10.009
18. Zhao L., Mo C., Ma J., Chen Z., Yao C. LSTM-MFCN: A time series classifier based on multi-scale spatial–temporal features. *Computer Commun*. 2022;182(3):52–59. https://doi.org/10.1016/j.comcom.2021.10.036
19. Rasjid Z.E., Setiawan R., Effendi A. A Comparison: Prediction of Death and Infected COVID-19 Cases in Indonesia Using Time Series Smoothing and LSTM Neural Network. *Procedia Comput. Sci*. 2021;179(5):982–988. http://doi.org/10.1016/j.procs.2021.01.102
20. Dubey A.K., Kumar A., García-Díaz V., Sharma A.K., Kanhaiya K. Study and analysis of SARIMA and LSTM in forecasting time series data. *Sustain. Energy Technol. Assess*. 2021;47:101474. https://doi.org/10.1016/j.seta.2021.101474
21. Wu Z., Yin H., He H., Li Y. Dynamic-LSTM hybrid models to improve seasonal drought predictions over China. *J. Hydrol*. 2022;615:128706. https://doi.org/10.1016/j.jhydrol.2022.128706
22. Yan Y., Wang X., Ren F., Shao Z., Tian C. Wind speed prediction using a hybrid model of EEMD and LSTM considering seasonal features. *Energy Rep*. 2022;8:8965–8980. https://doi.org/10.1016/j.egyr.2022.07.007
23. Bian S., Wang Z., Song W., Zhou X. Feature extraction and classification of time-varying power load characteristics based on PCANet and CNN+Bi-LSTM algorithms. *Electric Power Systems Research*. 2023;217(6):109149. https://doi.org/10.1016/j.epsr.2023.109149

24. Sangiorgio M., Dercole F. Robustness of LSTM neural networks for multi-step forecasting of chaotic time series. *Chaos, Solitons & Fractals*. 2020;139(8):10045. https://doi.org/10.1016/j.chaos.2020.110045
25. Liu X., Lin Z., Feng Z. Short-term offshore wind speed forecast by seasonal ARIMA – A comparison against GRU and LSTM. *Energy*. 2021;227:120492. http://doi.org/10.1016/j.energy.2021.120492
26. Shahid F., Zameer A., Muneeb M. Predictions for COVID-19 with deep learning models of LSTM, GRU and Bi-LSTM. *Chaos, Solitons & Fractals*. 2020;140:110212. https://doi.org/10.1016/j.chaos.2020.110212
27. Wang J., Wang P., Tian H., Tansey K., Liu J., Quan W. A deep learning framework combining CNN and GRU for improving wheat yield estimates using time series remotely sensed multi-variables. *Comput. Electron. Agric*. 2023;206(4):107705. https://doi.org/10.1016/j.compag.2023.107705
28. Hua H., Liu M., Li Y., Deng S., Wang Q. An ensemble framework for short-term load forecasting based on parallel CNN and GRU with improved ResNet. *Electric Power Syst. Res*. 2023;216(3):109057. https://doi.org/10.1016/j.epsr.2022.109057
29. Zhang D., Sun W., Dai Y., Liu K., Li W., Wang C. A hierarchical early kick detection method using a cascaded GRU network. *Geoenergy Sci. Eng*. 2023;222(3):211390. https://doi.org/10.1016/j.geoen.2022.211390
30. Gramovich I.V., Musatov D.Yu., Petrusevich D.A. Implementation of bagging in time series forecasting. *Russ. Technol. J*. 2024;12(1):101–110 (in Russ.). https://doi.org/10.32362/2500-316X-2024-12-1-101-110
31. McLeod A., Li W. Diagnostic checking ARMA time series models using squared residual autocorrelations. *J. Time Ser. Anal*. 1983;4(4):269–273. https://doi.org/10.1111/j.1467-9892.1983.tb00373.x

About the authors

Bakhtierzhon Pashshoev, Student, MIREA – Russian Technological University (78, Vernadskogo pr., Moscow, 119454 Russia). E-mail: bahtiyorposhshoev@gmail.com. https://orcid.org/0009-0000-2019-2642

Denis A. Petrusevich, Cand. Sci. (Phys.-Math.), Associate Professor, Higher Mathematics Department, Institute of Artificial Intelligence, MIREA – Russian Technological University (78, Vernadskogo pr., Moscow, 119454 Russia). E-mail: petrusevich@mirea.ru, petrdenis@mail.ru. Scopus Author ID 55900513600, ResearcherID AAA-6661-2020, RSCI SPIN-code 7999-6345, https://orcid.org/0000-0001-5325-6198

Об авторах

Пашшоев Бахтиёржон, студент, ФГБОУ ВО «МИРЭА – Российский технологический университет» (119454, Россия, Москва, пр-т Вернадского, д. 78). E-mail: bahtiyorposhshoev@gmail.com. https://orcid.org/0009-0000-2019-2642

Петрусевич Денис Андреевич, к.ф.-м.н., доцент, кафедра высшей математики, Институт искусственного интеллекта, ФГБОУ ВО «МИРЭА – Российский технологический университет» (119454, Россия, Москва, пр-т Вернадского, д. 78). E-mail: petrusevich@mirea.ru, petrdenis@mail.ru. Scopus Author ID 55900513600, ResearcherID AAA-6661-2020, SPIN-код РИНЦ 7999-6345, https://orcid.org/0000-0001-5325-6198

Translated from Russian into English by Lyudmila O. Bychkova
Edited for English language and spelling by Dr. David Mossop

MIREA – Russian Technological University.
78, Vernadskogo pr., Moscow, 119454 Russian Federation.
Publication date July 30, 2024.
Not for sale.

МИРЭА – Российский технологический университет.
119454, РФ, г. Москва, пр-т Вернадского, д. 78.
Дата опубликования 30.07.2024 г.
Не для продажи.